EVALUATION OF ZINC ELECTRODEPOSITION KINETICS FROM ACIDIC ZINC SULFATE SOLUTIONS USING A UPD MODIFIED PLATINUM SUBSTRATE

by

EDUARD GUERRA

B.Sc., Laurentian University of Sudbury, 1993

B.Eng., Laurentian University of Sudbury, 1993

M.A.Sc., The University of British Columbia, 1998

A THESIS SUBMITTED IN PARTIAL FULFILMENT OF

THE REQUIRMENTS OF THE DEGREE OF

DOCTOR OF PHILOSOPHY

in

THE FACULTY OF GRADUATE STUDIES

Department of Metals and Materials Engineering

We accept this thesis as conforming

to the required standard

THE UNIVERSITY OF BRITISH COLUMBIA

May 2003

In presenting this thesis in partial fulfilment of the requirements for an advanced degree at the University of British Columbia, I agree that the Library shall make it freely available for reference and study. I further agree that permission for extensive copying of this thesis for scholarly purposes may be granted by the head of my department or by his or her representatives. It is understood that copying or publication of this thesis for financial gain shall not be allowed without my written permission.

Department of Metals and Materials Engineering

The University of British Columbia
Vancouver, Canada

Date May 16, 2003

Abstract

Zinc is produced mainly by electrowinning from acidic zinc sulphate electrolytes. Electrowinning performance is often reported in terms of the specific electrical energy consumption, *SEEC*, which is a function of cell voltage, *U*. There is a fundamental relationship between cell voltage and current density. Establishing the parameters governing this relationship, as a function of solution composition and temperature, is critical for the design and optimisation of zinc electrowinning reactors. Zinc is a soft and reactive metal, which makes preparation of an electrode of well-defined and reproducible surface area, on which to conduct electrochemical polarization experiments, difficult. In addition, bulk zinc deposition occurring during cathodic polarization of the electrode causes irreversible morphology changes that alter the real surface are of the electrode.

In general, underpotential deposition, UPD, describes the formation of a two-dimensional layer of metal onto a foreign substrate at a potential more positive than that for overpotential deposition, OPD, of the metal. Use of this phenomenon is proposed as a novel technique for generating smooth and reproducible electrode surfaces of reactive metals, using zinc UPD on platinum as a model case. The technique involves polarization of a polished platinum electrode to cause zinc UPD followed by a pulsed polarization step to grow a bulk zinc metal deposit on the electrode. The steady-state zinc deposition rate is recorded as a function of the applied potential. Mass transfer effects are controlled by the use of a rotating disc electrode. After each potential step, the electrode is polarized to a potential near the UPD potential, which dissolves the bulk zinc and regenerates the original smooth electrode. In this manner the voltage – current density relationship for the zinc deposition reaction may be mapped for a particular solution composition.

Experiments were conducted to characterize UPD of zinc on platinum in magnesium sulphate and sulphuric acid supporting electrolytes. UPD of zinc on platinum occurs at a voltage approximately 1 V more positive than that of bulk zinc deposition with an estimated charge density of 260 ±30 $\mu C\ cm^{-2}$, which is in the order of a monolayer of zinc. The UPD layer was determined to evolve into a Pt-Zn alloy which further inhibited hydrogen evolution, relative to the freshly deposited UPD layer. Bulk zinc deposition experiments were carried out in pure zinc sulphate solutions at 25 °C, using the developed technique, and kinetic parameters were evaluated and compared to previously reported values. The Tafel slope for zinc deposition from

pH neutral electrolytes was determined to be *ca.* 60 mV dec^{-1}, while in highly acid electrolytes was *ca.* 30 mV dec^{-1}, due to the inhibiting effect of hydrogen adsorption. The transition of zinc deposit morphology from a relatively smooth deposit to a dendritic deposit was confirmed to occur at *ca.* 1000 A m^{-2} in 1.0 mol dm^{-3} $ZnSO_4$. By virtue of the low value of the Tafel slope, the current density for zinc deposition is highly sensitive to overpotential (increasing tenfold for every 30 mV increase). Dendritic growth in industrial zinc electrowinning at a conventional current density of *ca.* 500 A m^{-2} was attributed to the effects on the local current distribution from the vertical distribution of ohmic drop in the electrolyte and screening of the cathode by attached bubbles. The use of forced convection to mitigate these effects is proposed as a means of extending the current density range of zinc electrowinning.

Table of Contents

List of Figures

List of Tables

Acknowledgments

Firstly, I would like to thank Dan Bizzotto. Without his support and technical assistance, this project would never have been completed. I'd like to also acknowledge David Dreisinger, who, through the Industrial Research Chair in Hydrometallurgy, provided much of the financial support for this project. Thanks too to Geoff Kelsall for his continued assistance with this project after leaving UBC.

On a more personal level, to my wife, Christine Guerra, through the disappointment at U of T, the endless late nights and meals alone, and all the times when I didn't think I'd make it; Thank you so much for standing by me. I'd also like to thank my parents, Anselmo and Maria-Teresa Guerra, and my wife's parent Bill and Louise Chandler, for their encouragement and support. I want to acknowledge the companionship and camaraderie of my labmates and colleagues: Erin Young, Pat Turner, Massimiliano Bestetti, Marie Li, Emily Chung, John Agak, Yanguo Yang, Robin Stoodley, and, in particular, Jeff Shepherd for keeping me sane with his sense of humour and friendship. I'd also like to credit my faith in God and Jesus Christ with giving me strength during the darker days of this project.

Finally, I'd like to thank Mary Mager for her help with the SEM and EDX analyses, Phil Wong and Ken Wong for the XPS analyses, Anders Ballestad for his help with interpretation of the AFM images, Alberto Gonzalez for the solution analyses, Canadian Scientific Glassblowing for constructing my electrochemical cells, and Ross McLeod and Carl Ng for constructing the lids for the cells.

1 Introduction

Zinc metal is mainly produced by electrowinning in parallel plate electrolytic cells from aqueous solutions containing primarily zinc sulphate, 55 to 75 g dm^{-3} Zn^{2+}, and sulphuric acid, 125 to 175 g dm^{-3} H_2SO_4, at 35 to 45 °C. Zinc electrowinning involves at least three cathodic reactions: zinc deposition, hydrogen evolution and oxygen reduction:

$$Zn^{2+} + 2e^- \rightarrow Zn \qquad \text{Equation 1.1}$$

$$2H^+ + 2e^- \rightarrow H_2 \qquad \text{Equation 1.2}$$

$$O_2\,(aq) + 4H^+ + 4e^- \rightarrow 2H_2O \qquad \text{Equation 1.3}$$

The current efficiency of zinc electrowinning, Φ_e, is the ratio of the zinc deposition current, I_{Zn} (A), to the total current, I (A). Hydrogen evolution and oxygen reduction represent the main sources of current inefficiencies. The anodic reaction is, conventionally, oxygen evolution:

$$2H_2O \rightarrow O_2 + 4H^+ + 4e^- \qquad \text{Equation 1.4}$$

Electrowinning performance is extremely sensitive to electrolyte purity and resulting zinc deposit purity. Hydrogen evolution on impure zinc can be in the order of 1000 times that on pure zinc [1]. Even after conventional solution purification stages, iron hydrolysis and zinc dust cementation; zinc electrolytes will typically contain significant quantities of magnesium, manganese, and ammonia, along with trace amounts of other elements as well as organic additives. Industrial research into how zinc electrolyte composition affects electrowinning performance has, thus, largely focused on electrolytes that contain impurities within concentration ranges encountered in industrial electrolytes using cell designs and operating conditions which mirror industrial practise. The possible application of solvent extraction [2, 3, 4] and insoluble dimensionally stable anodes [4, 5, 6, 7, 8, 9], capable of maintaining ultra-pure zinc electrolytes, raises the possibility of electrowinning zinc under conditions outside the ranges

of conventional practise. However, there is a lack of a broad body of fundamental research on zinc electrodeposition from pure acidic sulphate solutions. The inconsistent and often conflicting values of kinetic parameters, reported in the few published studies in the literature, make it impossible to predict electrowinning performance under non-conventional operating conditions or to design non-conventional cells to operate at high current density.

Electrowinning performance is often reported in terms of the specific electrical energy consumption, *SEEC*, which is a function of cell voltage, U (V), current efficiency, Φ_e, the molecular mass of zinc, M_{Zn} (g mol^{-1}), the number of electrons in the overall deposition reaction, $n = 2$, and Faraday's constant, F (96485 C eq^{-1}).

$$SEEC\ /\ kWh\,(tonne\ Zn)^{-1} = \frac{nF|U|}{3.6 M_{Zn}\Phi_e} \qquad \text{Equation 1.5}$$

Zinc electrowinning consumes a large amount of electricity, *ca.* 3300 kWh (tonne Zn)$^{-1}$. Lowering the cell voltage is an important consideration when attempting to lower the *SEEC*. The cell voltage is conventionally represented as a function of current density, j (A m^{-2}), which is the current normalized on a per unit electrode area basis, and is equal to the sum of the reversible potentials for the anodic and cathodic reactions, E_{H_2O} and E_{Zn}, their associated overpotentials, $\eta_{H_2O}(j)$ and $\eta_{Zn}(j)$ and ohmic potential drop through the cell, jA_eR.

$$U(j) = -\left(E_{H_2O} + \eta_{H_2O}(j) - E_{Zn} - \eta_{Zn}(j) + jA_eR\right) \qquad \text{Equation 1.6}$$

where; A_e is the electrode area (m^2), and R is the total resistance (Ω). Methods for estimating the separate contributions of these voltage components to the overall cell voltage have been previously reported by the author [10] and by Barton and Scott [11]. The application of these estimates for optimisation of electrowinning current density, with the goal of minimizing operating costs, has been described by Bestetti et al. [4] for Zn electrowinning in particular and by Walsh [12], for electrochemical reactors in general.

The combination of the zinc equilibrium potential and zinc deposition overpotential typically account for only *ca.* 24 % of the overall cell voltage in conventional zinc electrowinning [13]. However, these are the only elements which are intrinsic to the electrolytic production of zinc from acidic sulphate electrolytes. The voltages associated with anode reaction and ohmic drop

may be reduced by use of an alternative electrolytic cell such as a hydrogen gas diffusion anode in a drum cell. Thus, accurately establishing the relationship between current density and voltage requirements for zinc electrodeposition is critical for the design and optimisation of zinc electrowinning reactors. The following research will focus on estimating the zinc equilibrium potential and overpotential requirements for zinc electrodeposition from highly pure acidic zinc sulphate electrolytes. The relationship between overpotential and zinc deposition current density, discussed in the proceeding sections, contains a number of interacting parameters that depend on solution composition. These effects will be modelled through the results of a series of electrochemical polarization experiments. The importance of performing zinc overpotential deposition, OPD, experiments on a smooth electrode will be addressed by examining the use of zinc UPD on platinum as a method for generating a suitable electrode surface. The issues of solution purity, control of mass transfer effects, and the accurate estimation of the physical properties of zinc electrolytes will also be addressed. Ultimately, by applying a fundamental approach to the study of the kinetics of zinc electrodeposition from a pure electrolyte, the effects of current density, zinc concentration and sulphuric acid concentration on the voltage requirement for zinc electrodeposition at 25 °C will be elucidated. These results will be discussed in terms of their implications towards industrial zinc electrowinning at high current density.

2 Literature Review

This section reviews the current state of knowledge for predicting the voltage requirement of zinc electrodeposition from acidic zinc sulphate electrolytes. In general, this voltage is composed of the sum of the equilibrium potential (the potential where zinc deposition and dissolution occur at equal rates, i.e. no net reaction occurs), E_{Zn} (V), and the overpotential, η_{Zn} (V), the voltage which causes deviations from equilibrium.

The zinc equilibrium potential may be calculated from the Nernst Equation:

$$E_{Zn} = E^{\circ}_{Zn} + \frac{RT}{nF}\ln\left(\frac{aZn^{2+}}{aZn}\right) \qquad \text{Equation 2.1}$$

where; $E^{o}{}_{Zn}$, is the standard reduction potential for zinc electrodeposition, -762 mV (NHE) or -1004 mV (SCE), R is the universal gas constant, 8.31447 (J mol^{-1} K^{-1}), T is the absolute temperature (K), aZn is the activity of zinc metal (equal to unity for pure zinc), and aZn^{2+} is the molal activity of zinc ions. As indicated, prediction of the equilibrium potential requires an estimation of the activity of zinc ions which will be addressed in Section 2.3.

The zinc deposition overpotential is defined as the difference between the applied potential at the electrode surface, E, and zinc equilibrium potential, E_{Zn}.

$$\eta_{Zn} = E - E_{Zn} \qquad \text{Equation 2.2}$$

At large cathodic polarizations, more negative than *ca.* -100 mV, and in the absence of mass transfer effects, the relationship between overpotential, η_{Zn}, and the resulting deposition current density, j_{Zn}, may be modelled by the familiar Tafel Equation:

$$\eta_{Zn} = \frac{2.303RT}{\alpha nF}\log(j_{0,Zn}) - \frac{2.303RT}{\alpha nF}\log(j_{Zn}) = a - b\log(j_{Zn}) \qquad \text{Equation 2.3}$$

where; a (V) is the Tafel constant and b (V dec^{-1}) is the Tafel slope.

A more rigorous expression of the zinc current density-overpotential relationship is the Extended Butler-Volmer Equation which includes provisions to account for mass transfer effects and the rate of anodic dissolution of zinc at low deposition overpotentials:

$$j_{Zn} = \frac{I_{Zn}}{A_e} = \frac{-j_{0,Zn}\left[e^{\frac{-\alpha nF\eta_{Zn}}{RT}} - e^{\frac{(1-\alpha)nF\eta_{Zn}}{RT}}\right]}{1 - \frac{j_{0,Zn}}{j_{\lim,Zn}} e^{\frac{-\alpha nF\eta_{Zn}}{RT}}}$$ Equation 2.4

where; I_{Zn} (A) is the zinc deposition current, A_e (m^2) is the zinc electrode area, j_{Zn} (A m^{-2}) is the zinc deposition current density, $j_{\lim,Zn}$ (A m^{-2}) is the limiting current density, $j_{0,Zn}$ (A m^{-2}) is the exchange current density, and, α ($1 \geq \alpha \geq 0$) is the transfer coefficient, typically having a value of 0.5 [14]. A derivation of the Extended Butler-Volmer Equation appears as Appendix A. In the following chapters, the significance of each of the above parameters were examined in terms of their physical meanings, previous estimates of their values or equations for their calculation which are reported in literature, and experimental considerations for their measurement. Particular emphasis was placed on sulphate based electrolytes because of their relevance to zinc electrowinning.

2.1 Zinc Deposition Current Efficiency

Zinc electrodeposition from acidic sulphate electrolytes is always accompanied by some degree of hydrogen evolution. When estimating zinc deposition current density, the first issue that must be addressed is isolation of the zinc deposition current from the total current, i.e. the measurement of current efficiency. Deoxygenation of the electrolyte prior to zinc electrodeposition eliminates current inefficiencies due to oxygen reduction.

Experimental evaluation of current efficiency is often based on comparing the mass of zinc deposited and the total quantity of charge passed, Q (C):

$$\Phi_e = \frac{g\ Zn\ deposited}{Q}\frac{2F}{M_{Zn}}$$ Equation 2.5

However, this procedure is tedious, requiring careful handling and weighing of the cathode and deposition of relatively large quantities of zinc for each set of experimental conditions, in order to minimize errors due to redissolution and surface oxidation. Faster techniques have recently been used to determine current efficiency during zinc electrodeposition such as; detection of evolved hydrogen using a rotating ring disc electrode [15, 16, 17] and normal pulse voltammetry

[18]. The details of the application of these techniques are discussed in Sections 3.1.3 and 3.3.2, respectively.

2.1.1 Effect of Electrolyte Purity

Solution purity is an important factor to consider when attempting to measure current efficiency as a function of electrolyte composition. Current efficiencies in industrial zinc electrowinning are, typically, > *ca.* 90 % even though the hydrogen evolution overpotential is more negative than *ca.* -800 mV. This feature is expressed in the relatively small value of mean exchange current density for hydrogen evolution on zinc in 0.5 mol dm^{-3} H_2SO_4 at 25 °C, 3.16×10^{-7} A m^{-2} [19]. The highest achievable current efficiencies occur in impurity-free electrolytes. The lower current efficiencies, observed in industrial zinc electrolytes, are due to enhanced hydrogen evolution on codeposited impurities [20, 21, 22, 23]. With respect to this issue, current efficiencies of 95 to 99 % have been reported for highly purified acidic zinc sulphate electrolytes [15, 20, 24, 25, 26, 27]. Thus, this research will focus on impurity-free electrolytes to minimize the magnitude of hydrogen evolution and its impact in the calculation of the zinc deposition current as well as to provide a better idea of the limits of current efficiency for electrolytic production of zinc.

2.1.2 Effect of Electrolyte Composition

The concentrations of zinc sulphate and sulphuric acid are the major factors affecting current efficiency of zinc electrodeposition. The following empirical relationship, which is commonly referred to as Wark's rule [28], predicts current efficiency in industrial zinc electrowinning based on the ratio of zinc sulphate and sulphuric acid:

$$\frac{\Phi_e}{1-\Phi_e} = \frac{1}{k}\frac{zinc\,sulphate\,concentration}{sulphuric\,acid\,concentration} \qquad \text{Equation 2.6}$$

As previously mentioned, current efficiency in zinc electrowinning is sensitive to electrolyte purity and, hence, the magnitude of k depends on the nature and concentration ranges of impurities for a particular electrolyte. The value of k, based on Wark's data [21] for a highly purified industrial electrolyte which contained 15 mg dm^{-3} SiO_2 and 0.6 mg dm^{-3} Mn, was approximately 0.033, while Biegler and Frazer [26] estimated k to be 0.0137 using synthetic electrolytes containing no detectable impurities. As indicated in Figure 1, Wark's rule appears to

hold for $[ZnSO_4]/[H_2SO_4]$ ratios of between 0.3 and 2.0, which brackets the range of 0.5 to 0.75, typical of most industrial zinc plants [26].

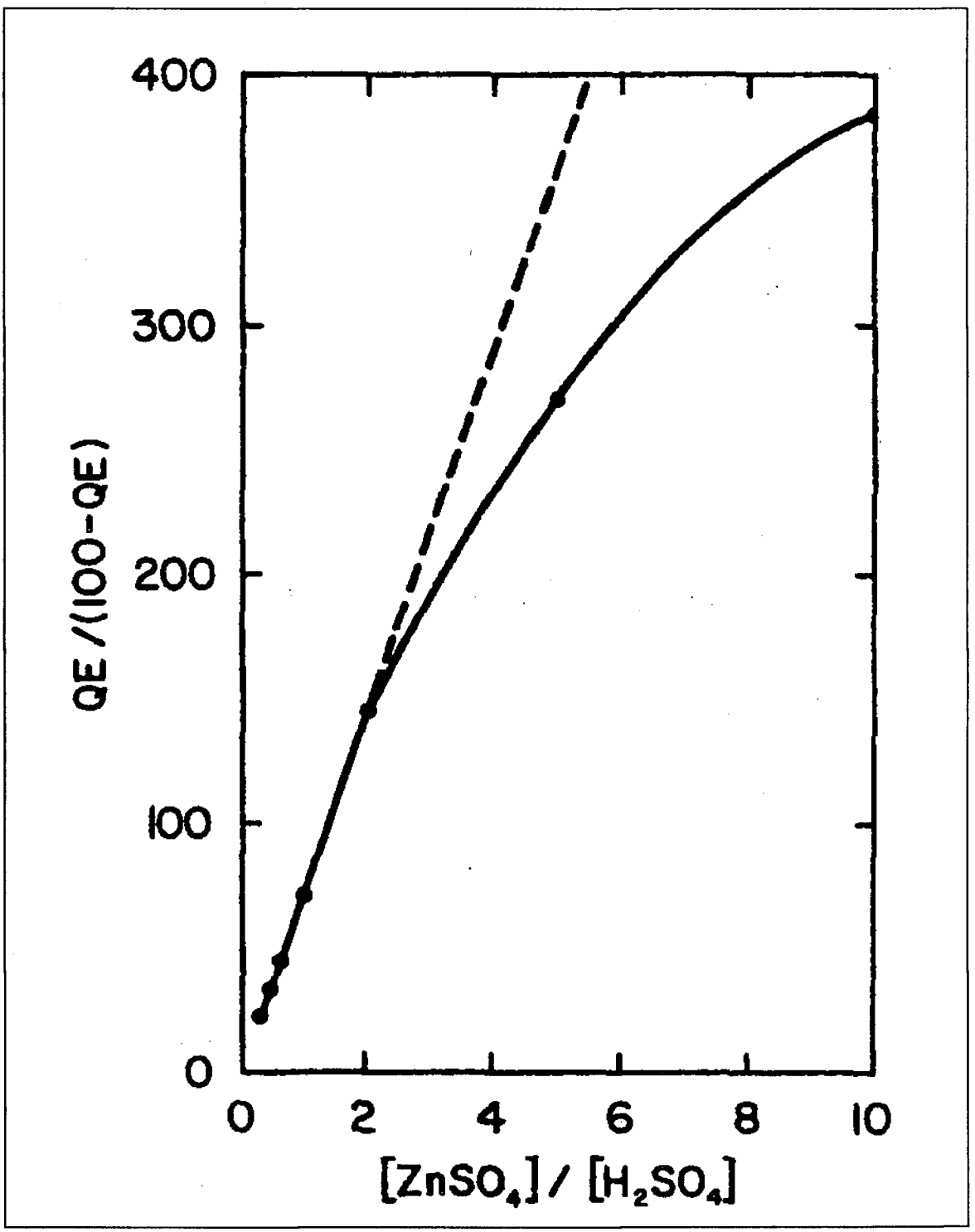

Figure 1: Test of Wark's Rule for deposition of zinc from ultra-pure zinc sulphate/sulphuric acid electrolytes onto an aluminum rotating disc electrode, 2300 rpm rotation speed, current density of 890 A m^{-2}, 54 minute deposition time, 61 °C. Taken from [26].

The theoretical basis of Wark's Rule was derived, on the presumption of Tafel kinetics, by Bratt [29] who assigned αn, the product of the transfer coefficient and the number of electrons transferred in the rate determining step, values of 1.0 for zinc deposition and 0.5 for hydrogen evolution:

$$\frac{1}{k} = \frac{K_{Zn}\gamma Zn^{2+}}{K_H \gamma H^+} \exp\left(\frac{-\eta_{Zn}F}{RT} + \frac{0.5\eta_H F}{RT}\right) \qquad \text{Equation 2.7}$$

where; K_{Zn} and K_H are constants which are related to the exchange current densities for zinc deposition and hydrogen evolution, respectively. The consistency in k is attributed to a relatively constant ratio of the activity coefficients of zinc and hydrogen ions over the compositional range of typical zinc electrowinning electrolytes. In the model of zinc electrowinning developed by Barton and Scott [11], the values of the zinc ion activity coefficient and proton activity coefficient are treated as being independent of electrolyte composition and are fixed at 0.1 and 0.5, respectively. In reality, the activity coefficients should be a function of the ionic strength of the electrolyte which varies with electrolyte composition. This issue will be addressed later in Section 2.3.2.

2.1.3 Effect of Current Density

Implicit in Wark's rule is that current efficiency is insensitive to current density, which is generally observed in conventional zinc electrowinning. However, Cachet and Wiart [30] have demonstrated that current efficiency decreases dramatically at zinc deposition current densities less than *ca.* 20 A m^{-2} in deoxygenated electrolytes. This may be expected since zinc dissolution rates are probably significant at this low of a current density. In addition, several researchers have observed that current efficiency actually increases with increasing current density in systems employing non-conventional cell designs or forced convection [24, 31, 32, 33]. By inspection of Equation 2.7, the value of k should be only relatively constant at low zinc deposition overpotentials where the exponential term is dominated by the hydrogen evolution overpotential. There is an error in Bratt's derivation beyond this point. After rightly indicating that the zinc deposition reaction and hydrogen evolution reactions occur at the same electrode potential, $E = E_H = E_{Zn}$, the derivation proceeds as though the overpotentials were equal, which they are not, $\eta_H \neq \eta_{Zn}$. However, this oversight does not affect the validity of Bratt's ultimate conclusion, that k should decrease (current efficiency should increase) as the zinc deposition

overpotential is shifted to larger negative values and correspondingly higher current densities [29].

2.2 Zinc Electrode Area

The current density term in the Butler-Volmer Equation is based on the assumption that the electrode is a smooth planar surface with a uniform potential distribution. DeLevie [34] calculated the potential distribution an electrode surface composed of semi-infinite pores which was likened to the surface of an extremely rough electrode. The predicted effect on electrode kinetics was a doubling of the Tafel slope compared to otherwise identical smooth electrode, i.e. twice as much overpotential is required to cause an order of magnitude change in current density on a rough electrode compared to a smooth electrode. Therefore, the reproducible preparation of a smooth electrode surface is extremely important for accurate estimation of the kinetic parameters for electrodeposition reactions. However, the growth of deposits from electrodeposition reactions, by their nature, can significantly alter the morphology and surface area of the electrode on which they occur. The preparation and maintenance of zinc electrode surfaces using pure zinc, zinc electrodeposition on aluminium, and zinc electrodeposition on platinum will be discussed with respect to these issues.

2.2.1 Pure Zinc Electrode

Using pure zinc is a natural choice for electrode material on which to conduct zinc electrodeposition studies, but zinc is soft and oxidizes readily, which makes preparation of a smooth and reproducible zinc electrode surface difficult. Historically, zinc electrodes have been prepared from high purity zinc rods which were polished using emery paper and then etched with diluted HCl or $HClO_4$ [35, 36, 37, 38]. More recent studies [39, 40, 41, 42] also employed abrasive papers and polishing cloths with diamond or alumina pastes to polish zinc electrodes without the use of chemical etchants.

There are several restrictions and limitations to the use of pure zinc electrodes. The electrodes must be used immediately after polishing in order to avoid excessive oxidation. Another drawback of using a zinc electrode is that, due to irreversible changes to the electrode surface morphology resulting from deposition of zinc, the electrodes must be removed from solution and laboriously re-polished after each polarization routine.

2.2.2 Zinc Electrodeposition on Aluminium

Deposition of zinc on aluminium to create a zinc coated electrode is an attractive notion since the underlying electrode geometry is unaffected by repeated cycles of zinc deposition and stripping. Industrially, zinc is electrowon onto aluminium alloy cathodes on which zinc deposits heterogeneously at grain boundaries and on intermetallic particles, predominantly Fe, which disrupt the alumina layer and act as electrical pathways [43, 44, 45]. On a macroscopic scale, these nuclei are relatively closely spaced and, with the aid of a levelling agent, grow together and spread out over the aluminium cathode creating a sheet of zinc. The fact that the zinc layer is only mechanically attached to the aluminium substrate at nucleation sites permits the deposited zinc layer to be stripped off relatively easily, thereby allowing the aluminium cathodes to be cleaned and reused. Unfortunately, these traits that are of practical benefit to industrial zinc electrodeposition: heterogeneous nucleation, three dimensional growth, and a loosely adherent deposit, make the production of a smooth, well-defined and reproducible zinc surface on pure aluminium extremely difficult. Cachet and Wiart [30, 46] have used aluminium rotating disc electrodes for zinc electrodeposition studies which were polished with 1200 grit emery paper before each use. This procedure probably resulted in a relatively thin and discontinuous alumina layer onto which zinc would appear to deposit relatively homogenously. However, the nuclei would still have required time to grow together to cover the electrode, which is probably why the steady-state deposition current densities were recorded after relatively long polarization times, typically, greater than 10 minutes. Such long polarization times are disadvantageous in that they lead to outward growth of the deposit which increases the geometric area of the electrode and, subsequently, lead to overestimation of the current density (typically the current density is calculated based on the original geometric area of the electrode).

2.2.3 Zinc Electrodeposition on Platinum

Platinum is an unlikely candidate as a substrate for zinc deposition from acidic electrolytes. From Figure 2, which was generated by Kelsall [47] from published Tafel constants [19], hydrogen evolution on platinum is predicted to be in the order of 10^7 A m^{-2} at a potential near the standard reduction potential of zinc, *ca.* -762 mV (NHE). The solubility of dissolved hydrogen in aqueous electrolytes is in the order of a few ppm and this evolution rate would certainly lead to complete coverage of the platinum electrode by hydrogen gas bubbles. This type of bubble layer would prevent any zinc deposition, let alone deposition of a uniform and smooth zinc layer.

However, there are numerous reports of zinc electrodeposition on platinum from acidic sulphate electrolytes [48, 49, 50, 51, 52], yet there has been little mention of the underlying inhibition of hydrogen evolution that must have occurred to allow for zinc deposition. A possible explanation for the utility of platinum as a substrate for zinc deposition lies in the occurrence of zinc UPD on platinum, at *ca.* -250 mV (SCE), which has been recently identified and studied by Aramata et al. [53, 54, 55, 56, 57, 58, 59, 60].

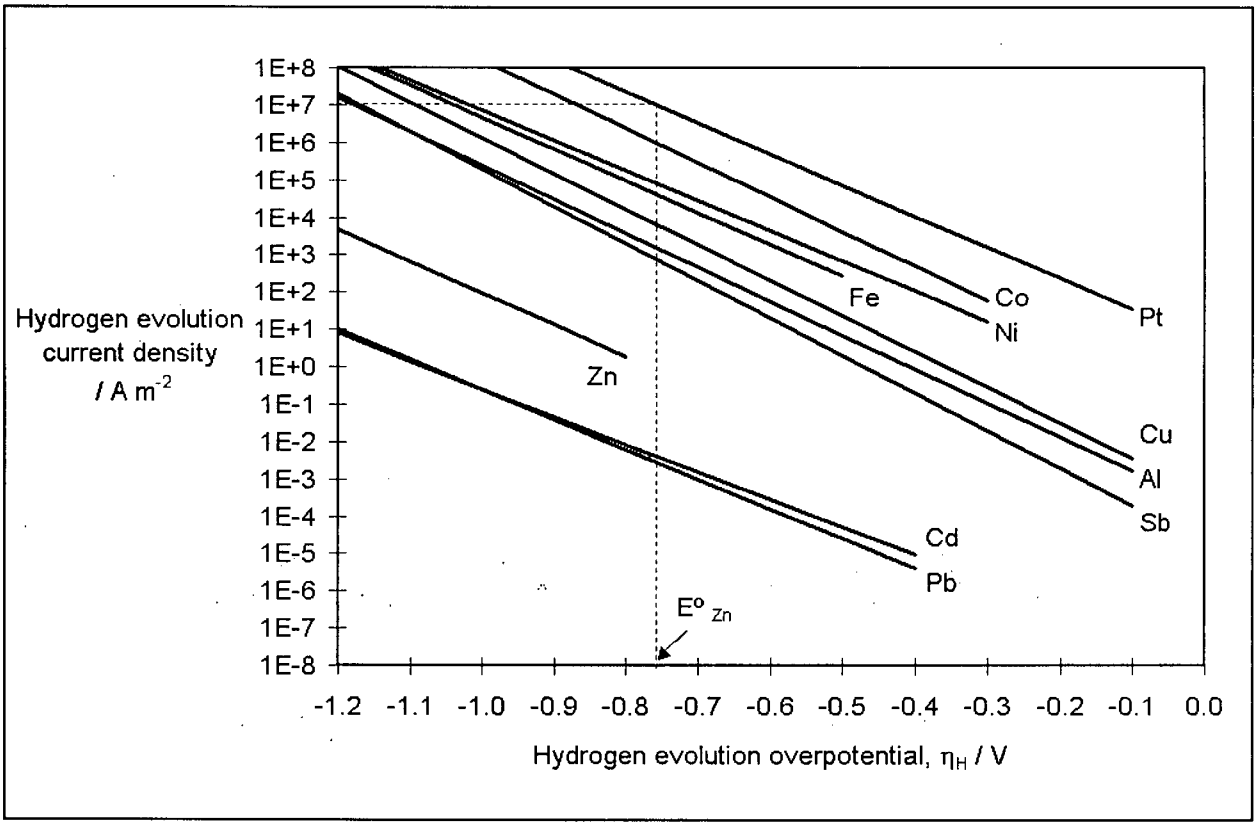

Figure 2: Hydrogen evolution current density on various substrate metals in 1 mol dm^{-3} H_2SO_4 at 25 °C, as a function of hydrogen evolution overpotential.

In general, underpotential deposition, UPD, describes the formation of a two-dimensional layer of metal, Me, onto a foreign substrate, S, at a potential more positive than that for bulk deposition of the metal. The reduction potentials for bulk Zn deposition and Zn UPD on Pt are obtained by the Nernst equation as follows:

$$E_{Zn} = E^{\circ}_{Zn} + \frac{RT}{nF}\ln\left(\frac{aZn^{2+}}{aZn}\right) \qquad \text{Equation 2.1}$$

$$E_{Zn\,upd} = E^{\circ}_{Zn\,upd} + \frac{RT}{nF}\ln\left(\frac{aZn^{2+}}{aZn_{upd}}\right)$$ Equation 2.8

The potential difference between bulk Zn deposition and Zn UPD on Pt, ΔE (called the "UPD shift"), is obtained by subtracting Equation 2.1 and Equation 2.8 as follows:

$$\Delta E = E_{Zn} - E_{Zn\,upd} = E^{\circ}_{Zn} - E^{\circ}_{Zn\,upd} + \frac{RT}{nF}\ln\left(\frac{aZn_{upd}}{aZn}\right)$$ Equation 2.9

The UPD shift is independent of ion activity (provided that the number of electrons transferred in the UPD reaction is equal to that of the bulk deposition reaction) and represents the difference in chemical potentials due to the interaction between Zn and the interaction between Zn and Pt. As the UPD layer is a condensed phase, its activity should be constant. However, the UPD potential, $E_{Zn\,upd}$, has been reported to be somewhat dependent on the nature of the electrolyte. The small variations in the potential shift for the onset of Zn UPD are attributed to the effects on its activity of different adsorbed species over the UPD layer which ranges from 1.04 V to 1.19 V [54]. Whatever the value of $E_{Zn\,upd}$, the UPD layer is stable at potentials more negative than this value. The main point is that the UPD shift represents a relatively constant potential window between the UPD and OPD and, in the case of Zn UPD on Pt, this potential window is in the order of one Volt.

In the absence of UPD layer formation, or in cases where a significant crystallographic misfit between the depositing metal and the substrate exists, overpotential deposition, OPD, of the metal over the substrate results in an increase in the real surface area of the electrode. In these cases, metal deposition must overcome a significant energy barrier related to the interfacial energy between the depositing metal phase and the substrate as well as between the depositing metal and the solution. In order for bulk deposition to initiate, this energy must be overcome by supplying an overpotential which is termed the critical overpotential, η_{crit} (V). If the critical overpotential is relatively large, e.g. *ca.* -100 mV as is the case of Zn OPD on Al, then as nuclei are formed, metal growth at these sites proceeds rapidly leading to extremely heterogeneous and rough deposits. However, if a Me-S UPD system can be selected such that the degree of crystallographic misfit is small, then the critical overpotential should be relatively small. OPD of the metal over such a UPD covered substrate should progress by epitaxial layer-by-layer growth, referred to as Franck-van der Merwe growth mode. Thus, the crystallographic orientation and

surface area of the OPD Me can be taken to be the same as the original surface of the substrate. Metal deposition on UPD modified substrates has been reviewed [61], and the more general literature on electrochemical phase formation and growth, including growth on UPD modified substrates [62]. The identification of a particular Me-S UPD system can be accomplished experimentally, using standard electrochemical techniques, or predicted from theoretical calculations [63, 64].

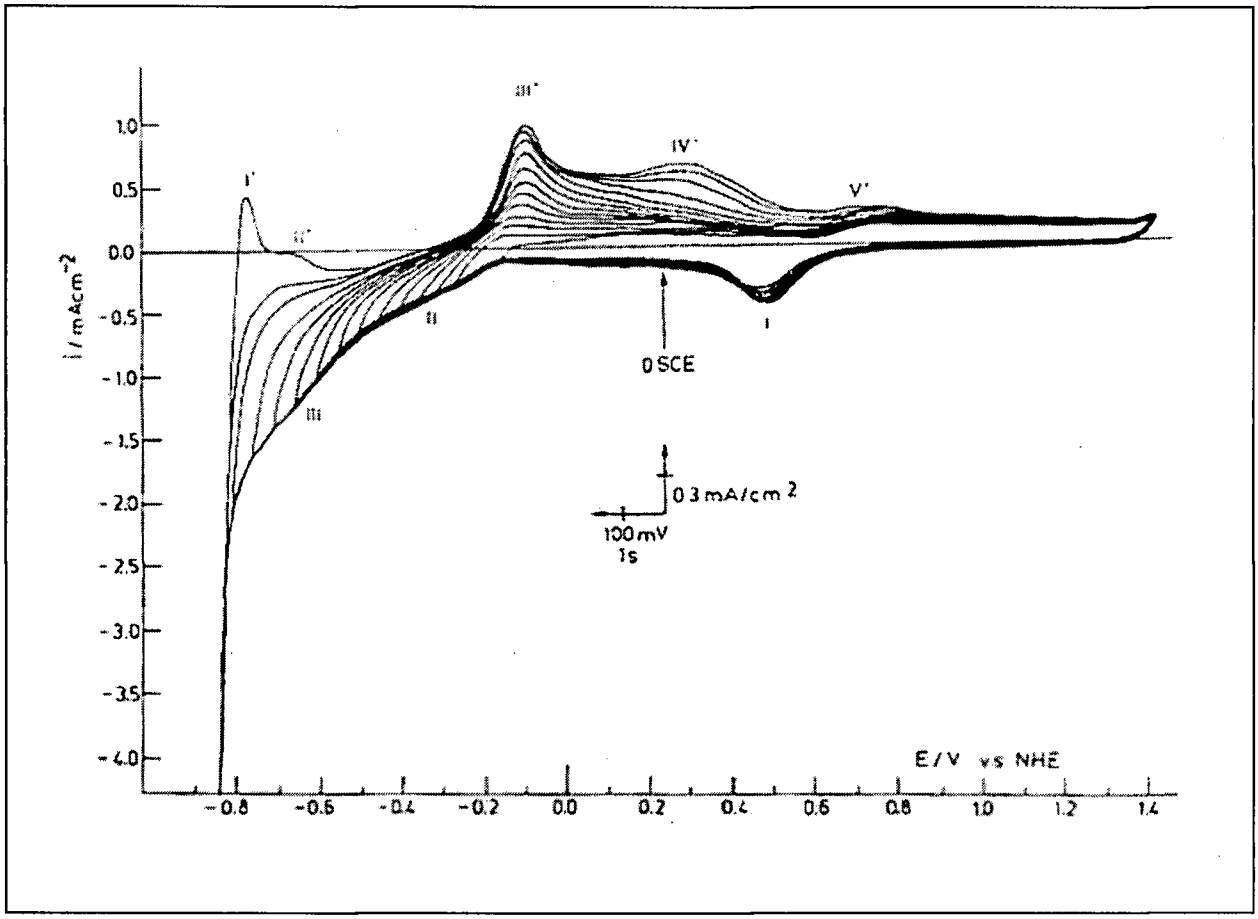

Figure 3: Cyclic voltammograms of a stationary polycrystalline platinum electrode in 1.5 mol dm^{-3} $ZnSO_4$ with 0.02 mol dm^{-3} $Al_2(SO_4)_3$ and 0.17 mol dm^{-3} Na_2SO_4, pH = 3.5, at 25 °C, scan rate 100 mV s^{-1}. Taken from [51].

The UPD of zinc on platinum was first described by Despić and Pavlović [51], who recognized a potential region, labelled **III** in Figure 3, at which a monolayer quantity of zinc deposits prior to bulk zinc deposition. However, as previously indicated, this was not the potential region where the UPD layer first forms, but where a zinc overlayer probably deposits on an already UPD modified surface. The region in Figure 3, where the current increases sharply at *ca.* – 0.85 V (NHE), is the region of zinc deposition. The fact that the current became sharply cathodic (went straight down on the voltammogram) and then retraced itself indicated that the critical

overpotential for Zn OPD on Pt was relatively small, which had been previously described by Lackmann and Linsel [49].

By applying relatively low overpotential pulses for extended times, Despić and Pavlović also found that the corresponding bulk zinc deposition current response on platinum was independent of time (Figure 4). This suggested that the real surface area of the electrode was independent of time, consistent with two-dimensional layer-by-layer growth of the zinc deposit, which would have maintained the original surface area of the underlying platinum electrode [51]. This result is compatible with the Zn-Pt crystallographic misfit, f, which is calculated from the inter-atomic distances, d, between Zn-Zn, 2.665 Å, and Pt-Pt, 2.775 Å:

$$f = \frac{d_{0,Zn} - d_{0,Pt}}{d_{0,Pt}} = \frac{2.665 - 2.775}{2.775} = -0.04 \qquad \text{Equation 2.10}$$

The relatively small negative value of the crystallographic misfit suggests that, in the absence of specifically adsorbed anions, UPD zinc can fully occupy interstitial sites on the platinum surface.

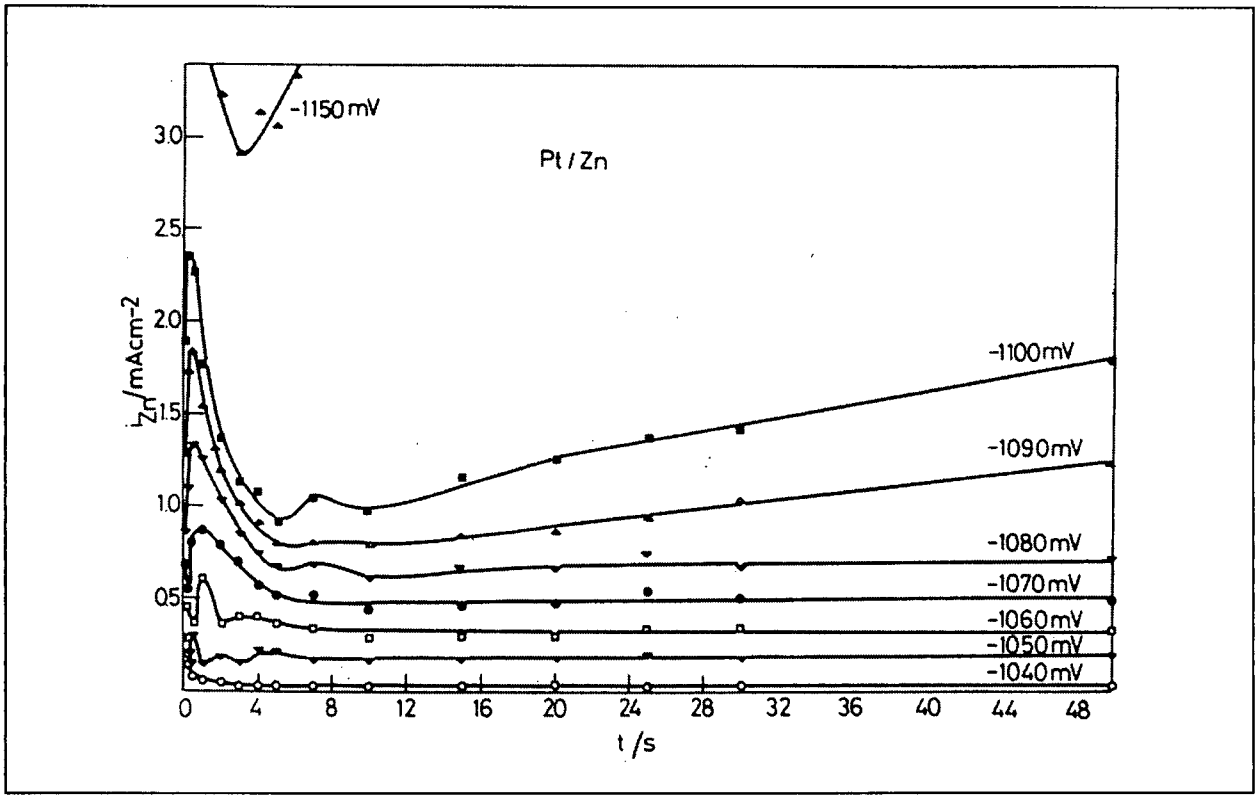

Figure 4: Current density of zinc deposition from 1.5 mol dm^{-3} $ZnSO_4$ with 0.02 mol dm^{-3} $Al_2(SO_4)_3$ and 0.17 mol dm^{-3} Na_2SO_4, pH = 3.5, at 25 °C, as a function of cathodic pulse duration at different overpotentials on a stationary platinum electrode. Taken from [51].

The rise in the stripping current in region **V'** in Figure 3, was interpreted as resulting from the formation of an alloy, from which zinc was oxidised only as the platinum substrate was oxidized [51]. The electrodeposition of zinc onto platinum from sulphate solution has long been determined to result in the formation of a 1:1 Zn-Pt surface alloy [48]. The alloy resulting from bulk zinc deposition cannot be removed with hot nitric or hot hydrochloric acid, but can be removed using aqua regia (which would also dissolve the platinum substrate) [48]. Inspection of the Pt-Zn phase diagram, Figure 5, reveals a large stability region for the 1:1 Pt-Zn alloy. Although no thermodynamic data are available for this system [65] there is obviously a strong interaction between zinc and platinum.

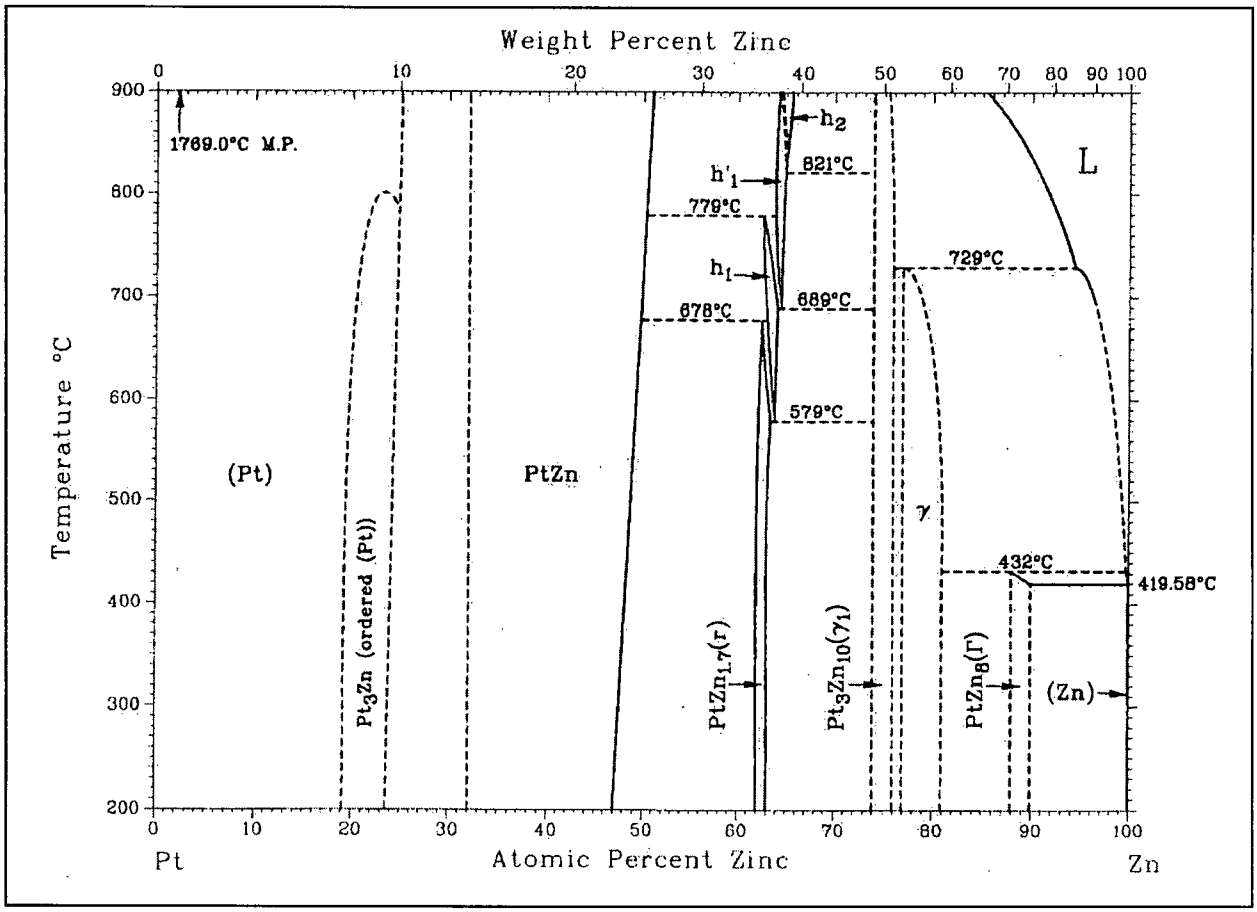

Figure 5: Partial Pt-Zn Phase Diagram. Taken from [65].

Overall, the inherent inhibition of hydrogen evolution on a zinc UPD layer on platinum and the apparent homogeneous nucleation and growth of OPD zinc above the UPD layer suggest that this is a promising system for the preparation of a zinc electrode to study the kinetics of zinc electrodeposition.

2.3 Zinc Deposition Overpotential

As previously described, evaluation of zinc deposition overpotential, at a given applied potential, requires an estimation of the equilibrium potential for zinc deposition. The zinc equilibrium potential is related through the Nernst Equation to the molal activity of zinc ions, aZn^{2+}, which, in turn, is equal to the product of molality, mZn^{2+} (mol kg^{-1}), and molal activity coefficient, γZn^{2+}, as indicated in Equation 2.11:

$$aZn^{2+} = mZn^{2+}\gamma Zn^{2+} \qquad \text{Equation 2.11}$$

In concentrated electrolytes, up to an ionic strength of *ca.* 0.1 mol$^{-1/2}$ kg$^{1/2}$, the effect of electrostatic interactions on the activity coefficient of a specific ionic species, *i*, may be calculated using the Debye-Hückel Limiting Law, DHLL:

$$\log \gamma_i = \frac{-Az_i^2\sqrt{I_m}}{1 + a_i B\sqrt{I_m}} \qquad \text{Equation 2.12}$$

where; A (0.51159 mol$^{-1/2}$ kg$^{1/2}$ at 25 °C)and B (3.2914×10^9 m^{-1} at 25 °C) are the temperature dependent Debye-Hückel constants, z_i is the charge of the ion, a_i (m) is the ion size parameter, and I_m (mol$^{-1/2}$ kg$^{1/2}$) is the ionic strength of the electrolyte:

$$I_m = \frac{1}{2}\sum_i z_i^2 m_i \qquad \text{Equation 2.13}$$

In the Debye-Hückel equation, the numerator accounts for long range electrostatic interactions while the denominator accounts for short range interactions.

2.3.1 Modeling of Zinc Ion Activity in Neutral Zinc Sulphate Electrolytes

Several authors have proposed models for predicting the activities and species distribution of concentrated zinc sulphate solutions [66, 67, 68, 69, 70] which are based on further extensions of the DHLL. The deviation of zinc sulphate activity from that predicted by the Debye-Hückel equation at relatively low concentrations is attributed, mainly, to the formation of uncharged zinc sulphate ion-pairs, $Zn^{2+}SO_4^{2-}(aq)$. The correction of predicted activities is conventionally accomplished by reducing ionic strength through the following reaction:

$$Zn^{2+} + SO_4^{2-} \xleftrightarrow{K} Zn^{2+}SO_4^{2-}(aq)$$ Equation 2.14

$$K = \frac{aZn^{2+}SO_4^{2-}(aq)}{aZn^{2+}aSO_4^{2-}} = \frac{\gamma Zn^{2+}SO_4^{2-}(aq)mZn^{2+}SO_4^{2-}(aq)}{\gamma Zn^{2+}mZn^{2+}\gamma SO_4^{2-}mSO_4^{2-}} = \frac{(1-\alpha)\gamma Zn^{2+}SO_4^{2-}(aq)}{\gamma Zn^{2+}\gamma SO_4^{2-}\alpha^2 mZnSO_4}$$ Equation 2.15

where; K is the equilibrium constant for zinc sulphate ion-pair formation, $mZnSO_4$ is the total molality of zinc sulphate, and α is the fraction of zinc sulphate dissociated. Since the zinc sulphate ion-pair species is uncharged and, thus, unaffected by electrostatic interactions, its activity coefficient, $\gamma Zn^{2+}SO_4^{2-}(aq)$, is often assigned a value of unity. The formation constant for the zinc sulphate ion-pair has been estimated by spectroscopic methods [68, 71, 72], calorimetry [73, 74, 75], conductivity [76, 77, 78, 79], and EMF measurements [66]. Alternatively, deviations from the DHLL caused by weak ion interactions, including ion-pair formation, may be described by Pitzer [80] parameters which are, typically, applied to the stoichiometric concentrations of ions. Although an examination of the theoretical basis of the Pitzer Model is beyond the scope of this work, the determination of Pitzer parameters by fitting isopiestic data is relatively straightforward and is described in Appendix B. Once the parameters are determined, the Pitzer Model, generally, offers the most accurate predictions of the thermodynamic properties of strong electrolytes.

2.3.2 Modelling of Zinc Ion Activity in Acidic Zinc Sulphate Electrolytes

The Pitzer Model has been applied for systems similar to $ZnSO_4$-H_2SO_4-H_2O, including Na_2SO_4-H_2SO_4-H_2O [81], $CuSO_4$-H_2SO_4-H_2O [82], $NiSO_4$-H_2SO_4-H_2O [83] and $FeSO_4$-H_2SO_4-H_2O [84]. In fact, Pitzer parameters for the $ZnSO_4$-H_2SO_4-H_2O system at 25 °C, which may be used to calculate the zinc ion activity, have been reported by Klocker et al. [85] from a fit of the isopiestic data of Majima et al. [86].Though the activity of zinc sulphate in acidic zinc sulphate electrolytes has also been reported by Tartar et al. [87] and Horváth and Wéber [88], these data do not appear to have been considered by Klocker.

The only thermodynamic model, in reviewed literature, applicable for predicting the activity of zinc ions in acidic sulphate electrolytes was developed by Filippou et al. [89] and later extended by Wang and Dreisinger [90]. The method outlined consists of solving a system of simultaneous equations for the activity of each constituent species along with charge and mass balance equations. The activity coefficients for each species are calculated using extended forms of the DHLL containing empirical correction terms which are functions of ionic strength. In particular,

the degree of hydrogen sulphate dissociation is predicted from the work of Dickson et al. [91], who developed an equation, similar in form to that of the Pitzer Model, from the examination of the effect of sodium chloride concentration on sulphuric acid speciation. The effect of ionic strength on the dissociation of other salts are modelled using simpler forms of extended Debye-Hückel equation such as the following equation for pure zinc sulphate [66]:

$$\log(\gamma Zn^{2+}) = \log(\gamma SO_4^{2-}) = -Az^2\left[\frac{\sqrt{I_m}}{1+\sqrt{I_m}} - 0.2I_m\right] \qquad \text{Equation 2.16}$$

Though folding all ion interactions into the single effect of ionic strength is a convenient simplification, it must also be recognized as a potential source of error when using this model to describe concentrated solutions containing significant quantities of species other than those which were used to generate it. Although predicted and measured pHs showed generally good agreement when tested for zinc sulphate electrolytes [89, 90] it may be useful to re-examine the manner in which zinc equilibrium potential may be predicted.

2.4 Zinc Deposition Limiting Current Density

Mass transport of zinc ions during electrowinning occurs by a combination of migration, under the influence of the potential gradient that exists between the anode and cathode, and diffusion, due to a concentration gradient in the diffusion boundary layer, which may be assumed to obey Fick's law. The mass transport of zinc ions to the electrode and the electron transfer reaction at the electrode surface occur in series and thus, at steady state, these fluxes through the electrode area are equal.

$$\left(\frac{dZn^{2+}}{dt}\right)_{rxn} = \left(\frac{dZn^{2+}}{dt}\right)_{mig} + \left(\frac{dZn^{2+}}{dt}\right)_{dif} \qquad \text{Equation 2.17}$$

At a sufficiently high reaction rate, the concentration of zinc ions at the electrode surface approaches zero, corresponding to the limit of mass transport by diffusion, and further increases in reaction rate are limited to the contribution of the migrational flux. The corresponding zinc deposition current density is termed the limiting current density, $j_{\lim,Zn}$.

$$j_{\lim,Zn} = \frac{-D_{Zn^{2+}}}{\delta(1-t_{Zn^{2+}})} nF\left([Zn^{2+}]^{bulk}\right)$$ Equation 2.18

where; t_{Zn}^{2+} is the transport number of zinc ions, D_{Zn}^{2+} ($m^2\ s^{-1}$) is the diffusion coefficient of zinc ions, δ (m) is the diffusion boundary layer thickness, and $[Zn^{2+}]^{bulk}$ (mol m^{-3}) is the bulk zinc ion concentration. Estimation of these parameters is discussed in the following sections. However, it should be noted that Equation 2.18 is based on an ideal case that assumes a uniform potential gradient and constant transport numbers of species throughout the diffusion layer, and that a more accurate approach to predicting the limiting current density would involve solving the full Nernst-Planck equation.

2.4.1 Zinc Ion Transport Number

The transport number of zinc ions, by definition, is equal to the fraction of the total current carried by zinc ions through the electrolyte, and is related to the concentrations of species in solution and their corresponding diffusion coefficients as follows:

$$t_{Zn^{2+}} = \frac{z_{Zn^{2+}}^{2} D_{Zn^{2+}}[Zn^{2+}]}{\sum z_i^{2} D_i[i]}$$ Equation 2.19

There does not appear to be a report in literature containing estimations of the transport number for zinc in acidic zinc sulphate electrolytes. However, Hinatsu and Foulkes [92] have used Equation 2.19 to estimate the transport number of copper ions, t_{Cu}^{2+}, in the concentration range of 0.002 to 1.0 mol dm^{-3} $CuSO_4$ in 0.51 mol dm^{-3} H_2SO_4, by assuming that the ratios of the magnitudes of diffusion coefficients are the same as at infinite dilution, i.e. all ions are similarly affected by increasing concentration. The accurate estimation of the speciation of the zinc electrolytes, which is the missing component necessary for implementation of this method, may be determined through Pitzer Model calculations.

2.4.2 Zinc Ion Diffusion Coefficient

Zouari and Lapique [40] reported the following expression for the diffusion coefficient of zinc ions, D_{Zn}^{2+} ($m^2\ s^{-1}$), in 0.2 mol dm^{-3} Na_2SO_4 supporting electrolyte, which was generated from limiting current density data at a rotating disc electrode in the concentration range of 0.01 to 0.15 mol dm^{-3} $ZnSO_4$:

$$D_{Zn^{2+}} = 0.78 \times 10^{-6} \exp\left(\frac{-2186}{T}\right)$$ Equation 2.20

However, the above expression is for a pH neutral electrolyte of relatively low ionic strength and is not applicable to industrial zinc electrolytes. In this regard, there have been only few reported estimations of zinc ion diffusion coefficients in industrial zinc electrolytes [40, 96, 97], and each for a single electrolyte composition.

The diffusion coefficient of zinc sulphate in water, D_{ZnSO_4} ($m^2\ s^{-1}$), was measured by Albright and Miller [93] in the concentration range of 0 to 3.2 mol dm^{-3}. Awakura et al. [94] also measured the diffusion coefficient of zinc sulphate in 0 to 2.0 mol dm^{-3} $ZnSO_4$, as well as in the presence of 0 to 2.0 mol dm^{-3} H_2SO_4 at 25 °C. Awakura's data has been used to estimate the diffusion coefficient of zinc ions in 1.0 mol dm^{-3} $ZnSO_4$ and 1.8 mol dm^{-3} H_2SO_4 [97]. The zinc ion diffusion coefficient may be separated from the diffusion coefficient of zinc sulphate according to the following fundamental relationship:

$$D_{Zn^{2+}} = \frac{D_{ZnSO_4}\left[\nu_{Zn^{2+}} \frac{D_{SO_4^{2-}}}{D_{Zn^{2+}}} + \nu_{SO_4^{2-}}\right]}{\frac{D_{SO_4^{2-}}}{D_{Zn^{2+}}}\left(\nu_{Zn^{2+}} + \nu_{SO_4^{2-}}\right)\left[1 + \frac{d \ln y_{\pm} ZnSO_4}{d \ln[ZnSO_4]}\right]}$$ Equation 2.21

where; $\nu_{Zn^{2+}}$ (1) and $\nu_{SO_4^{2-}}$ (1) are the numbers of each ion formed by complete dissociation of zinc sulphate, and $y_{\pm}ZnSO_4$ is the stoichiometric mean molar activity coefficient of zinc sulphate. However, assuming that the activity coefficient of zinc sulphate is not affected by changes in composition over the concentration range of industrial zinc electrolytes, as suggested by Barton and Scott [11], and that the ratio of $D_{Zn^{2+}}$ to $D_{SO_4^{2-}}$ is close to that at infinite dilution, as suggested by Hinatsu and Foulkes [92], then Equation 2.21 simplifies to the following form:

$$D_{Zn^{2+}} \approx \frac{D_{ZnSO_4}}{2}\left[1 + \frac{D^{\circ}_{Zn^{2+}}}{D^{\circ}_{SO_4^{2-}}}\right]$$ Equation 2.22

where; $D^{\circ}_{Zn^{2+}}$ and $D^{\circ}_{SO_4^{2-}}$ ($m^2\ s^{-1}$), are the diffusion coefficients of Zn^{2+} and SO_4^{2-} at infinite dilution.

2.4.3 Boundary Layer Thickness

In parallel plate electrolysis cells, the thickness of the boundary layer at the electrode surfaces is generally regarded as being dominated by microconvective mixing caused by gas evolution. Several researchers [13, 95, 96, 97] have employed an equation of the following form to relate mass transport coefficient, k_m (m s^{-1}), to hydrogen gas evolution during zinc electrowinning:

$$k_m = \frac{D_i}{\delta} = K(j_{H_2})^n \qquad \text{Equation 2.23}$$

where; K (units depend on n) and n are constants, and j_{H_2} (A m^{-2}) is the hydrogen evolution current density. These types of relationships are often developed using a single electrolyte composition and temperature and it should be recognized that the magnitude of K will be depend on the transport properties of the electrolyte.

In laboratory scale parallel plate electrolytic cells, the evaluation of boundary layer thickness may be accomplished by the tracer method developed by Ettel et al. [98] which has been employing for zinc electrowinning using copper [99] and cadmium [95, 96, 97] as tracers. In general, this technique involves the addition of a small, but finite, level of a relatively noble impurity, M^{n+}, into the electrolyte which is codeposited as zinc electrodeposition progresses. Since the concentration of the tracer in solution is relatively low, it is deposited at its limiting current density which is measured directly from an elemental analysis of its content in the electrodeposited zinc. An additional simplification, resulting from the relatively low concentration of the tracer, is that the contribution of migration flux to its mass transport is assumed to be negligible, i.e. the transport number of the tracer is close to zero, which allows the boundary layer thickness to be calculated directly from rearranging Equation 2.18:

$$\delta = \frac{-D_{M^{n+}}}{j_{\lim,M}} nF\left([M^{n+}]^{bulk}\right) \qquad \text{Equation 2.24}$$

A drawback of using this technique is, as previously mentioned, zinc deposition kinetics and current efficiency are highly sensitive to even trace levels of impurities. Alternatively, experimental control of the boundary layer during zinc electrodeposition, from pure electrolytes, may be achieved through the use of a rotating disc electrode [15, 25, 26, 30, 35, 42, 100]. The rotating disc electrode is composed of a rod of electrode material which is sheathed in an

insulating material such that only the bottom face of the electrode is exposed to the electrolyte. The action of electrode rotation in the electrolyte creates a uniform boundary layer through which molecular transport of a species to, or from, the disc surface can be actuated by the application of a suitable electrode potential. For a given electrode rotation speed, ω (rad s^{-1}), the diffusion boundary layer thickness, δ (m), may be predicted using the Levich equation [101]:

$$\delta = 1.61 D_{Zn^{2+}}^{1/3} \eta^{1/6} \rho^{-1/6} \omega^{-1/2} \qquad \text{Equation 2.25}$$

where; $D_{Zn^{2+}}$ (m^2 s^{-1}) is the diffusion coefficient of the zinc ion, η (kg m^{-1} s^{-1}) is absolute viscosity of the electrolyte, and ρ (kg m^{-3}) is the density of the electrolyte. Further details of the application of a rotating disc electrode are described in Section 3.1.3.

Two expressions for calculating absolute viscosity of zinc electrolytes as a function of composition (mol dm^{-3}) were found in literature:

$$\eta = \left\{ \begin{array}{l} 255.6 + 9.1[H_2SO_4] + 1.0[H_2SO_4]^2 - 4.0(T-273) \\ + 0.036(T-273)^2 - 1.6([Zn^{2+}] + 0.83[Mn^{2+}])(T-273) \end{array} \right\} \times 10^{-5} \text{ [102]} \qquad \text{Equation 2.26}$$

$$\eta = \left\{ \begin{array}{l} 17.7 + 4.1[H_2SO_4] - (1.0 + 2.5[H_2SO_4])([Zn^{2+}] + [Mg^{2+}]) \\ \exp\left(\dfrac{15200 + (1850 + 225[H_2SO_4])([Zn^{2+}] + [Mg^{2+}])}{RT} \right) \end{array} \right\} \times 10^{-7} \text{ [103]} \qquad \text{Equation 2.27}$$

Viscosities reported by Cathro [97] for 1.0 mol dm^{-3} $ZnSO_4$ and 1. 8 mol dm^{-3} H_2SO_4 between 30 and 70 °C averaged *ca.* 1 % below those predicted by Equation 2.27. Notwithstanding, the viscosity values calculated using the above expressions differ significantly, *ca.* 100 % over the typical industrial zinc electrolyte compositional range, 0.84 to 1.15 mol dm^{-3} $ZnSO_4$ and 1.27 to 1.78 mol dm^{-3} H_2SO_4, and temperature range, 35 to 45 °C, and, therefore, needs to be validated.

Several equations for calculating zinc electrolyte density, ρ (kg m^{-3}), as a function of electrolyte composition (mol dm^{-3}) were found in literature:

$$\begin{array}{l} \rho = 1153.82 + 66.748[H_2SO_4] + 181.436[Zn^{2+}] \\ \quad + 158.354[Fe^{2+}] + 396.312[Fe^{3+}] - 0.55T \end{array} \text{ [89]} \qquad \text{Equation 2.28}$$

$$\rho = 1054 + 39[H_2SO_4] + 130([Zn^{2+}] + 0.83[Mn^{2+}]) - 0.47(T-273) \text{ [102]} \qquad \text{Equation 2.29}$$

$$\rho = 1000 + 54.9[H_2SO_4] + 142.6([Zn^{2+}] + 0.93[Mn^{2+}] + 0.74[Mg^{2+}] + 0.41[NH_4^+])$$ [11] Equation 2.30

$$\rho = 1011.2 + 61.1[H_2SO_4](1 - 0.08[M]) + 156.8[M] - (0.44 + 0.08[H_2SO_4] + 0.13[M])(T - 273)$$ [103] Equation 2.31

$$[M] = [Zn^{2+}] + 0.83[Mn^{2+}] + 0.68[Mg^{2+}] + 0.32[Na^+] + 0.37[K^+]$$

All the above expressions yield relatively close predictions of electrolyte density for typical zinc electrolytes, but the relations of Barton and Scott [11] and Umetsu et al. [103] match almost perfectly at 308 K (the temperature at which Barton and Scott's density measurements were made). The latter relation, which incorporates the effect of temperature and was developed from measured densities of electrolytes containing between 1 and 2 mol dm^{-3} H_2SO_4 and 0 to 1.2 mol dm^{-3} $ZnSO_4$ over the temperature range of 20 to 60 °C, was selected for calculating zinc electrolyte density in this study.

2.5 Zinc Exchange Current Density and Transfer Coefficient

The zinc exchange current density, $j_{0,Zn}$, and transfer coefficient, α, are the two most important parameters when describing the kinetics of zinc electrodeposition. In general, determining these parameters, for a given solution composition, involves fitting the Tafel Equation or Butler-Volmer Equation to the current responses resulting from a series of applied overpotentials. When the electrode is polarized such that it is at the zinc equilibrium potential, zinc deposition and dissolution occur at equal rates and no net reaction occurs. The current density corresponding to this situation is termed the exchange current density. By inspection of the Bulter-Volmer Equation, Equation 2.32, when an overpotential is applied, the net current density of zinc deposition, j_{Zn}, in the absence of mass transfer limitations, i.e. when $j_{\lim,Zn} >> j_{0,Zn}$, varies directly with exchange current density, $j_{0,Zn}$.

$$j_{Zn} = \frac{I_{Zn}}{A_e} = \frac{-j_{0,Zn}\left[e^{\frac{-\alpha nF\eta_{Zn}}{RT}} - e^{\frac{(1-\alpha)nF\eta_{Zn}}{RT}}\right]}{1 - \frac{j_{0,Zn}}{j_{\lim,Zn}} e^{\frac{-\alpha nF\eta_{Zn}}{RT}}} \approx -j_{0,Zn}\left[e^{\frac{-\alpha nF\eta_{Zn}}{RT}} - e^{\frac{(1-\alpha)nF\eta_{Zn}}{RT}}\right]$$ Equation 2.32

The transfer coefficient, α, which represents the fraction of the overpotential that contributes to accelerating the cathodic reaction, appears in the exponential terms of the Butler-Volmer

Equation. The transfer coefficient is always accompanied by the number of electrons transferred in the rate determining step, n, and their product, αn, is often combined and denoted as β. In systems such as copper or silver deposition where univalent ions may exist in solution, a two-electron transfer mechanism is highly unlikely [104]. In the absence of clear evidence of the existence of such an intermediate species, as with Ni deposition, experimental validation of a stepwise mechanism is required [105]. In principle, the value of the transfer coefficient can be separated from β by examining the effect of zinc ion activity on exchange current density through the following expression [106]:

$$j_{0,Zn} = k_0 \left(aZn^{2+}\right)^{1-\alpha} \left(aZn\right)^{\alpha} \qquad \text{Equation 2.33}$$

where; k_0 (A m^{-2}) is the standard exchange current density.

2.5.1 Zinc Electrodeposition Kinetics in Weakly Acidic Sulphate Electrolytes

The zinc deposition reaction may be written as a single step reaction, involving the transfer of two electrons, i.e. $n = 2$, according to the overall stoichiometry:

$$Zn^{2+} + 2e^- \rightarrow Zn \qquad \text{Equation 1.1}$$

In such a case, the value of the transfer coefficient is expected to be near 0.5, i.e. $\beta = 1.0$. Alternatively, reaction models for zinc deposition from sulphate media involving multiple single electron transfer reactions have been proposed Despić and Pavlović [51], Jović et al. [41], Hurlen and Brevik [107] as well as Wiart et al. [35]. The kinetics of zinc electrodeposition from sulphate electrolytes has been rigorously studied by Wiart and his collaborators [30, 35, 36, 39, 46, 115, 116, 108] and Wiart's original model of zinc electrocrystallization, which has been simplified for the absence of H^+, appears below:

$$Zn^{2+} + e^- \rightarrow Zn^+{}_{ad} \qquad \text{Equation 2.34}$$

$$Zn^{2+} + Zn^+{}_{ad} + e^- \leftrightarrow 2Zn^+{}_{ad} \qquad \text{Equation 2.35}$$

$$Zn^+{}_{ad} + e^- \rightarrow Zn \qquad \text{Equation 2.36}$$

This model has been used to explain the lack of reproducibility in zinc electrodeposition experiments [109, 110] and the conflicting values of kinetic parameters in literature (see Table 1)

since at relatively low overpotentials, the competitive rates of these reactions creates multiple steady state current responses. However, at overpotentials more negative than *ca.* -50 mV, where Tafel kinetics are observed, the autocatalytic nature of the second reaction ensures a surplus of Zn^{+}_{ad} and the third reaction becomes rate limiting. Wiart et al. [35] assign β a value of 1.0 for this reaction, i.e. the value of β is the same as the theoretical value for the two electron transfer case, which means that α is also equal 1.0, since the reaction involves the transfer of a single electron. Zouari and Lapique [40] demonstrated that Wiart's model provided a slightly better fit of their voltammetric data for zinc deposition in sodium sulphate supporting media, though concluded that the marginal improvement in fit did not justify the model's added complexity and opted to fit their results according to the simpler single step reaction model with β also equal to 1.0. A final note on Wiart's simplified model; since the rate limiting reaction does not involve the solvated zinc ion species, Zn^{2+}, there is an inherent prediction that the effect of overpotential on zinc deposition current density is insensitive to zinc concentration.

Table 1: Kinetic Parameters for Zinc Electrodeposition from Near-Neutral Sulphate Electrolytes

Zinc Sulphate Concentration	Supporting Electrolyte	pH	Temp. / °C	β	$j_{0,Zn}$ / A m^{-2}	Source
0.005 mol kg^{-1}	(x – 0.005) mol kg^{-1} $MgSO_4$ + H_2SO_4 (to adjust pH)	3.0	25	0.5	7.0 (x = 0.5) 5.0 (x = 1.0,1.5) 4.5 (x = 2.0,2.5) 4.0 (x = 3.0)	107
0.01 mol dm^{-3} 0.07 mol dm^{-3} 0.15 mol dm^{-3}	0.2 mol dm^{-3} Na_2SO_4	5.7 5.1 4.8	25	1.0	0.02 2.5 8.6	39
0.011 mol dm^{-3} 0.14 mol dm^{-3} 0.50 mol dm^{-3} 0.88 mol dm^{-3}	(1.5 – [$ZnSO_4$]) mol dm^{-3} Na_2SO_4	3.0-3.4	24	?	4.94 3.66 10.9 12.6	37
0.025 mol dm^{-3}	1.0 mol dm^{-3} $MgSO_4$	?	25	0.52	52.4	111
0.1 mol dm^{-3} 1.0 mol dm^{-3}	none	?	room temp.	0.58	1.2 12	112
0.5 mol dm^{-3} 1.0 mol dm^{-3} 1.5 mol dm^{-3}	0.05 mol dm^{-3} $Al_2(SO_4)_3$ + 0.5 mol dm^{-3} Na_2SO_4	3.5	25	?	21, 28 31 46	41
1 mol dm^{-3}	none	?	room temp.	1.0	0.2	113
1.5 mol dm^{-3}	0.04 mol dm^{-3} $Al_2(SO_4)_3$ + 0.4 mol dm^{-3} Na_2SO_4	3.5	25	1.0	1.0	51
10^{-5} – 0.4 mol dm^{-3}	(0.5 – [$ZnSO_4$]) mol dm^{-3} Na_2SO_4	5-6.5	room temp.	0.55-0.70	$10[Zn^{2+}]^{0.44}$ * $1.5[Zn^{2+}]^{0.21}$**	38

* bare zinc ** oxide covered zinc (both expressions are based on anodic dissolution of zinc)

2.5.2 Zinc Electrodeposition Kinetics in Highly Acidic Sulphate Electrolyte

The addition of acid further complicates zinc electrodeposition kinetics by causing a shift in the current-potential curve towards more negative polarization potentials, which has been attributed to the inhibiting effect of adsorbed hydrogen, ZnH_{ad} [35]. The effect of acid was modelled by Wiart through the following two reactions:

$$Zn + H^+ + e^- \xrightarrow{K_1} ZnH_{ad} \qquad \text{Equation 2.37}$$

$$ZnH_{ad} + H^+ + e^- \xrightarrow{K_2} Zn + H_2 \qquad \text{Equation 2.38}$$

The inhibiting effect of acid has also been observed in zinc deposition from chloride media by Sierra-Alcazar and Harrison [114], who measured a decrease in the exchange current density with decreasing pH.

Wiart's original reaction model was altered to account for observed changes in deposit morphology by including reaction paths involving active zinc atoms at kink sites, Zn^*, in the following reaction scheme [30, 46, 115, 116] which are in addition to Equation 2.37 and Equation 2.38:

$$Zn^{2+} + e^- \xrightarrow{K_3} Zn^+{}_{ad} \qquad \text{Equation 2.34}$$

$$Zn^+{}_{ad} + e^- \xrightarrow{K_4} Zn \qquad \text{Equation 2.36}$$

$$Zn^+{}_{ad} + e^- \xrightarrow{K_5} Zn^* \qquad \text{Equation 2.39}$$

$$Zn^* \xrightarrow{K_6} Zn \qquad \text{Equation 2.40}$$

$$Zn^{2+} + Zn^* + 2e^- \xrightarrow{K_7} Zn + Zn^* \qquad \text{Equation 2.41}$$

$$Zn \xrightarrow{K_8} Zn^{2+} + 2e^- \qquad \text{Equation 2.42}$$

The partial current densities for zinc deposition and hydrogen evolution are calculated using the fractional coverages, θ_i, of each surface active species; $Zn^+{}_{ad}$, Zn^*, and ZnH_{ad}, which are modelled according to a Langmuir isotherm, and rate constants for each reaction, which are calculated according to Tafel's law. Further details of the application of this model to calculate the partial zinc deposition and hydrogen evolution current densities as a function of electrolyte

composition are given in Appendix C. With increasing overpotential, the electrode coverage by adsorbed hydrogen decreases while that of zinc species increases (see Figure 6). The above model of zinc electrodeposition, including the reactions involving H^+, is hereafter referred to as 'Wiart's Model'.

Dendritic growth during zinc electrodeposition at high current density is predicted to occur due to an increase in the nucleation rate of Zn^*, which is a function of overpotential [115]. Popov et al. [50] previously estimated the critical overpotential for zinc dendrite formation, in 0.84 mol dm^{-3} $ZnSO_4$ and 1.2 mol dm^{-3} H_2SO_4 at 25 °C, to be -173 mV, which appears to correspond to the calculated increase of Zn^* coverage in Figure 6. Wiart has not reported current density data beyond *ca.* 1000 A m^{-2}, corresponding to this overpotential limit and, as such, the model should be experimentally validated for higher zinc deposition current densities.

There are few independent and credible studies to compare against the findings of Wiart. Cavallotti [117], in unpublished notes, generated a regression fit of zinc exchange current densities from various acidic solutions at 25 °C from which the following expression was extracted:

$$j_{0,Zn} = 308[Zn^{2+}]^{1.19} \qquad \text{Equation 2.43}$$

Tripathy et al. [118] have recently reported exchange current densities and transfer coefficients for zinc electrodeposition from a pure zinc electrolyte containing 0.84 mol dm^{-3} $ZnSO_4$ and 1.53 mol dm^{-3} H_2SO_4 at room temperature, but the values are suspect since they are based solely on the cathodic branches of sweep voltammograms on an aluminium electrode and do not include ohmic drop corrections. Barton and Scott [11] have also published kinetic parameters for zinc electrowinning, but the values were based on experiments conducted in a pilot-plant scale cell using an industrial electrolyte which contained significant quantities of magnesium, manganese, and ammonia, along with trace amounts of other elements as well as organic additives. In fact, the Tafel slope adopted by Barton and Scott was not explicitly measured, but rather was fixed at 70 mV dec^{-1} after consulting with Allen J. Bard, who had previously examined the mechanism of zinc deposition from alkaline media [119].

Although Wiart's description of the kinetics of zinc electrodeposition in acidic sulphate media is quite thorough, there is a lack of corroborative data at high current densities. Wiart's Model is

also rather complex and, although rooted in the same Tafel kinetics as the Extended Butler-Volmer Equation, does not incorporate mass transfer effects.

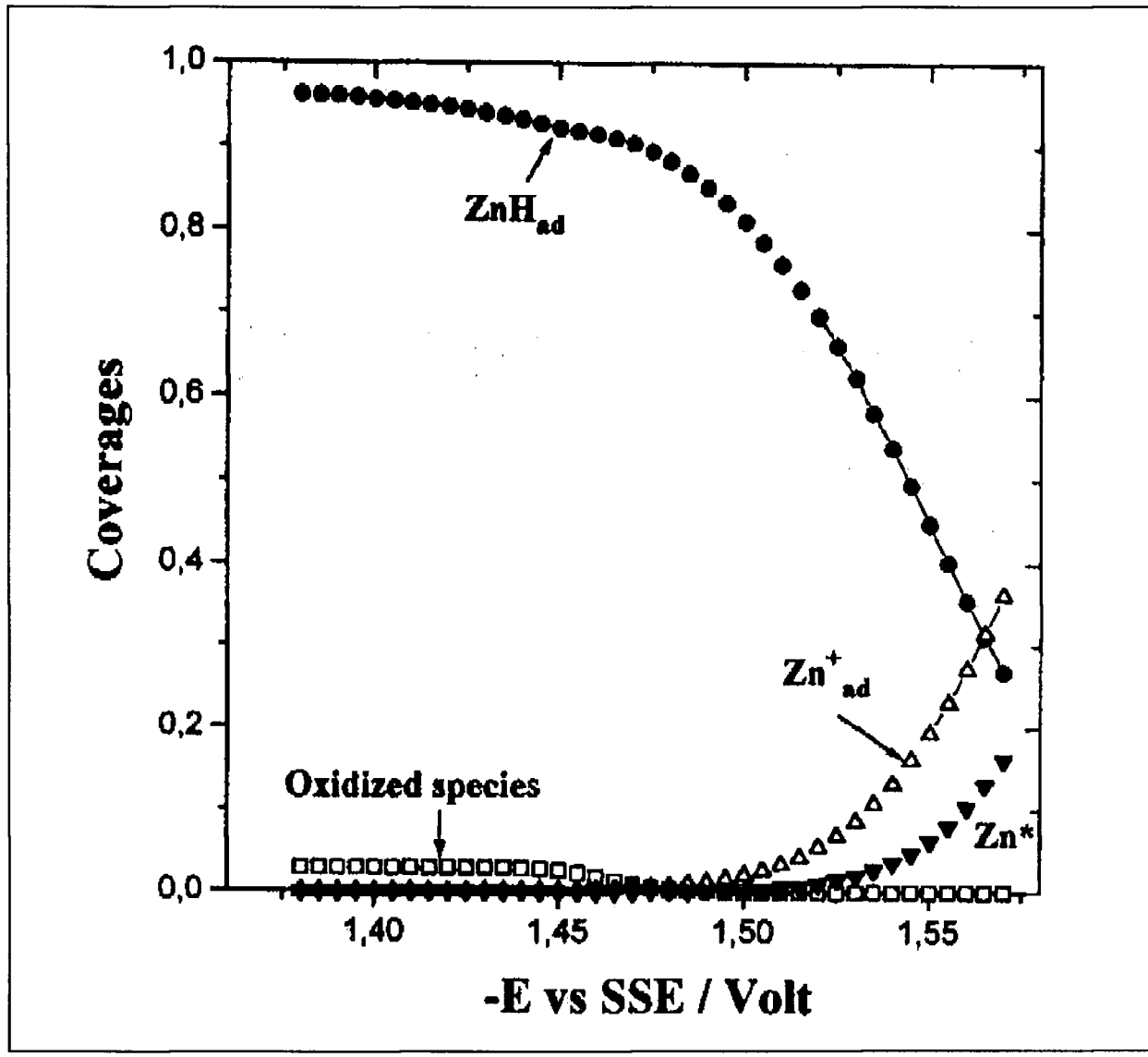

Figure 6: Calculated electrode coverage as a function of potential in 0.84 mol dm^{-3} $ZnSO_4$ and 1.2 mol dm^{-3} H_2SO_4 at room temperature, E_{Zn} = -1.40 V (SSE). Taken from [30].

2.6 Summary

The operation of conventional electrowinning cells or the design of novel electrowinning cells to operate at high current densities, > *ca.* 500 A m^{-2}, is of interest to industrial zinc producers given recent advances in solution purification technology. However, there is lack of reliable information on the voltage demands of zinc electrodeposition under such conditions. The Extended Butler-Volmer Equation is often used to predict the effect of overpotential and mass

transfer effects on the current density of electrochemical reactions, but requires precise measurements of current density and overpotential under controlled mass transfer conditions in order to obtain reliable values for kinetic parameters; limiting current density, exchange current density, and transfer coefficient.

When a voltage is applied to cause zinc electrodeposition, the overpotential is the measure of the difference between the applied voltage and the equilibrium potential (the minimum voltage demand). The equilibrium potential is a thermodynamic quantity and may be calculated from the Nernst Equation using extended forms of the Debye-Hückel Limiting Law, such as the Pitzer Model, to predict the values of activity coefficients. The zinc deposition current density is traditionally based on the calculated current efficiency from the measurements of the mass of deposited zinc after relatively long polarization experiments. Faster methods of separating the zinc deposition and hydrogen evolution currents have recently been employed such as detection of hydrogen using a rotating ring disc electrode and normal pulse voltammetry. The use of a rotating disc electrode is also the most appropriate method of controlling mass transfer conditions when using ultra-pure electrolytes, though the physical properties of the electrolyte must be well established.

Smooth electrode surfaces are extremely important for accurate estimation of the kinetic parameters for electrodeposition reactions. With respect to this issue, platinum seems a promising substrate for zinc electrodeposition, though there is a need for a more thorough examination of the inhibition of hydrogen evolution on platinum in zinc sulphate electrolytes and characterisation of OPD zinc deposit morphology on platinum.

Of the existing models relating overpotential and zinc deposition current density from these types of electrolytes, the most rigorously developed is that of Wiart. However, Wiart's Model does not take into account mass transfer limitations and does not appear to have been validated for current densities > *ca.* 1000 A m^{-2}. In addition, there are conflicting values for the kinetic parameters for zinc electrodeposition in the literature and a clear need to re-examine zinc deposition kinetics from acidic sulphate electrolytes, especially at high current density.

3 Experimental Details

This section describes the apparatus, reagents and experimental procedures utilized in the course of this investigation. The first section describes the instrumentation employed for electrochemical polarization experiments, both practical details and background theory concerning their use. Next, the reagents employed are listed along with relevant information concerning their preparation and use. The different polarization experiments employed and the type and accuracy of data generated are described along with sample calculations. Finally, the surface characterization techniques which were used to complement and support the findings of the electrochemical polarization experiments are outlined.

3.1 Equipment for Electrochemical Experiments

Electrochemical experiments were conducted using a jacketed three-compartment cell, illustrated in Figure 7, or an unjacketed single-compartment cell, illustrated in Figure 8. Both cells employed a saturated calomel reference electrode (SCE) and a platinum flag counter electrode. The potentiostat was an Eco-Chemie PSTAT 30, equipped with BIPOT, FRA2 and SCAN-GEN modules. In the case of the jacketed cell, the working electrode was a MTI34 (99.99 %+) platinum ring-disc electrode (PINE Instrument Co.), 0.283 cm^2 disc area. The temperature was controlled to 25 ±0.5 °C using a refrigerated circulating bath (Fisher Scientific Isotemp Model 900). The rotation speed of the ring-disc electrode was regulated by an AFMSRX Analytical Rotator (PINE Instrument Co.). The working electrode employed in the unjacketed cell was a planar platinum electrode, 0.36 cm^2 surface area, manufactured from an ingot of platinum which was attached, at the back, to an insulated copper wire and embedded in Epofix (Struers) cold cure epoxy. The electrode surfaces were polished to a mirror finish using silicon-carbide/paper grinding discs from 600 to 1200 Grit (Buehler) as well as 6 μm and 1 μm diamond slurries (Leco).

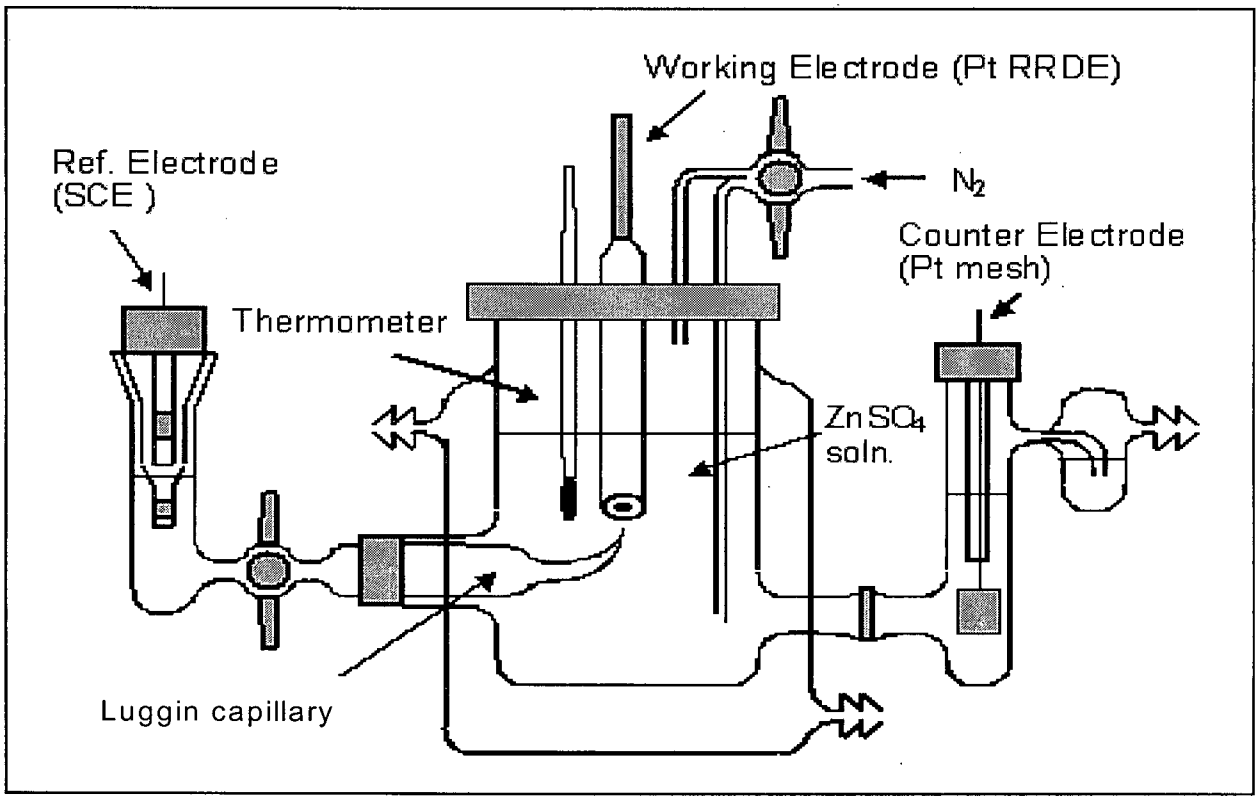

Figure 7: Schematic diagram of a jacketed three-chamber electrochemical cell.

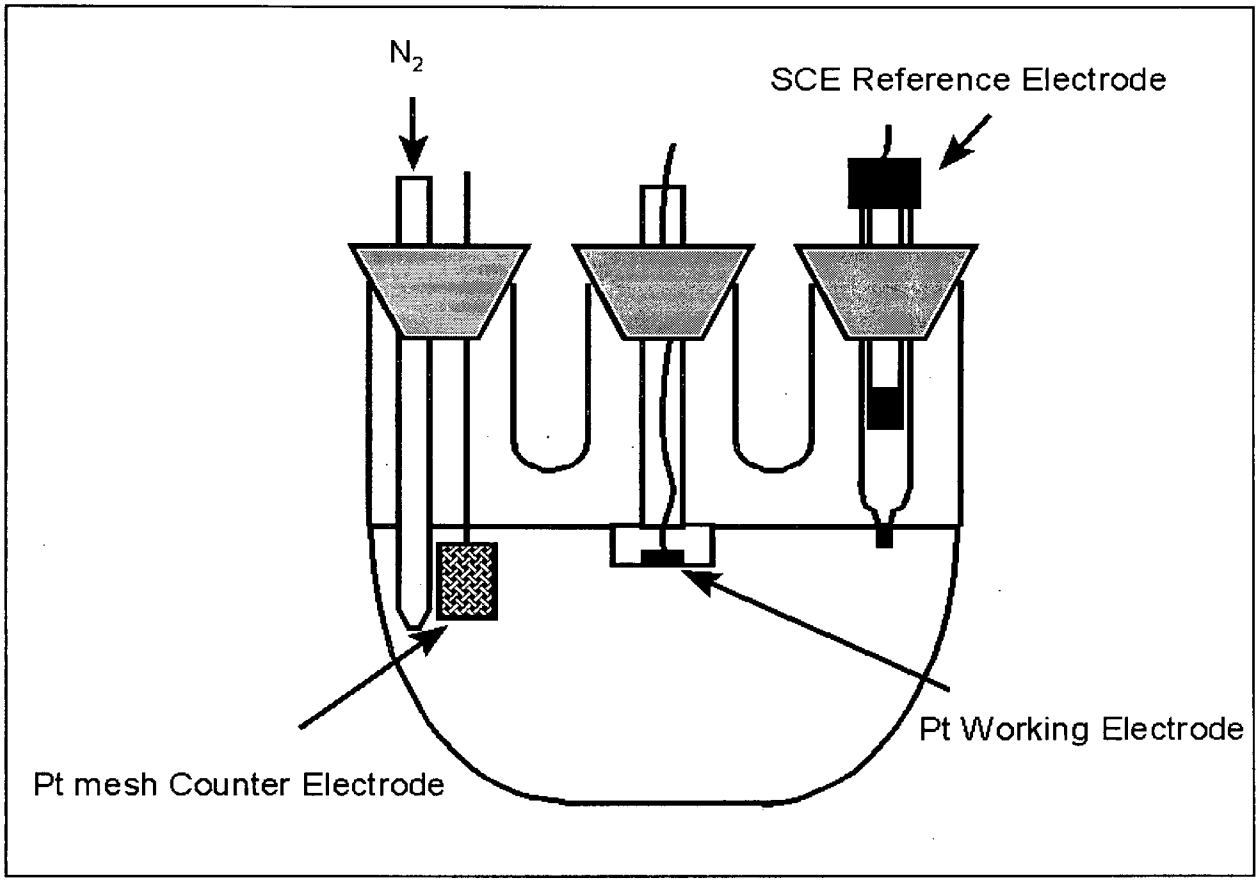

Figure 8: Schematic diagram of an unjacketed single-compartment electrochemical cell.

3.1.1 Cleaning Procedures

The glass components of both electrochemical cells, as well as other glassware, were periodically cleaned by immersing them, overnight, in a bath containing a 1:1 mixture of nitric and sulphuric acid, at room temperature. The platinum ends of the working electrodes were cleaned by quickly immersing and withdrawing them, while using a swirling motion, from a hot bath, 60 to 80 °C, of the acid mixture described above. The platinum counter electrodes were flamed using a butane torch. All cleaning procedures were followed by rinsing with Millipore Milli-Q ultra-pure water.

3.1.2 Electrochemical Cell Filling Procedure

The general procedure for filling the jacketed electrochemical cell, starting with a disassembled cell, begins by filling the Luggin compartment of the Luggin/reference electrode assembly with the same electrolyte that is to be contained in the main chamber of the cell through the reference electrode compartment. The stopcock, which controls solution flow between the Luggin compartment and the reference electrode compartment, was then set to the closed position, and any electrolyte retained in the reference electrode compartment was discarded. The entire Luggin/reference electrode compartment module was then inserted into the main chamber of the cell, such that the tip of the Luggin was positioned approximately in the centre of the cell, and tightened into place by means of a HDPE compression fitting with a Viton® o-ring. The cell was rinsed with small aliquots of solution, tared on a balance with 0.1 g accuracy, and then filled with a predetermined mass of electrolyte, typically between 350 and 450 g. The platinum counter electrode, thermometer and sparger were inserted into the cell through the cap which was subsequently tightened into place. The reference electrode chamber was then filled with 4 mol dm^{-3} NH_4Cl. The solution in the reference electrode compartment would normally be the same as that contained within the electrode itself, e.g. saturated KCl in the case of a SCE. However, the change was necessitated due to oscillations in potential between the working and reference electrodes which were presumed to result from precipitation of K_2SO_4 in the stopcock between the Luggin compartment and the reference electrode compartment. Solution from the reference electrode compartment was drawn across the ground glass joint of the stopcock by rotating it back and forth several times. This was done to ensure an excess of NH_4^+ and Cl^- ions in the liquid junction relative to Zn^{2+} and SO_4^{2-}. Since NH_4^+ and Cl^- have similar equivalent conductivities, it was desirable that their concentrations be greater relative to other species so

they would carry a greater fraction of current across the junction and minimize any liquid junction potential.

The rotating ring-disc electrode was lowered into the electrolyte and fixed at a distance of approximately one centimetre from the tip of the Luggin, so as not to disrupt the hydrodynamics of the rotating disc electrode. The cell electrodes were connected to the potentiostat and the electrolyte was de-aerated by bubbling with nitrogen gas, which passed through an activated charcoal filter (Supelco) prior to entering the cell, for a period of at least 30 minutes. At this time bubbling was terminated, though a nitrogen gas overpressure was maintained throughout the electrochemical polarization experiments. The procedure for filling the unjacketed cell was similar to that of the jacketed cell without the special measures involving the Luggin.

3.1.3 Rotating Ring-Disc Electrode

The ring-disc electrode was employed to control mass transport during some experiments by rotating it in the electrolyte at one of three rotation speeds; 42 rad s^{-1} (400 rpm), 168 rad s^{-1} (1600 rpm), or 377 rad s^{-1} (3600 rpm). As previously described, for a given electrode rotation speed, ω (rad s^{-1}), the diffusion boundary layer thickness, δ (m), was predicted using the following equation:

$$\delta = 1.61 D_{Zn^{2+}}{}^{1/3} \eta^{1/6} \rho^{-1/6} \omega^{-1/2} \qquad \text{Equation 2.25}$$

where; $D_{Zn}{}^{2+}$ (m^2 s^{-1}) is the diffusion coefficient of the zinc ion, η (kg m^{-1} s^{-1}) is the absolute viscosity of the electrolyte, and ρ (kg m^{-3}) is the density of the electrolyte.

When a species is evolved from the disc, of a rotating ring-disc electrode, it is transported away by a combination of diffusion and convection. As illustrated in Figure 9, by applying a suitable potential on the ring electrode, such that the evolved species reaching the ring surface reacts immediately upon contact, a specific fraction of the evolved species will be reacted while the remainder will escape into the solution. This fraction is termed the ring collection efficiency, N_0, which is a geometric constant relating ring current, I_{ring}, to disc current, I_{disc}, as follows:

$$I_{ring} = I^{o}_{ring} - N_0 I_{disc} \qquad \text{Equation 3.1}$$

where; I^{o}_{ring} is the ring current when the disc current is equal to zero. The theoretical collection efficiency of the ring-disc electrode used in this study, $N_0 = 0.240$, was calculated from the radius of the disc ($r_1 = 0.300$ cm), the inner radius of the ring ($r_2 = 0.375$ cm), and the outer radius of the ring ($r_3 = 0.425$ cm), according to the standard procedure described elsewhere [120].

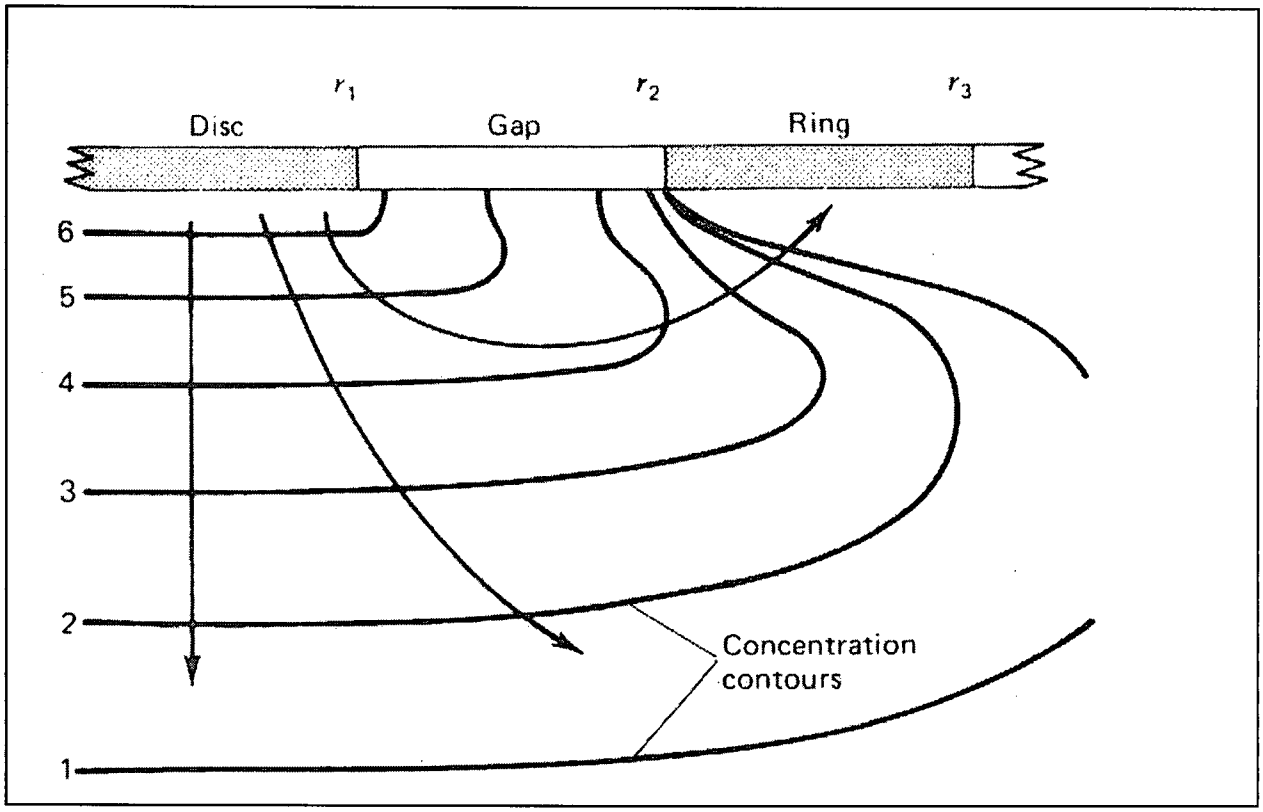

Figure 9: Concentration profile at a Rotating Ring-Disc Electrode. Taken from [120].

During zinc electrodeposition from de-aerated acidic zinc sulphate electrolyte, hydrogen evolution and zinc deposition are the only faradaic reactions that occurred at the disc. Thus, when the electrode was polarized in the potential region of zinc deposition, the resulting zinc deposition current, $I_{disc,Zn}$, was equal to the difference between the total disc current, I_{disc}, and the hydrogen evolution current I_{disc,H_2}:

$$I_{disc,Zn} = I_{disc} - I_{disc,H_2} \qquad \text{Equation 3.2}$$

The hydrogen evolution disc current was calculated from the ring current by substituting the measured collection efficiency, $N_0 = 0.228 \pm 0.011$ (see Appendix D), into Equation 3.1 and rearranging:

$$I_{disc,H_2} = \frac{I_{ring} - I^o_{ring}}{0.228}$$ Equation 3.3

The instantaneous current efficiency for zinc deposition was calculated from the disc and ring currents by combining Equation 3.2 and Equation 3.3.

$$\Phi_e = \frac{I_{Zn,disc}}{I_{disc}} = 1 - \frac{I_{ring} - I^o_{ring}}{0.228 I_{disc}}$$ Equation 3.4

3.2 Reagents

Sulphuric acid and magnesium sulphate supporting electrolytes were prepared from ACS grade reagents (Fisher Scientific) and Millipore Milli-Q ultra-pure water. The sulphuric acid, 97.25 ±0.05 %, was standardized by titration with 1.000 N NaOH Solution (Fisher Scientific) using the Gran plot method described elsewhere [121]. Zinc was introduced into supporting electrolytes by spiking with 0.1 mol dm^{-3} $ZnSO_4$ solution, through ports in the tops of the cells, using a thin glass tube attached to a syringe with ±0.005 cm^{-3} accuracy. The electrolyte was mixed by sparging with nitrogen as well as by the action of the rotating disc electrode, when present. The various supporting electrolytes employed in this study are listed in Table 2. The pH values for the electrolytes that do not contain added H_2SO_4 were measured with an Accumet model 810 (Fisher Scientific) pH meter using an RJ model pH electrode (Analytical Sensors, Inc.) which was standardized using pH 4.0 and 7.0 buffer solutions (Fisher Scientific). Because of the difficulty of accurately measuring low pHs in concentrated electrolytes, the pH values for the acidified electrolytes were calculated using Pitzer Model parameters.

Table 2: Supporting Electrolyte Solutions

$MgSO_4$ / mol dm^{-3}	H_2SO_4 / mol dm^{-3}	$ZnSO_4$ / mol dm^{-3}	pH
0.10	0	0	5.8
0.10	0	10^{-4}	5.8
0.10	0	2.0×10^{-2}	5.8
0	0.10	0	0.7
0	0.10	10^{-3}	0.7

Zinc sulphate solutions were prepared using aliquots of a strong, 2 mol dm^{-3} $ZnSO_4$ solution, which was prepared from puriss p.a. grade zinc sulphate heptahydrate, $ZnSO_4.7H_2O$ (Fluka) and

Millipore Milli-Q ultra-pure water. Impurities were reduced from the concentrated zinc solution by pre-electrolysis, using a platinum flag electrode polarized at -1000 mV (SCE) for approximately 6 hours while the solution was stirred vigorously under a nitrogen atmosphere. Small volumes of sulphuric acid, *ca.* 0.2 cm^{-3} ±0.005 cm^{-3} (0.00357 ±0.00009 mol) H_2SO_4, were added by spiking with concentrated sulphuric acid using the procedure outlined above. Larger volumes of sulphuric acid were added using 2 mL and 20 mL pipettes, which were determined to deliver 0.03543 ±0.00006 mol H_2SO_4 and 0.3604 ±0.0006 mol H_2SO_4, respectively. Concentrated acid was employed rather than a diluted solution in order to minimize the amount of water carried with the acid so as not to affect the molality of the zinc electrolytes. The composition of zinc sulphate based electrolytes employed in this study are detailed in Table 3.

Table 3: Zinc Sulphate Electrolytes

$ZnSO_4$ / mol kg^{-1}	H_2SO_4 / mol kg^{-1}	pH	$ZnSO_4$ / mol kg^{-1}	H_2SO_4 / mol kg^{-1}	pH
0.10	0.00	4.9	1.00	0.01	2.4
0.50	0.00	4.9	1.00	0.10	1.4
1.00	0.00	4.9	1.00	1.00	0.2

In instances where it was necessary to convert concentration between molality and molarity, e.g. during preparation of the electrolytes or to obtain inputs for the various equations which calculate electrolyte properties, the following fundamental expressions were employed:

$$m_i = \frac{1000[i]}{\rho - \sum [j] M_j} \qquad \text{Equation 3.5}$$

$$[i] = \frac{\rho m_i}{1000 + \sum m_j M_j} \qquad \text{Equation 3.6}$$

where; m_i (mol kg^{-1}) is the molality of species i, $[i]$ (mol dm^{-3}) is the concentration of species i, M_i (g mol^{-1}) is the molar mass of species i, and ρ (kg m^{-3}) is the density of the electrolyte, calculated using Equation 2.31.

3.3 Electrochemical Polarization Techniques

The electrochemical experiments in this study, in general, involved polarizing an electrode in a prepared electrolyte, at potentials referenced to SCE, and measuring the ensuing current response. According to the Autolab's hardware specifications, the accuracy of the applied

potentials was ±0.2 % of the voltage setting with an additional absolute uncertainty of ±2 mV, while the current data, recorded by the Autolab's 16 bit parallel ISA card, had a relative accuracy of ±0.2 % of the measured current with an additional uncertainty of ±0.2 % of the current range. The Eco-Chemie instrument employs automatic gaining and sample averaging and each data point is, in fact, the weighted average of several AD conversions that are collected at variable attenuations. The estimation of uncertainty in measured quantities was usually taken from the reported accuracy of the measuring instrument and from standard deviation of measurements made under the same experimental conditions (when applicable). Though not explicitly shown, the propagation of uncertainty through subsequent calculations followed standard procedures described elsewhere [121]. The specific electrochemical techniques employed in this study were; cyclic voltammetry, normal pulse voltammetry, staircase voltammetry, and AC impedance spectroscopy. Many of these methods are combined during the execution of a single zinc deposition "Project" (see Appendix F, written for Autolab GPES version 4.8 software), which was repeated three times for each zinc sulphate electrolyte and electrode rotation rate tested. Details of the application of each of these methods are discussed in the proceeding sections.

3.3.1 Cyclic Voltammetry

Cyclic voltammetry is one of the most widely used electrochemical methods for qualitatively characterizing the redox reactions of an electrode/electrolyte system. The technique involves sweeping the potential at a fixed rate, back and forth, between two potential limits while recording the current response. This method was used to qualitatively characterize hydrogen evolution on platinum in magnesium sulphate and sulphuric acid supporting electrolytes, both in the absence and presence of zinc ions. In addition, the overpotential deposition, OPD, of zinc on platinum in pure zinc sulphate electrolyte was also characterized by cyclic voltammetry. Though not typically applied to yield quantitative data, cyclic voltammetry was employed to estimate the reversible potential for zinc OPD on zinc in zinc sulphate/sulphuric acid electrolytes. Unless otherwise stated, cyclic voltammetry was carried out on the disc electrode of the platinum ring-disc electrode at a rotation speed of 1600 rpm and scan rate 20 mV s^{-1} at 25 °C.

3.3.1.1 Magnesium Sulphate Supporting Electrolyte

Cyclic voltammetry was performed in 0.1 mol dm^{-3} $MgSO_4$, whereby the disc potential was swept continuously back and forth between -800 mV (SCE) (corresponding to the onset of massive hydrogen evolution), and 1050 mV (SCE) (where oxygen evolution becomes evident)

until consecutive current–voltage curves traced. This procedure was repeated between -800 mV (SCE) and 200 mV (SCE) (near the potential where platinum oxidises). The same scan procedures were reapplied to the magnesium sulphate solution containing 10^{-4} mol dm^{-3}, except that the cathodic potential limit was changed to -1100 mV (SCE) (~100 mV more negative than the standard reduction potential of zinc) in order to examine the effect of UPD Zn on hydrogen evolution kinetics.

3.3.1.2 Sulphuric Acid Supporting Electrolyte

Cyclic voltammetry was carried out in 0.1 mol dm^{-3} H_2SO_4, in the same manner as in magnesium sulphate supporting electrolyte, between -270 mV (SCE) and 1185 mV (SCE) to establish the characteristics of hydrogen adsorption and evolution on bare platinum. After addition of zinc, to 10^{-3} mol dm^{-3} $ZnSO_4$, scanning was resumed between the same potential limits to examine its effect on hydrogen evolution. In addition, to examine the effect of time on hydrogen evolution, single cyclic voltammograms were recorded between -270 mV (SCE) to 1185 mV (SCE), starting and ending at -200 mV (SCE), after conditioning the electrode at -200 mV (SCE) for 900 s, 1800 s, and 3600 s. Between scans the electrode potential was set to 900 mV (SCE) to oxidize the platinum surface and expel any accumulated adsorbates.

3.3.1.3 Zinc Sulphate Electrolytes

Cyclic voltammetry in 0.1 mol dm^{-3} $ZnSO_4$, was carried out by sweeping continuously between the cathodic potential limits of -400 mV (SCE) to -1100 mV (SCE), at 100 mV intervals, to the anodic limit of 1100 mV (SCE). In addition, after conditioning the electrode at -400 mV (SCE) for 120 s, 600 s , and 1200 s, single cyclic voltammograms were recorded between -400 mV (SCE) and 1100 mV (SCE) (to examine the possibility of alloy formation) as well as between -400 mV (SCE) and -1100 mV (SCE) (to examine the effect on hydrogen evolution and zinc overpotential deposition). After each scan the electrode potential was set to 900 mV (SCE).

The equilibrium potentials for zinc deposition were taken from voltammograms created, for all zinc sulphate based electrolytes, by sweeping the potential back and forth between -950 mV (SCE) and -1150 mV (SCE), starting and ending at -1100 mV (SCE), at a scan rate of 10 mV s^{-1} (see Figure 10). By inspection, the forward and reverse sweeps trace relatively well indicating that zinc deposition/dissolution is quite reversible. This procedure is referred to as "Reversible Potential" in Appendix F. The hydrogen evolution current density on zinc is relatively small, in

the order of a few A m^{-2}, even in highly acidic solutions and, thus, the currents bracketing the equilibrium potential are dominated by zinc dissolution and deposition. The equilibrium potential was taken as the mean potential between when the anodic current crossed to cathodic current, when sweeping toward more negative potentials, and when the cathodic current crossed to anodic current, when sweeping back toward more positive potentials [122].

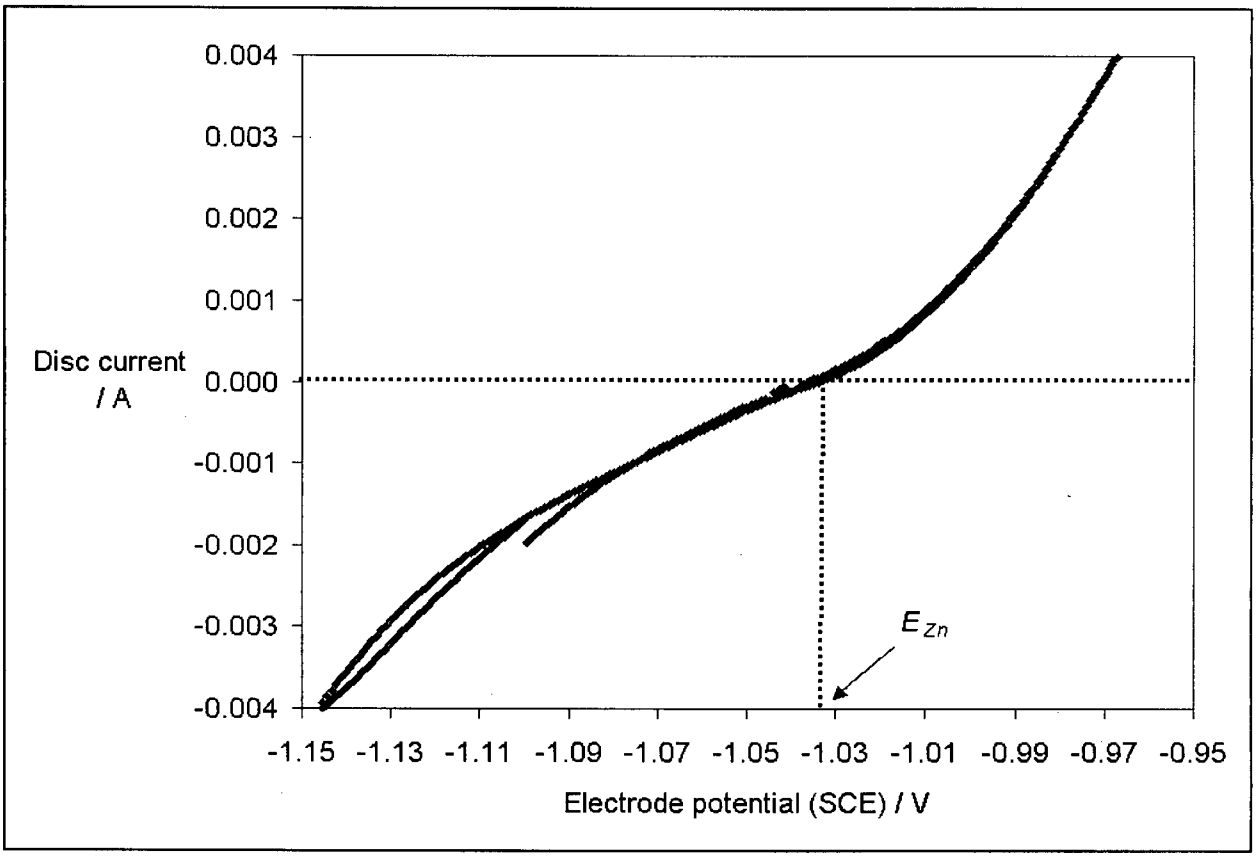

Figure 10: Cyclic voltammogram of a zinc coated rotating disc electrode in acidic zinc sulphate electrolyte. Generated in 1.0 mol dm^{-3} $ZnSO_4$ with 0.01 mol dm^{-3} H_2SO_4, pH = 2.4 at 25 °C, scan rate 10 mV s^{-1}, and 3600 rpm electrode rotation speed.

3.3.2 Normal Pulse Voltammetry

Normal pulse voltammetry is the simplest form of a class of electrochemical polarization techniques referred to as potential step chronoamperometry and chronocoulometry. Potential step chronoamperometry refers to the measurement of current response to an applied potential pulse having a square waveform. Chronocoulometry involves calculation of the corresponding charged passed, Q, by integration of the current versus time, during the potential step routine. By varying the amplitude of the pulses, the relationship between potential and steady-state current can be established without the hysteresis associated with potential sweeping techniques. Normal pulse

voltammetry (see Figure 11) specifically, refers to a pulse routine which begins and ends at a base potential, E_b, where the electrode is inactive [123]. In this manner the redox reaction which occurs at the pulse potential, E_p, is reversed when the potential is returned to base potential until the electrode once again becomes inactive.

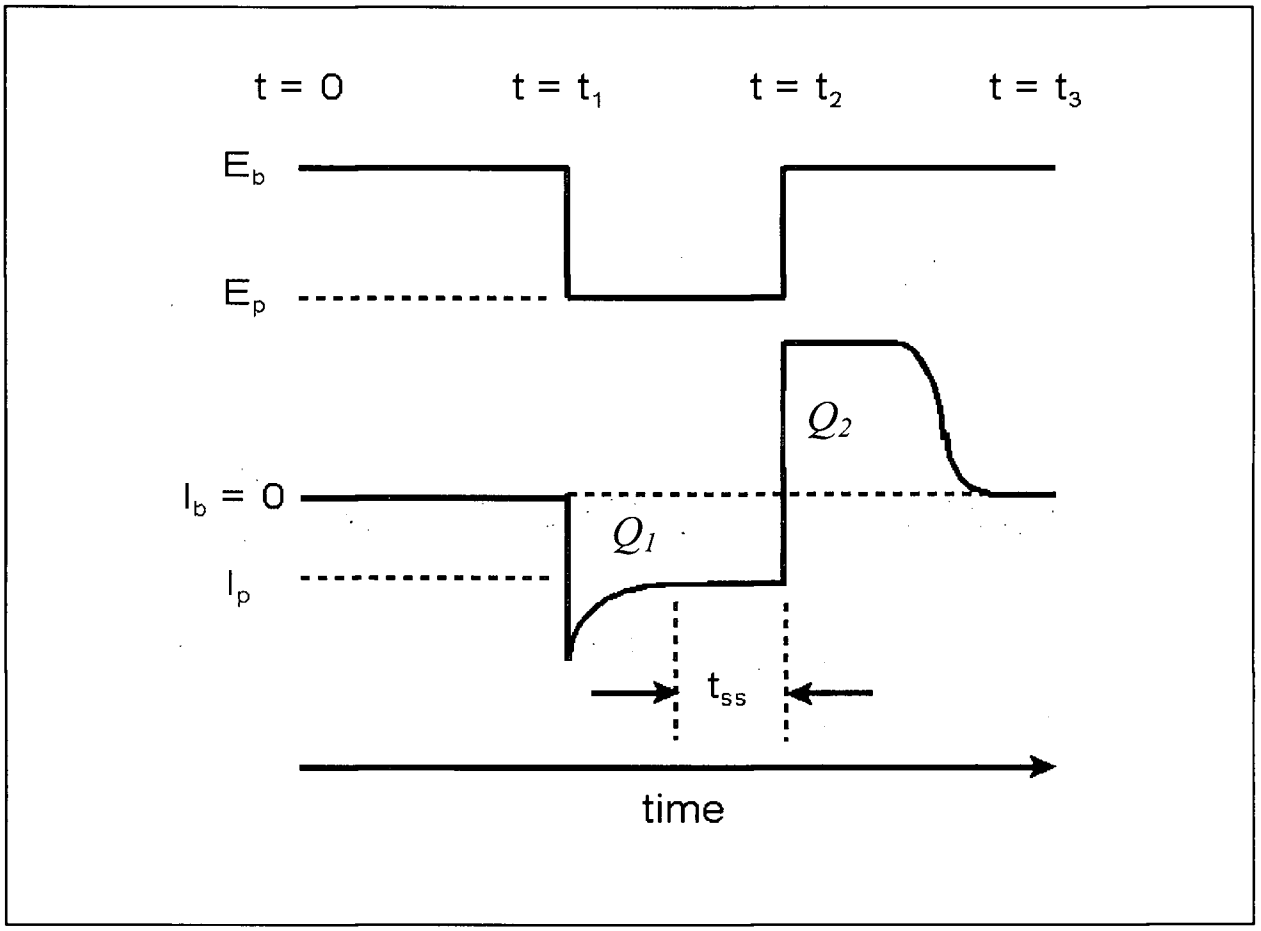

Figure 11: Schematic representation of a normal potential pulse and resulting current response of an electrodeposition reaction.

Indicated in the above figure are the base and pulse potentials, E_b and E_p, the associated current response, I_b and I_p, and integrated deposition and stripping charges, Q_1 and Q_2, as well as the times, t, when the pulses are initiated. The steady state current response is taken as the average current during a specified time interval, t_{ss}, at the end of the pulse. This technique is particularly well-suited to the calculation of overall current efficiency of an electrodeposition reaction by integrating and comparing the charge transferred during the stripping pulse, Q_2, and the deposition pulse, Q_1:

Equation 3.7

$$\Phi_e = \frac{Q_2}{Q_1} = \frac{\sum_{t_2}^{t_3} I(t)\Delta t}{\sum_{t_1}^{t_2} I(t)\Delta t}$$

where; $I(t)$ (C s^{-1}) is the instantaneous current, and Δt (s) is the current sample time.

3.3.2.1 Magnesium Sulphate Supporting Electrolyte

Normal pulse voltammetry was used to estimate the charge density of the Zn UPD layer in magnesium sulphate supporting electrolyte. The pulse sequence is outlined in Table 4.

Table 4: Potential pulse sequence for investigation of Zn UPD on Pt in 0.1 mol dm^{-3} $MgSO_4$ with 10^{-4} mol dm^{-3} Zn^{2+}, pH = 5.8, 950 mV (SCE) rest potential.

Potential / mV (SCE)	Duration / s	Current Data Acquisition Rate / s^{-1}
-400	20	0
	0.2	2000
200	0.1	2000
	20	200
-400	0.05	2000
	19.95	200

A relatively high current range of 10 mA, with an accuracy of ±0.02 mA, and fast sampling rate, 2000 s^{-1}, were employed during the initial application of the pulses in order to capture the relatively large transient currents.

3.3.2.2 Zinc Sulphate Electrolytes

The normal pulse method was modified slightly for use in zinc sulphate based electrolytes, except the highest acid electrolyte containing 1.0 mol kg^{-1} H_2SO_4, in a manner akin to differential normal pulse voltammetry [124]. In this method a second potential step, called a modulation step, is superimposed over the initial potential step (see Figure 12). The disc electrode base potential was -250 mV (SCE) while, as described in Appendix D, the ring electrode potential was held at 250 mV (SCE) to detect evolved hydrogen throughout the potential step sequence. The first potential step, E_{pre}, was -1100 mV (SCE) for 30 s (in order to pre-coat the disc electrode with zinc) which was followed by a modulation step, E_{dep}, to either -1100, -1125, -1150, -1200, -1250, -1300, -1400, -1500, -1750, -2000, or -2500 mV (SCE), for

10 s, before returning to the base potential. The current response was measured using the 100 mA range, with an accompanying accuracy of ±0.2 mA, and the sample times were 1 ms during the first second of the pulses and 20 ms for the remaining duration of the pulses. The combination of fewer samples being averaged at higher sampling rates and jitters in the current response, due to automatic variations in gain, sometimes results in off-scale measurements (see Figure 12), which are not included in the calculation of steady state current. However, as the potential difference between the working and counter electrode increases, at more negative applied potentials, there are larger oscillations in current response due to small overshoots of the feedback control loop which are included in the calculated standard deviation in the mean current response. The steady-state current responses to the modulation potentials were taken as the average current during the final 5 s of the pulses (250 data points).

The overall current efficiency during each modulation pulse, $\Phi_e(E_{dep})$, was calculated from the steady-state disc and ring currents, according to Equation 3.4, and from the charge transferred during the modulation pulse, Q_{dep}, and stripping pulse, Q_{strip} (which was adjusted to account for the zinc deposited during the pre-treatment pulse):

$$\Phi_e(E_{dep}) = \frac{Q_{strip} - Q_{pre}\Phi_e(E_{pre})}{Q_{dep}} \qquad \text{Equation 3.8}$$

By inspection, the accuracy of the overall current efficiency calculated from Equation 3.8 was dependant on both the accuracy of the current–time data and the current efficiency during the pre-treatment pulse, which was calculated using Equation 3.8 when E_{dep} equalled E_{pre} from repetitions of the same experiment.

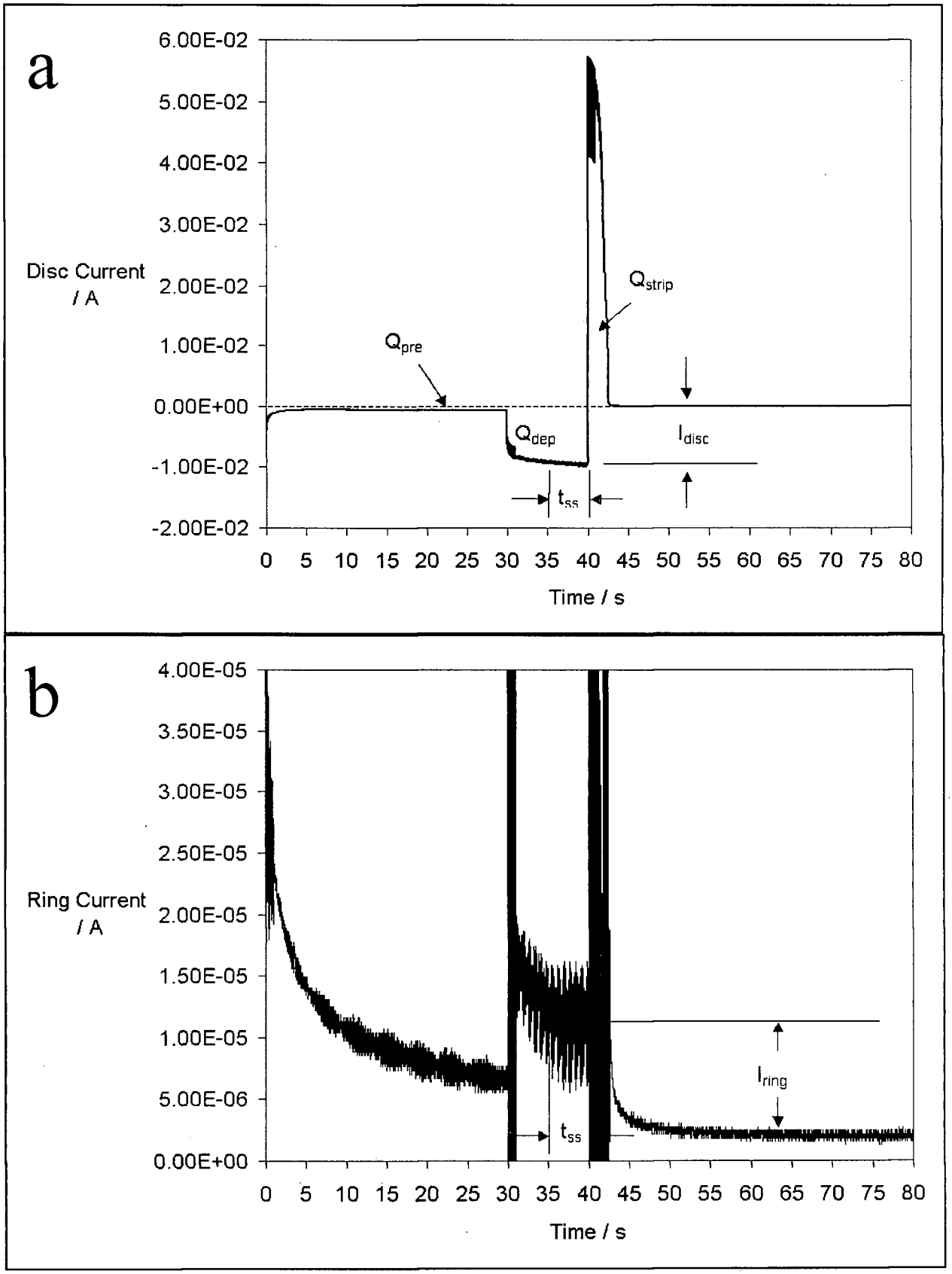

Figure 12: Disc (a) and ring (b) current responses to a differential normal pulse sequence in acidic zinc sulphate electrolyte. Generated in 1.0 mol dm^{-3} $ZnSO_4$ with 0.01 mol dm^{-3} H_2SO_4, pH = 2.4 at 25 °C, and 3600 rpm electrode rotation speed.

3.3.3 Staircase Voltammetry

Staircase voltammetry refers to the measurement of current response to the application of a series of potential steps (see Figure 13). Unlike normal pulse voltammetry, the electrode is not renewed after each potential step and, thus, the current response is generally affected by the previous potential steps. Staircase voltammetry was employed for all zinc sulphate electrolytes using many of the same potential levels employed in the normal pulse experiments. The first potential step was to -1100 mV (SCE) for 30 s which was followed by a series of 9 potential steps; -1125, -1150, -1200, -1250, -1300, -1400, -1500, -1750, and -2000 mV (SCE), each 10 s long. The sample time employed was 100 ms, enabling the use of the Autolab's automatic current ranging feature which increased the accuracy of the measured currents. However, this reduced the number of data points averaged when calculating the steady-state current response, during the final 5 s of each pulse, to 50.

In the case of electrolyte containing 1.0 mol kg^{-1} $ZnSO_4$ with 1.0 mol kg^{-1} H_2SO_4, due to formation of some hydrogen bubbles on the disc electrode during the initial pulse from -250 mV to -1100 mV (SCE), the staircase voltammetry procedure was modified. Rather than depositing zinc from the mixed electrolyte for 30 s at -1100 mV (SCE), zinc was depositing onto the electrode from neutral 1.0 mol kg^{-1} $ZnSO_4$ for 180 s at -1100 mV (SCE), prior to the cell being disabled and the electrode raised, under a nitrogen atmosphere, to a position above the solution. After acid was added and the electrolyte was allowed to cool back to 25 °C, *ca.* 10 minutes, the electrode was lowered back into the solution and the cell was immediately enabled at -1100 mV (SCE). This was quickly followed by initiation of the staircase voltammetry experiment as previously described.

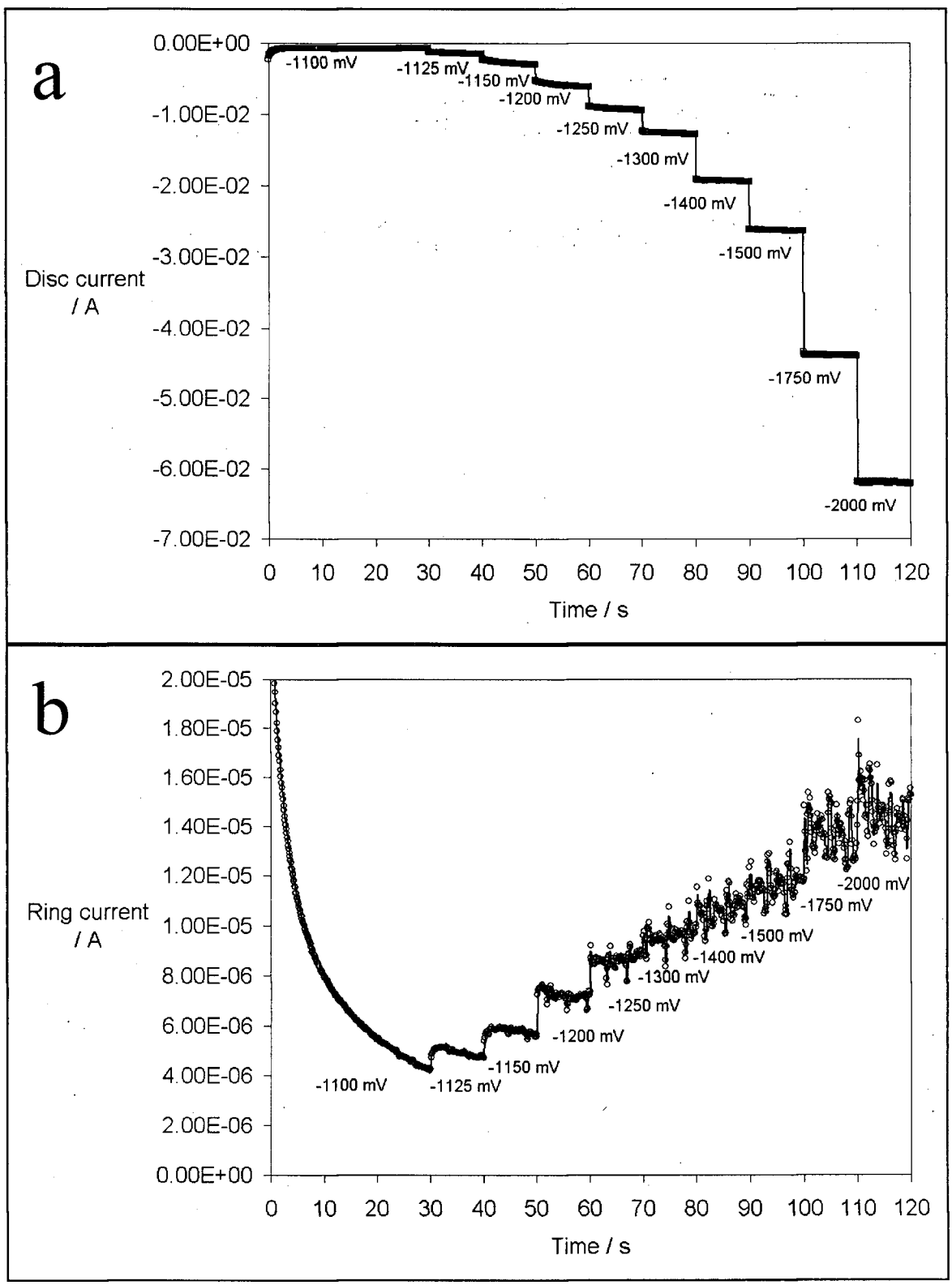

Figure 13: Staircase voltammetry in an acidic zinc sulphate electrolyte. Disc (a) and Ring (b) current responses in 1.0 mol dm^{-3} $ZnSO_4$ with 0.01 mol dm^{-3} H_2SO_4, pH = 2.4 at 25 °C, and 3600 rpm electrode rotation speed.

3.3.4 AC Impedance Spectroscopy

Electrochemical impedance spectroscopy was employed to estimate the solution resistances of the zinc electrolytes in order to calculate the electrode potential from the applied deposition potentials as follows:

$$E = E_{dep} - I_{disc} R_{soln} \qquad \text{Equation 3.9}$$

The procedure, referred to as "FRA Low Acid Project" in Appendix F, involved polarizing the electrode for 5 minutes at the base potential used during normal pulse experiments, -250 mV (SCE), followed by the application of a 10 mV rms perturbation in a sine wave format in the frequency range of 100 to 1000 Hz. The real and imaginary components of the measured cell impedance, Z' and Z'', were modelled as a series resistor–pseudocapacitor circuit (see Figure 14) according to Equation 3.10.

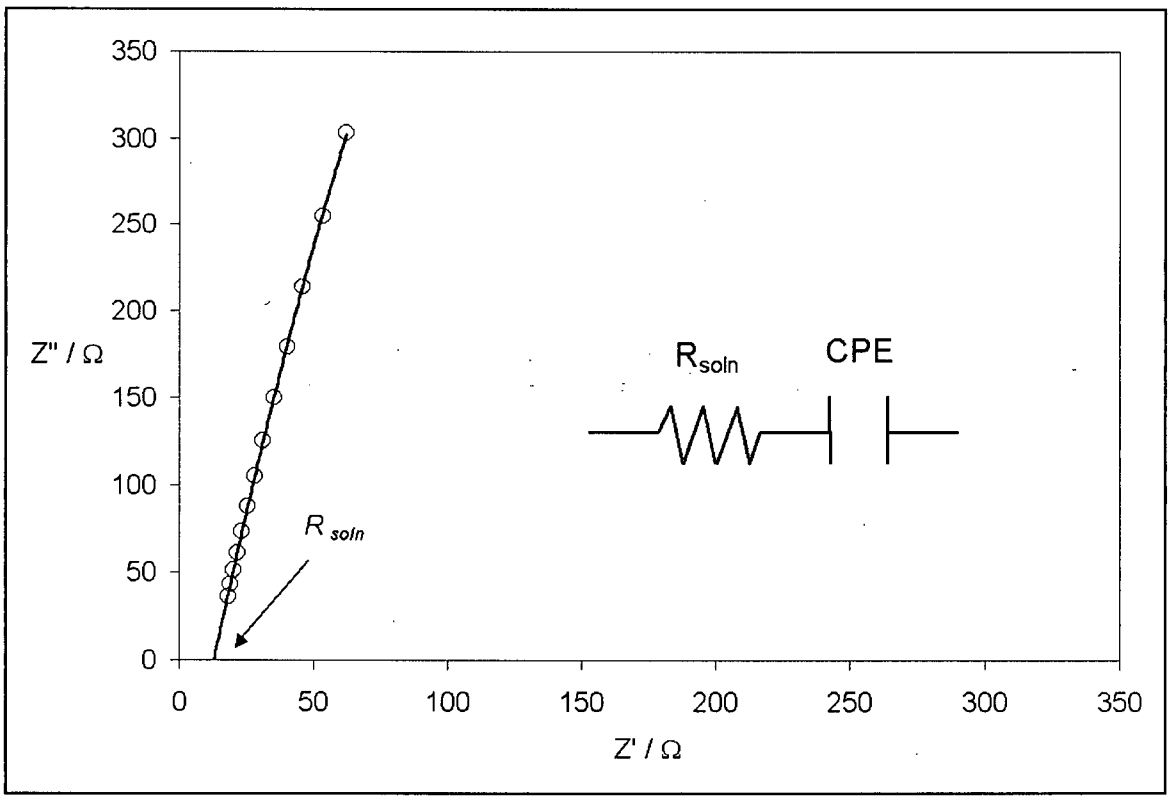

Figure 14: Nyquist plot of impedance data generated using "FRA Low Acid Project" on a platinum electrode in acidic zinc sulphate electrolyte. Generated in 1.0 mol dm^{-3} $ZnSO_4$ with 0.01 mol dm^{-3} H_2SO_4, pH = 2.4 at 25 °C, and 3600 rpm electrode rotation speed.

$$Z = R_{soln} + (i\omega CPE)^{-\xi}$$ Equation 3.10

where; *CPE* is the constant phase element, *i* is the imaginary number ($\sqrt{-1}$), and ω (rad s^{-1}) is the frequency of the voltage perturbation. The solution resistance, along with an estimation of relative error, was obtained using the "Fit and Simulation" utility of Autolab FRA version 4.8 software.

3.4 Surface Analyses

Several surface characterization techniques were employed to supplement the findings of the electrochemical experiments. Selected electrode surfaces were analysed by x-ray photoelectron spectroscopy, XPS, atomic force microscopy, AFM, and/or scanning electron microscopy, SEM.

3.4.1 XPS Analyses

XPS analysis was performed to examine the electrode surface after extended polarization at -400 mV (SCE) in magnesium sulphate electrolyte containing 0.020 mol dm^{-3} $ZnSO_4$. Prior to analysis by XPS, samples were rinsed with deionised water and dried in air. XPS analyses were performed using a Leybold MAX200 spectrometer with a MgKα source (1253.6 eV) operated at 15 kV, 20 mA, and a system pressure of 1×10^{-9} mbar. Spectra were obtained with a pass energy of 192 eV. Binding energies were referenced to the Au 4f1/2 peak at 84.0 eV.

3.4.2 AFM Analyses

Atomic force microscopy was employed to examine the morphology of zinc deposits and the evolution of the substrate electrode morphology resulting from zinc deposition on platinum. AFM analyses were accomplished using a PicoSPM AFM (Molecular Imaging) operated in contact mode using Si_3N_4 tips (Molecular Imaging) which had typical force constant of 0.50 N m^{-1}. Specimens were imaged, while still wet, immediately upon removal from the electrochemical cells. A solution film was maintained over the specimens by periodic additions of deionised water. The real surface area and rms roughness of specimens were calculated from AFM images, from the arrays of 256 x 256 'z' position data, using a Matlab script which summed of the areas of triangles between all groups of three adjacent points (see Appendix E). The rms roughness calculated using the Matlab script was verified by checking it against that calculated by PicoScan version 4.19 software.

3.4.3 SEM Analyses

Scanning electron micrographs were obtained using a Hitachi S-3000N SEM equipped with a Quartz XOne EDX system. Samples were rinsed with deionised water and air-dried prior to being placed in the vacuum chamber. An acceleration voltage of 5 keV was employed to generation spectra for elemental analyses, which were fit using Quartz Imaging software.

4 Results and Discussion

The results of this study are broken into two main sections; Zinc Underpotenital Deposition on Platinum, and Zinc Overpotential Deposition. The modifying effect of UPD of zinc on a platinum electrode was examined as a method of preparing an electrode substrate on which to conduct zinc OPD experiments. The usefulness of this system was then tested in the examination of the kinetics of OPD Zn in acidic sulphate electrolytes relevant to industrial zinc electrowinning. Where applicable, the results are discussed in terms of their relevance toward industrial zinc electrowinning. Unless otherwise indicated, the 'Solver' utility of Microsoft Excel 2000 software was employed for minimizing the sum of the square of errors, *SSE*, during modelling of data.

4.1 Zinc Underpotential Deposition on Platinum

Zinc UPD on Pt was characterized in sulphuric acid, magnesium sulphate and zinc sulphate electrolytes. The experiments were undertaken in order to examine the suitability of platinum as a substrate for measuring the kinetics of Zn OPD in acidic sulphate electrolytes, the requisite properties being; inhibition of hydrogen evolution, to prevent blocking of the electrode by hydrogen gas bubbles, and homogeneous nucleation and growth of Zn OPD, in order to generate a relatively smooth zinc overlayer on the electrode.

4.1.1 Behaviour in Sulphuric Acid Supporting Electrolyte

The voltammograms in Figure 15 are similar to those reported by Aramata [53]. The features identified are the onset of UPD Zn formation, **I** at *ca.* 0 V (SCE) , H_2 evolution, **II** at < *ca.* -250 mV (SCE), and stripping of UPD Zn, **I'** at *ca.* -200 mV (SCE); the symmetry between regions **I** and **I'** indicate that the formation and stripping of the UPD Zn layer is quite reversible. In sulphuric acid solution the regions of hydrogen adsorption and Zn UPD overlap. The rate of hydrogen evolution at potentials < *ca.* -250 mV (SCE) appears to have been barely inhibited by the presence of the Zn UPD layer (see **II** in Figure 15). Mascaro-Lucia et al. [125] have described a strong inhibition of hydrogen evolution due to increased coverage of Zn UPD on polycrystalline Pt in acidic fluoride media relative to acid sulphate media, for which corresponding stripping charges of the Zn UPD layer were 210 and 350 $\mu C\ cm^{-2}$, respectively.

From this observation it was concluded, by Mascaro-Lucia et al., that adsorbed sulphate or hydrogen sulphate partially blocked Zn UPD in acidic sulphate electrolytes and that 350 μC cm^{-2} was closer to the value for complete coverage of the electrode by Zn UPD.

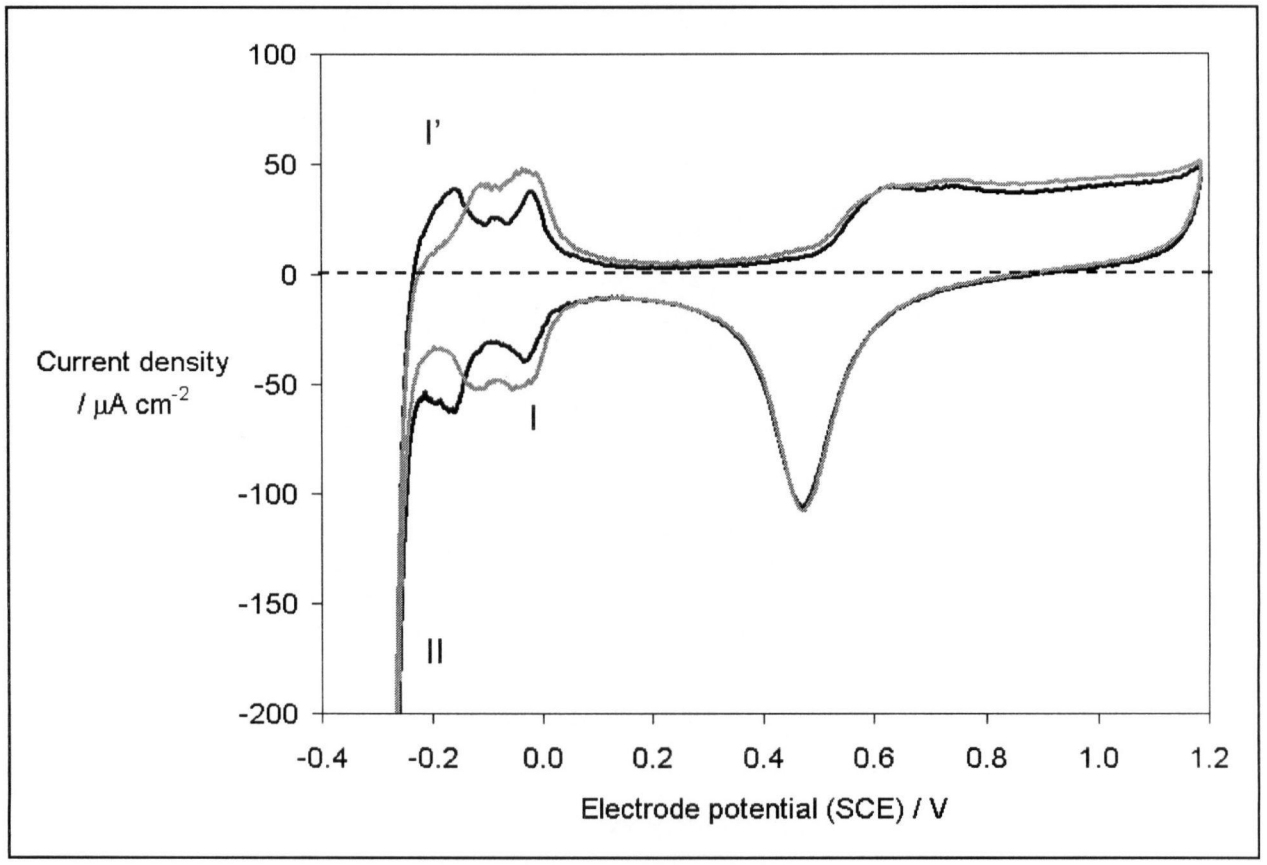

Figure 15: Cyclic voltammograms of polycrystalline platinum in 0.1 mol dm^{-3} H_2SO_4, pH = 0.7, with (——) and without (——) 10^{-3} mol dm^{-3} $ZnSO_4$ at 25°C, scan rate 20 mV s^{-1}, 1600 rpm electrode rotation speed.

Aramata et al. [58] have described a shift of the onset of Zn UPD on Pt(111) towards more negative potentials with decreasing pH in phosphate media, which was attributed to preferential adsorption of phosphate species relative to Zn UPD. This effect was reportedly absent in sulphate media for the pH range of 0.8 to 3.7 [55]. However, the conclusions were based on interpretations of cyclic voltammograms which, in fact, showed a clear difference when the pH was shifted from 3.2 to 3.7 [55]. Furthermore, Lachenwitzer et al. [126] have determined that, in the potential range of sulphate/hydrogen sulphate adsorption on Pt(111), hydrogen sulphate is the predominantly adsorbed species at pH < 3.3 while sulphate is more prevalent at pH > 4.7. Thus, it is reasonable to assume that in this study, at a pH of 0.7 in sulphuric acid supporting electrolyte and at *ca.* -250 mV (SCE), there were regions of the electrode which were not occupied by UPD

Zn, due to the blocking effect of specifically adsorbed hydrogen sulphate anions. These facets catalysed hydrogen evolution when the potential was swept to more negative values.

As illustrated in Figure 16, when the electrode was conditioned by holding it at a potential more negative than the UPD Zn potential, -200 mV (SCE) in this case, the stripping current of the UPD Zn layer, **I'**, diminished, indicative of the formation of a surface alloy. As previously described by Despić and Pavlović [51], it is only as the platinum substrate begins to oxidize, **III**, that the alloyed zinc is released. Surface alloy formation resulting from such polarization routines has been reported for several UPD systems including; Pb-Au[127, 128], Pb-Ag[128], Cd-Ag[129], Cd-Au[130, 131], Tl-Ag [132], and Sn-Au [133]. Increased conditioning time on a UPD Zn surface, presumed to form a Pt-Zn surface alloy, appears to slightly inhibit hydrogen evolution current, < *ca.* -250 mV (SCE), shifting it toward more negative potentials as indicated by the arrow in Region **II** of Figure 16. The theoretical basis for alloy formation in this system and its potential effect hydrogen evolution kinetics will be discussed later.

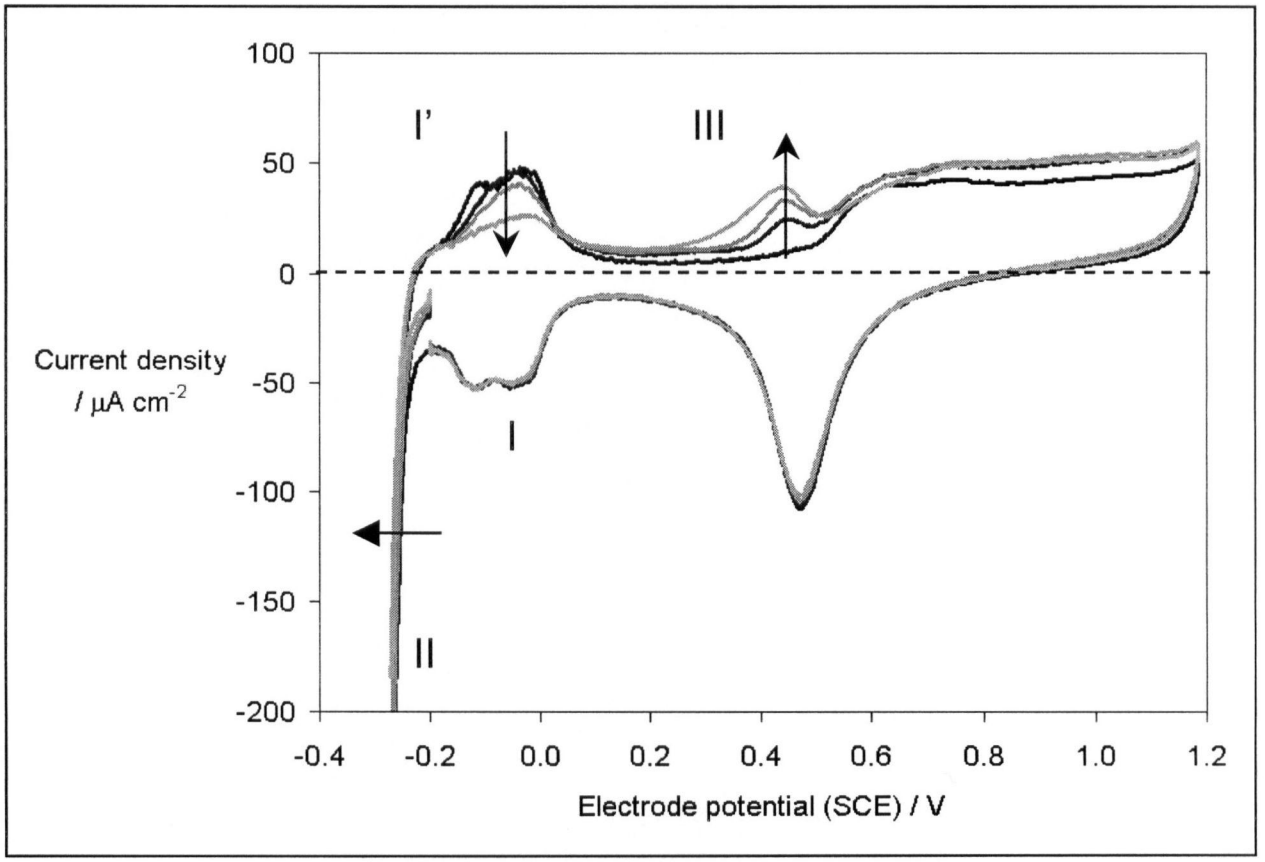

Figure 16: Cyclic voltammograms of polycrystalline platinum in 0.1 M H_2SO_4 , pH = 0.7, with 10^{-3} mol dm^{-3} $ZnSO_4$ at 25 °C, scan rate 20 mV s^{-1}, 900 mV (SCE) rest potential, 1600 rpm electrode rotation speed, as a function of conditioning time at -200 mV (SCE), 0 s (——), 900 s (——), 1800 s (——), 3600 s (——).

4.1.2 Behaviour in Magnesium Sulphate Supporting Electrolyte

Experiments were conducted in neutral magnesium sulphate solution, to maximize the surface coverage of UPD Zn and to separate the regions of UPD Zn and hydrogen adsorption on Pt. As illustrated in Figure 17, the potential region of hydrogen adsorption, **II**, was shifted to a more negative potential, < *ca.* -400 mV (SCE), together with bulk hydrogen evolution, **III**, which then occurred at < *ca.* -800 mV (SCE), and oxidation of adsorbed hydrogen, **II'**, at between *ca.* -500 to -200 mV (SCE). After addition of 10^{-4} mol dm^{-3} zinc sulphate, the potential region of Zn UPD, **I**, between *ca.* -400 and 0 mV (SCE), appeared clearly separate from hydrogen adsorption. The potential range for Zn UPD and the shape of the voltammogram appeared quite similar to Zn UPD on polycrystalline Pt from 0.1 mol dm^{-3} KH_2PO_3 buffered at pH = 5.9 [53].

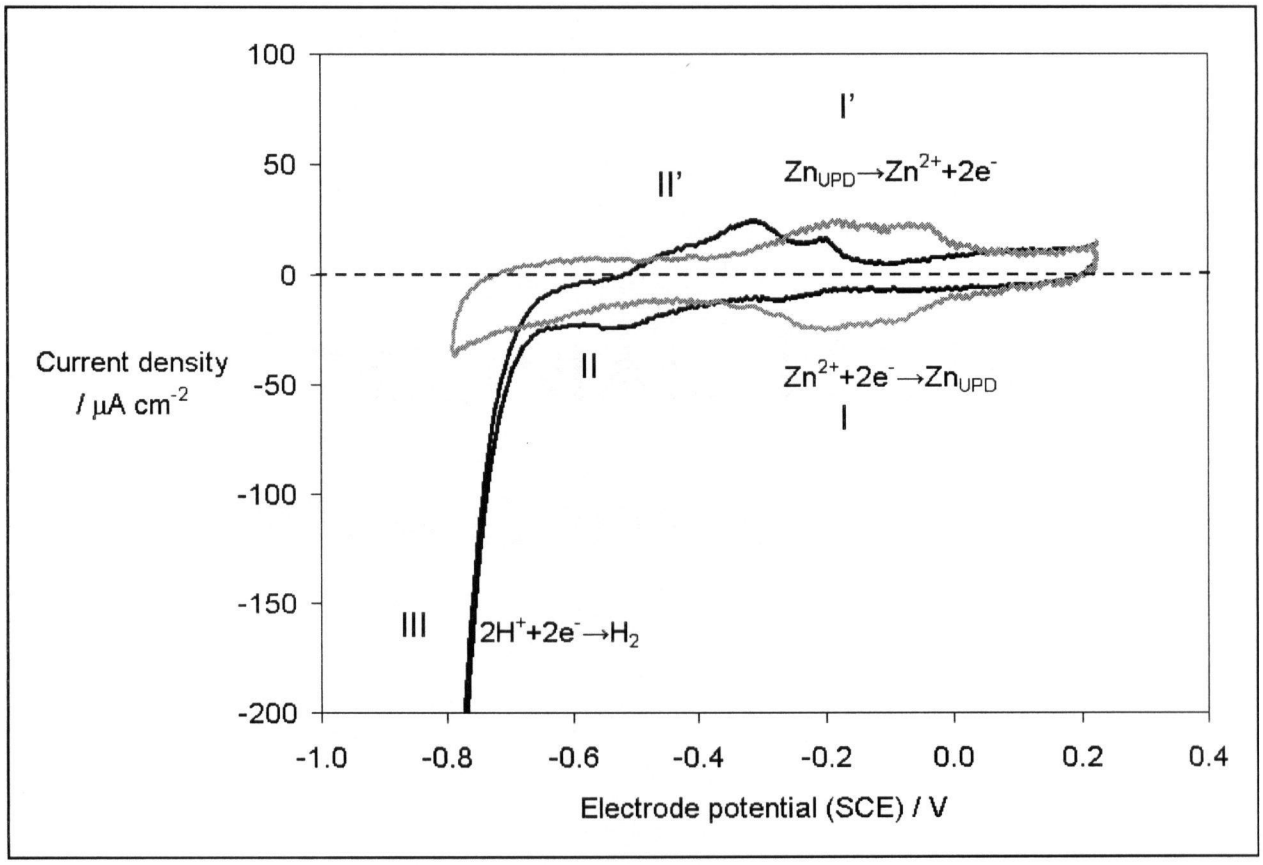

Figure 17: Cyclic voltammograms of polycrystalline platinum in 0.1 mol dm^{-3} $MgSO_4$, with (——) and without (——) 10^{-4} mol dm^{-3} $ZnSO_4$, pH = 5.8, at 25 °C, scan rate 20 mV s^{-1}, 1600 rpm electrode rotation speed.

The charge density for Zn UPD formation was estimated to be 260 ±30 μC cm^{-2}, as illustrated in Figure 18, by integrating the current response to a potential pulses between 200 to -400 mV (SCE). The relatively large range in the charge density for Zn UPD was due, mainly, to the

uncertainty resulting from the use of a current range setting of 10 mA during the pulse sequence which had an accompanying accuracy of ±0.02 mA. As mentioned previously, this current range was necessary to capture the surge in current that occurs during the initial stages of the potential pulse, due to depletion of zinc ions from the electrolyte near the Pt electrode surface.

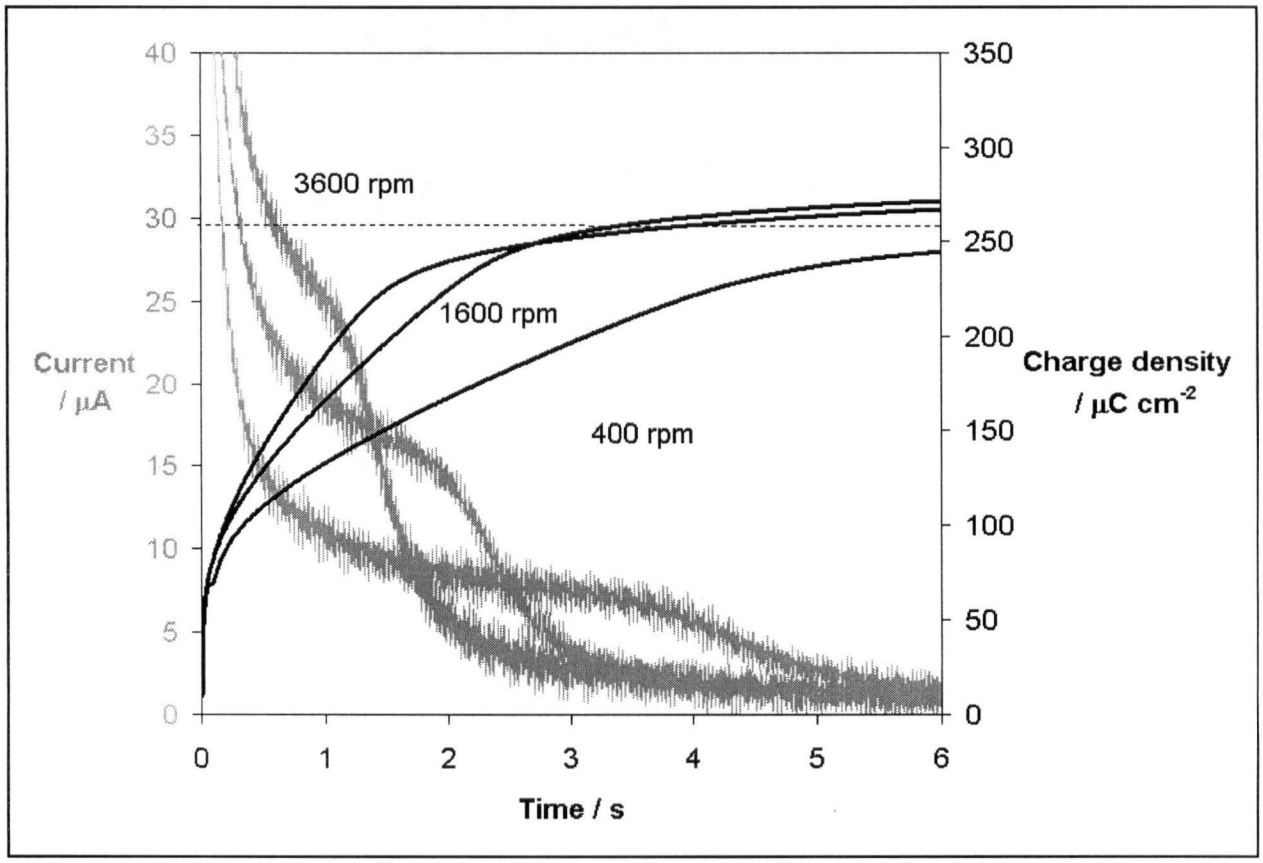

Figure 18: Current (———) and charge density (———) response of polycrystalline platinum in 0.1 mol dm^{-3} $MgSO_4$ with 10^{-4} mol dm^{-3} $ZnSO_4$ pH = 5.8, at 25 °C, to a potential pulse from 200 to -400 mV (SCE), for indicated electrode rotation speed.

The current responses appeared to be consistent with mass transport control of Zn^{2+} coupled with rapid heterogeneous UPD, which tended to zero as Zn filled sites on the Pt surface [134]. During the initial stages of the pulses, the currents were determined to vary directly with the square root of time, which is typical of semi-infinite linear diffusion of Zn^{2+} to the electrode during relaxation of the diffusion boundary layer. Zn UPD on polycrystalline Pt is reportedly similar to Pt (110) (the facet on which Zn UPD occurs to the greatest extent) [58]. The calculated charge density for Zn UPD in this study was somewhat smaller than the figure of 320 μC cm^{-2} reported for Zn UPD formation on Pt(110) in 0.1 M KH_2PO_4 at pH = 3.7 [58]. However, 260 μC cm^{-2} was not unreasonable when considering that the theoretical charge densities for full coverage of UPD Zn on Pt(110) is 294 μC cm^{-2}, as calculated below:

$$\sigma(\mu C\, cm^{-2}) = zF\Gamma = 2 \times 96485 \times \frac{1 \times 10^{6}}{d^{2}.N_{A}.\sqrt{2}} = 294$$ Equation 2.25

where; d (2.775×10^{-8} cm) is the Pt-Pt bond length, and N_A (6.0221367×10^{23} mol^{-1}) is the Avogadro number.

In order to ensure that the calculated charge density was not overestimated, the polished platinum electrode was characterized using AFM and SEM. The resulting images, see Figure 19, revealed a relatively flat surface with a surface roughness of approximately 50 Å rms. The real surface area of a 10×10 μm square was estimated, from the array of 256 x 256 'z' position data of the AFM image, by simply calculating the sum of the areas of triangles between all groups of three adjacent points (see Appendix E). This value was only approximately 0.4 % greater than the geometric area of 100 μm^2.

A notable feature of the presence of a Zn UPD layer in pH = 5.8 electrolyte was its dramatic effect on hydrogen evolution kinetics. As illustrated in Figure 20, even at relatively large overpotentials, e.g. 300 mV corresponding to *ca.* -1100 mV (SCE), at which zinc bulk deposition occurs, the corresponding hydrogen evolution current density (*ca.* -300 $\mu A\ cm^{-2}$) was close to that observed in the absence of zinc at *ca.* -800 mV (SCE). The presence of the UPD Zn layer on platinum has some enhanced property of inhibiting hydrogen evolution over bare platinum though clearly not to the same extent as pure zinc.

It is likely that the relatively neutral pH of the magnesium sulphate solution was related to the more complete coverage of the platinum substrate by the zinc UPD layer, resulting in its increased inhibition of hydrogen evolution. The implication is that a Zn UPD modified platinum electrode, to be used for bulk deposition experiments, should be prepared in a near neutral solution, as this diminishes the reversible potential and hence the kinetics of hydrogen adsorption and/or hydrogen sulphate adsorption, so biasing the competitive adsorption on Pt in favour of Zn. The upper pH limit would be dictated by the ultimate precipitation of $Zn(OH)_2$.

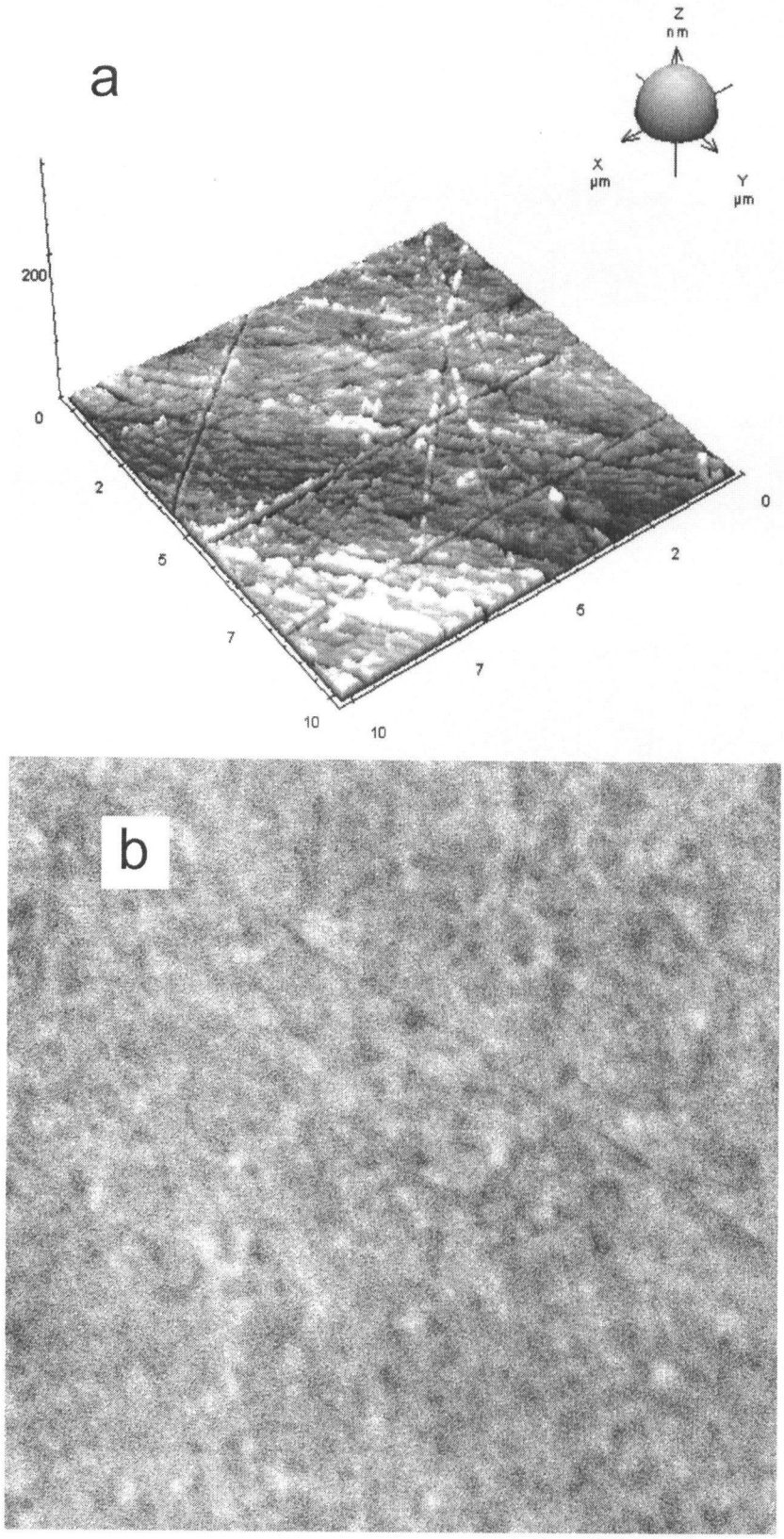

Figure 19: 10 × 10 µm square AFM image (a) and SEM photomicrograph (10000× magnification) (b) of polished platinum substrate.

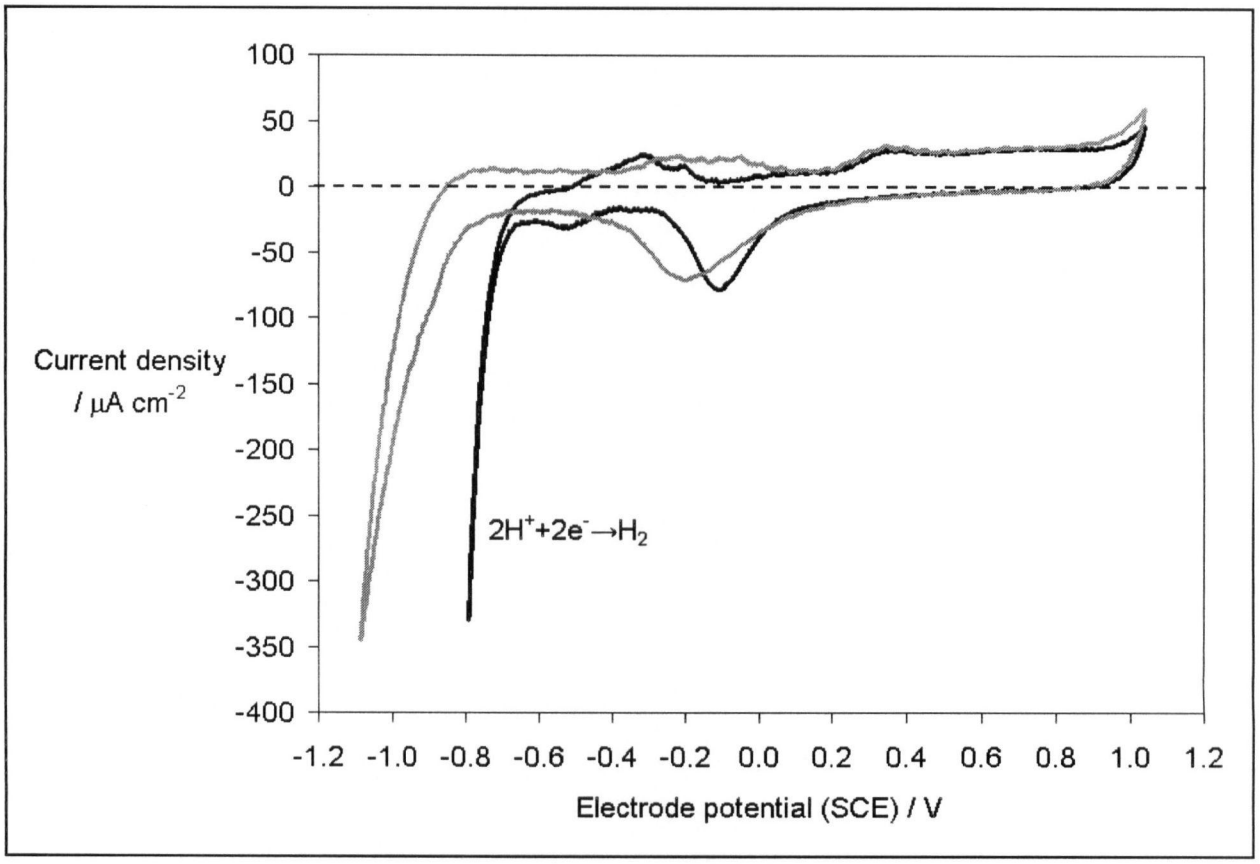

Figure 20: Cyclic voltammograms of polycrystalline platinum in 0.1 mol dm^{-3} $MgSO_4$ with (——) and without (———) 10^{-4} mol dm^{-3} $ZnSO_4$ pH = 5.8, at 25 °C, scan rate 20 mV s^{-1}, 1600 rpm electrode rotation speed.

4.1.3 Voltammetry in Aqueous Zinc Sulfate Electrolyte Solutions

Cyclic and linear sweep voltammetry were employed to further study zinc overpotential deposition and alloy formation in zinc sulphate electrolytes. The absence of a current loop during bulk zinc deposition and stripping, **IV** and **IV'** in Figure 21, by virtue of the lack of a significant critical overpotential, was further evidence that zinc overpotential deposition occurs uniformly over the platinum substrate. Other features indicated on Figure 21 are; **I**, platinum oxide reduction, **II**, hydrogen evolution, **III**, deposition of a monolayer quantity of Zn, **III'** stripping deposition of a monolayer quantity of Zn, **V**, stripping of zinc UPD layer, and **I'**, platinum oxidation. Regions **III** and **III'** are somewhat masked due to simultaneous hydrogen evolution, but the perturbations in cyclic voltammogram are readily observable. Further evidence of alloy formation in this system will be addressed later.

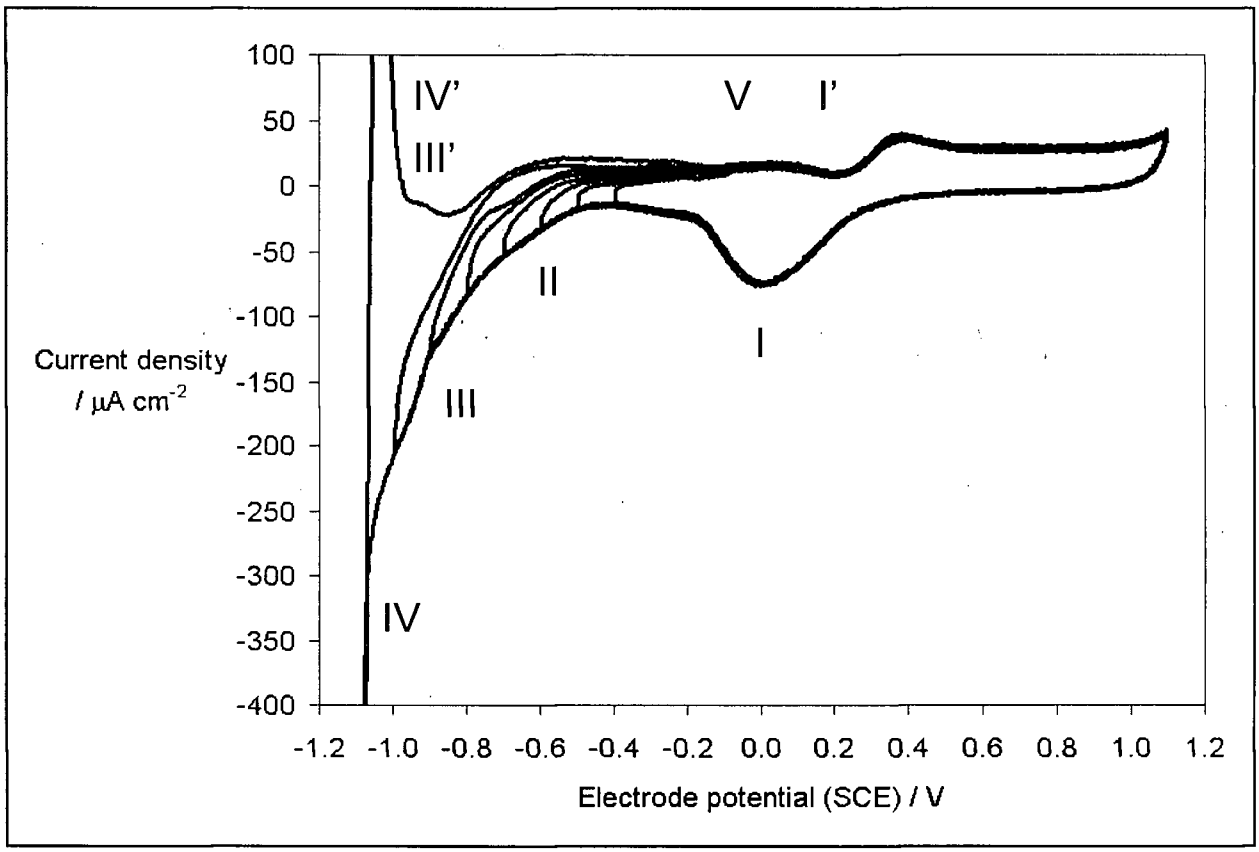

Figure 21: Cyclic voltammetry on polycrystalline platinum in 0.1 mol dm^{-3} $ZnSO_4$, pH = 4.9 at 25 °C, scan rate 20 mV s^{-1}, 1600 rpm electrode rotation speed.

In order to reproduce the 2-D surface alloy formed in sulphuric acid supporting electrolyte (Figure 15), and examine its effect on overpotential zinc deposition, the electrode was polarized for various times at -400 mV (SCE), which is slightly more positive than potentials at which hydrogen evolution occurs. As illustrated in Figure 22, when the potential was swept towards more positive potentials, the stripping current in the UPD Zn potential region decreased as waiting time increased, indicated by the down arrow, while current in the potential region of platinum oxidation increased, indicated by the up arrow. When the same experiment was repeated using a conditioning potential of 200 mV (SCE), there was no increase in the stripping current in the region of platinum oxidation. This was interpreted as further evidence that the observed effect of electrode conditioning at -400 mV (SCE) was not due to adsorption of a contaminant since the same contaminant was likely to have adsorbed at 200 mV (SCE) and been oxidized subsequently at 300 mV (SCE).

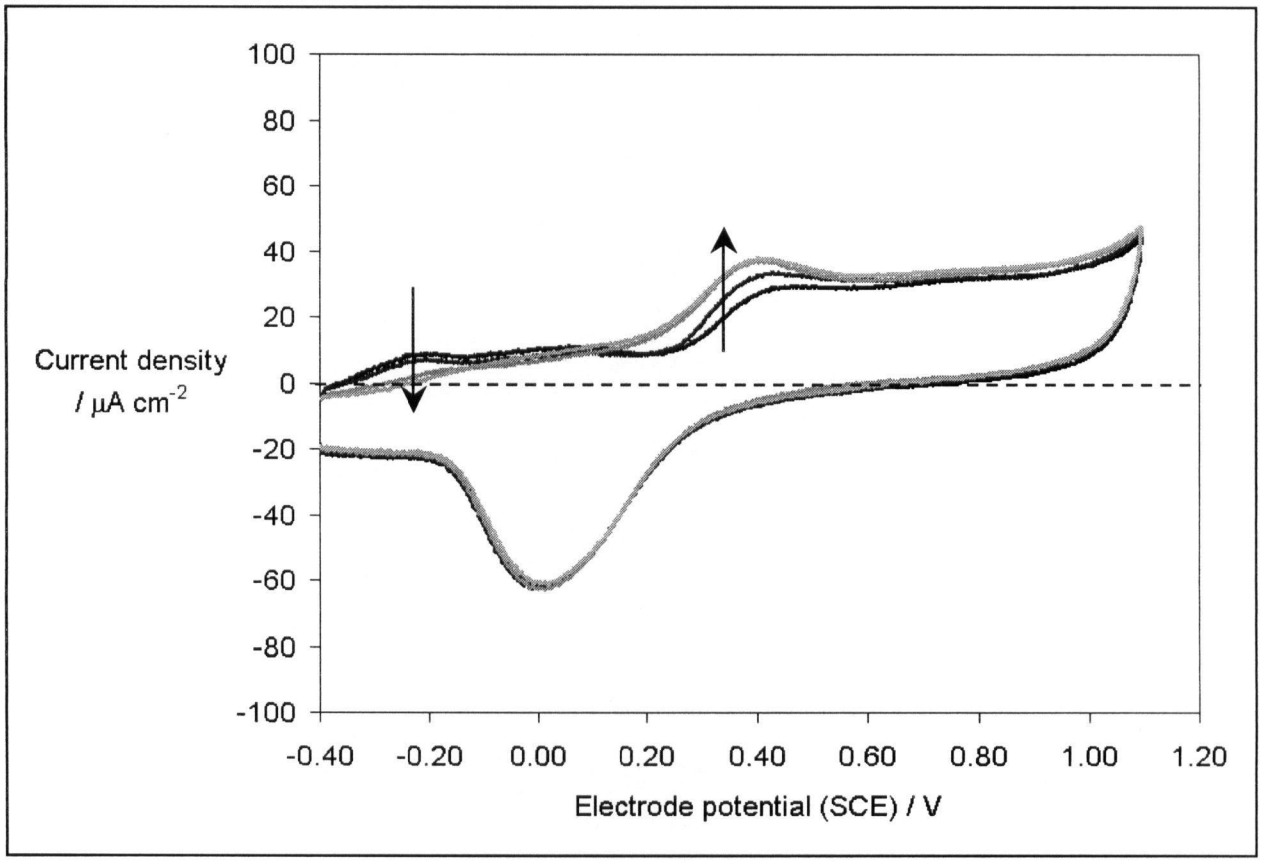

Figure 22: Sweep voltammetry of polycrystalline platinum in 0.1 mol dm^{-3} $ZnSO_4$, pH = 4.9 at 25 °C, scan rate 20 mV s^{-1}, 1600 rpm electrode rotation rate, as a function of waiting time at -400 mV (SCE), 0 s (———), 120 s (———), 600 s (———), 1200 s (———).

The changes in the voltammogram due to conditioning were limited to approximately the first 600 s; this was interpreted as the time for termination of the transformation of the UPD layer to a surface alloy. However, to be clear, it is not claimed that the entire UPD layer was transformed to an alloy, only that whatever fraction of the surface which would have undergone transformation to a 2-D alloy did so within 600 s. As shown in Figure 23, X-ray photoelectron spectroscopic, XPS, analysis of a freshly polished platinum electrode subjected to a thirty minute conditioning period at -400 mV (SCE) in the presence of zinc ions, confirmed the retention of some zinc on the electrode surface. In addition, the XPS analysis did not contain any peaks attributable to the deposition of inorganic impurities, which verified the purity of the electrolyte. EDX analysis was also attempted on this sample to confirm the presence of retained zinc and though the spectra showed some evidence of the presence of zinc, the results were inconclusive (due to the general lack of surface sensitivity of the EDX, the estimated error in zinc concentration was in the same range as the detected zinc concentration).

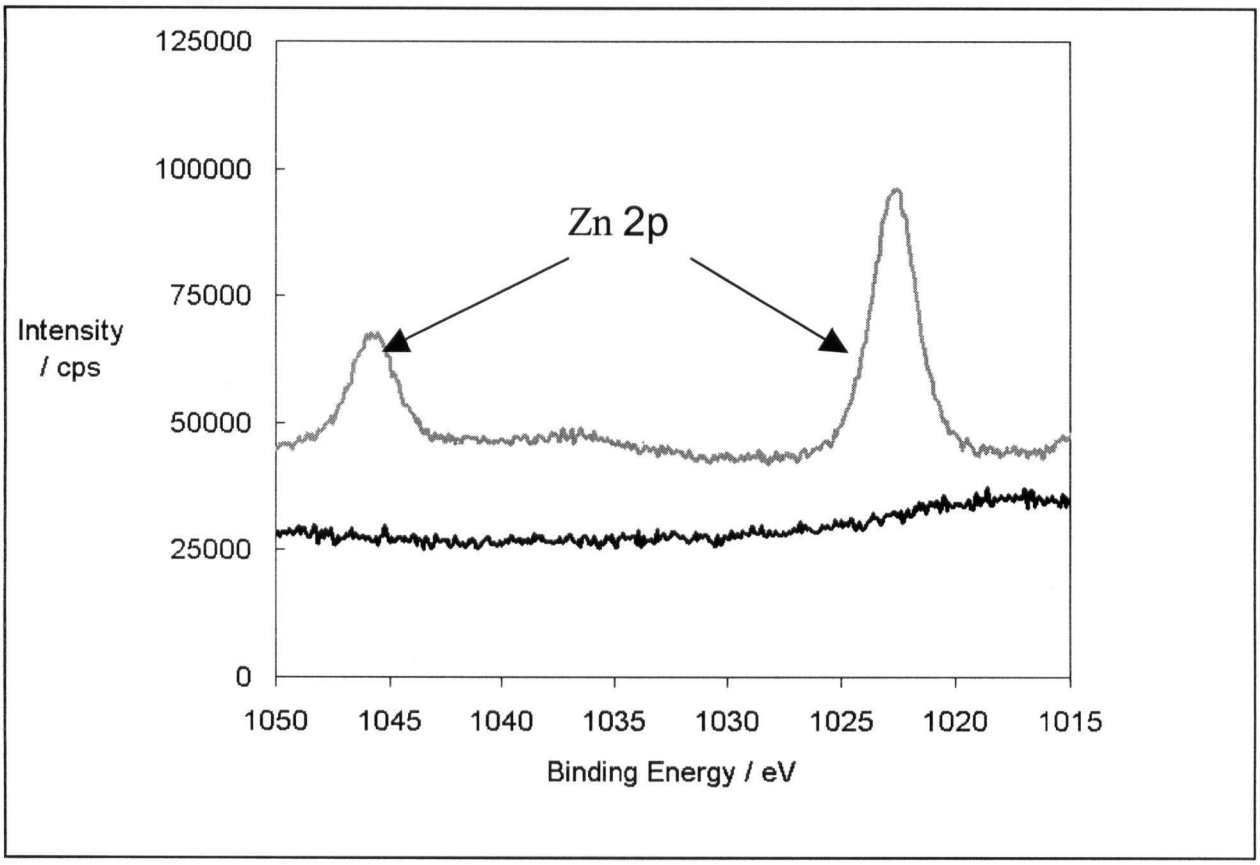

Figure 23: XPS analysis of bare platinum (———), offset for clarity, and a platinum electrode conditioned at -400 mV (SCE) for 1800 s (———) in 0.1 mol dm^{-3} $MgSO_4$ with 0.02 mol dm^{-3} $ZnSO_4$, pH = 5.0 at 25 °C.

The effect of conditioning the electrode at -400 mV (SCE) on Zn OPD was examined by sweeping the potential region of bulk zinc deposition after conditioning. As shown by region **II** in Figure 24, a complementary effect on zinc deposition kinetics was observed. The conditioned substrate appeared to be more amenable to OPD of Zn. This confirmed that the previous observation, interpreted as evidence of 2-D alloy formation, was not due to an organic contaminant, since such a contaminant would likely block sites for zinc deposition and adversely affect Zn OPD. In addition, the rate of hydrogen evolution in region **I** of Figure 24 appeared to be diminished, as indicated by the arrow. According to Wiart's Model, zinc adsorption, as Zn^{+}_{ad}, competes with hydrogen adsorption, as ZnH_{ad}, as the first step in zinc electrocrystallization. If this model is accepted, these results suggest that hydrogen adsorption on the conditioned electrode was simply not as favourable as on a freshly deposited UPD Zn layer. This would explain both the diminished hydrogen evolution, since hydrogen adsorption always precedes evolution, and enhanced zinc deposition, since zinc adsorption would more favourable compared to hydrogen adsorption. In this regard, H adsorption on Au-Pt alloys has been demonstrated to be significantly weaker than on pure Pt [135].

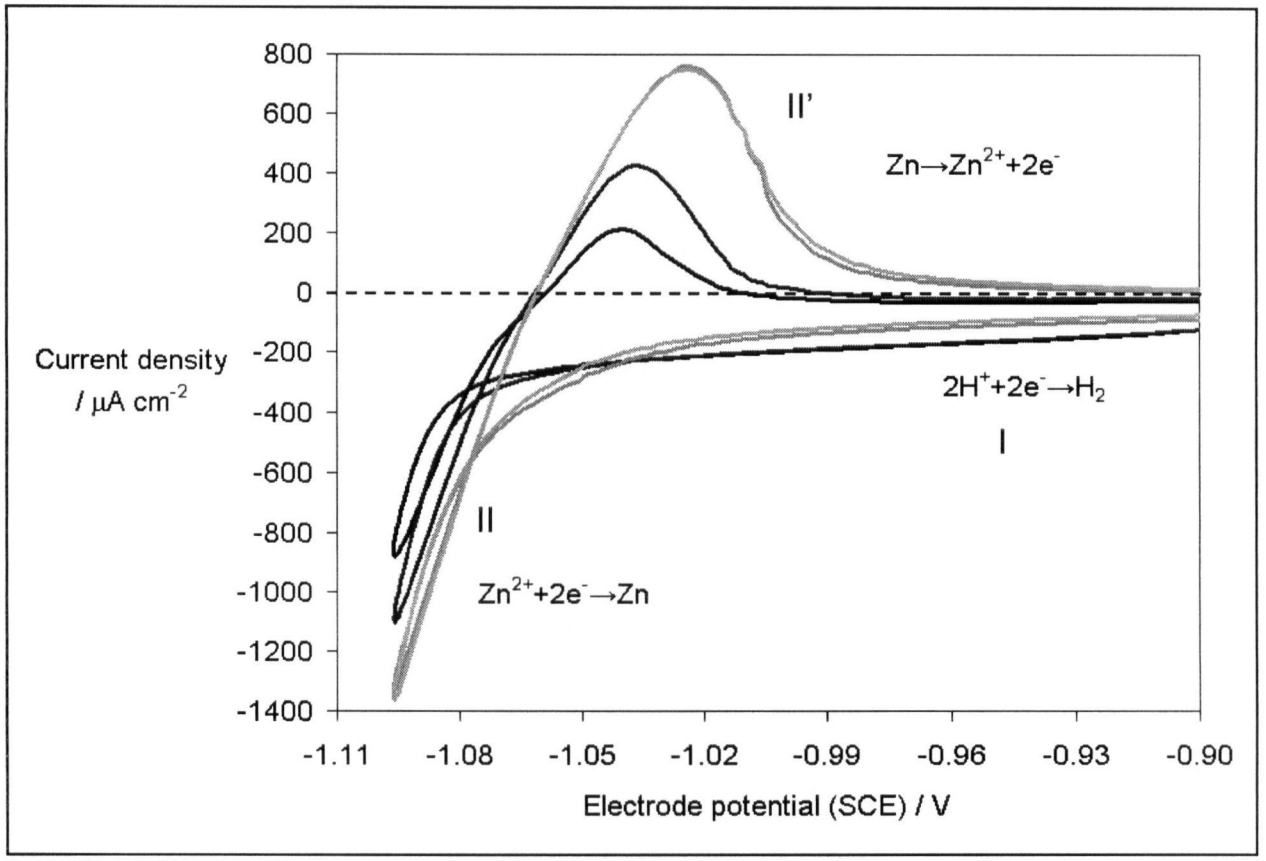

Figure 24: Sweep voltammetry of polycrystalline platinum in 0.1 mol dm^{-3} $ZnSO_4$, pH = 4.9 at 25 °C, scan rate 20 mV s^{-1}, 1600 rpm electrode rotation speed, as a function of waiting time at -400 mV (SCE), 0 s (———), 120 s (———), 600 s (———), 1200 s (———).

If the electrode was oxidized, by sweeping the potential to 1100 mV (SCE), then subsequent voltammograms appeared similar to that of the original unconditioned electrode. If on the other hand, after conditioning, the electrode potential was swept back to -250 mV (SCE) and then returned to the potential region of zinc deposition, the enhancement of zinc OPD kinetics remained. Thus, it was concluded that -250 mV (SCE) may be used as a potential to strip zinc from the electrode while retaining its enhanced properties. This potential is significant, since it corresponds to the reversible potential for hydrogen evolution from a highly acidic solution of pH *ca.* 0. This should have allowed for the measurement of current efficiency for bulk zinc deposition over a wide composition range of acidic zinc sulphate electrolytes. The specific manner in which this technique was employed to measuring current efficiency was to integrate the current-time transients, at the disc electrode, to potential steps for zinc deposition and stripping, and then calculate the ratio of the total charge passed for each step (see Section 3.3.2). The results of Zn OPD experiments, where -250 mV (SCE) was employed as the stripping potential, will be discussed in the Section 4.2.

When addressing the evidence of alloy formation presented for this system it is necessary to differentiate between the 2-D surface alloy phase and a 3-D bulk alloy phase. The behaviour of the cyclic voltammograms, conducted after the various polarization routines, is claimed to be evidence of 2-D alloy formation, which would have occurred by a site exchange between Zn and Pt. The thermodynamic driving force for such a process would be the difference in binding energy between the 2-D Zn UPD layer and the 2-D Zn-Pt surface alloy. Though no thermodynamic data exist for this system, the stability of the 2-D alloy was assumed to be consistent with that of the 3-D Zn-Pt alloy phase, observed by Uhlig [48] to be resistant to attack by strong acids at elevated temperatures.

Bulk 3-D alloy phase formation, though preceded by 2-D alloy formation, occurs by mutual diffusion of Zn-Pt into the Pt, at a site that is subsequently replenished by Pt and UPD of Zn. As one can imagine, 3-D alloy formation may lead to significant roughening of the electrode surface especially since the rate of Zn-Pt diffusion would be dependent on the crystal face. This type of alloy formation generally occurs at potentials much closer to that for bulk metal deposition, with the rate of alloy formation obeying the following parabolic rate law, typical of semi-infinite linear diffusion through a product layer [62]:

$$\Delta q(\Delta E, t) = 2zF\sqrt{\frac{D_{Zn-Pt}}{\pi}}\frac{1}{f^{*}Zn}\left[\exp\frac{-zF\Delta E}{RT}\right]\sqrt{t} \qquad \text{Equation 4.1}$$

where; Δq ($\mu C\ cm^{-2}$) is the charge density associated with Zn UPD, which follows 3-D alloy formation, ΔE (V) is the difference between the conditioning potential and the bulk Zn deposition potential, $f^{*}Zn$ is the activity of Zn at the surface.

When Despić and Pavlović [51] noted an increase in cathodic current density, during cyclic voltammetry, at *ca.* -800 mV (SCE) (ΔE = 300 mV more positive than the equilibrium Zn deposition potential), this was probably due to 3-D alloy formation. The fact that the associated current was observable during cyclic voltammetry at room temperature (**III** in Figure 21 and Figure 3) and at such a large ΔE, was an indication of extremely rapid 3-D alloy formation in the Zn-Pt system. Bulk 3-D alloy formation and its effect on the underlying electrode morphology, were examined and the results are outlined the following section.

4.2 Zinc Overpotential Deposition

Surface analyses of Zn OPD morphology were conducted to confirm the homogenous nucleation and growth on Pt suggested by cyclic voltammetry and further examine alloy formation in this system. In order to predict the zinc equilibrium as a function of electrolyte composition, Pitzer Model parameters were fit to the $ZnSO_4$-H_2SO_4-H_2O system at 25 °C and calculated zinc equilibrium potentials were compared to those obtained by cyclic voltammetry. The limiting current densities for zinc deposition were also estimated as a function of electrolyte composition and electrode rotation speed. Finally, the kinetics of Zn OPD in near-neutral and highly acidic zinc sulphate electrolytes were examined by normal pulse and staircase voltammetry.

4.2.1 Substrate Morphology

In the first step of each Zn OPD polarization experiment, the electrode was coated with zinc for 30 s at -1100 mV (SCE) at corresponding current densities of between *ca.* 20 and 90 A m^{-2}, depending on zinc concentration. Though Zn OPD growth is clearly not epitaxial on Pt, the deposit is relatively homogenous and uniform (see Figure 25) with an estimated increase in surface area, from examination of the AFM image, of < *ca.* 2 %. In the case of the AFM image, the sample was imaged immediately after deposition under a film of deionised water, to mitigate morphology changes due to oxidation, while the SEM sample was necessarily imaged in vacuum after rinsing and drying, and is highly oxidized. However, the zinc deposit was easily scraped away from the platinum substrate during AFM imaging at high force by the rastering action of the tip, which probably indicated that the surface had become oxidized to a soft and gelatinous hydroxide, $Zn(OH)_2$. This was not surprising given the nature of the water film above the sample; it was thin, which would have allowed oxygen to readily diffuse to the sample surface, had a relatively high pH and a lack of complexing ions, which would have increased the stability of the hydroxide. This made estimation of the real surface area of zinc films by AFM extremely difficult. In fact, careful inspection of the AFM image in Figure 26 revealed that scanning of the surface, the direction of which is indicated by the arrow, had likely slightly flattened the Zn deposit, even while using a relatively low force.

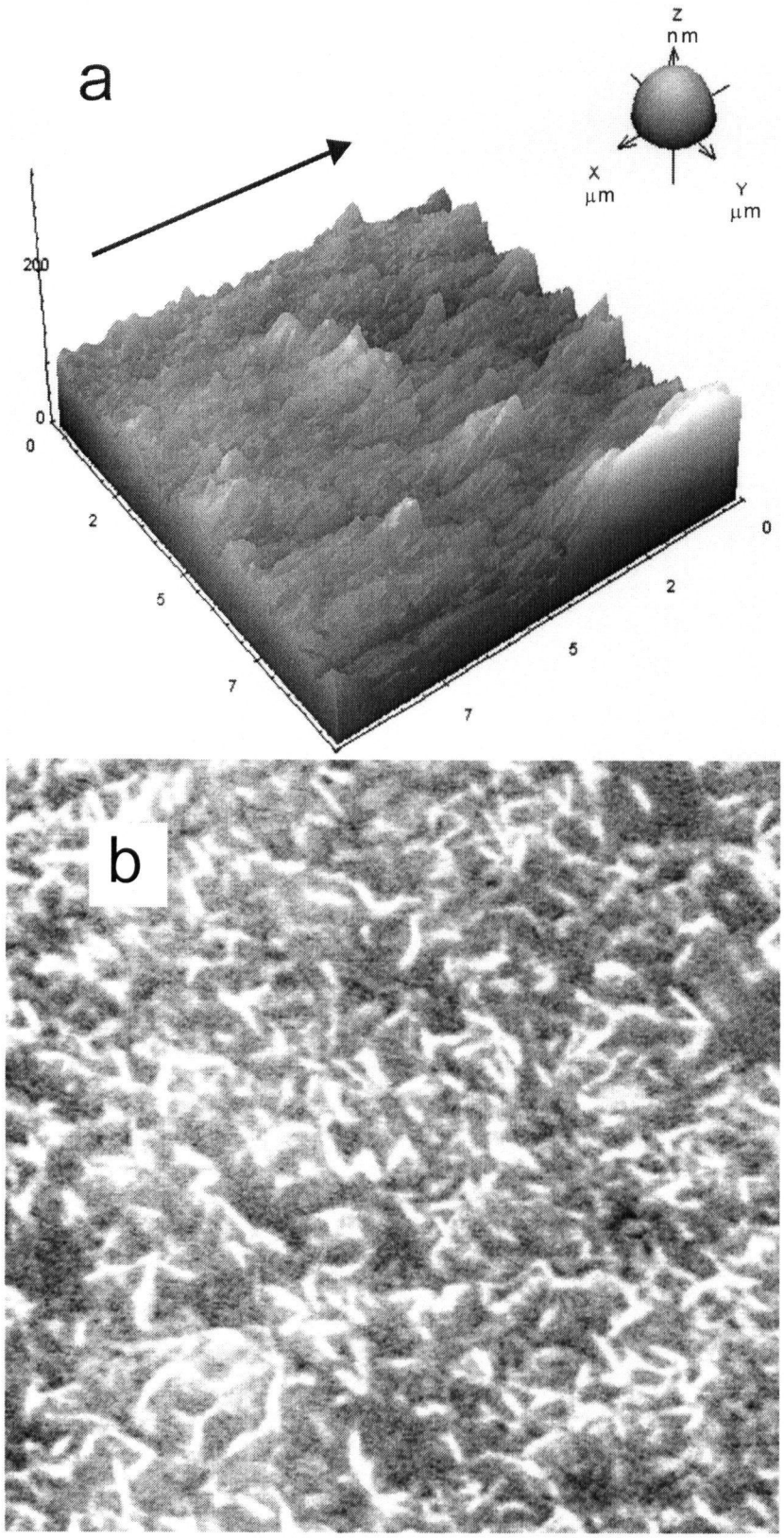

Figure 25: 10 × 10 µm square AFM image (a) and SEM photomicrograph (3000× magnification) (b) of zinc deposited on platinum at -1100 mV (SCE) for 30 s, ~20 A m^{-2}, from 0.1 mol dm^{-3} $ZnSO_4$, pH = 4.8 at *ca.* 22 °C.

In order to examine the effects of bulk alloy formation on electrode morphology, zinc was deposited on the electrode for 30 minutes at -1100 mV (SCE) in 0.1 mol dm^{-3} $ZnSO_4$, then removed by washing the electrode with a hot mixture of sulphuric and nitric acid. As reported by Uhlig [48], the alloy residue was visible to the naked eye as a dark grey and/or a black residue that was darker on some grains of the platinum compared to others. This may be attributed to greater rates of alloy formation on preferred crystal orientations. The fact that the alloy was visible after only 30 minutes confirmed that alloy formation proceeded extremely rapidly. This was a reflection of the relatively large diffusion coefficient of zinc into polycrystalline platinum, which Uhlig [48] measured at 100 °C to be 5.0×10^{-15} cm^2 s^{-1}, *ca.* 10^7 times greater than the diffusion coefficient of Zn into Cu.

As illustrated in Figure 26, the electrode morphology was significantly altered by bulk alloy formation, which appeared as nodular clusters similar to alloys formed in other UPD systems [130, 131, 133]. The increase in surface area, calculated from AFM images, was up to *ca.* 60 % in certain areas, but varied depending on the electrode region scanned. The SEM photomicrograph in Figure 26 is of a comparatively smooth region of the electrode with relatively few nodules. This allowed the EDX detector of the SEM to be focused on both a nodule cluster, Spot 1, and a smoother electrode region, Spot 2, the analysis of which confirmed that the nodules were likely alloy clusters, since they contained a greater fraction of zinc compared to the smoother region. Since the degree of alloy formation and, hence substrate roughening increased with increasing Zn deposition time, deposition pulses were held to 40 seconds during normal pulse experiments and two minutes during staircase voltammetry experiments, prior to zinc stripping at -250 mV (SCE) for two minutes. It should be noted that the diffusion rate of Zn into Pt will increase at higher temperatures, according the activation energy for diffusion, which probably limits the use of this technique to temperatures near room temperature.

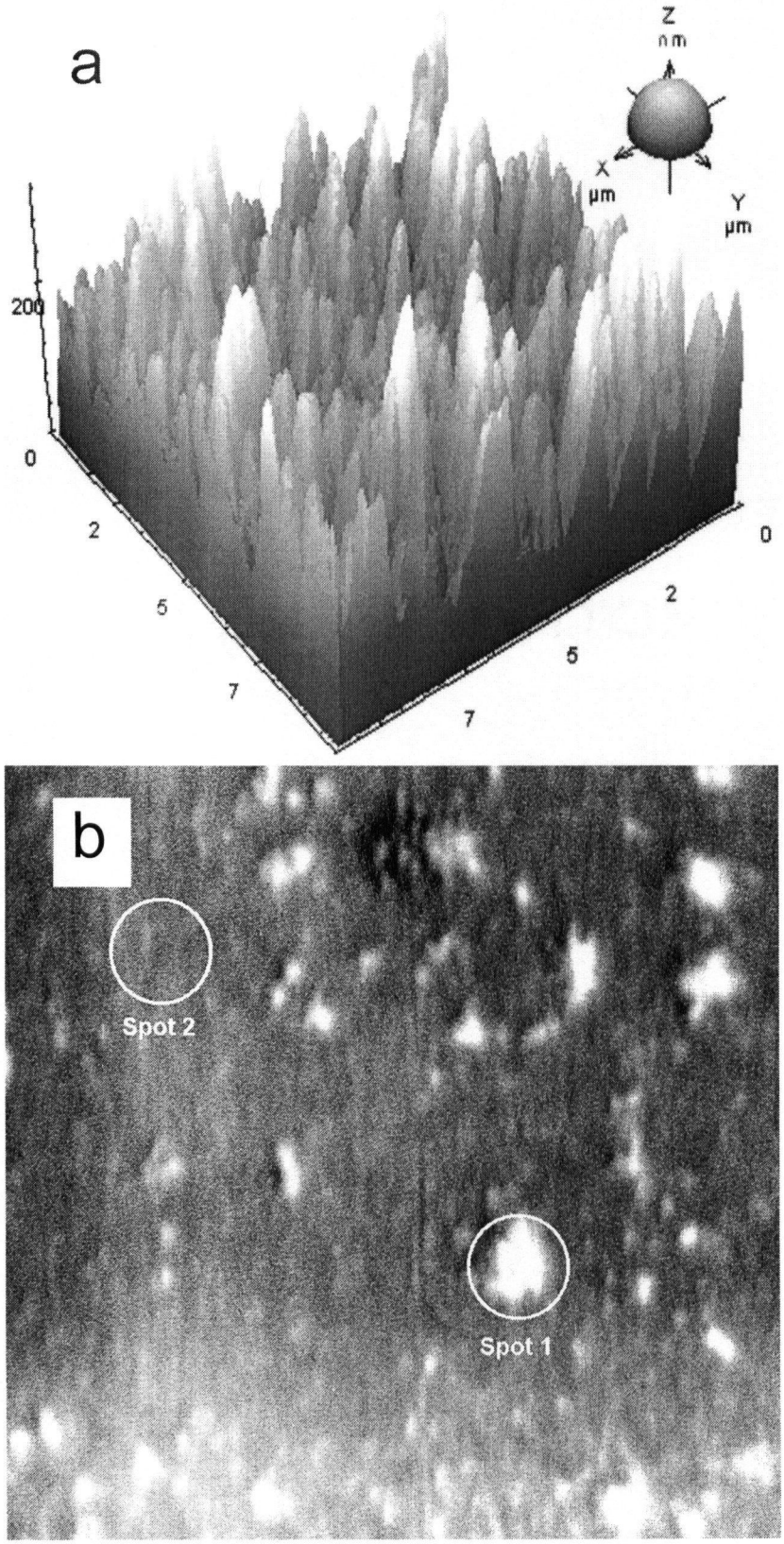

Figure 26: 10 × 10 µm square AFM image (a) and SEM photomicrograph (9000× magnification) (b) of platinum electrode after 30 minutes of zinc deposition and subsequent rinsing with a 1:1 mixture of nitric and sulphuric acid.

After each experiment (10 normal pulse experiments and one staircase experiment at a given electrode rotation rate), impedance spectroscopy was employed to estimate solution resistance, R_{soln} (Ω), from which the exponent of the *CPE* was obtained. The exponent of the *CPE* may be used as a measure of the smoothness of the electrode surface; 1.0 for a perfectly smooth surface to 0.5 for a highly contorted surface [136]. The average exponent values of all experiments conducted without added acid are given in Table 5. Overall, the exponent had an average value of 0.93 ±0.01, with no discernable trend towards lower exponent values, i.e. there was no discernable increase in electrode roughness due to the experimental procedure. Normal pulse experiments, in which zinc was deposited at -1100 mV (SCE) for 30 s and subsequently stripped for 60 s at -250 mV (SCE) were also conducted to verify this effect. After 100 cycles of deposition and stripping (*ca.* 10 times that of a normal experiment), the increase in surface area, from analysis of various AFM images, was < *ca.* 2 %. Nonetheless, Pt electrodes were polished after each set of experiments.

Table 5: Constant Phase Element exponent, ξ, as a function of Experimental Run Number

Run No.	CPE exponent		
	400 rpm	1600 rpm	3600 rpm
1	0.94 ±0.02	0.93 ±0.02	0.92 ±0.01
2	0.92 ±0.02	0.92 ±0.03	0.92 ±0.01
3	0.93 ±0.00	0.93 ±0.00	0.93 ±0.01

4.2.2 Zinc Deposition Equilibrium Potential

The estimation of the equilibrium potential for zinc deposition as a function of electrolyte composition may be calculated accurately using the Pitzer Model. Several sets of Pitzer parameters and corresponding χ^2 'goodness of fit parameter' values, for the $ZnSO_4$-H_2SO_4-H_2O system were generated according to the procedure described in Appendix B. By inspection of Figure 27, the calculated mean activity coefficients of zinc sulphate using the Pitzer parameters reported by Klocker et al. [85] do not match the values reported by Majima et al. [86] for pure zinc sulphate. This is unfortunate given these parameters were purportedly derived, solely, from a fit of the data set of Majima et al.. The values of zinc sulphate activity reported by Majima et al. closely match those reported recently by Albright et al. [70] and Malatesta and Zamboni [69], which suggested that the data sets of Horváth and Wéber [88] and Tartar et al. [87] may be ignored (see Figure 27).

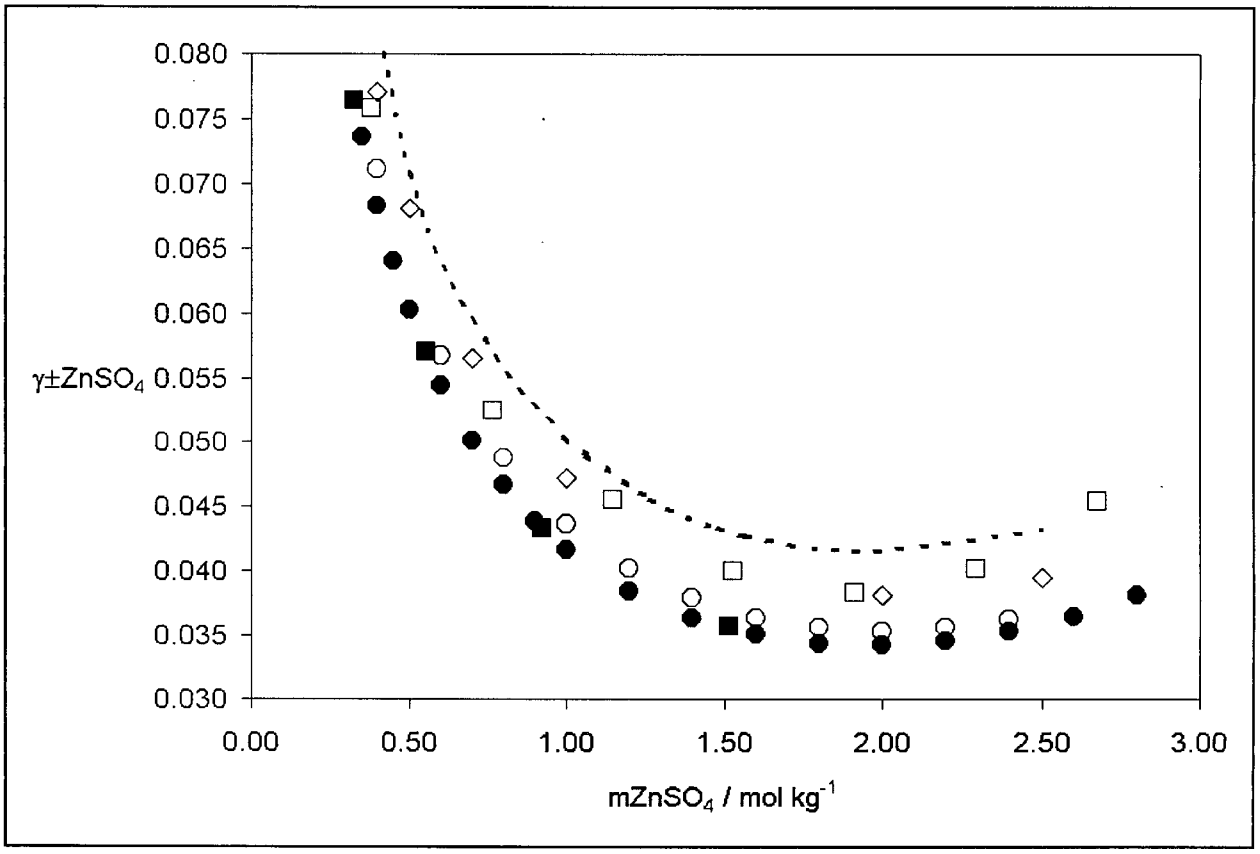

Figure 27: Mean activity coefficient of zinc sulphate at 25 °C, from (-----) Klocker et al. [85], (□) Horváth and Wéber [88], (○) Majima et al. [86], (◊) Tartar et al. [87], (●) Albright et al. [70], and (■) Malatesta and Zamboni [69] plotted against zinc sulphate molality.

For calculation of χ^2, the uncertainty in the osmotic coefficient data of Majima et al., σ_{obs}, was estimated from variances of the differences in corresponding osmotic coefficient values reported by Albright et al. [70] for $ZnSO_4$, σ_{Zn}, and Clegg [137] for H_2SO_4, σ_H, which were assumed to be accurate.

$$\sigma_{obs} = \sqrt{(\sigma_{Zn})^2 + (\sigma_H)^2} = \sqrt{(0.059)^2 + (0.003)^2} = 0.059 \qquad \text{Equation 4.2}$$

Various sets of Pitzer parameters were adjusted in order to minimize the *SSE* between observed and calculated stoichiometric osmotic coefficients, ϕ_{obs} and ϕ_{calc}. The Pitzer parameters for interactions between Zn^{2+} and SO_4^{2-} were fitted using the set of 62 observed osmotic coefficients, $N_{obs} = 62$, of Albright et al. [70] for pure $ZnSO_4$ (see Table 6) while other interaction parameters were fitted subsequently using the set of 69 observed osmotic coefficients, $N_{obs} = 69$, of Majima et al. [86] for the mixed $ZnSO_4$-H_2SO_4 electrolyte (see Table 7). The Pitzer parameters for H_2SO_4 of Hovey et al. [81] (see Appendix G) were not modified since they are relatively well established and have been used to generate ternary mixing parameters for similar systems [81,

82, 83, 84, 85]. These parameters may be useful for modelling solvent extraction equilibria when used in combination with the set generated by the author.

Table 6: Single salt Pitzer parameters for 0 to 4.3 mol dm^{-3} $ZnSO_4$ at 25 °C, σ_{zn} = 0.059, N_{obs} = 62.

$\beta^{(0)}$ Zn^{2+}-SO_4^{2-}	$\beta^{(1)}$ Zn^{2+}-SO_4^{2-}	$\beta^{(2)}$ Zn^{2+}-SO_4^{2-}	C^{ϕ} Zn^{2+}-SO_4^{2-}	χ^2
0.189	2.870	66.467	0.0329	0.020

Table 7: Ternary system Pitzer parameters for 0 to 2.5 mol dm^{-3} $ZnSO_4$ and 0 to 2.0 mol dm^{-3} H_2SO_4 at 25 °C, σ_{obs} = 0.059, N_{obs} = 69.

Set	$\beta^{(0)}$ Zn^{2+}-HSO_4^-	$\beta^{(1)}$ Zn^{2+}-HSO_4^-	C^{ϕ} Zn^{2+}-HSO_4^-	ψ Zn^{2+}-HSO_4^--SO_4^{2-}	χ^2
1	0.600				0.205
2	0.538	3.281			0.044
3	0.587	2.906	-0.0201		0.044
4	0.545	3.190		-0.0090	0.045
5	0.590	2.920	-0.0515	0.0584	0.043

The addition of more ternary mixing parameters did not improve the fit significantly and resulted in higher χ^2 values. Though parameter Sets 2 to 5 yielded similar χ^2 values, Set 3 was accepted as the best choice, since their values were within typical ranges for similarly evaluated parameters [80]. In comparison, the value of χ^2 calculated using the parameter set of Klocker et al. was 0.084. The distribution of residuals using parameter Set 3 (see Figure 28) also appeared random, which adds further confidence for accepting them for this system.

The zinc equilibrium potentials, E_{Zn} (V), were measured by cyclic voltammetry (see Table 8) for each solution composition in order to obtain reference points from which zinc deposition overpotentials were calculated. Though not intended as a means of validating the Pitzer Model predictions, corresponding zinc equilibrium potentials and pHs were calculated using Set 3 as well as by the model of Filippou et al. [89]. These results were added for the sake of completeness, since this was the only model, in open literature, previously applied to calculate the thermodynamic properties of zinc electrolytes. In general, both models showed reasonably good agreement between measured and predicted equilibrium potentials, except for the case of 1.0 mol dm^{-3} $ZnSO_4$ and 1.0 mol dm^{-3} H_2SO_4, which is explained in the following paragraph.

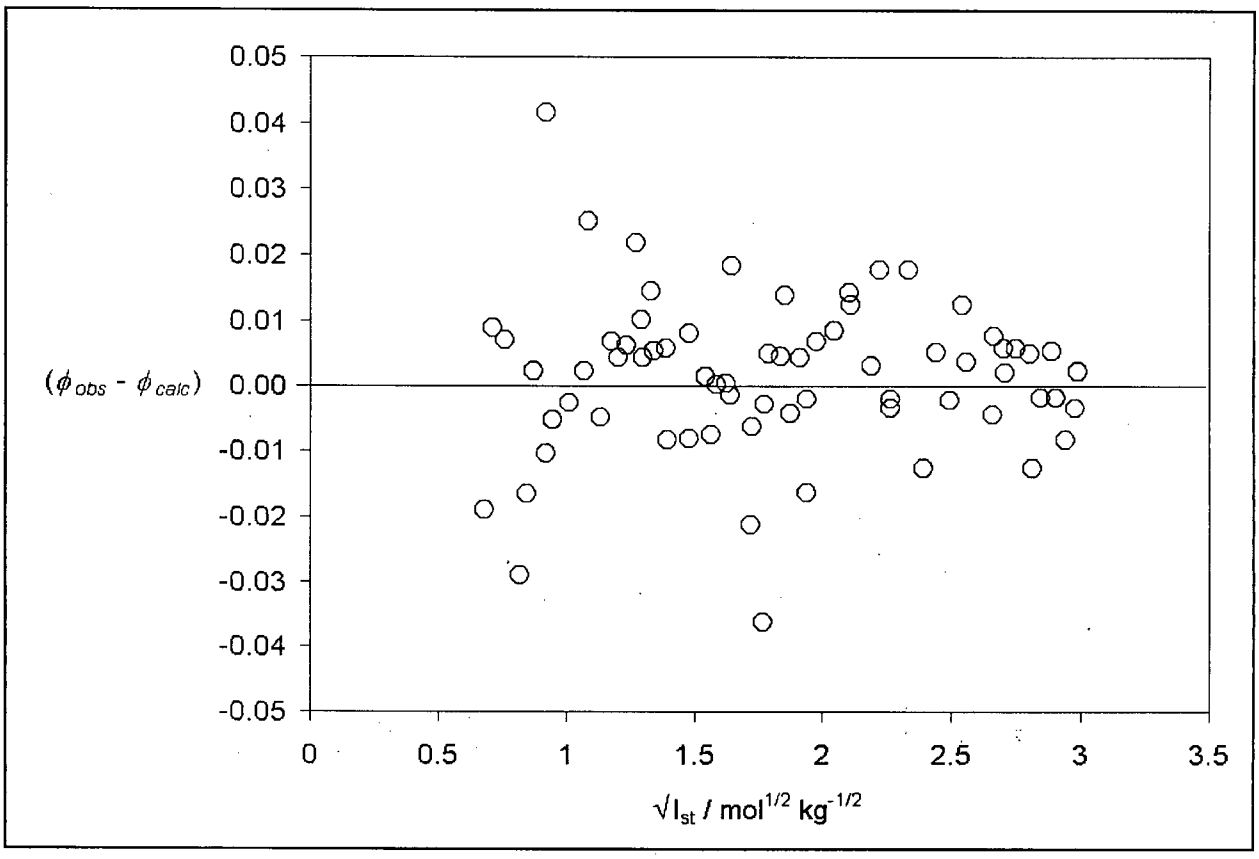

Figure 28: Deviations between measured [86] and fitted stoichiometric osmotic coefficient for $ZnSO_4$-H_2SO_4-H_2O, ○, at 25 °C, plotted against the square root of stoichiometric ionic strength.

Table 8: Measured and predicted zinc equilibrium potential and pH as function of electrolyte composition at 25 °C.

$ZnSO_4$ / mol kg^{-1}	H_2SO_4 / mol kg^{-1}	E_{Zn} (measured) / mV (SCE)	E_{Zn} (Set 3) / mV (SCE)	E_{Zn} (Fillipou) / mV (SCE)	pH (Set 3)	pH (Fillipou)
0.10	0.00	-1055 ± 0	-1058	-1055		
0.50	0.00	-1040 ± 1	-1048	-1044		
1.00	0.00	-1032 ± 0	-1044	-1039		
1.00	0.01	-1032 ± 1	-1044	-1039	2.4	2.0
1.00	0.10	-1036 ± 2	-1043	-1041	1.4	1.0
1.00	1.00	-1060 ± 0*	-1030	-1035	0.2	0.2

* Includes significant diffusion potential. See text for details

The uncertainties in measured potential, listed in Table 8, are the standard deviations for repetitions of the same experiment and do not include the uncertainty due to the limitations of the instrumentation. They are presented to illustrate that the measured potentials are steady and repeatable, especially in the case where acid was added in order to generate a 1.0 mol dm^{-3} H_2SO_4 solution and a significant, *ca.* 30 mV, diffusion potential was generated. The diffusion potential occurred since the Luggin chamber was filled with neutral 1.0 mol dm^{-3} $ZnSO_4$

electrolyte, so when acid was added to the main chamber of the electrolytic cell, protons and sulphate species naturally diffused into the Luggin capillary. Since the mobility of H^+ is *ca.* 10 times greater than that of either SO_4^{2-} or HSO_4^-, protons diffused faster into the capillary, causing a net charge to build up within it. The addition of the acid generated heat and while the solution was cooled back to 25 °C, for *ca.* 10 minutes, the charge reached steady state, since the protons dragged counter ions with them, through electrostatic attraction, as they diffused along the length of the Luggin capillary. When both the Luggin and main cell chambers were both filled 1.0 mol dm^{-3} $ZnSO_4$ and 1.0 mol dm^{-3} H_2SO_4, the zinc equilibrium potential was measured to be -1028 mV (SCE), which was close to the expected value of -1030 mV (SCE).

Data for the variation of E° with temperature has been compiled by Silva and de Bethune [138]. Extrapolation of Pitzer Model calculations to temperatures more relevant to industrial zinc electrowinning, *ca.* 35 to 45 °C, should be possible via temperature corrections of the Debye-Hückel term, A, and equilibrium constant for hydrogen sulphate dissociation, K.

$$A \approx 0.377 + 4.684\times10^{-4}(T\text{-}273.15) + 3.74\times10^{-6}(T\text{-}273.15)^2 \quad [139] \qquad \text{Equation 4.3}$$

$$\log(K) \approx 562.69486 - 102.5154\ln(T) - 1.117033\times10^{-4}T^2 + 0.2477538T - 13273.75/T \quad [137] \qquad \text{Equation 4.4}$$

The reversible potential for oxygen evolution, the conventional anodic reaction in zinc electrowinning, comprises *ca.* 30 % of the cell voltage in zinc electrowinning [13].

$$E_{H_2O} = E^\circ{}_{H_2O} + \frac{RT}{nF}\ln\left[\frac{(aH_2O)^2}{(aH^+)^4\, pO_2}\right] \qquad \text{Equation 4.5}$$

The calculated water activity, aH_2O, and proton activity, aH^+, from application of the Pitzer Model should yield relatively accurate estimations for the reversible potential for oxygen evolution as a function of electrolyte composition.

4.2.3 Zinc Deposition Limiting Current Density

The limiting current density for zinc deposition , $j_{lim,Zn}$ (A m^{-2}), was predicted for each solution composition and electrode rotation rate employed in this study. The parameters necessary for estimating limiting current density; the zinc ion transport number, the diffusion coefficient of zinc ions, and the diffusion boundary layer thickness, were calculated from a theoretical basis in

order to generate correlations that may be used to calculate the transport properties of electrolytes. This was done with the aim of extending the results to conventional zinc electrowinning and to facilitate the design of non-conventional zinc electrowinning reactors. The limiting zinc deposition current densities, $j_{\lim,Zn}$ (A m^{-2}), were calculated according to Equation 2.18, from the calculated transport numbers for zinc ions, $t_{Zn^{2+}}$, the zinc ion diffusion coefficients, $D_{Zn^{2+}}$ (m^2 s^{-1}), and boundary layer thicknesses, δ (m):

$$j_{\lim,Zn} = \frac{-D_{Zn^{2+}}}{\delta(1-t_{Zn^{2+}})} nF\left([Zn^{2+}]^{bulk}\right) \qquad \text{Equation 2.18}$$

However, the calculated limiting current densities must be considered as approximate values according to the limitations of Equation 2.18 outlined in Section 2.4. The details for the calculations these parameters are described in the following sections and the results are summarized in Table 9.

4.2.3.1 Zinc Ion Transport Numbers

Zinc ion transport numbers, $t_{Zn^{2+}}$, were calculated according to the method of Hinatsu and Foulkes [92], outlined in Section 2.4.1. The activity coefficients and species distribution of each electrolyte were calculated using the Pitzer Model parameters previously generated. The values for diffusion coefficients at infinite dilution, substituted into Equation 2.19, were those reported in the CRC Handbook of Chemistry and Physics [140]; $D°_{Zn^{2+}} = 0.703$, $D°_{SO_4^{2-}} = 1.065$, $D°_{HSO_4^-} = 1.385$, and $D°_{H^+} = 9.311$ (×10^{-9} m^2 s^{-1}).

$$t_{Zn^{2+}} \approx \frac{z_{Zn^{2+}}^2 D°_{Zn^{2+}}[Zn^{2+}]}{\sum z_i^2 D°_i[i]} = \frac{[Zn^{2+}]}{[Zn^{2+}]+1.51[SO_4^{2-}]+0.49[HSO_4^-]+3.31[H^+]} \qquad \text{Equation 2.19}$$

4.2.3.2 Zinc Ion Diffusion Coefficients

The following expression was employed to calculate the diffusion coefficient of zinc sulphate, D_{ZnSO_4} (m^2 s^{-1}), as a function of electrolyte composition (mol dm^{-3}):

$$\begin{aligned} D_{ZnSO_4} &= [8.083 - 7.496([ZnSO_4]+0.296[H_2SO_4])^{0.5} + 4.105[ZnSO_4] \\ &\quad + 3.924[H_2SO_4] - 0.739([ZnSO_4]+1.615[H_2SO_4])^{1.5}]\times 10^{-10} \end{aligned} \qquad \text{Equation 4.6}$$

The above expression was generated by the author by a least-squared fit of the data set of Awakura [94] for D_{ZnSO_4} in 0 to 2.0 mol dm^{-3} $ZnSO_4$ in the presence of 0 to 2.0 mol dm^{-3} H_2SO_4 at 25 °C (see Figure 29). The standard deviation of differences in the reported and calculated diffusion coefficients using this expression was $\pm 0.17\times10^{-10}$ m^2 s^{-1}. The form of the equation is similar to that developed by Albright and Miller [93] for D_{ZnSO_4} in 0 to 3.2 mol dm^{-3} $ZnSO_4$ at 25 °C. The zinc ion diffusion coefficient, $D_{Zn^{2+}}$ (m^2 s^{-1}), was related to D_{ZnSO_4} according to Equation 2.22 after inputting values for $D°_{Zn^{2+}}$ and $D°_{SO_4^{2-}}$ as illustrated below:

$$D_{Zn^{2+}} \approx \frac{D_{ZnSO_4}}{2}\left[1+\frac{D°_{Zn^{2+}}}{D°_{SO_4^{2-}}}\right] = \frac{D_{ZnSO_4}}{2}\left[1+\frac{7.03\times10^{-10}\,m^2s^{-1}}{1.065\times10^{-9}\,m^2s^{-1}}\right] = 0.83D_{ZnSO_4} \qquad \text{Equation 2.22}$$

Using this method, the diffusion coefficient of zinc ions in 0.84 mol dm^{-3} $ZnSO_4$ with 1.54 mol dm^{-3} H_2SO_4 at 25 °C was estimated to be 3.7×10^{-10} m^2 s^{-1}, which is close to 3.8×10^{-10} m^2 s^{-1}, measured by Hosney et al. [96].

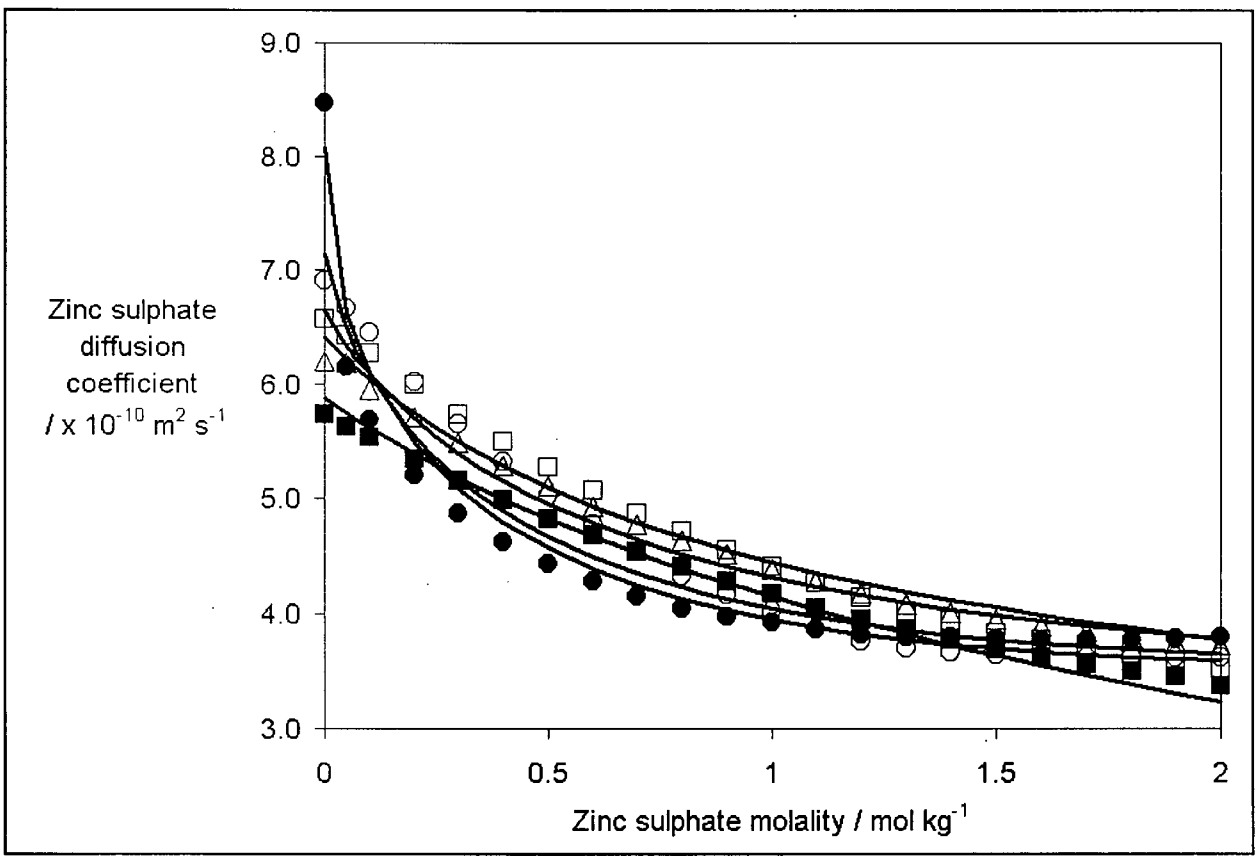

Figure 29: Diffusion coefficient of zinc sulphate in 0 mol dm^{-3} H_2SO_4 (●),0.1 mol dm^{-3} H_2SO_4 (○), 0.5 mol dm^{-3} H_2SO_4 (□),1.0 mol dm^{-3} H_2SO_4 (Δ) and 2.0 mol dm^{-3} H_2SO_4 (■) at 25 °C, and corresponding fitted curves (——) using Equation 4.6, plotted against zinc sulphate molality. Data taken from [94].

Estimation of the effect of increasing temperature on diffusion may be made through the corresponding absolute viscosities, η (kg m^{-1} s^{-1}), using the following relation:

$$D_2 \approx \left(\frac{T_2}{T_1}\right)\left(\frac{\eta_1}{\eta_2}\right)D_1 \qquad \text{Equation 4.7}$$

The origin of the above expression is the Einstein-Stokes Equation which relates diffusion to the viscosity of the solution as follows:

$$\frac{D_1\eta_1}{T_1} = \frac{D_2\eta_2}{T_2} = \frac{k}{6\pi r_i} \qquad \text{Equation 4.8}$$

where; r_i (m) is the radius of the solvated ion i, and k (1.38062×10^{-23} J K^{-1}) is the Boltzmann constant. According to Foulkes [141] this expression is fairly accurate up to *ca.* 50 °C which should be adequate to predict the effect of temperature on diffusion for conventional zinc electrowinning. Beyond 50 °C thermal vibrations may cause the average solvation numbers of aqueous molecules to decrease and, hence, cause deviations in Equation 4.8. Alternatively, Cathro [97] has suggested multiplying the zinc diffusion coefficient by a factor of 1.022 per °C increase in temperature.

4.2.3.3 Boundary Layer Thickness

The thickness of the diffusion boundary layer, δ (m), during experiments was calculated for each electrolyte composition as a function of electrode rotation speed, ω (rad s^{-1}), according to the Levich Equation:

$$\delta = 1.61 D_{Zn^{2+}}{}^{1/3}\eta^{1/6}\rho^{-1/6}\omega^{-1/2} \qquad \text{Equation 2.25}$$

The zinc ion diffusion coefficient, $D_{Zn^{2+}}$ (m^2 s^{-1}), electrolyte density, ρ (kg m^{-3}), were calculated as previously described. The absolute viscosity of the electrolyte, η (kg m^{-1} s^{-1}), was calculated from the electrolyte composition (mol dm^{-3}) using the following equation:

$$\eta = (0.4332344 - 4.998831\times10^{-3}T + 2.174276\times10^{-5}T^2 - 4.216447\times10^{-8}T^3 + 3.072309\times10^{-11}T^4)\exp(0.6182[ZnSO_4] + 0.1801[H_2SO_4]) \qquad \text{Equation 4.9}$$

The above expression was generated by the author through a minimization of the sum of the square of differences between calculated and reported viscosity data of pure water, 0 to 100 °C, zinc sulphate solutions, 0.03 to 1.17 mol dm^{-3} $ZnSO_4$ at 21 °C, and sulphuric acid solutions, 0.05 to 9.17 mol dm^{-3} H_2SO_4 at 21 °C [140]. This type of model was recently employed by Immura and Toguri [142] to represent the viscosity of nickel electrolytes. The pre-exponential polynomial calculates the temperature dependent viscosity of the pure solvent (see Figure 30), while the exponential terms represent the modifying effect of each salt's concentration (see Figure 31). Although developed independently, Equation 4.9 fits the data of Umetsu et al. [103] almost as well as their own expression, Equation 2.27. The standard deviation between predicted and measured absolute viscosities [103] was 5.9×10^{-5} kg m^{-1} s^{-1} using Equation 4.9 and 4.2×10^{-5} kg m^{-1} s^{-1} using Equation 2.27. The proposed model has the added advantage in that it can be easily modified to incorporate the effects of additional salts, since each exponent is obtained from an independent set of viscosity data for a particular salt.

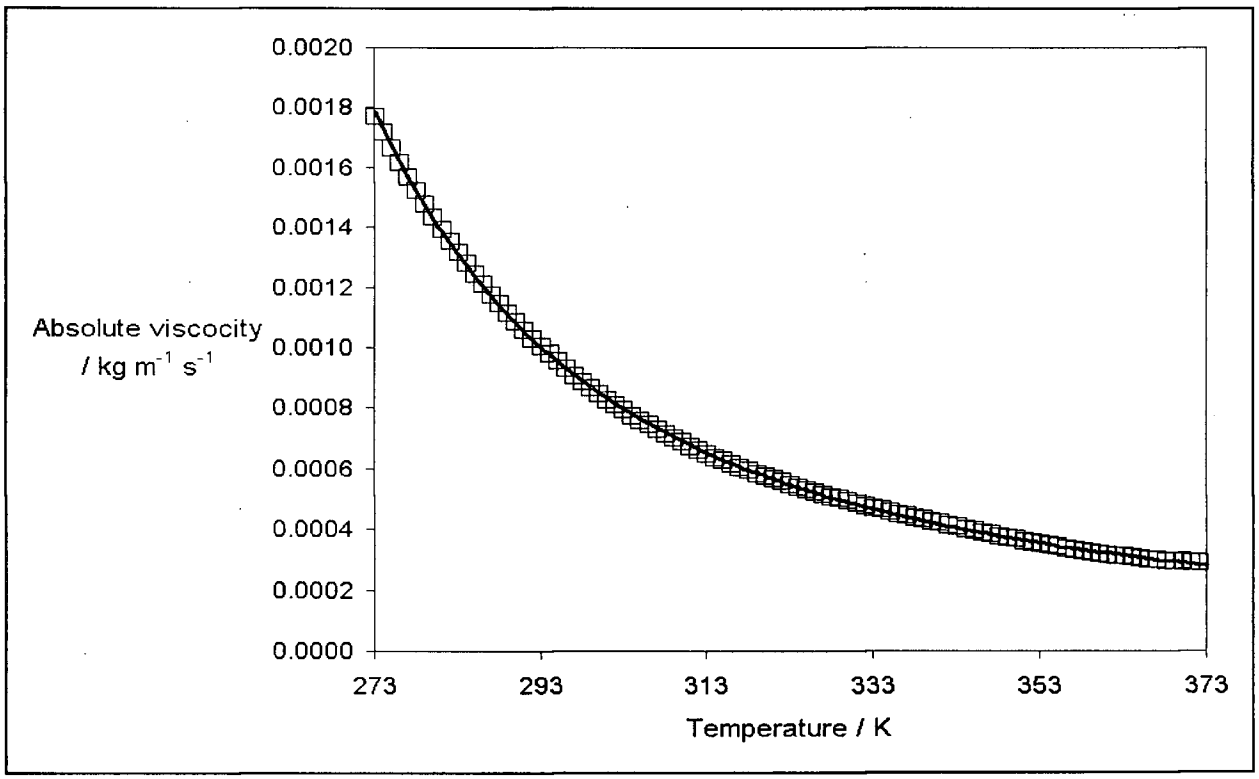

Figure 30: Absolute viscosity of pure water (□) and corresponding fitted curve (——) according to Equation 4.9, plotted against absolute temperature. Data taken from [140].

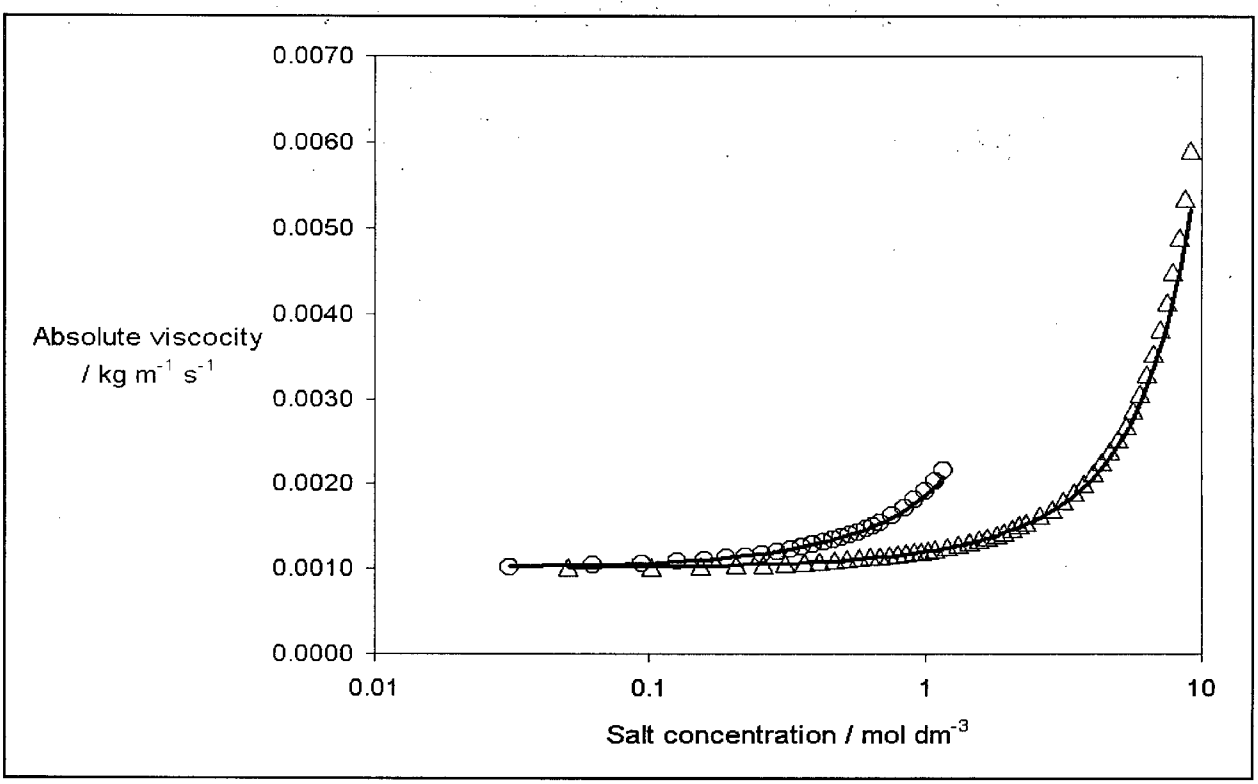

Figure 31: Absolute viscosity of aqueous zinc sulphate (○) and sulphuric acid (Δ) at 21 °C and corresponding fitted curves (——) according to Equation 4.9, plotted against salt concentration. Data taken from [140].

4.2.4 Zinc Electrodeposition Kinetics in Weakly Acidic Sulphate Electrolytes

The kinetics of zinc deposition from pure zinc sulphate electrolytes, *ca.* pH = 4.9 at 25 °C, were examined by normal pulse and staircase voltammetry as a function of zinc sulphate concentration and electrode rotation speed. The current efficiencies for zinc deposition from these electrolytes was always 100 % at all applied overpotentials, whether calculated from the ring current or by amperometric integration of the normal potential pulse sequences. The results from staircase voltammetry generally matched well with normal pulse experiments and, hence, were treated as replicates of the same experiment. The results of the three experiments were averaged together to generate Tafel plots for each $ZnSO_4$ concentration level; Figure 32, Figure 33, and Figure 34. Note that each data point in these figures represents several replicates of the same experiment and the error bars include both the estimated uncertainty due instrumental limitations and random errors (calculated as the standard deviation of measurements made under the same conditions).

Table 9: Calculated properties of zinc sulphate electrolytes at 25 °C.

Property	0.10 $ZnSO_4$ 0.00 H_2SO_4 / mol kg^{-1}	0.50 $ZnSO_4$ 0.00 H_2SO_4 / mol kg^{-1}	1.00 $ZnSO_4$ 0.00 H_2SO_4 / mol kg^{-1}	1.00 $ZnSO_4$ 0.01 H_2SO_4 / mol kg^{-1}	1.00 $ZnSO_4$ 0.10 H_2SO_4 / mol kg^{-1}	1.00 $ZnSO_4$ 1.00 H_2SO_4 / mol kg^{-1}
aH_2O	0.9979	0.9914	0.9830	0.9825	0.9777	0.9193
Zn^{2+} / mol kg^{-1}	0.10	0.50	1.00	1.00	1.00	1.00
SO_4^{2-} / mol kg^{-1}	0.10	0.50	1.00	1.00	1.00	1.11
HSO_4^- / mol kg^{-1}	0.00	0.00	0.00	0.01	0.10	0.89
H^+ / mol kg^{-1}	0.00	0.00	0.00	0.01	0.10	1.11
$\gamma_{Zn^{2+}}$	0.145	0.062	0.043	0.043	0.048	0.112
$\gamma_{SO_4^{2-}}$	0.145	0.062	0.043	0.043	0.040	0.025
$\gamma_{HSO_4^-}$	0.625	0.437	0.378	0.380	0.397	0.593
γ_{H^+}	0.859	1.07	1.41	1.42	1.48	1.962
t_{Zn}^{2+}	0.40	0.40	0.40	0.39	0.35	0.15
D_{Zn}^{2+} / m^2 s^{-1}	5.0×10^{-10}	3.8×10^{-10}	3.2×10^{-10}	3.3×10^{-10}	3.3×10^{-10}	3.7×10^{-10}
ρ / kg m^{-3}	1019	1078	1152	1152	1157	1198
η / kg m^{-1} s^{-1}	9.44×10^{-4}	1.21×10^{-3}	1.65×10^{-3}	1.65×10^{-3}	1.67×10^{-3}	1.85×10^{-3}
δ / m (42 rad s^{-1})	1.96×10^{-5}	1.84×10^{-5}	1.81×10^{-5}	1.82×10^{-5}	NA	NA
δ / m (168 rad s^{-1})	9.79×10^{-6}	9.18×10^{-6}	9.03×10^{-6}	9.12×10^{-6}	NA	NA
δ / m (377 rad s^{-1})	6.53×10^{-6}	6.12×10^{-6}	6.02×10^{-6}	6.08×10^{-6}	6.09×10^{-6}	6.40×10^{-6}
$[Zn^{2+}]^{bulk}$ / mol m^{-3}	1.00×10^2	4.99×10^2	9.90×10^2	9.90×10^2	9.90×10^2	9.52×10^2
$j_{lim,Zn}$ / A m^{-2} (42 rad s^{-1})	825	3330	5700	5740	NA	NA
$j_{lim,Zn}$ / A m^{-2} (168 rad s^{-1})	1650	6660	11400	11500	NA	NA
$j_{lim,Zn}$ / A m^{-2} (377 rad s^{-1})	2480	9980	17100	17200	16100	13100

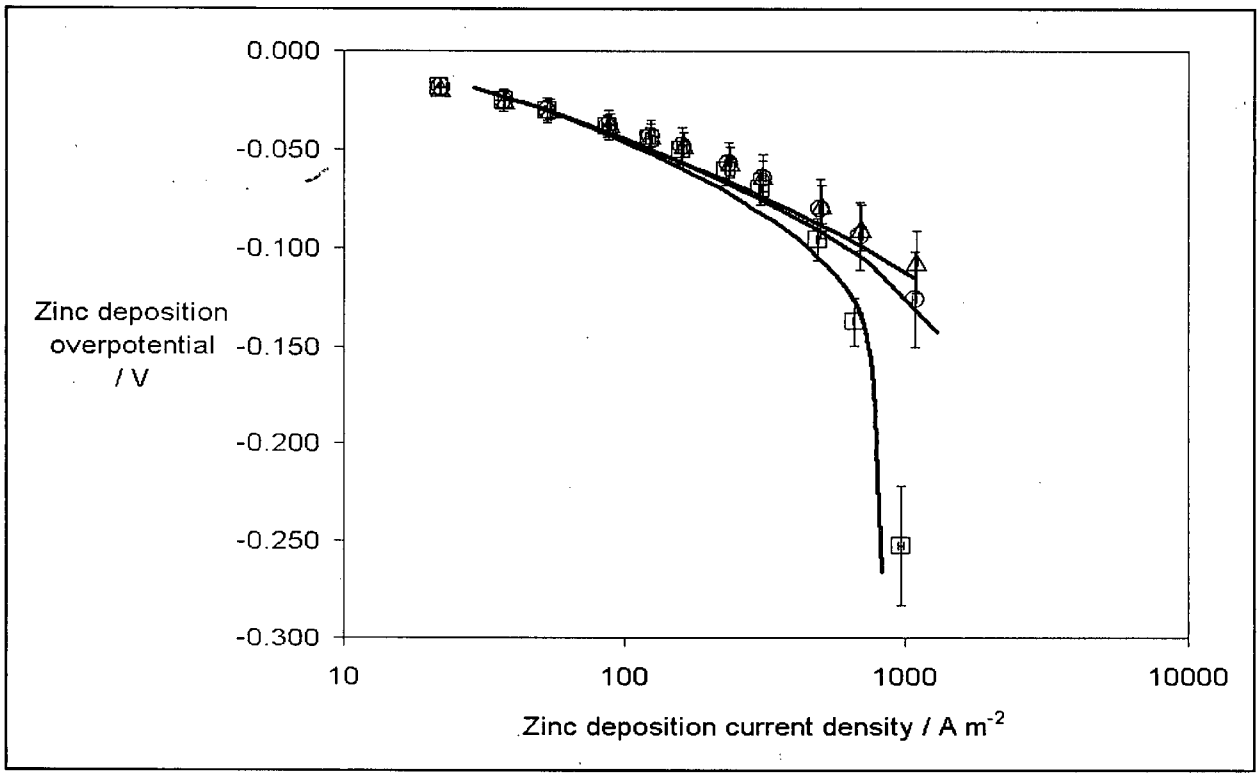

Figure 32: Tafel plot for zinc deposition from 0.10 mol kg^{-1} $ZnSO_4$, pH = 4.9 at 25 °C, 400 rpm (□), 1600 rpm (○), and 3600 rpm (Δ) electrode rotation speed.

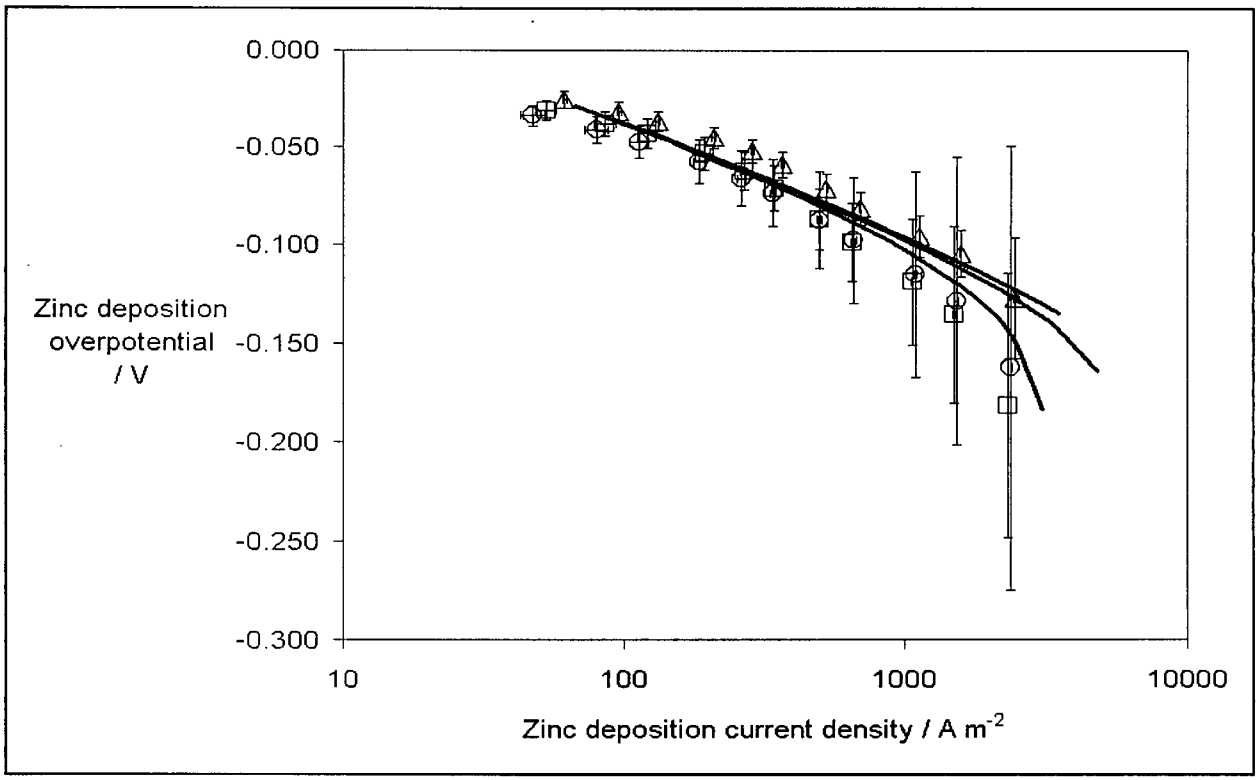

Figure 33: Tafel plot for zinc deposition from 0.50 mol kg^{-1} $ZnSO_4$, pH = 4.9 at 25 °C, 400 rpm (□), 1600 rpm (○), and 3600 rpm (Δ) electrode rotation speed.

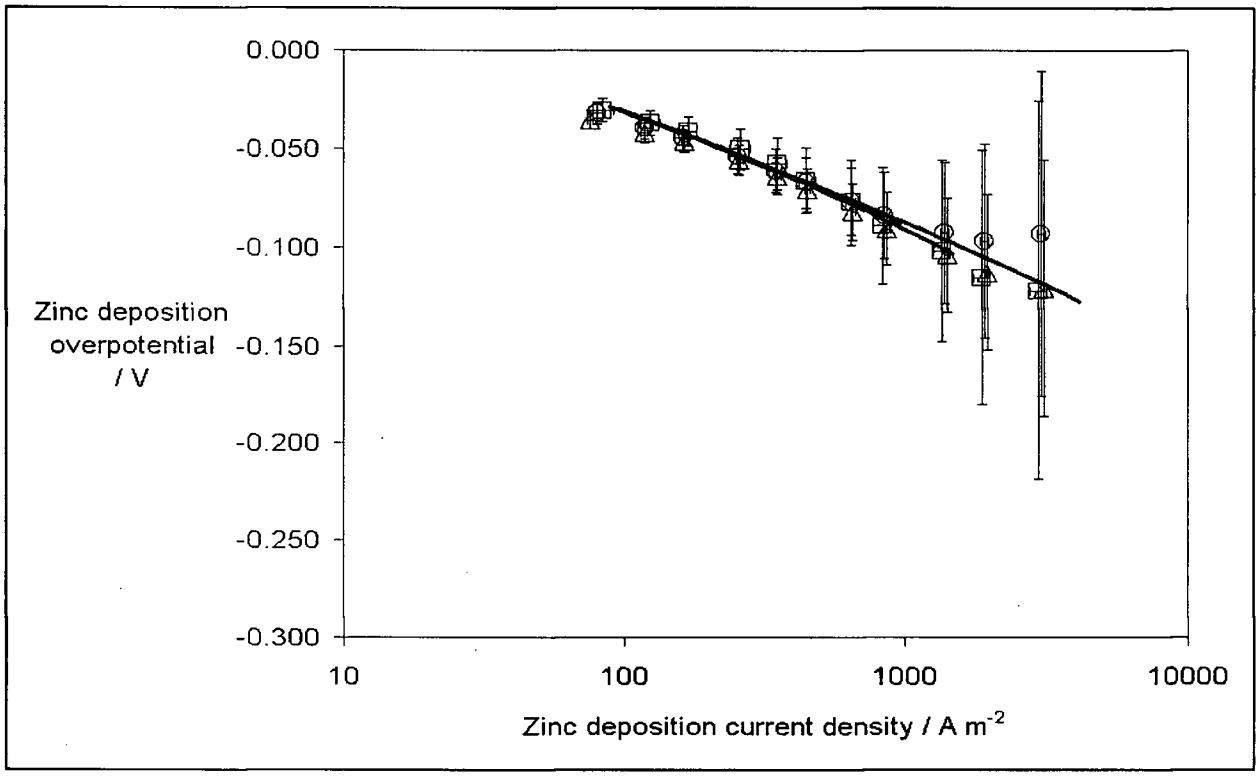

Figure 34: Tafel plot for zinc deposition from 1.00 mol kg^{-1} $ZnSO_4$, pH = 4.9 at 25 °C, 400 rpm (□), 1600 rpm (○), and 3600 rpm (Δ) electrode rotation speed.

The relatively large uncertainties in overpotentials at high current densities were mainly due to the uncertainties in the solution resistances, obtained from electrochemical impedance spectroscopy at -250 mV (SCE), and are not so much a reflection of the repeatability of the experiments. The solid lines in the Tafel plots were fitted according to the Extended Butler-Volmer Equation, Equation 2.4. The limitations of Equation 2.18 for predicting the zinc deposition current density can be observed for the experiment conducted at 400 rpm in 0.1 mol kg^{-1} $ZnSO_4$. However, contrary to expectation, the limiting current density appears to have been underestimated (see Figure 32). Initially, all the data were fitted simultaneously to obtain the values for zinc exchange current densities, $j_{0,Zn}$, corresponding to each zinc sulphate concentration, as well as the value of $\beta(\alpha n)$. The fitting method was a weighted least-squared fit [143] of the differences in the natural logarithms of the observed and calculated current densities, using the inverse of the uncertainty in overpotential as the weighting parameter.

$$SSE = \sum_{i=1}^{N_{obs}} \frac{\left(\ln(j_{Zn}(\eta_i)_{obs}) - \ln(j_{Zn}(\eta_i)_{calc})_i\right)^2}{(\sigma_\eta)_i} \qquad \text{Equation 4.10}$$

Natural logarithms of the currents were used in the expression for *SSE,* so that the fit would be more appropriate for the semi-log scale of Tafel plots. Using this method, the best fit value of β was 1.08, which was close to the theoretical value of 1.0 (Tafel slope of 60 mV dec^{-1} at 25 °C) adopted by Zouari and Lapique [40], Despić and Pavlović [51] and Wiart et al.[35]. Due to covariance between the transfer coefficient, α, and exchange current density, j_0, (they are related through Equation 2.33), a value of 1.0 was adopted for β and the zinc exchange current densities were recalculated along with their variances, (see 'Observed' values in Table 10).

$$j_{0,Zn} = \left(aZn^{2+}\right)^{1-\alpha}\left(aZn\right)^{\alpha} = k_0\left(\gamma Zn^{2+} mZn^{2+}\right)^{1-\alpha} \qquad \text{Equation 2.33}$$

In order to establish whether the rate limiting step of zinc electrodeposition is a single electron transfer process, $n = 1$ and $\alpha = 1$, as suggested by Jović et al. [41], Despić and Pavlović [51] and Wiart et al. [35], or a two electron transfer process, $n = 2$ and $\alpha = 0.5$, as adopted by Zouari and Lapique [40]; calculated zinc current densities were obtained by fitting Equation 2.33 for both mechanisms. Fitted values for the standard exchange current density, k_0 (A m^{-2}), were obtained by minimization of the *SSE* between observed and calculated zinc exchange current densities using the zinc ion activities coefficients listed in Table 9. The corresponding χ^2 value were calculated from the following expression:

$$\chi^2 = \sum\left[\frac{(j_{0,Zn})_{obs} - (j_{0,Zn})_{calc}}{\sigma_{obs}}\right]^2 \qquad \text{Equation 4.11}$$

The number of degrees of freedom, ν, does not appear in the above equation because there were three observed exchange current densities and two fitting parameters (k_0 and α), i.e. there was only one degree of freedom. Both mechanisms appeared to fit the data of this study, and though the χ^2 was slightly lower for the case of a two electron transfer process (see Table 10), the relatively small degree of improvement was hardly compelling evidence to accept this mechanism over the other. Certainly the weight of previous evidence resides with adoption of a single electron transfer mechanism. In fact, the exchange current densities measured in this study matched almost perfectly with those recently reported by Jović et al. [41] (see Figure 35), who also adopted a model of zinc electrocrystallization as a series of single electron transfer reactions.

Table 10: Observed and calculated zinc exchange current densities for zinc deposition from zinc sulphate electrolytes, pH = 4.9 at 25 °C, $\beta = 1.0$.

	$j_{0,Zn}$ / A m^{-2}			k_0 / A m^{-2}	χ^2
	0.10 $ZnSO_4$ / mol kg^{-1}	0.50 $ZnSO_4$ / mol kg^{-1}	1.00 $ZnSO_4$ / mol kg^{-1}		
Observed	21 ±5	23 ±7	28 ±5		
Calculated ($\alpha = 1.0$)	23	23	23	23	1.2
Calculated ($\alpha = 0.5$)	18	26	31	154	0.9

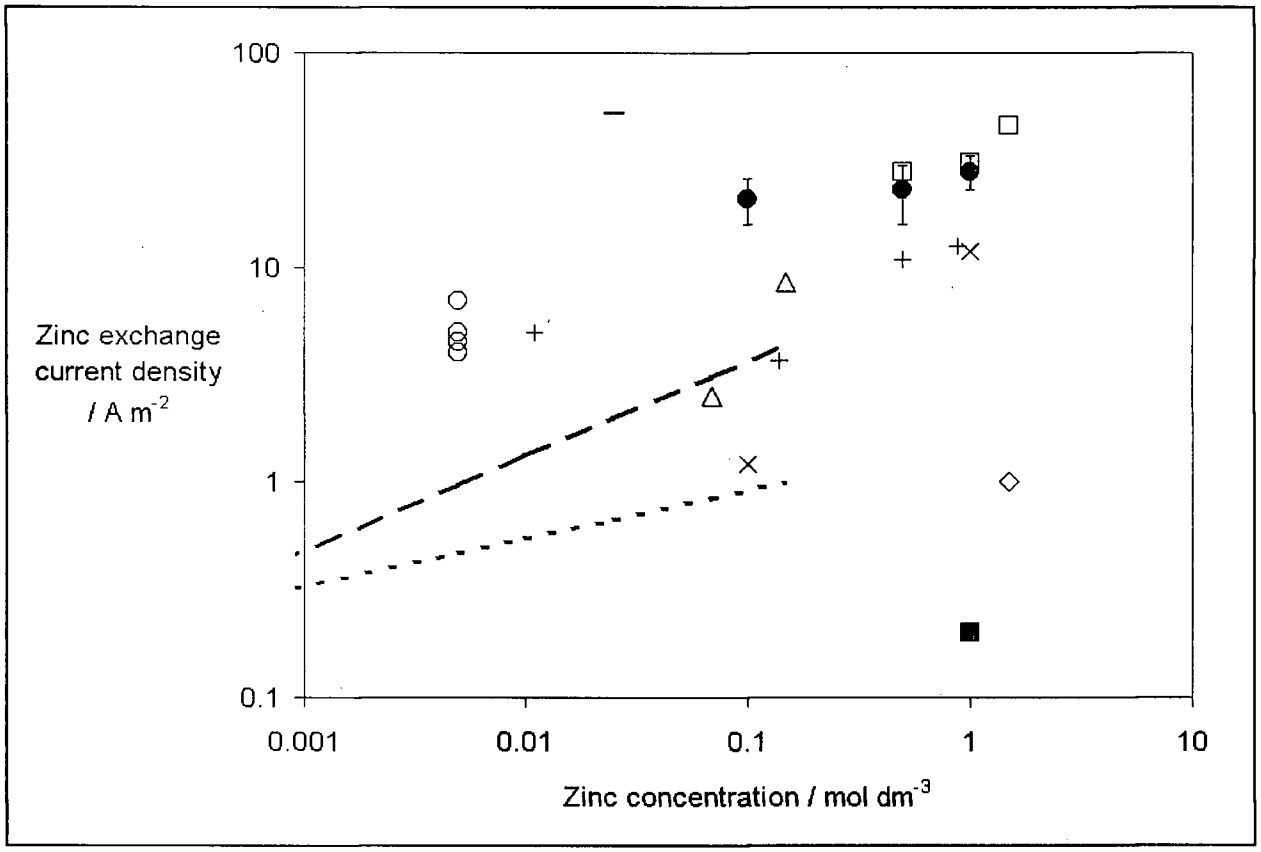

Figure 35: Effect of zinc concentration on zinc exchange current density in sulphate based electrolytes at 25 °C, from (●) this study, (-----) Sziráki and Kiss [38], (– – –) Sziráki and Kiss [38], (Δ) Zouari and Lapique [40], (□) Jović et al. [41], (◊) Despić and Pavlović [51], (○) Hurlen and Brevik [107], (–) Budov and Losev [111], (×) Kahanda and Tomkiewicz [112], (■) Parsons [113], and (+) Sierra-Alcazar and Harrison [114].

When the polarization experiments were repeated after addition of 0.01 mol kg^{-1} H_2SO_4 to the electrolyte containing 1.0 mol kg^{-1} $ZnSO_4$, the polarization curves were observed to shift (see Figure 36). As mentioned, Wiart et al. [35] had previously reported that addition of a small quantity of acid caused a shift in the polarization curve to more negative potentials after

adjusting the pH of an electrolyte containing 1.5 mol dm^{-3} $ZnSO_4$ with 1 mol dm^{-3} Na_2SO_4 from 4.3 to 2.0. Wiart et al. explained the effect of addition of acid as stabilising ZnH_{ad} on the zinc electrode surface, which resulted in more negative overpotentials being required to displace it in favour of Zn^+_{ad}, the autocatalytic species that is the precursor to Zn deposition.

Closer examination of Figure 36 revealed further evidence of the dramatic effect of acid on zinc deposition kinetics. It appeared that zinc deposition at low overpotentials was more inhibited at higher rotation rates. The adverse effect on zinc deposition kinetics of increased rotation speed was probably related to faster mass transport of acid species (H_3O^+ and HSO_4^-) to the electrode surface, which assisted in maintaining the a low interfacial pH. However, at higher zinc deposition overpotentials, increased hydrogen evolution would have consumed protons at rates sufficient to have caused an increase in the interfacial pH (a phenomena previously reported by Fabri-Miranda et al. [52]). The result was that after an initial inhibition of zinc deposition at low overpotentials, at higher overpotentials the kinetics of zinc deposition became more typical of neutral electrolytes. Although obviously more complicated than a simple shift in the curves, one can approximate the effect of acid, in this case, as having decreased the exchange current density to *ca.* 6 A m^{-2}.

More direct comparisons to Wiart's results in weakly acidic electrolytes are impractical since the model yields multiple predictions for steady-state currents which disappear at lower pHs [35, 109, 110]. However, it was obvious that the presence of small amounts of acid had a significant impact on zinc deposition kinetics, which probably contributed to the scatter of previously reported zinc exchange current densities (see Figure 35), which were measured at pHs ranging from 3.0 to 6.5 (see Table 1).

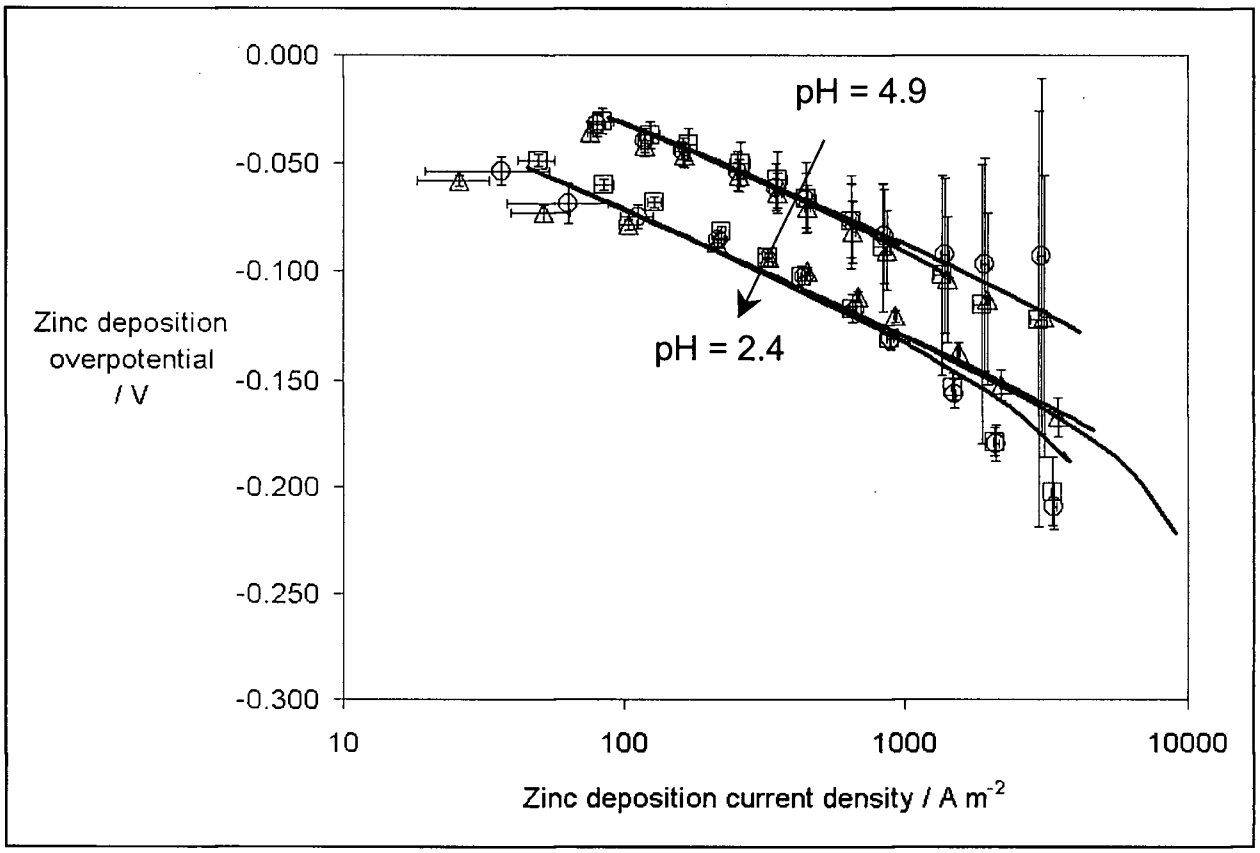

Figure 36: Polarization curves for zinc deposition from 1.0 mol kg^{-1} $ZnSO_4$, with (pH = 2.4) and without (pH = 4.9) addition of 0.01 mol kg^{-1} H_2SO_4, at 25 °C, 400 rpm (□), 1600 rpm (○), and 3600 rpm (△) electrode rotation speed.

4.2.5 Zinc Electrodeposition Kinetics in Highly Acidic Electrolytes

The kinetics of zinc deposition were examined from 1.0 mol kg^{-1} $ZnSO_4$ electrolytes with additions of 0.10 mol kg^{-1} H_2SO_4, by normal pulse and staircase voltammetry, and 1.0 mol kg^{-1} H_2SO_4, by staircase voltammetry. During the course of polarization experiments, which were conducted in the presence 0.10 mol kg^{-1} H_2SO_4, hydrogen gas bubbles were observed to form on the Teflon insulator of the RRDE between the disc and ring electrodes at the lower electrode rotation speeds of 400 and 1600 rpm. Since the presence of these bubbles would have affected the collection efficiency for detection of evolved hydrogen, these experiments were discarded and further experiments were conducted at 3600 rpm, for which no bubble formation was visible. During normal pulse experiments, in the presence of 1.0 mol kg^{-1} H_2SO_4, small bubbles were observed to form on the disc electrode surface. Consequently, these experiments were abandoned and the procedure for pre-treatment of the electrode surface, prior to staircase voltammetry, was modified as described in Section 3.3.3. Using the modified method at an electrode rotation speed of 3600 rpm, no bubble formation was visible either on the disc electrode surface or on the

Teflon insulator of the RRDE. The maximum hydrogen evolution current density recorded during these experiments was 23 ±3 A m^{-2}, which is consistent with the observations of Frazer and Hamilton [15], who previously reported that hydrogen evolution rates < *ca.* 19.5 A m^{-2}, on a Au-Pt RRDE rotating at 1200 rpm, did not lead to a decay in ring response for detection of evolved hydrogen.

The results of current efficiency measurements for zinc deposition from the two highly acidic electrolytes examined are presented in Figure 37 and Figure 38. Each data point in Figure 37 is the mean value of three replicated experiments, whereas the data points in Figure 38 are individual measurements. Thus, the error bars in Figure 38 were based solely on the uncertainties due to instrumental limitations, while the error bars in Figure 37 include the standard deviation of the replicated experiments (representing random errors). The overall current efficiencies, measured by current integration of the normal pulses, were lower than the instantaneous current efficiencies calculated from ring current measurements since, during the initial stages of the pulses, hydrogen evolution rates were higher and asymptotically approach the steady-state current responses (see Figure 12). The overall current efficiencies were calculated by integrating over the entire duration of the pulses, whereas the instantaneous current efficiencies reported from the ring current measurements were calculated from the average ring current and disc currents at the end of each pulse. The use of longer pulse times would probably have resulted in improved convergence between the two measurements, but this was not practical given the problem of electrode roughening due to extended zinc deposition times. Therefore, the instantaneous current efficiency was more representative of steady-state conditions. Consequently, further references to measured current efficiencies in this study are for those calculated from ring current measurements.

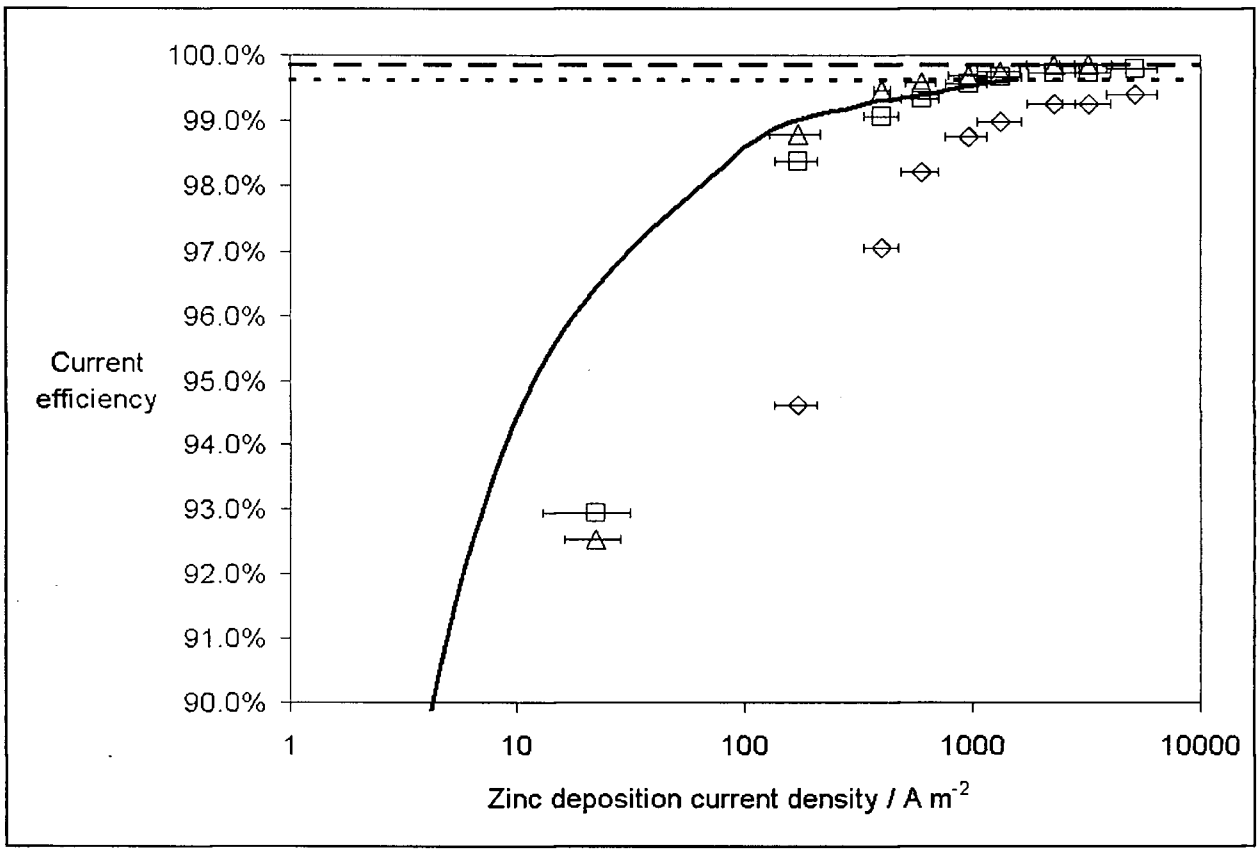

Figure 37: Current efficiency during zinc deposition from 1.0 mol kg^{-1} $ZnSO_4$, with 0.10 mol kg^{-1} H_2SO_4, pH = 1.4 at 25 °C, 3600 rpm electrode rotation speed, measured from ring current during (Δ) staircase voltammetry, (□) normal pulse voltammetry, and from charge integration during (◊) normal pulse voltammetry, and predicted (——) by Wiart's Model [30], and Wark's rule where (-----) k = 0.0137 [26], and (– – –) k = 0.033 [28].

The current efficiencies measured for the electrolyte containing 0.1 mol kg^{-1} H_2SO_4 matches well with those calculated using Wiart's Model, (see Appendix C), but were higher than those predicted at 1.0 mol kg^{-1} H_2SO_4. However, the results of this study are accepted as being accurate since they are more consistent with current efficiencies predicted by Wark's rule, using the constant determined by Biegler and Frazer [26] for high purity electrolytes (measured between 200 and 800 A m^{-2}), as well as those observed for electrolytes of similar composition and purity [15, 25]. Though current efficiencies clearly increased with increasing current density, Wark's rule is probably sufficient for engineering calculations for predicting current efficiency as a function of solution composition in the range of current densities relevant to industrial electrowinning.

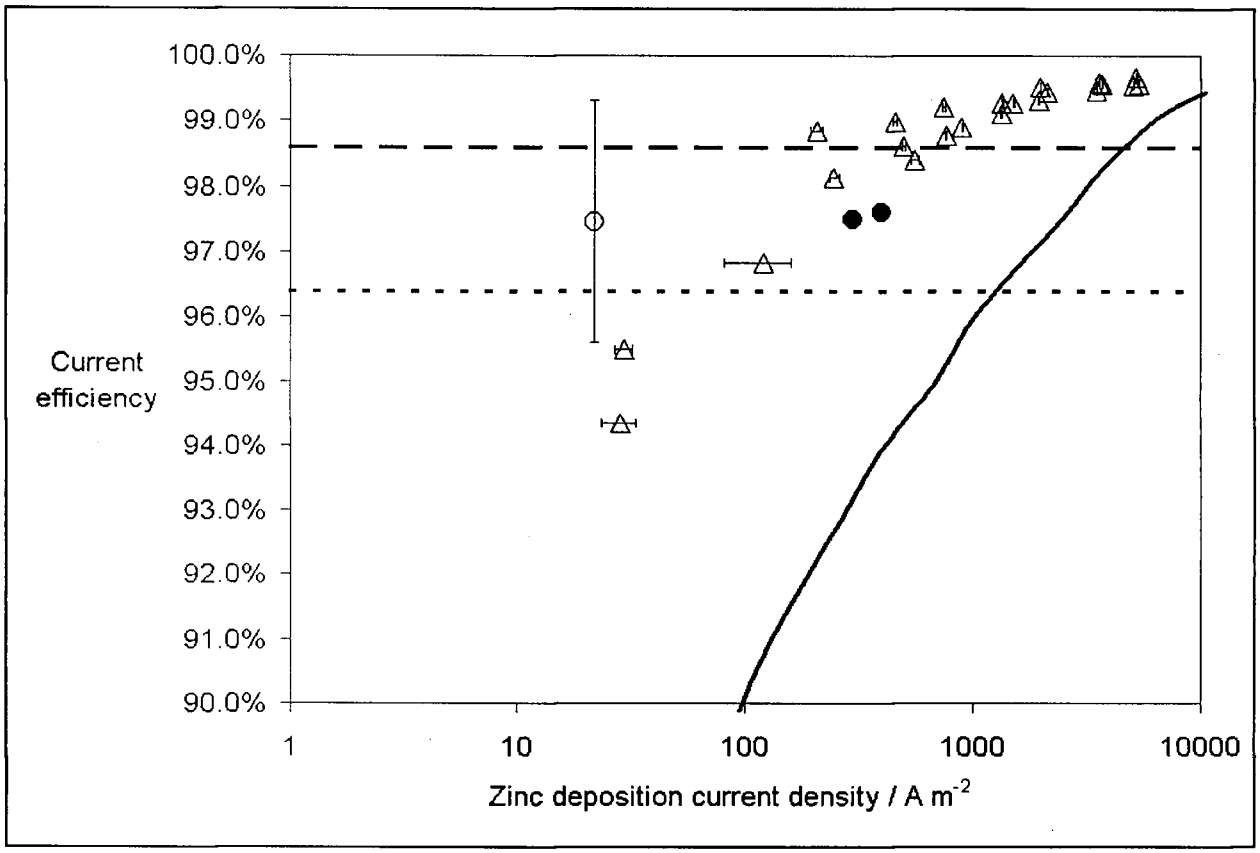

Figure 38 Current efficiency during zinc deposition from 1.0 mol kg^{-1} $ZnSO_4$, with 1.0 mol kg^{-1} H_2SO_4, pH = 1.4 at 25 °C; 3600 rpm electrode rotation speed, measured from ring current during (Δ) staircase voltammetry, and predicted (——) by Wiart's Model [30], and Wark's rule where (-----) $k = 0.0137$ [26], and (– – –) $k = 0.033$ [28]. Also plotted are data for 0.8 mol dm^{-3} $ZnSO_4$ with 1.07 mol dm^{-3} H_2SO_4 at 25°C, (•) [25], (○) [15].

The results of zinc deposition current measurements are plotted in Figure 39 and Figure 40, along with those predicted according to Wiart's Model [30] (see Appendix C). In general, the measured and predicted current densities matched relatively well at < *ca.* 1000 A m^{-2}, at which point a roll-off in potential was observed. When the polarization curves for the two acid levels were compared, their similarity suggested that, contrary to expectation, increasing acid concentration in already strongly acidic electrolytes had little effect on zinc deposition kinetics. Note that the curves generated using Wiart's Model, after the parameters were normalized to account for differences in proton concentration, also appeared almost identical for both acid levels. A fit of the Tafel equation to the linear regions of these plots, prior to the observed roll-off in potential, resulted in an exchange current density of *ca.* 0.02 A m^{-2} , which is *ca.* 1000 times smaller than those determined, in this study, for pH neutral electrolytes. The exchange current density was *ca.* 10000 times smaller than those reported by other researchers for similar electrolytes [11, 117, 118] and the Tafel slope, *ca.* 30 mV dec^{-1} ($\beta = 2.0$), was also significantly

different from the Tafel slopes reported by Barton and Scott [11] (*ca.* 70 mV dec^{-1}) and Tripathy et al. [118] (*ca.* 120 mV dec^{-1}). However, as outlined in Section 2.5.2, the results from the aforementioned studies are suspect. At the very least, the results of this study provide independent confirmation of the predictions of Wiart's Model for the kinetics of zinc deposition from acidic sulphate electrolytes at current densities < *ca.* 1000 A m^{-2}.

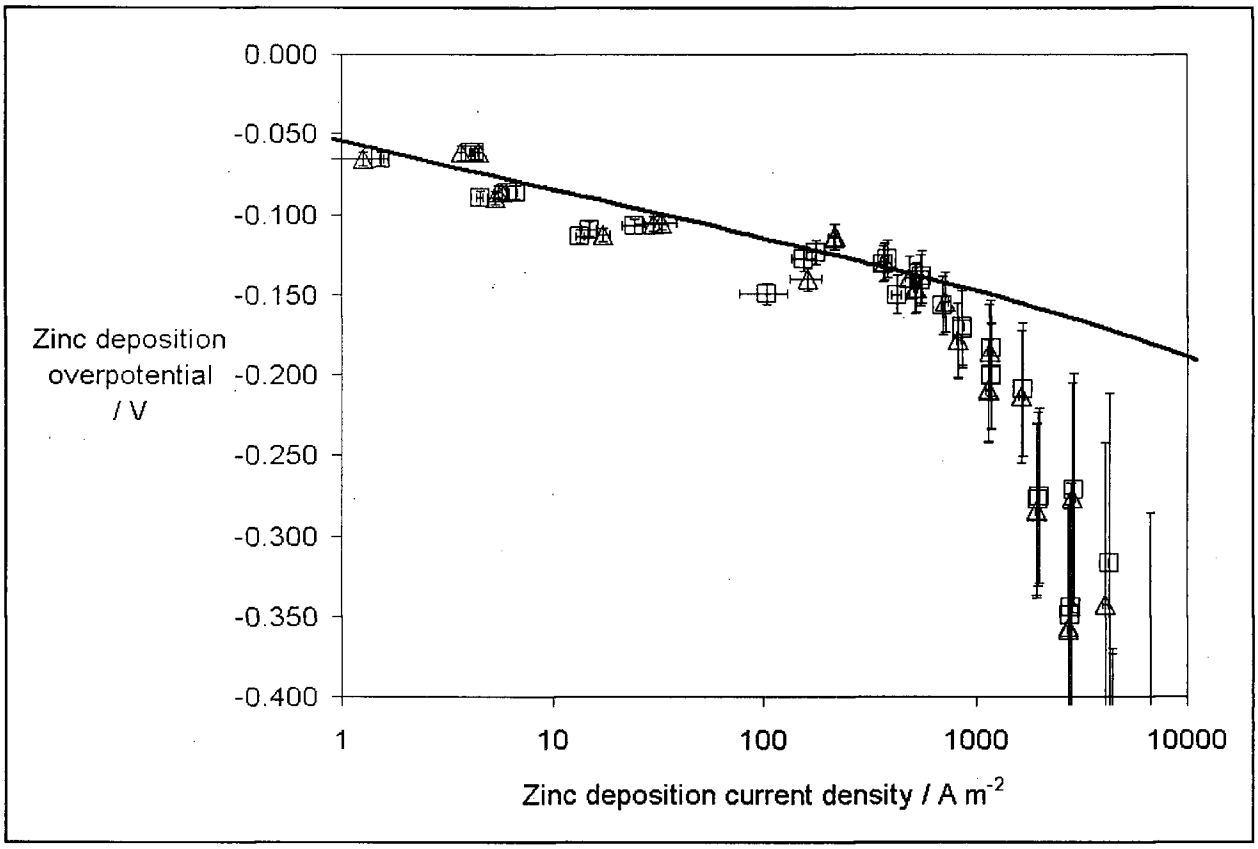

Figure 39: Tafel plot for zinc deposition from 1.00 mol kg^{-1} $ZnSO_4$, with 0.10 mol kg^{-1} H_2SO_4, pH = 1.4 at 25 °C, 3600 rpm electrode rotation speed, measured by (Δ) staircase voltammetry, and (□) normal pulse voltammetry, and predicted (——) by Wiart's Model [30].

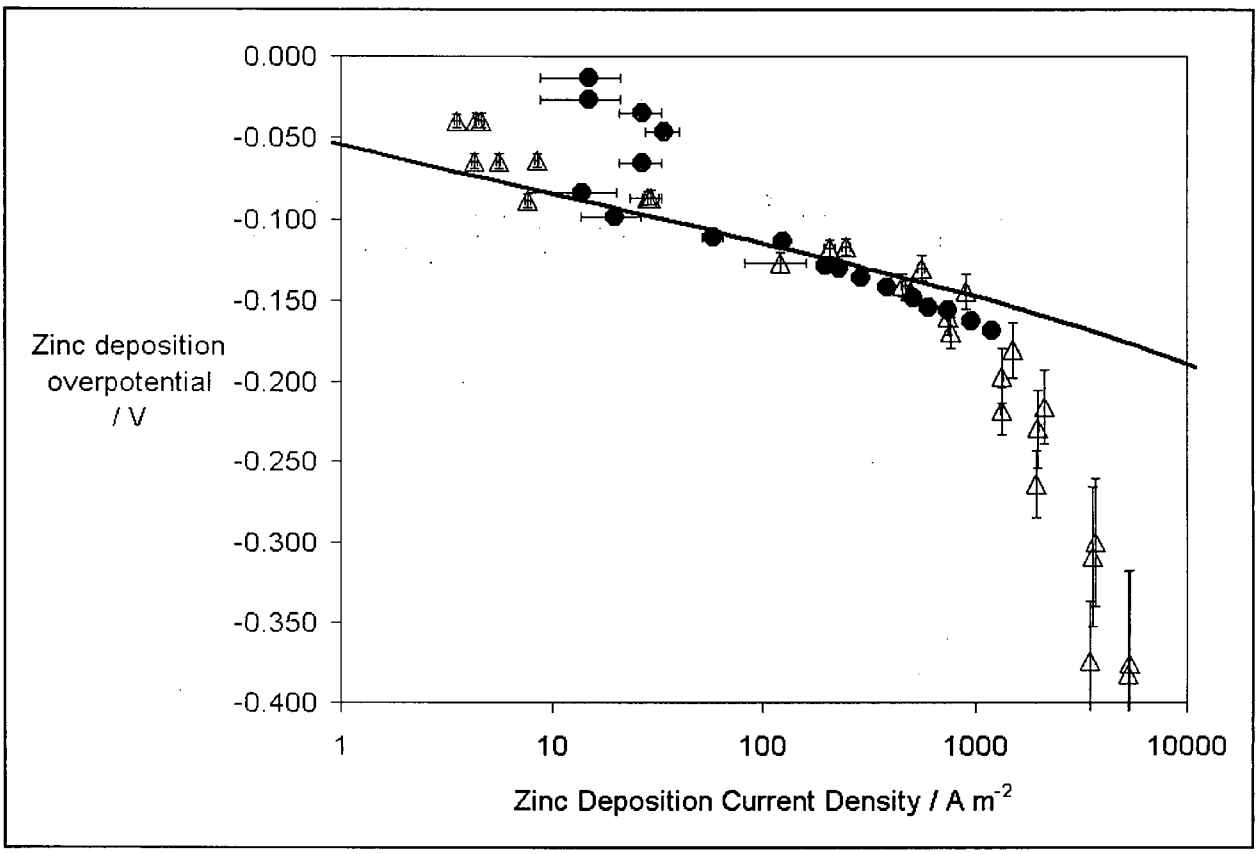

Figure 40: Tafel plot for zinc deposition from 1.00 mol kg^{-1} $ZnSO_4$ with 1.00 mol kg^{-1} H_2SO_4, pH = 0.2 at 25 °C, 3600 rpm electrode rotation speed, measured by (Δ) staircase voltammetry, and predicted (——) by Wiart's Model [30]. Also plotted are data for total current density for 0.84 mol dm^{-3} $ZnSO_4$ with 1.22 mol dm^{-3} H_2SO_4, at room temperature, and 1500 rpm electrode rotation speed, taken from [30].

With respect to the observed roll-off in potential at *ca.* 1000 A m^{-2}, the first suspicion was that this behaviour was due to mass transfer limitations. In this regard, the calculated limiting current densities listed in Table 9 were probably overestimated. During zinc electrodeposition from highly acidic electrolytes, protons migrate to the cathode, but since hydrogen evolution is strongly inhibited, the protons do not react immediately and collect in the boundary layer. The result is a proton concentration in the boundary layer that is greater than the bulk proton concentration. This condition would have reduced the zinc ion transport number in the boundary layer according to Equation 2.19. However, even if the zinc transport numbers were equal to zero, the corresponding limiting current densities for zinc deposition would have occurred at *ca.* 11000 A m^{-2}. It is more likely that the change in Tafel slope was caused by extreme roughing of the zinc deposit at high deposition overpotentials. According to Delevie [144], the effect of surface roughening on electrode kinetics may be introduced into Butler-Volmer Equation by inserting the power term of the Constant Phase Element, ξ, as follows:

$$j_{Zn} = \frac{I_{Zn}}{A_e} = \frac{-j_{0,Zn}\left[e^{\frac{-\xi\alpha nF\eta_{Zn}}{RT}} - e^{\frac{\xi(1-\alpha)nF\eta_{Zn}}{RT}}\right]}{1 - \frac{j_{0,Zn}}{j_{\lim,Zn}} e^{\frac{-\xi\alpha nF\eta_{Zn}}{RT}}}$$ Equation 4.12

Therefore, the change in Tafel slope at current densities > *ca.* 1000 A m^{-2}, observed in this study, was likely due to a change in deposit morphology from a relatively flat and homogeneous deposit ($\xi \approx 1.0$) to a dendritic deposit ($\xi \approx 0.5$).

Wiart's Model predicts dendritic zinc deposition to occurs at high overpotentials, due to an increase in the nucleation rate of Zn^*, the self-perpetuating crystal defect which is a zinc species at kink sites. Note that the upper end of current density range of the data of Cachet and Wiart [30] is coincident with the occurrence of the potential roll-off phenomena and the prediction of dendritic growth (see Figure 40). In addition, recall that Popov et al. [50] had previously reported the critical overpotential for dendrtic growth in 0.84 mol dm^{-3} $ZnSO_4$ with 1.2 mol dm^{-3} H_2SO_4 at 25 °C is -173 mV, which is also consistent with where the change in Tafel slope was observed to occur. Further evidence that the change in growth mode of zinc deposited at high current densities is not due to mass transfer limitation was reported by Weymeersch et al. [145]. In their study, forced convection was utilized to eliminate mass transfer limitations in a parallel plate cell composed of a stainless steel cathode and a zinc anode. As illustrated in Figure 41, the zinc deposited at 1000 A m^{-2} appeared relatively fine grained, while the zinc deposited at 15000 A m^{-2} was composed of large columnar dendrites.

The analysis of the results of this study suggest that the technique developed may be applied to characterize the kinetics of zinc deposition and current efficiency for a desired zinc electrolyte composition. It also confirms the utility of Wiart's Model to predict the inception of dendritic morphology for zinc deposition from pure acidic zinc sulphate electrolytes. Parameters for Wiart's Model have also been published for electrolytes containing nickel impurities [46, 146] and perfluorinated surfactants [30]. In the absence of these data, the technique developed can be applied directly to predict the transition between relatively smooth deposition and dendritic growth.

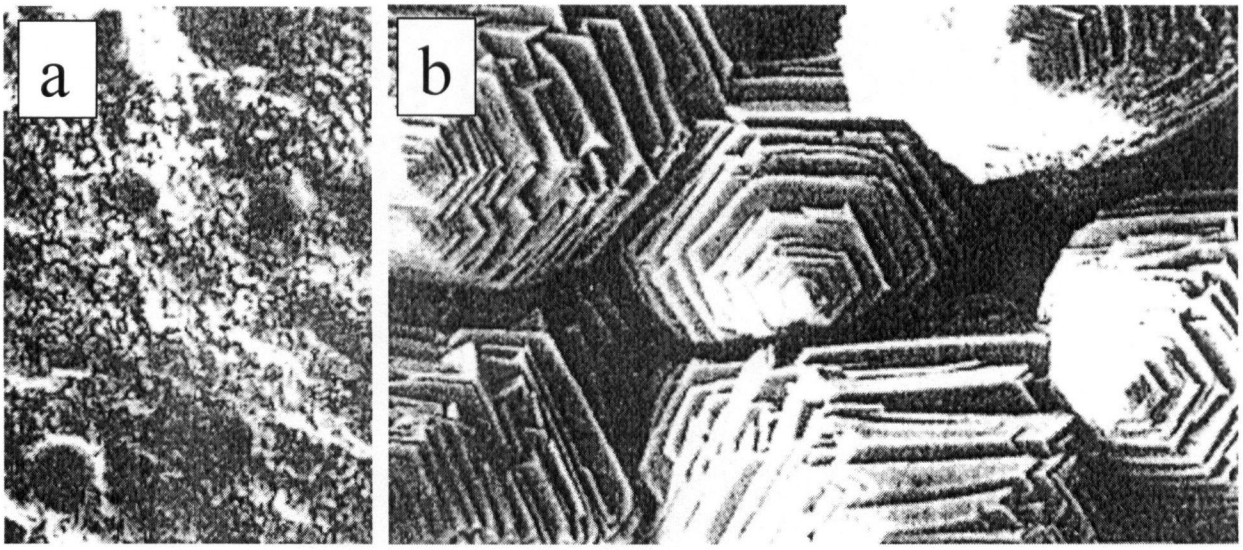

Figure 41: SEM photomicrographs (1000 × magnification) of the thin, ≤ 200 μm, films of zinc deposited from 1.22 mol dm^{-3} Zn^{2+} and 1.34 mol dm^{-3} H_2SO_4 at 50 °C, at electrolyte flowrates ≥ 3 m s^{-1}, and current densities of 1000 A m^{-2} (a), and 15000 A m^{-2} (b), taken from [145].

One criticism of Wiart's Model may be that the complex set of calculations of partial coverages and competing reactions resulted in a relationship between zinc deposition current density and overpotential which may be modelled by a simple Tafel equation. When comparing the kinetics for zinc deposition between the pH neutral electrolytes and the highly acidic electrolytes, the differences in Tafel slopes and exchange current densities suggest that zinc deposition simply occurred by different mechanisms. Recall, from Equation 2.3, that the Tafel slope, *b*, contains the number of electrons transferred in the rate determining step, *n*, and the transfer coefficient, α.

$$\eta_{Zn} = \frac{2.303RT}{\alpha nF}\log(j_{0,Zn}) - \frac{2.303RT}{\alpha nF}\log(j_{Zn}) = a - b\log(j_{Zn}) \qquad \text{Equation 2.3}$$

The Tafel slope of 30 mV dec^{-1} suggested a two electron transfer mechanism, n = 2, which involved a surface active species which 'felt' the full fraction of the applied overpotential, $\alpha = 1$. The low zinc exchange current density in the highly acidic electrolyte was also consistent with what would be expected for a two electron transfer mechanisms since the simultaneous transfer of two electrons is statistically much less likely than for two successive single electron transfer events. The obvious difference between the two types of electrolytes is that one contained an excess quantities of H_3O^+ and HSO_4^- while the other did not. A possible mechanism for zinc deposition from highly acidic sulphate solutions may involve a reaction between zinc ions and a species such as $ZnHSO_4^-$ (representing adsorbed HSO_4^- on *Zn*) appears below:

$$Zn^{2+} + ZnHSO_4^- + 2e^- \longrightarrow Zn + ZnHSO_4^-$$ Equation 4.13

The above mechanism is similar to Reaction 7 of Wiart's model, with $ZnHSO_4^-$ substituted for the Zn^*. In fact, the effect of such an adsorbed anion species would likely be similar to that attributed to Zn^*. Hydrogen sulphate adsorption may be stronger at dislocations and step edges on the zinc surface. The effect of such an adsorbed anion would be to induce positive mirror charge in the crystal lattice next to it, which would repel zinc ions, thereby inhibiting metal deposition at these sites, i.e. promote the creation of more kink sites. This is notionally similar to what Wiart described as the self-propagating active species at a kink site, Zn^*. However, a literature search for hydrogen sulphate adsorption on zinc did not yield evidence to support or disprove this theory, though strong hydrogen sulphate adsorption onto ZnO surfaces has been described by the Radiotracer method [147]. Hence, further examination into the mechanism of zinc deposition may require this type of examination of the nature of surface active species.

5 Conventional Zinc Electrowinning at High Current Density

The results of the experiments of Zn OPD from highly acidic sulphate electrolytes are now discussed in terms of their implications for zinc electrowinning at current densities beyond the conventional upper limit of *ca.* 500 A m^{-2}. This current density limit is due, in large part, to the problems within the electrowinning cell related to poor deposit morphology, such as short-circuiting and lower current efficiency, the latter likely being caused by fragile dendrites breaking and redissolving from the violent action of hydrogen gas evolution, as well as problems in terms of cathode handling and stripping. One may note that 500 A m^{-2} is approximately half of the current density at which dendritic growth was predicted to occur. The reasons for this discrepancy and the potential measures which may extend the current density range of conventional zinc electrowinning, are probably related to screening of cathode surfaces by attached bubbles and the distribution of the ohmic drop through the electrolyte. These effects are discussed in the following sections, along with the potential role of forced convection, which is currently not employed to any significant degree in industrial zinc electrowinning, as a way of mitigating the aforementioned effects.

5.1 Bubble Screening of the Cathode

The kinetic parameters reported in this study were measured under conditions which prevented bubble formation on the cathode and, thus, the reported current densities are calculated on the basis of the geometric area of the electrode. However, in industrial electrowinning the electrolyte is saturated with dissolved hydrogen and the cathode surface is covered by gas bubbles and the true current density, j (A m^{-2}), must be adjusted for the fractional bubble coverage of the electrode, Θ, as follows:

$$j = \frac{I}{A_e}\frac{1}{1-\Theta} \qquad \text{Equation 5.1}$$

where; I (A) is the total current, and A_e (m^{-2}) is the electrode area. Dukovic and Tobias [148] suggested that the arrangement of bubbles on a vertical gas-evolving electrode may be approximated as an array of hexagonally close packed spheres of uniform diameter (see Figure 42), from which the fractional bubble coverage of the electrode may be calculated from the contact angle, θ, according to the following expression:

$$\Theta = \frac{\sqrt{3}\pi}{6}\sin^2\theta$$ Equation 5.2

Dukovic and Tobias further recommended a contact angle of 40° (Θ = 0.37) as a typical value, based on previously reported contact angles of hydrogen bubbles evolving on Pt, Ni, Cu and Fe electrodes in 30 % H_2SO_4 [149]. Electrolytic gas bubble evolution actually proceeds, predominantly, by bubble growth and detachment from nucleation sites which are small pockets of gas trapped in scratches and crevices on the electrode surface [150]. Thus, bubble contact angles change during their growth and the value quoted by Dukovic and Tobias is actually analogous to an average contact angle.

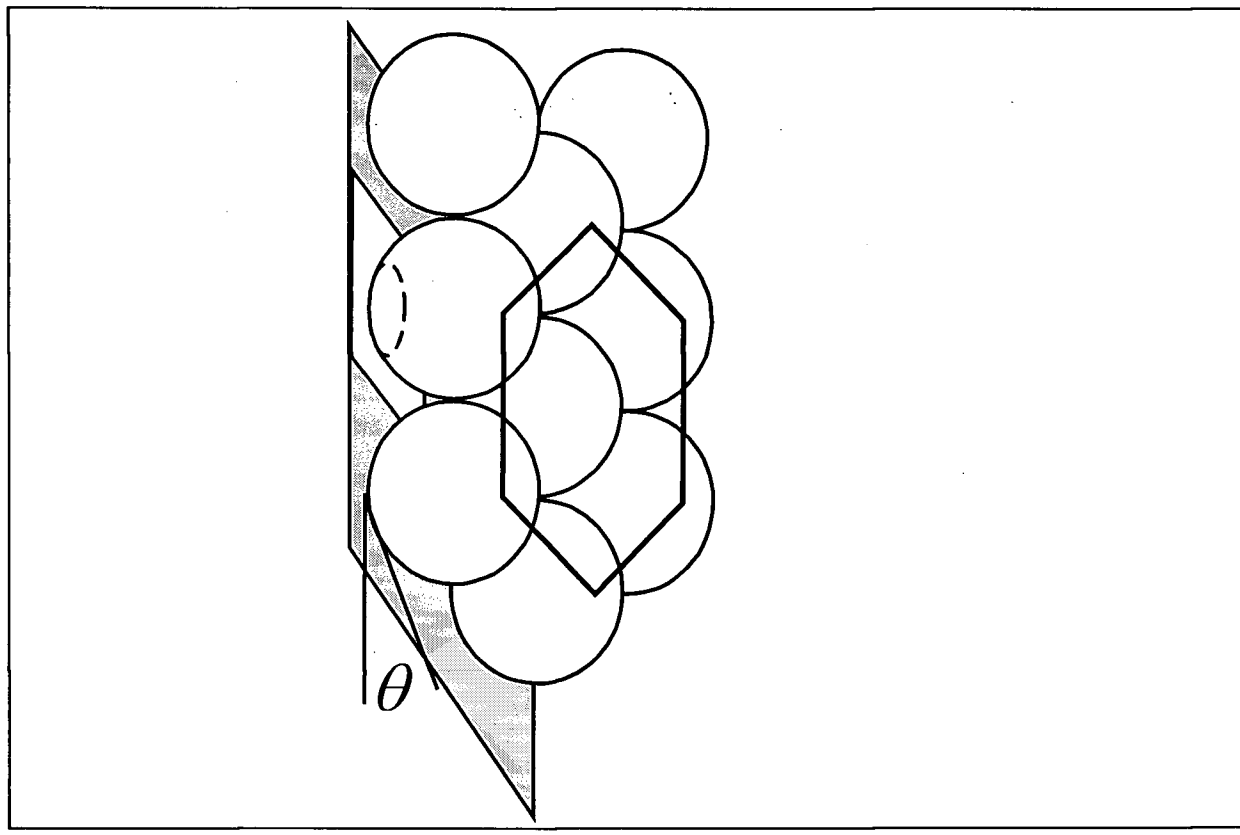

Figure 42: Idealized arrangement of bubbles on a vertical gas-evolving electrode.

The consequence of a large fractional bubble coverage is that it results in a larger true current density, which may be one of the causes of premature dendritic zinc deposition in industrial zinc electrowinning. For a contact angle of 40° the resulting true current density is calculated to be 1.6 times the geometric current density, e.g. a geometric current density of 500 A m^{-2} results in a true current density of 800 A m^{-2}, closer to the current density at which dendritic growth is predicted to occur.

Implicit in Equation 5.2 is that the fractional bubble coverage is insensitive to current density, which has been observed for hydrogen evolution on copper and stainless steel electrodes in 1 mol dm^{-3} KOH [151]. However, forced convection has a significant impact on fractional bubble coverage by dislodging the attached bubbles. Eigeldinger and Vogt [151] have developed the following empirical relationship to predict the effect of electrolyte flow velocity, v (m s^{-1}), on fractional bubble coverage in electrolytic cells employing forced convection:

$$\Theta = \frac{\Theta_0}{\left[1+(Cv)^2\right]^2} \qquad \text{Equation 5.3}$$

where; Θ_0 is the fractional bubble coverage for $v = 0$ and C (s m^{-1}) is an empirical constant which has a value of 8 for 1 mol dm^{-3} KOH. One may note that, using the above equation, fractional bubble coverages for flow velocities of > 0.4 m s^{-1} are < 1 % of their values in the absence of forced convection. The implication for zinc electrowinning is that forced convection may significantly reduce the fractional bubble coverage, thereby reducing the true current density to a value closer to the geometric current density.

The enhancement of mass transport attributed to microconvective mixing caused by the detachment of hydrogen gas bubbles at the electrode surface is not effective for transporting additives from the bulk solution to the electrode surface. In this regard, the effect of low mass transport rates of additives on deposit morphology has been demonstrated by Bressan and Wiart [108, 116]. Forced convection may also assist in mass transport of surfactants and additives to the electrode surface which render the zinc electrode surface hydrophilic (decrease the bubble contact angle) or improve deposit morphology by other mechanisms, though their effects on electrode kinetics would require examination.

5.2 Distribution of Ohmic Drop Through the Electrolyte

During zinc electrowinning, a fraction of the electrolyte becomes entrained with evolved oxygen and hydrogen gas bubbles. These bubbles may be assumed to act as insulating spheres which reduce the overall conductivity of the electrolyte. The fraction of entrained bubbles in the electrolyte increases from the bottom of the cell to the top since the bubbles are evolved along the entire height of the electrode, h (m), rapidly reaching a limiting rise velocity before exiting through the top of the cell with a mean superficial gas velocity, u^o_g (m s^{-1}). This results in a

bubble distribution within an industrial zinc electrowinning cell which appears as an inverted wedge [152] (see Figure 43). This description of the bubble distribution is also consistent with the observations of Janssen and Visser [153] have described a linear increase in electrolyte resistance with increasing height in tall vertical gas-evolving cells.

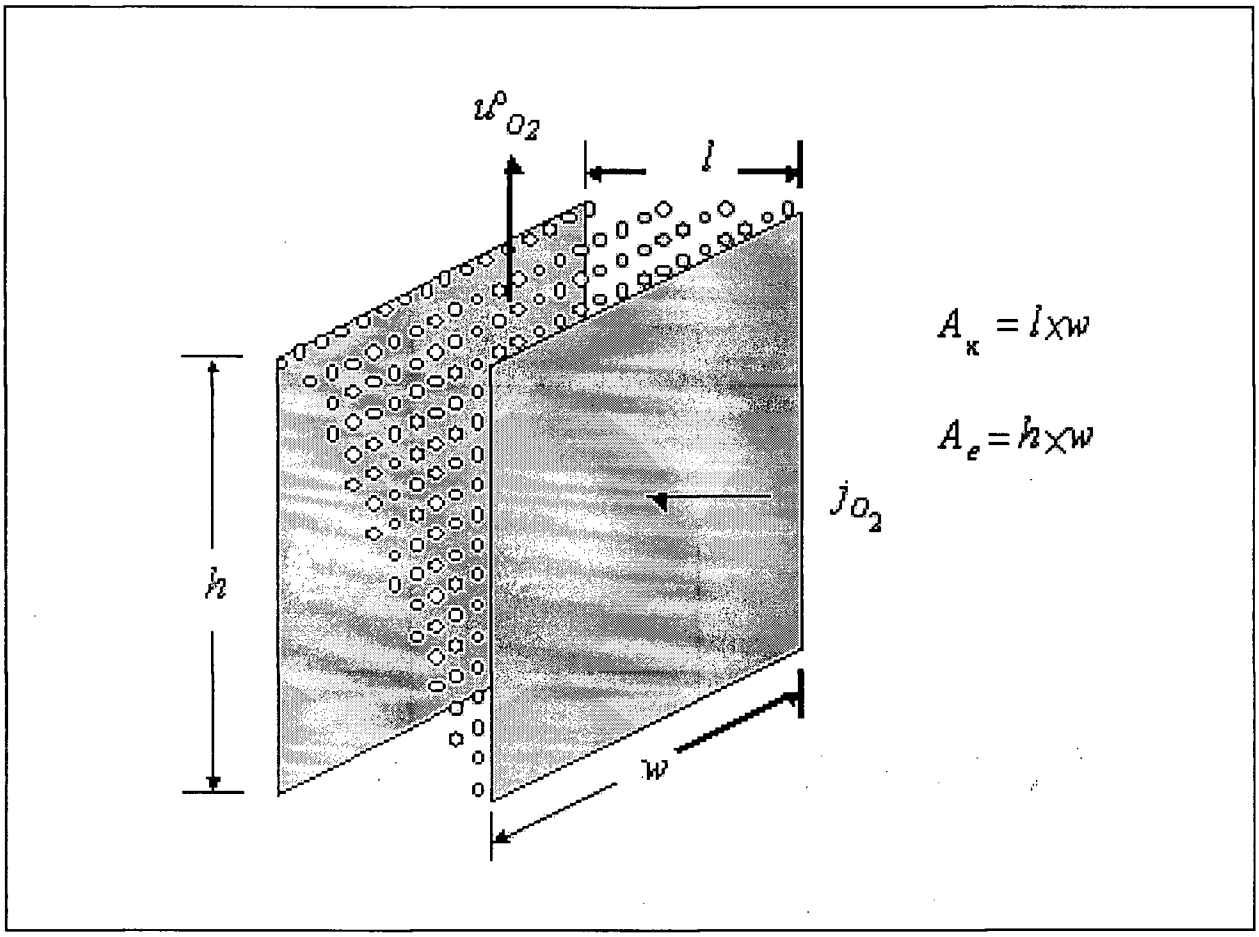

Figure 43: Schematic representation of idealized bubble distribution in a parallel plate electrolysis cell due to oxygen evolution.

The prediction of ohmic drop distribution in an electrolysis cell begins with an estimation of the specific conductivity of the bubble-free zinc electrolyte, σ (Ω^{-1} m^{-1}), for which there are several expressions in literature that are functions of electrolyte composition, mol dm^{-3}, and temperature, K.

$$\begin{aligned}\sigma = {} & 0.4 + 0.115(T-273) + 0.282[H_2SO_4](T-273) \\ & + 34.42[H_2SO_4] - 4.51[H_2SO_4]^2 + 2.86([Zn^{2+}]+[Mg^{2+}])^2 \\ & + ([Zn^{2+}]+[Mg^{2+}])(-0.114(T-273) - 10.58[H_2SO_4] - 2.24)\end{aligned}$$ [154] Equation 5.4

$$\sigma = 23.92 + 0.27[H_2SO_4](T-308) + 19.6[H_2SO_4] - 11.1([Zn^{2+}]+[Mn^{2+}]+[Mg^{2+}]+0.5[NH_4^+]) \quad [11]$$ Equation 5.5

$$\sigma = 23.88 + 13.93[H_2SO_4] - 16.09[Zn^{2+}] - 16.15[Mn^{2+}] - 17.14[Mg^{2+}] + 0.406(T-273) \quad [155]$$ Equation 5.6

$$\sigma = 12.3 + 18.93[H_2SO_4] - 7.78[Zn^{2+}] + 0.114(T-273) \quad [156]$$ Equation 5.7

$$\sigma = -10.79[Zn^{2+}] - 53.90[H_2SO_4] - 1.814[Zn^{2+}]^2 - 6.380[H_2SO_4]^2 - 1.027[Zn^{2+}][H_2SO_4] + 16.73[Zn^{2+}]^2[H_2SO_4] + 0.0585[Zn^{2+}]T + 12.46[Zn^{2+}][H_2SO_4]^2 - 6.762[Zn^{2+}]^2[H_2SO_4]^2 + 0.3345[H_2SO_4]T - 0.1341[Zn^{2+}][H_2SO_4]T$$ Equation 5.8

The final correlation, generated by the author, is a least-squares fit of the conductivity measurements reported by Hinatsu et al. [157] and matches their data to within ±0.55 Ω^{-1} m^{-1} (see Figure 44). All the above correlations give similar results in the range of a typical zinc electrolyte containing, *ca.* 1 mol dm^{-3} $ZnSO_4$ and 1.5 mol dm^{-3} H_2SO_4 at 308 K (38.42 ±0.75 Ω^{-1} m^{-1}), but otherwise differ significantly when applied to non-conventional electrolyte compositions and temperatures. The higher order expressions reported by Tozawa et al. [154] and this author were both generated for solutions containing 0 to 1.2 mol dm^{-3} Zn^{2+}, with < 2 mol dm^{-3} H_2SO_4, at 25 to 60 °C, and are probably more applicable for predicting electrolyte conductivity over a wider range of electrolyte compositions and temperatures as compared to the other expressions.

The calculated electrolyte conductivity may then be adjusted according to a prediction of the mean fraction of bubbles in the electrolyte, f_m. However, as pointed out by Coenen and Janssen [158], there have been few reliable studies on the estimation of bubble voidage in gas-evolving electrolytic cells. In fact, the method reported by Kreysa and Kuhn [159] for calculating the effective electrolyte conductivity of the electrolyte, σ' (Ω^{-1} m^{-1}), for gas evolution in a stationary liquid was the only such study referenced by Coenen and Janssen in their own paper on the subject. Barton and Scott [11] employed the method of Kreysa and Kuhn, outlined below, to estimated the overall ohmic drop during zinc electrowinning:

First, it is assumed that the cell is operating under steady-state conditions and that rate of input of gas, calculated according to the ideal gas law from the partial current densities, is equal to the rate of gas leaving the cell, which yields the superficial velocity, u^o_g (m s^{-1}), as follows:

$$u_g^o = \left(\frac{j_{O_2}}{4F} + \frac{|j_{H_2}|}{2F} \right) \frac{A_e RT}{A_x P}$$ Equation 5.9

where; A_e (m^2) is the area of the gas-evolving electrode, A_x (m^2) is the cross-sectional area between the electrodes, R (8.31447 J mol^{-1} K^{-1}) is the universal gas constant, T (K) is the absolute temperature, F (96 485 C mol^{-1}) is Faraday's constant, and P (Pa) is the atmospheric pressure above the electrolyte.

The gas fraction in the electrolyte increases with increasing gas evolution rate until a limiting void fraction, f_l, is reached. The gas void fraction at the top of the cell, f, is related to the limiting void fraction by the following empirical equation:

$$f = f_l \left(1 + \frac{u_{sw} f}{u_g^o} \right)^{-1}$$ Equation 5.10

where; u_{sw} (m s^{-1}) is the rise velocity of the bubble swarm. The bubble swarm velocity is calculated using the Marucci equation:

$$u_{sw} = u_s \frac{(1-f)^2}{1-f^{1.67}}$$ Equation 5.11

where; u_s (0.04 m s^{-1}) is the limiting rise velocity of the gas. Barton and Scott assume that the limiting void fraction and limiting rise velocity are the same as those of electrogenerated oxygen in 20% H_2SO_4 [159].

The mean void fraction, f_m, is then calculated by assuming that the void fraction increases uniformly from the bottom, where there are no gas bubbles, to the top of the cell.

$$f_m = \frac{f}{2}$$ Equation 5.12

Finally, the electrolyte conductivity is adjusted to account for the mean void fraction in the electrolyte according to the Maxwell equation. However, one should recognize that the Maxwell equation only applies to small gas fractions, *ca.* < 0.1 [160], and that there are a number of other correlations in the literature which may be more appropriate.

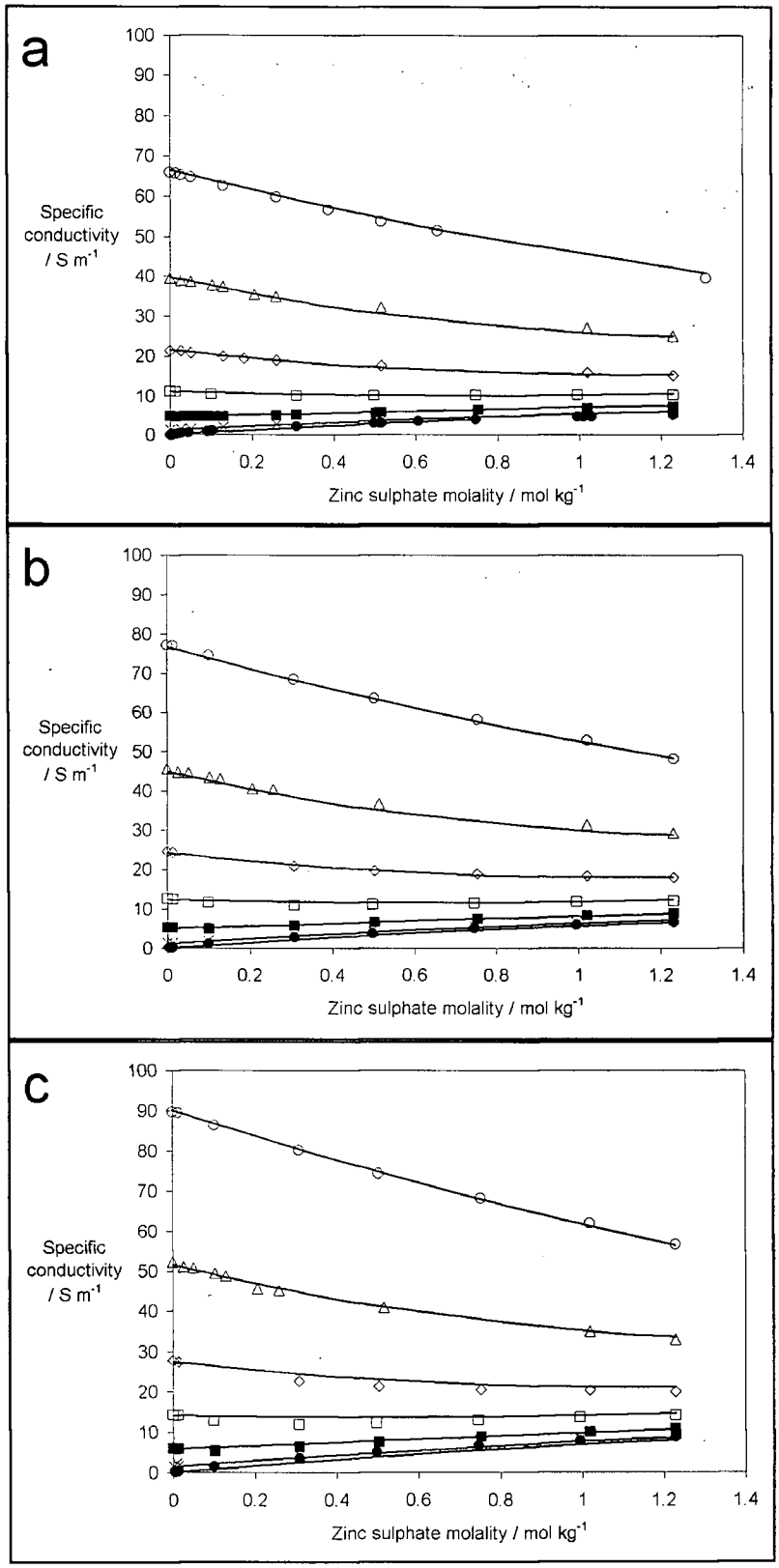

Figure 44: Effect of zinc sulphate concentration on specific conductivity of electrolytes containing 0 (●), 0.0253 (×), 0.101 (■), 0.253 (□), 0.507 (◊), 1.01 (Δ), and 2.02 (○) mol kg^{-1} H_2SO_4, at; 25 °C (a), 40 °C (b), and 60 °C (c), and corresponding fitted curves (——) according to Equation 5.8. Data taken from [157].

$$\sigma' = \sigma\left(\frac{1-f_m}{1+0.5f_m}\right)$$ Equation 5.13

The voltage drop through the electrolyte may then be calculated according to Ohm's law:

$$IR = \frac{I}{\sigma'}\left(\frac{l}{A_e}\right)$$ Equation 5.14

where; l is the interelectrode gap.

It should be noted that the mean void fraction quickly reaches an asymptote of 0.055 at current densities > *ca.* 100 A m^{-2}, which is half of the limiting void fraction of 0.11. It is apparent that a low estimate of the limiting void fraction results in a higher effective electrolyte conductivity and a lower prediction of the ohmic drop through the electrolyte. In this regard, Kreysa et al. [161] have subsequently claimed that the limiting void fraction for oxygen gas may be adequately described as a linear function of ionic strength for various sulphate salt solutions:

$$f_l \approx 0.2 + 0.17I$$ Equation 5.15

where; I < *ca.*1.2 mol dm^{-3}. By inspection, Equation 5.15 yields values for limiting void fractions that are always much greater than 0.11. There is clearly a great deal of uncertainty in the calculation of limiting void fraction which significantly affects the estimation of the distribution of bubbles in the electrolyte and, hence, the vertical distribution of the ohmic drop. For this reason no further calculations are presented.

Since the ohmic drop in a conventional zinc electrowinning cell increases from the bottom of the cell to the top, the corresponding local current density is predicted to decrease from the bottom to the top of the cell. Because the cathode may be considered an equipotential surface, less ohmic drop in one region means that there is, locally, more voltage available as overpotential to drive the deposition reaction. The shallow Tafel slope for zinc deposition observed in this study, 30 mV dec^{-1}, indicates that the rate of zinc deposition is extremely sensitive to small changes in overpotential. In addition, as the zinc deposit will tend to grow faster at the bottom of the cell relative to the top, this should accelerate the narrowing of the interelectrode gap in this region and further skew the current distribution as electrowinning proceeds. Thus, small differences in ohmic drop through the electrolyte between the top and bottom, caused by the bubble

distribution within the cell, may have profound effects on the current distribution on the cathode. Unless this issue is addressed, operation of zinc electrowinning at higher than conventional current densities will likely lead to dramatic increases in the occurrence of unsuitable zinc cathode morphology and short circuiting problems. Extending the depth of cathode slightly beyond that of the anode is a popular method to decrease the local current density, though this method is only effective at the very bottom of the cathode. The use of forced convection in a manner which displaces the electrolyte that contains bubbles with fresh bubble-free electrolyte or, at least, more evenly distribute bubbles within the cell, may also assist in alleviating this problem. Certainly, further study of the costs and benefits of retrofitting conventional zinc electrowinning cells to incorporate forced convection merits further consideration if electrowinning is to be conducted at higher current densities.

6 Conclusions

To create a suitable surface on which to study overpotential deposition of zinc, the UPD layer of Zn onto polycrystalline Pt has been characterized in acidic and neutral sulphate solutions, using electrochemical and XPS measurements. The charge density for UPD Zn deposition on platinum from neutral sulphate solution was estimated to be 260 ±30 $\mu C\ cm^{-2}$, which is in the order of a full monolayer. A decrease in H_2 evolution rates was also described as evidence of the presence of a Zn UPD layer. The UPD layer was found to evolve into a 1:1 Zn:Pt alloy when the electrode was polarized at potentials more negative than the UPD potential. The alloy was oxidised at the same potential as the oxidation of Pt, illustrating the large interaction between Zn and Pt. The alloy also decreased H_2 evolution rates and enhanced zinc OPD kinetics relative to the freshly deposited UPD layer.

The morphology of pulsed Zn OPD on Pt was characterised by AFM and SEM and determined to be suitable as a substrate on which to measure the kinetics zinc OPD by normal pulse and staircase voltammetry. However, roughening of the Pt electrode by bulk Zn-Pt alloy necessitated the use of relatively short pulse durations, < *ca.* 2 minutes. Several expressions for calculating the physical properties of acidic zinc electrolyte were generated as well as a set of Pitzer Model parameters, which are useful for calculating the equilibrium potential for zinc deposition.

The results of experiments examining the kinetics of zinc deposition from slightly acidic sulphate electrolytes, between 0.1 and 1.0 mol kg^{-1} $ZnSO_4$, were successfully modelled according to the Extended Bulter-Volmer Equation. The value of β, under these conditions, was confirmed to be *ca.* 1.0 with a corresponding Tafel slope of 60 mV dec^{-1}. However, whether the rate limiting step for zinc electrocrystallisation is a single electron transfer reaction or a two electron reaction could not be determined conclusively, since the data fit both mechanisms equally well.

The use of a RRDE electrode to detect hydrogen evolution during zinc electrodeposition from acidic zinc sulphate electrolytes was demonstrated to be effective for calculating current efficiency, provided that the ring is first platinised to mitigate problems with the decay in collection efficiency with time. The results confirmed that, in the absence of mass transfer limitations, current efficiency of zinc deposition increases with increasing current density, but can be approximated by Wark's rule over a relatively wide range of current densities. Zinc

electrowinning at high current density is limited by the detrimental effects of the onset of dendritic deposits. The kinetics of zinc deposition from these electrolytes were examined and it was confirmed that Wiart's Model provides accurate predictions of the overpotential for zinc electrodeposition as well as being able to predict the initiation of dendritic deposits. The Tafel slope for zinc deposition from acidic zinc sulphate electrolytes was measured to be *ca.* 30 mV dec^{-1} ($\beta = 2$), with an accompanying exchange current density of *ca.* 0.02 A m^{-2} at 1.0 mol dm^{-3} $ZnSO_4$. Overall, Zn OPD on a UPD modified Pt substrate has been demonstrated to be an effective tool for evaluating the kinetics of zinc deposition from acidic zinc sulphate electrolytes at 25 °C.

It was noted that there is a relatively large difference be tween the current density at which dendritic zinc deposition is predicted to occur, *ca.* 1000 A m^{-2}, and that which is observed in industrial zinc electrowinning, *ca.* 500 A m^{-2}. It was postulated by the author that this difference is related to screening of cathode by attached bubbles and the vertical distribution of bubbles in the electrolyte in industrial cells. Forced convection has been proposed as a way of mitigating the aforementioned effects and extending the current density range of conventional zinc electrowinning.

7 Recommendations for Future Work

The goal of this research was to gain insight into the voltage requirements of industrial zinc production. In doing so, a novel electrochemical technique, utilizing UPD of Zn on Pt, was developed to assist in estimating the kinetic parameters for zinc electrodeposition. This technique may be employed to study the kinetics of electrodeposition of other reactive metals, such as for thallium or cadmium, which both UPD on Au, Ag, Cu and Pt. Zinc electrodeposition morphology is known to be extremely sensitive to the presence of both inorganic impurities and organic additives. In terms of the study of zinc electrodeposition kinetics, the technique developed should be applied to determine how additives and impurities affect zinc deposition kinetics in conventional zinc electrolytes or one obtained by solvent extraction.

The Radiotracer method might be used to determine whether hydrogen sulphate adsorption on metallic zinc is related to the adverse effect of acid on the kinetics of zinc deposition. The technique principally involves detecting radioactive decay emissions from an adsorbed species at an electrode surface [147]. In order to apply the technique for the stated purpose, the supporting electrolyte would be prepared with an anion species, such as ClO_4^-, which does not specifically adsorb onto zinc. The zinc electrode would then be polarization in the potential region of metallic zinc stability, followed by injection of a small quantity of a hydrogen sulphate species containing an isotope such as ^{35}S. If hydrogen sulphate were to adsorb onto electrode, then the count rate of its radioactive decay would be detected to increase, according to the degree of electrode coverage. The count rate, and hence electrode coverage, could also be examined as a function of applied potential.

Presently, there is a lack of reliable data to estimate the distribution of ohmic drop in a zinc electrowinning cell, which should be examined prior to operating at current densities that are higher than *ca.* 500 A m^{-2}. The limiting gas void fraction and bubble distribution under conditions of industrial zinc electrowinning should be measured experimentally as a function of electrolyte composition and operating current density. The design of the experimental cell should be as close to an actual industrial cell as possible, in order to avoid scale-up issues given the reported lack of reproducible experiments [158]. The experimental apparatus should also include a provision to include the use of forced convection.

Kelsall and Li [162] have previously solved the steady state flux equations for each species in zinc electrowinning, by the finite element method, in order to generate predictions of the 2-D spatial current distribution. The reported results, with respect to enhanced zinc deposition at electrode edges, were in good agreement with industrial experience. It is worth updating the predictions of this model to include the vertical potential distribution due to accumulated bubbles and role of forced convection, once these elements have been experimentally established. Also, the model should also be altered to include provisions to calculate current inefficiencies due to oxygen reduction, which appears in Appendix H, as well as the anodic overpotential for oxygen evolution using alternative anode materials, which appears in Appendix I.

Ultimately, a more thorough understanding of zinc electrodeposition should lead to the modification of existing zinc electrowinning plants or design of new reactors to lower the energy demands of zinc production.

Nomenclature

Symbol	Physical Meaning	Units
F	Faraday constant, 96 485	C mol^{-1}
k	Boltzmann constant, 1.38062×10^{-23}	J K^{-1}
N_A	Avogadro number, 6.0221367×10^{23}	mol^{-1}
R	(a) Universal Gas constant, 8.31441	J mol^{-1} K^{-1}
a	Tafel constant	V
ai	Activity of species I	1
a_i	Ionic size parameter of species I	m
A	Debye-Hückel constant	mol$^{-1/2}$ kg$^{1/2}$
A_e	Electrode Area	m^2
A_x	Cross-sectional area between electrodes	m^2
A_o	Arrhenius distribution constant	C mol^{-1} m s^{-1}
b	Tafel slope	V dec^{-1}
B	Debye-Hückel parameter	m^{-1}
CPE	Constant phase element	S$^{1/\xi}$
d	Interatomic distance	m
dec	Order of magnitude	1
D_i	Diffusion coefficient of species I	m^2 s^{-1}
E	Electrode potential versus reference electrode	V
E°	Equilibrium electrode potential under standard conditions vs. reference electrode	V
f	(a) Crystallographic misfit (b) Frequency (c) Void fraction in electrolyte due to bubbles	1 s^{-1} 1
f_l	Limiting voidage in electrolyte due to bubbles	1
f_m	Mean void fraction in electrolyte due to bubbles	1
$[i]$	Electrolyte concentration of species I	mol dm^{-3}
i	Imaginary number	$\sqrt{-1}$
I	Electric Current	A
I_m	Molal ionic strength	1
j	Current density	A m^{-2}
j_{lim}	Limiting current density	A m^{-2}
j_o	Exchange current density	A m^{-2}
k_m	Mass transport rate coefficient	m s^{-1}
k_0	Standard exchange current density	A m^{-2}
K	(a) Stoichiometric molal equilibrium constant (b) Constant relating mass transfer rate to gas evolution rate at a gas evolving electrode	1 1
l	Inter-electrode gap	m
m_i	Molal concentration of species I	mol kg^{-1}
M_i	Molar mass of species I	g mol^{-1}

n	(a) Number of electrons transferred in rate determining step (b) Exponent applied to gas evolution rate in correlation of mass transport coefficient to gas evolution rate at a gas evolving electrode	1 1
N_o	Collection efficiency of a RRDE	1
P	Pressure	Pa
OPD	Overpotential deposition	
Q	Electrical Charge	C
r	Radius of an electrode	m
R	(b) Resistance	Ω
R_e	Reynolds number	1
t	Time	s
t_i	Transport number of species I	1
T	Absolute temperature	K
U	Electrochemical reactor terminal voltage	V
UPD	Underpotential deposition	
u^o_g	Superficial gas velocity	$m\ s^{-1}$
u^o_l	Superficial liquid velocity	$m\ s^{-1}$
u_{sw}	Rise velocity of a bubble swarm	$m\ s^{-1}$
u_s	Limiting rise velocity of a gas	$m\ s^{-1}$
w	Width	m
$y\pm$	Stoichiometric mean molar activity coefficient	1
z_i	Charge number of species I	1
α	(a) Transfer coefficient (b) Fraction of a salt dissociated	1 1
β	Product of transfer coefficient, α, and number of electrons transferred in rate determining step, n.	1
β_{MX}	Pitzer Model second viral coefficient for interactions of oppositely charged ions, M and X.	1
C^{ϕ}_{MX}	Pitzer Model third viral coefficient describing ion triplet formation.	1
$\theta_{MM'}$, $\theta_{XX'}$	Pitzer Model terms which account for interactions between like charged ions, where $M \neq M'$ and $X \neq X'$.	1
$\psi_{MM'X}$, $\psi_{XX'M}$	Pitzer Model terms which account for the modifying influence of an oppositely charged ion on θ interactions	1
γ_i	Molal activity coefficient of species I	1
$\gamma\pm$	Stoichiometric mean molal activity coefficient	1
δ	Diffusion layer thickness	m
ΔG	Molar change in Gibbs free energy	$J\ mol^{-1}$
ΔG°	Molar change in Gibbs free energy under standard conditions	$J\ mol^{-1}$
η	(a) Overpotential (b) Absolute viscosity	V $kg\ m^{-1}\ s^{-1}$
λ_i	Equivalent conductivity of species I	$m^2\ \Omega^{-1}\ eq.^{-1}$
λ_i^o	Equivalent conductivity of species i at infinite dilution	$m^2\ \Omega^{-1}\ eq.^{-1}$
ν	Kinematic viscosity	$m^2\ s^{-1}$

ν_i	Number of ions of species i formed by complete dissociation of a unit of salt	1
ρ	Density	kg dm^{-3}
σ	Electrolyte specific conductivity	Ω^{-1} m^{-1}
σ'	Effective conductivity	Ω^{-1} m^{-1}
ϕ	Molal Osmotic Coefficient	1
Φ_e	(Fractional) Current efficiency	1
χ	Inverse radius of an ion cloud	m^{-1}
χ^2	Chi-square statistical parameter	1
ω	Rotation speed of electrode	rad s^{-1}
ξ	Power term of Constant Phase Element	1

References

1 A.J. Bard (Ed.), Encyclopedia of Electrochemistry of the Elements, Vol. 5, Marcel Dekker Inc., New York, NY, U.S.A., pg. 51, (1986).

2 R.M. Grant, in H.Y. Sohn (Ed.), Metallurgical Processes for Early Twenty-First Century: Proceedings of the Second International Symposium on Metallurgical Processes for the Year 2000 and Beyond, TMS, Warrendale, PA, U.S.A., pp. 125-149, (1994).

3 G. Diaz, D. Martin, C. Frias, and F.Sanchez, *JOM*, **53**(12), pp. 30-31, (2001).

4 M. Bestetti, U. Ducati, G.H. Kelsall, G. Li, and E. Guerra, *Can. Metall. Q.*, **40**(4), pp. 451-458 (2001).

5 E.R. Cole, and T.J. O'Keefe, Insoluble Anodes for Electrowinning Zinc and Other Metals, United States Bureau of Mines Investigation, No. 8531, (1981).

6 K.R. Koziol and E.F. Wenk, *Schiftenreiche der GDMB Gesellschaft Deutscher Metallhutten und Bergleute*, **37**, pp. 409-428, (1982).

7 K. Mushiake K., N. Masuko, and M. Takahashi, *Metallurgical Review of MMIJ*, **2**(2), pp. 35-51, (1985).

8 Y. Liu, L. Wu, and B. Yuan, *Youse Jinshu*, **37**(3), pp. 53-8, (1985).

9 E.A. Kalinovskii, V.L. Moskalevich, O.A. Khan, and N.I. Ful'man, *Tsvetn. Met*, 3, pp. 16-19, (1974).

10 G.H. Kelsall, E. Guerra, G. Li, and M Bestetti, in, F.M. Doyle and R. Woods (Eds.), Proceedings of the Fifth International Symposium on Electrochemistry in Mineral and Metal Processing, The Electrochemical Society, Pennington, NJ, U.S.A., pp. 326-337. (2000).

11 G.W. Barton, and A.C. Scott, *J. Appl. Electrochem.*, **22**, pp. 104-115, (1992).

12 F.C. Walsh, A First Course in Electrochemical Engineering, The Electrochemical Consultancy, Romsey, UK, (1993).

13 F. Ajersch, D. Mathieu, and D.L. Piron, *Canadian Metallurgical Quarterly*, **24**(1), pp. 53-63, (1985).

14 A.C. Fisher, in Electrode Dynamics, Oxford University Press, Oxford, U.K., pg. 6, (1996).

15 E.J. Frazer, and I.C. Hamilton, *J. Appl. Electrochem.*, **16**, pp. 387-392, (1986).

16 L. Mirkova, Ch. Tsvetkova, and S. Rashkov, S., *Trans. Inst. Met Finish.*, **74**(5), pp. 173-176, (1996).

17 L. Mirkova, Ch. Tsvetkova, I. Krastev, M. Monev, and S. Rashkov, *Trans. Inst. Met Finish.*, 73(2), pp. 44-47, (1995).

18 A.C. Beshore, B.J. Flori, G. Schade, and T.J. O'Keefe, *J. Appl. Electrochem.*, **17**, pp. 765-772, (1987).

19 A.J. Appelby, M. Chimla, H. Kitna, and G. Bronoël in A.J. Bard (Ed.), Encyclopedia of Electrochemistry of the Elements, Vol. 9, Part A, Marcel Dekker Inc., New York, NY, U.S.A., (1982).

20 D.J. MacKinnon, J.M. Brannen and P.L. Fenn, *J. Appl. Electrochem.*, **17**, pp. 1129-1143, (1987).

21 I.W. Wark, *J. Appl. Electrochem.*, **9**, pp.721-730, (1979).

22 D.R. Fosnacht, and T.J. O'Keefe, *J. Appl. Electrochem.*, **10**, pp. 495-504, (1980).

23 H. Fukushima, T. Akiyama, and K. Kiyotani, Metallurgical Review of MMIJ, **11**(2), pp. 16-25, (1994).

24 A.A. Salin, *Tsvetn. Met*, 34(8), pp. 28-33, (1961).

25 E.J. Frazer, and T. Lwin, *J. Appl. Electrochem.*, **17**, pp. 453-462, (1987).

26 T. Biegler, and E.J. Frazer, *J. Appl. Electrochem.*, **16**, pp. 654-662, (1986).

27 A.C. Scott, R.M. Pitblado, and G.W. Barton, *J. Appl. Electrochem.*, **18**, pp. 120-127, (1988).

28 I.W. Wark, in J.A. Friend and F. Gutman (Eds.), Proceedings of the first Australian Conference on Electrochemistry, held in Sydney, 13-15th February and Hobart, 18-20th February 1963, Pergamon Press, London, U.K., pg. 889-900, (1965).

29 G.C. Bratt in, Papers Presented and the Tasmania Conference, 1977, Australasian Institute of Mining and Metallurgy, Victoria, Australia, pp. 277-290, (1977).

30 R. Cachet, and R. Wiart, *Electrochim. Acta*, **44**, pp. 4743-4751, (1999).

31 V.V. Stender, *Tr. Leningr. Politekhn. Inst.*, **239**, 126-146, (1964).

32 K.J. Cathro, in R. Woods, and P.E. Richardson (Eds.), Proceedings of the Third International Symposium on Electrochemistry in Mineral and Metal Processing III, Electrochemical Society, Pennington, NJ, U.S.A., pp. 546-64, (1992).

33 A. Weymeersch, R. Winand, and L. Renard, *Plat. Surf. Finish.*, **68**(4), pp. 56-59, (1981).

34 R. DeLevie, in P. Dehlaney (Ed.), Advances in Electrochemistry and Electrochemical Engineering, Vol. 6, Interscience Publishers, Inc., New York, NY, U.S.A., pg. 341, (1967).

35 I. Epelboin, M. Ksouri, and R. Wiart, *J. Electrochem. Soc.*, **122**(9), pp. 1206-1214, (1975).

36 J. Bressan, and R. Wiart, *J. Appl. Electrochem.*, **7**, pp. 505-510, (1977).

37 J.T. Clark, and N.A. Hampson, *J. Electroanal. Chem. Interfacial Electrochem.*, 26, pp. 307-318, (1970).

38 L. Sziráki, and L. Kiss, *ACH Models in Chemistry*, **132**(4), pp. 653-671, (1995).

39 R. Cachet, and R. Wiart, *J. Appl. Electrochem.*, **20**, pp. 1009-1014, (1990).

40 I. Zouari, and F. Lapique, *Electrochim. Acta*, **37**(3), pp. 439-446, (1992).

41 V.D. Jović, J.N. Jovićević, M.G. Pavlović, and R.M. Stevanović, *J. Serb. Chem. Soc.*, **55**(6), pp. 341-351, (1990).

42 V. Jiricny, H. Choi, and J.W. Evans, *J. Appl. Electrochem.*, **17**, pp. 91-103, (1987).

43 D.J. MacKinnon, and J.M. Brannen, *J. Appl. Electrochem.*, **16**, pp. 127-133, (1986).

44 T. Xue, W.C. Cooper, R. Pascual, and S. Saimoto, *J. Appl. Electrochem.*, **21**, pp. 231-237, (1991).

45 P Gu, R. Pascual, M. Shirkhanxadeh, S. Saimoto, and J.D. Scott, *Hydrometallurgy*, **37**, pp. 261-281, (1995).

46 R. Cachet, and R. Wiart, *J. Electrochem Soc.*, **141**(1), pp. 131-140, (1994).

47 G.H. Kelsall, unpublished work presented at the Zinc Producers Meeting, (1999).

48 H.H. Uhlig, J.S. MacNairn, and D.A. Vaugn, *Acta Metall.*, **3**, pp. 302-304, (1955).

49 R. Lackmann, and D. Linsel, *Izvestiia Po Khimiia*, **11**(3/4), pp. 345-349, (1978).

50 K.I. Popov, M.G. Pavlović, M.D. Spasojević, and N.M. Nakić, *J. Appl. Electrochem.*, **9**, pp. 533-536, (1979).

51 A.R. Despić, and M.G. Pavlović, *Electrochim. Acta*, **27**(11), 1539-1549, (1982).

52 F.J. Fabri-Miranda, O.E. Barcia, O.R. Mattos, and R. Wiart, *J. Electrochem. Soc.*, **144**(10), pp. 3441-3449, (1997).

53 A. Aramata, Md.A. Quaiyyum, W.A. Balais, T. Atoguchi, and M. Enyo, *J. Electroanal. Chem.*, **338**, pp. 367-372, (1992).

54 Md.A. Quaiyyum, A. Aramata, S. Moniwa, S. Taguchi, and M. Enyo, *J. Electroanal. Chem.*, **373**, pp. 61-66, (1994).

55 S. Taguchi, and A. Aramata, *J. Electroanal. Chem.*, **396**, pp. 131-137, (1995).

56 A. Aramata, S. Terui, S. Taguchi, T. Kawaguchi, and K. Shimazu, *Electrochim. Acta*, **41** (5), pp. 761-765, (1996).

57 G. Horányi, and A. Aramata, *J. Electroanal. Chem.*, **434**, pp. 201-207, (1997).

58 A. Aramata, S. Taguchi, T. Fukuda, M. Nakamura, and G. Horanyi, *Electrochim. Acta*, **44**, pp. 999-1007, (1998).

59 S. Taguchi, and A. Aramata, *J. Electroanal. Chem.*, **457**, pp. 73-81, (1998).

60 K. Igarashi, A. Aramata, and S. Taguchi, *Electrochim. Acta*, **46**, pp. 1773-1781, (2001).

61 G. Staikov, and W.J. Lorenz, *Z. Phys. Chem.*, **208**, pp. 17-42, (1999).

62 E. Budevski, G. Staikov, and W.J. Lorenz, *Electrochim. Acta*, **45**, pp. 2559-2574, (2000).

63 W. Lehnert, and W. Schmickler, *J. Electroanal. Chem.*, 310, pp. 27, (1991).

64 C. Sanchez, and E. Leiva, *J. Electroanal. Chem.*, **458**, pp. 183-189, (1998).

65 Z. Moser, *J. Phase Equilib.*, **12**(4), pp. 439-443, (1991).

66 V.S.K. Nair, and G.H. Nancollas, *J. Chem. Soc.*, pp. 3706-3710, (1958).

67 K.S. Pitzer, *J. Chem. Soc., Faraday Trans. 2*, **68**(1), pp. 101-113, (1972).

68 S. Waslykiewicz, *Fluid Phase Equilib.*, **57**, pp. 277-296, (1990).

69 F. Malatesta, and R. Zamboni, *J. Sol. Chem.*, **26**(8), pp.791-815, (1997).

70 J.G. Albright, J.A. Rard, S. Serna, E.E. Summers, and M.C. Yang, *J. Chem. Thermodyn.*, **32**, pp. 1447-1487, (2000).

71 A.C. Hayes, P. Kruus, and W.A. Adams, *J. Sol. Chem.*, **13**(1), pp. 61-75, (1984).

72 W.W. Rudolph, M.H. Brooker, and P. Tremaine, *J. Sol. Chem.*, **28**(5), pp. 621-630, (1999).

73 R.M. Izatt, D. Eatough, J.J. Christensen, and C.H. Bartholomew, *J. Chem. Soc. A*, pp. 49-53, (1969).

74 J.W. Larson, *J. Phys. Chem.*, **74**(18), pp. 3392-3396, (1970).

75 G.R. Hedwig, and H.K.J. Powell, *J. Chem. Soc. Dalton*, pp. 798-801, (1973).

76 S. Katayama, *J. Sol. Chem.*, **5**(4), pp. 241-249, (1976).

77 J.T. Hinatsu, V.D. Tran, and F.R. Foulkes, *J. Appl. Electrochem.*, **22**, pp. 215-223, (1992).

78 E.M. Hanna, A.D. Pethybridge, and J.E. Prue, *Electrochim. Acta*, **16**, pp. 677-686, (1971).

79 H. Yokoyama, and H. Yamatera, *Bull. Chem. Soc. Jpn.*, **54**(8), pp. 2286-2289, (1981).

80 K.S. Pitzer, Activity Coefficients in Electrolyte Solutions, 2nd ed., CRC Press, Boca Raton, FL, U.S.A., (1991).

81 J.K. Hovey, K.S. Pitzer, and J.A. Rard, *J. Chem. Thermodynamics*, 25, pp. 173-192, (1993).

82 C.F. Baes, E.J. Reardon, and B.A. Moyer, *J. Phys. Chem.*, **97**, pp. 12343-12348, (1993).

83 E.J. Reardon, *J. Phys. Chem.*, **93**(11), pp. 4630-4636, (1989).

84 E.J. Reardon, and R.D. Beckie, *Geochim. Cosmochim. Acta*, **51**(9), 2355-2368, (1987).

85 H. Klocker, C.I. Sainz-Diaz, B. Wachter, H.J. Bart, and R. Marr, in D.C. Shallcross, R. Paimin, and L.M. Prycic (Eds.), Proceedings of the International Solvent Extraction Conference – ISEC '96, University of Melbourne, Melbourne, Australia, pp. 617-622, (1996).

86 H. Majima Y. Awakura, and Y. Kawasaki, Activities of water and solutes in the aqueous solution systems H_2SO_4-$M_x(SO_4)_y$ and HCl-MCl_x, Agne Shofu Publishing Inc., Tokyo, Japan, (1988).

87 H.V. Tartar, W.W. Newschwander, and A.T. Ness, *J. Am. Chem. Soc.,* **63**, pp. 28-36, (1941).

88 Z. Horváth, and J. Wéber, *Acta Tech. Acad. Sci. Hung.*, **56**(1-2), pp. 55-64, (1966).

89 D. Filippou, G.P. Demopoulos, and V.G. Papengelakis, *AIChE J.*, **41**(1), pp. 171-184, (1995).

90 W. Wang, and D.B. and Dreisinger, *Met Trans. B*, **29**, pp. 1157-1166, (1998).

91 A.G. Dickson, D.J. Wesolowski, D.A. Palmer, and R.E. Mesmer, *J. Phys. Chem.*, **94**, pp. 7978-1985, (1990).

92 J.T. Hinatsu, and F.R. Foulkes, *J. Electrochem. Soc.*, **136**(1), pp. 125-132, (1989).

93 J.G. Albright, and D.G. Miller, *J. Sol. Chem.*, **4**(9), pp. 809-816, (1975).

94 Y. Awakura, T. Doi, T., H. and Majima, *Met Trans. B*, **19**, pp. 5-12, (1988).

95 H.M. Wang, S.F. Chen, T.J. O'Keefe, M. Degrez, and R. Winand, *J. Appl. Electrochem.*, **19**, pp. 174-182, (1989).

96 A.Y. Hosny, T.J. O'Keefe, J.W. Johnson, and W.J. James, *J. Appl. Electrochem.,* **21**, pp. 785-792, (1991).

97 K.J. Cathro, *J. Electrochem. Soc.*, **139**(8), pp. 2186-2192, (1992).

98 V.A Ettel, B. Tilak, and A.S. Gendron, *J. Electrochem. Soc.*, **121**(7), pp. 867-872, (1974).

99 T. Subbaiah, S.C. Das, and R.P. Das, *Erzmetall*, **41**(10), pp. 518-522, (1988).

100 F. Furuya, and T. Sakakibara, *J. Appl. Electrochem.*, **26**, pp. 58-62, (1996).

101 V.G. Levich, Physicochemical Hydrodynamics, 2nd ed., Prentice-Hall Inc., Englewood Cliffs, New Jersey, U.S.A., pp. 60-78, (1962).

102 M.I. Alkatsev, and I.H. Kabisov, *Soviet Non-Ferrous Metals Research*, **9(1)**, pp. 30-34, (1981).

103 Y. Umetsu, Q. Su, and K. Tozawa, *J. Min. Metall. Inst. Japan*, **104**(11), pp. 829-836, (1988).

104 B.E. Conway, and J. O'M. Bockris, Proc. R. Soc. London, Ser. A , **248**, pp. 394-403, (1958).

105 V.V. Losev, in B.E. Conway and J. O'M, Bockris (Eds.), Modern Aspects of Electrochemistry, Plenum Press, New York, NY, U.S.A., pg. 318, (1972).

106 P. Dehlaney, in P. Dehlaney (Ed.), Advances in Electrochemistry and Electrochemical Engineering, Vol. 1, Interscience Publishers, Inc., New York, NY, U.S.A., pg. 238, (1961).

107 T. Hurlen, and T.R. Breivik, *Acta Chem. Scand.*, **32**, pp. 447-453, (1961).

108 J. Bressan, and R. Wiart, *J. Appl. Electrochem.*, **9**, pp. 615-621, (1979).

109 M.D. Pritzker, and T.Z. Fahidy, *J. Electrochem Soc.*, **136(8)**, 2238-2250, (1989).

110 M.D. Pritzker, and T.Z. Fahidy, *J. Electrochem Soc.*, **136(12)**, 3602-3607, (1989).

111 G.M. Budov, and V.V. Losev, *Russ. J. Phys. Chem.*, **37**(7), pp. 784-787, (1963).

112 G.L.M.K.S. Kahanda, and M. Tomkiewicz, *J. Electrochem Soc.*, **136(5)**, 1497-1502, (1989).

113 R. Parsons, Handbook of Electrochemical Constants, Butterworths, London, U.K., (1959).

114 H.B. Sierra-Alcazar, and J.A. Harrison, *Electrochim. Acta*, **22**, pp. 627-630, (1977).

115 I. Epelboin, M. Ksouri, and R. Wiart, *Faraday Symposia of the Chemical Society*, **12**, pp. 115-125, (1978).

116 J. Bressan, and R. Wiart, *J. Electroanal. Chem.*, **107**, pp. 233-245, (1980).

117 P.L. Cavallotti in, unpublished short course on electrochemistry, Department of Applied Physical Chemistry, Polytechnic of Milan.

118 B.C. Tripathy, S.C. Das, P. Singh, and G.T. Hefter, *J. Appl. Electrochem.*, **29**, pp. 1229-1235, (1999).

119 D.A. Payne, and A.J. Bard, *J. Electrochem Soc.*, **119(12)**, 1665-1673, (1972).

120 W.J. Albery, and M.L. Hitchman, Ring-disc Electrodes, Clarendon Press, Oxford, U.K., pp. 18-22, (1971).

121 D.E. Harris, Quantitative Chemical Analysis, 2nd ed., W.H. Freeman and Co., New York, NY, U.S.A., (1987).

122 D.J. MacKinnon, and P.L. Fenn, *J. Appl. Electrochem.*, **14**, pp. 707-707, (1984).

123 Bard A.J., and Faulkner L.R., Electrochemical Methods: Fundamentals and Applications, 2nd ed., John Wiley& Sons, Inc., New York, NY, U.S.A., (2001).

124 C.M.A. Brett, and Brett A.M.O, Electrochemistry: principles, methods, and applications, Oxford University Press, Oxford, U.K., (1993).

125 H. Mascaro-Lucia, M.C. Santos, S.A.S. Machado, and L.A. Avaca, J. Brazil. Chem. Soc., **13**(4), pp. 529-534, (2002).

126 A. Lachenwitzer, N. Li, and J. Lipkowski, J. Electroanal. Chem., 532, pp. 85-98, (2002).

127 H.J. Pauling, G. Staikov, and K. Jüttner, *J. Electroanal. Chem.*, **376**, pp. 179-184, (1994).

128 U. Schmidt, S. Vinzelberg, and G. Staikov, *Surf. Sci.*, **348**, pp. 261-279, (1996).

129 V.D. Jović, and B.M. Jović, *Electrochim. Acta*, **47**, pp. 1777-1785, (2002).

130 R. Vindu, and S. Hara, *J. Electroanal. Chem.*, **475**, pp. 171-180, (1999).

131 G. Inzelt, and G. Horányi, *J. Electroanal. Chem.*, **491**, pp. 111-116, (2000).

132 D. Carnal, P.I. Oden, U. Müller, E. Schmidt, and H. Siegenthaler, *Electrochim. Acta*, **40** (10), pp. 1223-1235, (1995).

133 J.W. Yan, H. Tang, Y.Y. Yang, J.W. Wu, Z.X. Xie, S.G. Sun, and B.W. Mao, *Surf. Interface Anal.*, **32**, pp. 49-52, (2001).

134 S. Swathirajan, and S. Bruckenstein, *J. Electrochem. Soc.*, **129** (6), pp. 1202-1210, (1982).

135 G. Casalone, and G.F.Tantardini, *J. Chem. Soc. Faraday Trans.*, **86**(22), pp. 3793-5, (1990).

136 W.H. Mulder, J.H. Sluyters, T. Pajkossy, and L. Nyikos, *J. Electroanal. Chem. Interfacial Electrochem.*, **285**(1-2), pp. 103-15, (1990).

137 S.L. Clegg, J.A. Rard, and K.S. Pitzer, *J. Chem. Soc. Faraday Trans.*, **90**(13), pp. 1875-1894, (1994).

138 G.R. Salvi, and A.J. de Bethune, *J. Electrochem. Soc.*, **108**, pp. 672-676, (1961).

139 K.S. Pitzer, R.N. Roy, and L.F. Silvester, *J. Am. Chem. Soc.*, 99(15), pp. 4930-4936, (1977).

140 Weast, R.C., (Ed.), CRC Handbook of Chemistry and Physics, 70th Edition, CRC Press, Boca Raton, FL, U.S.A., (1990).

141 F.R. Foulkes in, unpublished course notes for Electrochemistry 553, University of Toronto, Canada, (1998).

142 M. Imamura, M., and J.M. Toguri, *Met Trans. B*, **25**, 637-644, (1994).

143 D.C. Montgomery, Design and Analysis of Experiments, 4th Ed. John Wiley & Sons Inc., New York, NY, U.S.A., (1997).

144 R DeLevie, J. Electroanal. Chem., **281**, pp.1-21, (1990).

145 A. Weymeersch, R. Winand, and L. Renard, *Plat. Surf. Finish.*, **68**(5), pp. 118-120, (1981).

146 F.J. Fabri Miranda, O.E. Barcia, O.R. Mattos, and R. Wiart, *J. Electrochem. Soc.*, **144**(10), pp. 3449-3457, (1997).

147 P. Joó and G. Horányi, J. Colloid Interface Sci., **223**, pp. 308-310, (2000).

148 J. Dukovic, and C.W. Tobias, *J. Electrochem. Soc.*, **134**(2), pp. 331-43, (1987).

149 J.P. Glas, and J.W. Westwater, *Int. J. Heat Mass Transfer*, 7, pp. 1427-1443, (1964).

150 H. Vogt, in E. Yeager, J.O'M. Bockris, B.E. Conway, and S. Sarangapani, (Eds.), Comprehensive Treatise of Electrochemistry, Vol. 6, Plenum Press, New York, NY, U.S.A., pp. 445-487, (1983).

151 J. Eigeldinger, and H. Vogt, Electrochim. Acta, **45**, pp. 4449-4456, (2000).

152 J.A. Gonzalez-Dominguez, Private Communication, (2000).

153 L.J.J. Janssen and G.J. Visser, *J. Appl. Electrochem.*, **21**, pp. 386-394. (1991).

154 K. Tozawa, Y. Umetsu, and Q. Su, in I.G. Mathew (Ed.), Proceedings of International Symposium - World Zinc '93, Australian Institute of Mining and Metallurgy Conference, Hobart, Tazmania, pp. 267-272, (1993).

155 Noranda Inc., Correlation presented at the *Zinc Producers Group Meeting*, Trail, B.C., Canada, (1999).

156 A.F. Nikiforov, and E.L. Natarova, *The Soviet Journal of Non-Ferrous Metals*, pg. 27, (1971).

157 J.T. Hinatsu, V.D. Tran, and F.R. Foulkes, *J. Appl. Electrochem.*, **22**, pp. 215-223, (1992).

158 E.L.J. Coenen, and L.J.J. Janssen, *J. Appl. Electrochem.*, **27**, pp. 1143-1148, (1997).

159 G. Kreysa, and M. Kuhn, *J. Appl. Electrochem.*, **15**, pp. 517-526, (1985).

160 G.H. Kelsall, Private Communication, (2003).

161 H. Kellermann, K. Juettner, and G Kreysa, *J. Appl. Electrochem.*, **28**(3), pp. 311-319, (1998).

162 G.H. Kelsall, and G. Li, in, F.M. Doyle and R. Woods (Eds.), Proceedings of the Fifth International Symposium on Electrochemistry in Mineral and Metal Processing, The Electrochemical Society, Pennington, NJ, U.S.A., pp. 303-314, (2000).

Appendix A: Derivation of the Extended Butler-Volmer Equation for a Simple Metal Deposition/Dissolution Reaction

Consider the general metal deposition/dissolution reaction between a metal ion in solution, M^{n+}, and its metallic state, M.

$$M^{n+} + ne^{-M} \longleftrightarrow M \qquad \text{Eq 1}$$

Kinetically, the reaction will be considered to occur in two steps [1]. The first step is a change in state of the metal ion as it passes between the solution, M^{n+}, and the metal phase, M^{n+M}, through an intermediate activated state, M^{n+*}. The second step is the reaction between the metal ion in the metal phase and 'n' electrons to produce the condensed metal phase.

$$M^{n+} + ne^{-M} \xleftrightarrow{Step\,1} M^{n+M} + ne^{-M} \xleftrightarrow{Step\,2} M \qquad \text{Eq 2}$$

The electrochemical potentials, $\overline{\mu}$ (J mol^{-1}), for the three metal species are given as follows:

$$\overline{\mu}^{M}_{M^{n+}} = \mu^{M}_{M^{n+}} + nF\phi^{M} \qquad \text{Eq 3}$$

$$\overline{\mu}_{M} = \mu_{M} \qquad \text{Eq 4}$$

$$\overline{\mu}^{S}_{M^{n+}} = \mu^{S}_{M^{n+}} + nF\phi^{S} \qquad \text{Eq 5}$$

where; μ (J mol^{-1}) is the chemical potential, and nFϕ (J mol^{-1}) is the electrical potential.

The reaction of the ions in the metal phase with the electrons is considered to be rapid and, thus, the metal ions in the metal phase are assumed to be in equilibrium with the metal phase, i.e. they have the same potentials.

$$\overline{\mu}^{M}_{M^{n+}} = \mu_{M} \qquad \text{Eq 6}$$

At this point, neither the solution nor the metal have a net charge, and thus, the electrical potentials terms, $nF\phi^{S}$ and $nF\phi^{M}$, are equal to zero. The electrochemical potential difference between the between the metal ions in metal and the metal ions in solution is, therefore, equal to the difference in chemical potential between the metal and metal ions in solution.

$$\Delta\overline{\mu} = \Delta\mu = \mu_M - \mu^S_{M^{n+}} \qquad \text{Eq 7}$$
$$= \mu^\circ_M + RT\ln(aM) - \left(\mu^\circ{}_{M^{n+}} + RT\ln\left(aM^{n+}\right)\right)$$
$$= \Delta\mu^\circ - RT\ln\left(\frac{aM^{n+}}{aM}\right)$$

where; $\Delta\mu$ is the change in chemical potential, $\Delta\mu^o$ (J mol^{-1}) is the standard change in chemical potential on the molal scale, and aM^{n+} and aM are the molal activities of the metal ion and metal, respectively. The molal activity of the metal ion is related to its molality, mM^{n+}, through the molal activity coefficient, γM^{n+}, as follows:

$$aM^{n+} = mM^{n+}\gamma M^{n+} \qquad \text{Eq 8}$$

The rate determining step, and the overall reaction rate, is modelled as changes of state of the metal ion as it passes between the solution and the metal phase through an intermediate activated state. This concept is illustrated in Fig 1.

$$M^{n+} \underset{k_{an}}{\overset{k_{cat}}{\rightleftarrows}} M^{n+M} \leftrightarrow M \qquad \text{Eq 9}$$

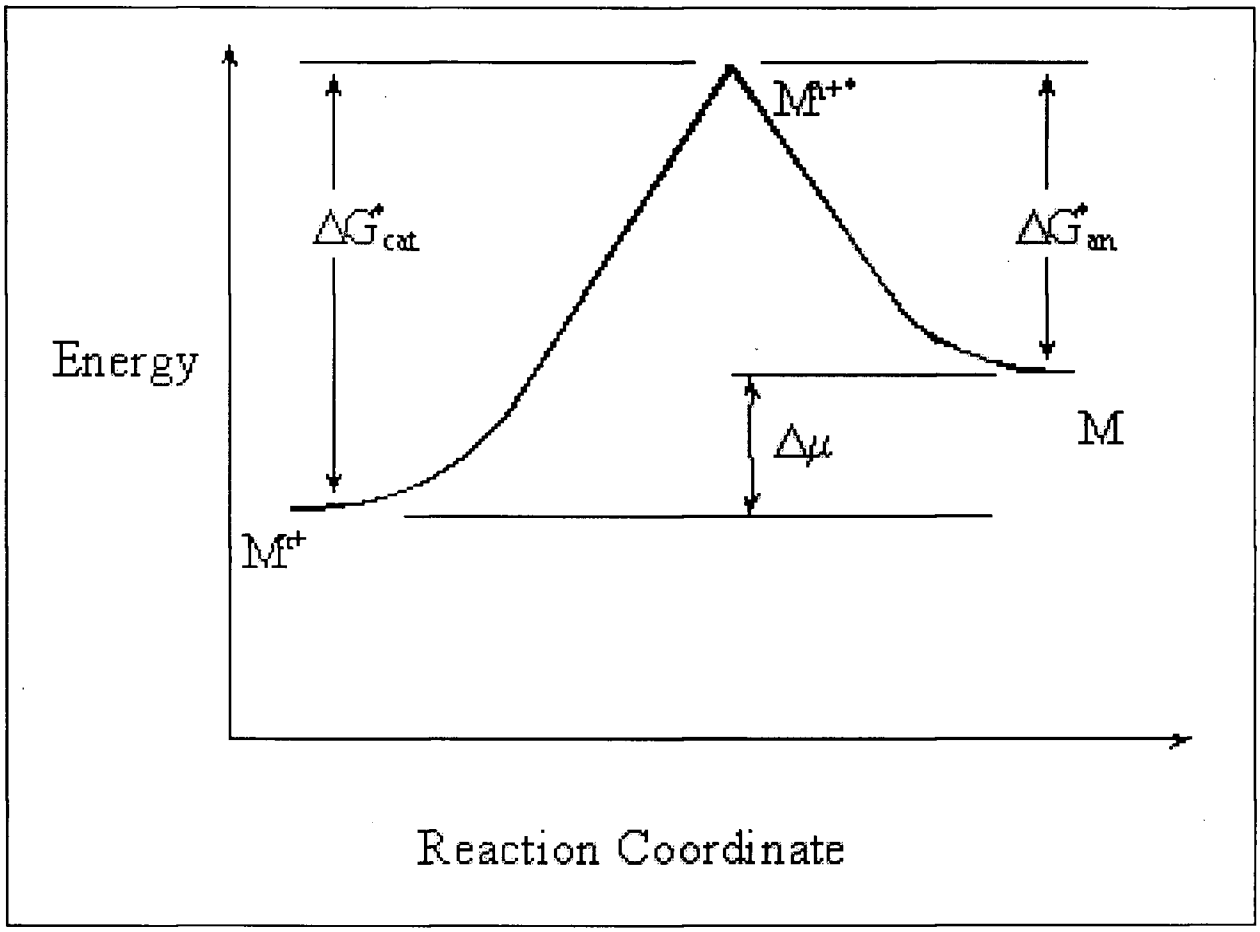

Fig 1: Reaction coordinate diagram of a metal deposition/dissolution reaction at an unpolarized metal surface.

The fluxes corresponding to the cathodic and anodic reactions may be modelled as simple first order reactions [1]:

$$\frac{d\left(\frac{M^{n+}}{V_{cat}}\right)}{dt} = -k_{cat}[M^{n+}] \qquad \text{Eq 10}$$

$$\frac{d\left(\frac{M}{V_{an}}\right)}{dt} = \frac{d\left(\frac{M^{n+M}}{V_{an}}\right)}{dt} = -k_{an}[M] \qquad \text{Eq 11}$$

where; $[M^{n+}]$ (mol m^{-3}) is the concentration of metal ions at the Outer Helmholz Plane, OHP, of the metal surface, $[M]$ (mol m^{-3}) is the concentration of metal ions in the metal phase, k_{cat} and k_{an} (s^{-1}) are the cathodic and anodic rate constants, and V_{cat} and V_{an} (m^3) are the volume elements through which the cathodic and anodic fluxes pass.

The OHP represents the closest distance of approach of the centre of the, fully complexed, metal ion in solution. This concept, as well the nature of the, partly complexed, activated metal ion species, are illustrated in Fig 2.

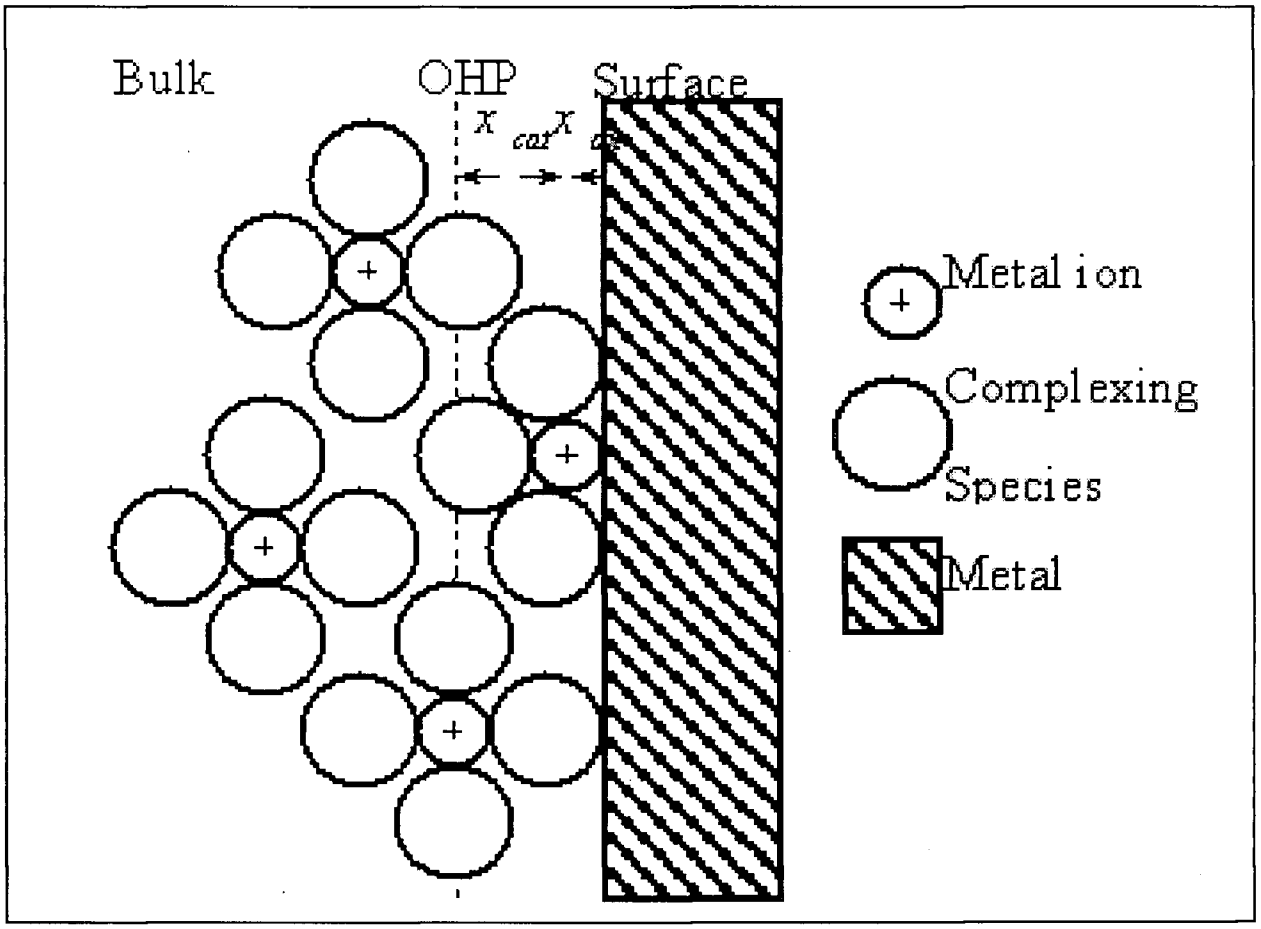

Fig 2: Representation of a metal/solution interface.

For a planar electrode of surface area A_e, m^2, V_{cat} and V_{an} may be calculated as follows:

$$V_{cat} = A_e x_{an} \qquad \text{Eq 12}$$

$$V_{an} = A_e x_{an} \qquad \text{Eq 13}$$

where; x_{an} (m) is the 1-D change in position of a metal ion resulting from the phase change between the activated metal ion species and the metal ion in the metal phase, and x_{cat} (m) is the 1-D change in position of a metal ion resulting from the phase change between the metal ion in solution and the activated metal ion species.

Overall, the fluxes due to the cathodic and anodic reactions are given by the following expressions:

$$\left(\frac{dM^{n+}}{dt}\right)_{cat} = -A_e x_{cat} k_{cat} [M^{n+}] \qquad \text{Eq 14}$$

$$\left(\frac{dM}{dt}\right)_{an} = -A_e x_{an} k_{an} [M] \qquad \text{Eq 15}$$

Since the anodic reaction results in the production of aqueous ions, the net flux of M^{n+} (mol s^{-1}) is the equal the flux from the cathodic reaction minus the flux of the anodic reaction.

$$\left(\frac{dM^{n+}}{dt}\right)_{rxn} = -A_e x_{cat} k_{cat} [M^{n+}] + A_e x_{an} k_{an} [M] \qquad \text{Eq 16}$$

The net flux of metal ions from the solution to the metal phase due to the electrochemical reaction is related to the net electrical current, I_{net} (A or C s^{-1}), by Faraday's law.

$$\left(\frac{dM^{n+}}{dt}\right)_{rxn} = \frac{I_{net}}{nF} \qquad \text{Eq 17}$$

where; F (96487 C eq^{-1}) is Faraday's constant, and n (eq mol^{-1}) is the number of electrons transferred in the deposition/dissolution reaction.

Implicit in the above equation is that a negative current corresponds to a forward flux of positive ions. Substituting Eq 17 into Eq 16, one obtains the following expression:

$$\frac{I_{net}}{nF} = -A_e x_{cat} k_{cat} [M^{n+}] + A_e x_{an} k_{an} [M] \qquad \text{Eq 18}$$

The above equation is normalized, with respect to the electrode area by rearranging in terms of net current density, j_{net} (A m^{-2}) as follows:

$$j_{net} = \frac{I_{net}}{A} = -nFx_{cat} k_{cat} [M^{n+}] + nFx_{an} k_{an} [M] \qquad \text{Eq 19}$$

The corresponding rate constants for the cathodic and anodic reactions, k_{cat} and k_{an} (s^{-1}), may be evaluated according to the Arrhenius Equation [1].

$$k_{cat} = \frac{kT}{h} e^{\frac{-\Delta G^{*}_{cat}}{RT}} \qquad \text{Eq 20}$$

$$k_{an} = \frac{kT}{h} e^{\frac{-\Delta G^{*}_{an}}{RT}} \qquad \text{Eq 21}$$

where; ΔG^{*}_{cat} and ΔG^{*}_{an} (J mol^{-1}) are the activation energy for the cathodic and anodic reactions, T (K) is the absolute temperature, k (1.381×10^{-23} J s) is the Boltzmann constant, and h (6.626×10^{-34} J K^{-1}) is the Planck constant.

Substituting Eq 21 and Eq 20 into Eq 19 we obtain the final form of the general equation for net current density.

$$j_{net} = -nFx_{cat} \frac{kT}{h} e^{\frac{-\Delta G^{*}_{cat}}{RT}} [M^{n+}] + nFx_{an} \frac{kT}{h} e^{\frac{-\Delta G^{*}_{an}}{RT}} [M] \qquad \text{Eq 22}$$

Consider the polarization of the electrode surface in order to achieve the equilibrium condition such that the difference in electrochemical energy between the metal ion in the metal phase and the metal ion in solution becomes equal to zero and there is no net reaction, as illustrated in Fig 3.

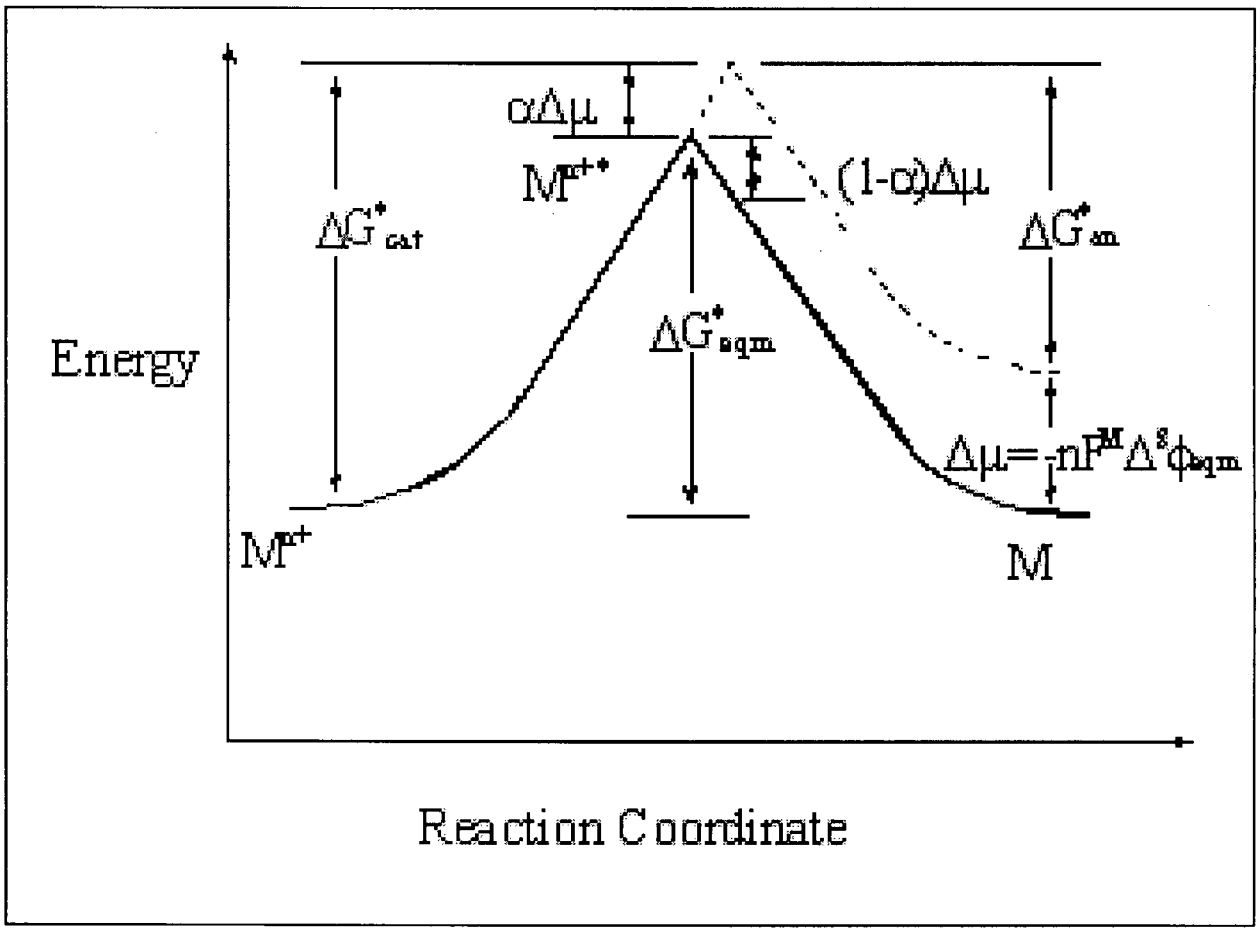

Fig 3: Reaction coordinate diagram of metal deposition/dissolution reaction under equilibrium conditions.

Physically, electrode polarization involves altering the electron density in the metal phase, $\phi^M \neq 0$, which results in an electrical potential difference between the metal and the solution. This condition can be generalized to include the case when both solution and metal have net potentials as follows:

$$nF^M \Delta^S \phi = nF\phi^M - nF\phi^S \qquad \text{Eq 23}$$

The electrical potential difference to achieve equilibrium is given the designation $-nF^M\Delta^S\phi_{eqm}$ (V), and is equal to the chemical potential difference, from Eq 7, as follows:

$$-nF^M \Delta^S \phi_{eqm} = \Delta\mu^\circ - RT \ln\left(\frac{aM^{n+}}{aM}\right) \qquad \text{Eq 24}$$

Rearranging the above equation, we obtain the Nernst Equation.

$$ {}^{M}\Delta^{S}\phi_{eqm} = -\frac{\Delta\mu^{\circ}}{nF} + \frac{RT}{nF}\ln\left(\frac{aM^{n+}}{aM}\right) \qquad \text{Eq 25} $$

This equation often appears in the following, more conventional, form:

$$ E_M = E_M^o + \frac{RT}{nF}\ln\left(\frac{aM^{n+}}{aM}\right) \qquad \text{Eq 26} $$

where; E_M (V) is the equilibrium potential, and E^o_M (V) is the standard reduction potential.

The effect of the polarizing the electrode on the kinetics of the reactions is partitioned between lowering the energy of the metal ion in the metal phase and lowering the energy of the activated metal ion species, by the transfer coefficient, α, which has a value between 0 and 1. At equilibrium the activation energies for the cathodic and anodic reactions are equal, having a value of ΔG^{*}_{eqm} (J mol^{-1}). The corresponding rate constants for the cathodic and anodic reactions, k_{cat} and k_{an}, are equal and may be evaluated according to the Arrhenius Equation.

$$ k_{cat} = k_{an} = \frac{kT}{h} e^{\frac{-\Delta G^{*}_{eqm}}{RT}} \qquad \text{Eq 27} $$

The net current density is obtained by substituting the above expressions into Eq 19.

$$ j_{net} = -nFx_{cat}\frac{kT}{h}e^{\frac{-\Delta G^{*}_{eqm}}{RT}}[M^{n+}] + nFx_{an}\frac{kT}{h}e^{\frac{-\Delta G^{*}_{eqm}}{RT}}[M] = 0 \qquad \text{Eq 28} $$

Under these conditions the currents densities for the forward and reverse reactions are equal and opposite, describing the steady state rate of exchange of metal ions and metal at the electrode surface, and the concentration of metal ions at the electrode surface is equal to its bulk concentration. This current density is termed the exchange current density, j_0, and may be represented as follows:

$$ j_o = nFx_{cat}\frac{kT}{h}e^{\frac{-\Delta G^{*}_{eqm}}{RT}}[M^{n+}]^{bulk} = nFx_{an}\frac{kT}{h}e^{\frac{-\Delta G^{*}_{eqm}}{RT}}[M] \qquad \text{Eq 29} $$

From Fig 3, the activation energy at equilibrium is related to the activation energy for the cathodic reaction of the unpolarized surface, ΔG^*_{cat}, as follows:

$$\Delta G^*_{eqm} = \Delta G^*_{cat} - \alpha\Delta\mu \qquad \text{Eq 30}$$

This activation energy is substituted into the expression for the exchange current density for the cathodic reaction, from Eq 29, as follows:

$$j_o = nFx_{cat}\frac{kT}{h}e^{\frac{-\Delta G^*_{cat}}{RT}}e^{\frac{\alpha\Delta\mu}{RT}}[M^{n+}]^{bulk} \qquad \text{Eq 31}$$

Substituting the change in chemical potential, from Eq 7, into Eq 31 results in the following expression for the exchange current density:

$$j_o = nFx_{cat}\frac{kT}{h}e^{\frac{-\Delta G^*_{cat}}{RT}}e^{\frac{\alpha\Delta\mu^\circ}{RT}}[M^{n+}]^{bulk}\left(aM^{n+}\right)^{-\alpha}aM^{\alpha} \qquad \text{Eq 32}$$

The metal ion concentration may be converted to molarity through the following expression:

$$[M^{n+}] = \rho\frac{mM^{n+}}{1000\left(1+\sum_i m_i M_i\right)} \qquad \text{Eq 33}$$

where; ρ (kg m^{-3}) is the density of the electrolyte, and M_i (g mol^{-1}) is the molecular mass of species i, and m_i (mol kg^{-1}) is the molarity of species i.

$$j_o = nFx_{cat}\frac{kT}{h}e^{\frac{-\Delta G^*_{cat}}{RT}}e^{\frac{\alpha\Delta\mu^\circ}{RT}}\rho\frac{mM^{n+}}{1000\left(1+\sum_i m_i M_i\right)}\left(\gamma M^{n+}mM^{n+}\right)^{-\alpha}aM^{\alpha} \qquad \text{Eq 34}$$

Applying the same procedure to the anodic reaction yields the following expression:

$$j_o = nFx_{an}\frac{kT}{h}e^{\frac{-\Delta G^*_{an}}{RT}}e^{\frac{-(1-\alpha)\Delta\mu^\circ}{RT}}[M]\left(\gamma M^{n+}mM^{n+}\right)^{1-\alpha}aM^{1-\alpha} \qquad \text{Eq 35}$$

These equations both predict that the exchange current density varies with ion concentration to the power of 1-α, and often appear in the following, simplified, form:

$$j_0 = k_0[M^{n+}]^{1-\alpha} \qquad \text{Eq 36}$$

However, it is more appropriate to represent the exchange current density as a function of the activities of the metal and metal ions [2]:

$$j_0 = k_0\left(aM^{n+}\right)^{1-\alpha}\left(aM\right)^{\alpha} \qquad \text{Eq 37}$$

When the electrode surface is polarized such that the reaction is not at equilibrium, the voltage required to deviate from equilibrium is called the overpotential , η (V or J C^{-1}), and is defined as the difference between the potential at the electrode surface, E, more specifically the Outer-Helmholz plane, and the equilibrium potential, E_M.

$$\eta = E - E_M \qquad \text{Eq 38}$$

When the two potentials are equal, the overpotential is equal to zero and equilibrium exists. As previously described, the effect of the overpotential on electrode kinetics is partitioned by the transfer coefficient, α. This point is demonstrated in Fig 4, which illustrates cathodic polarization of a metal electrode surface.

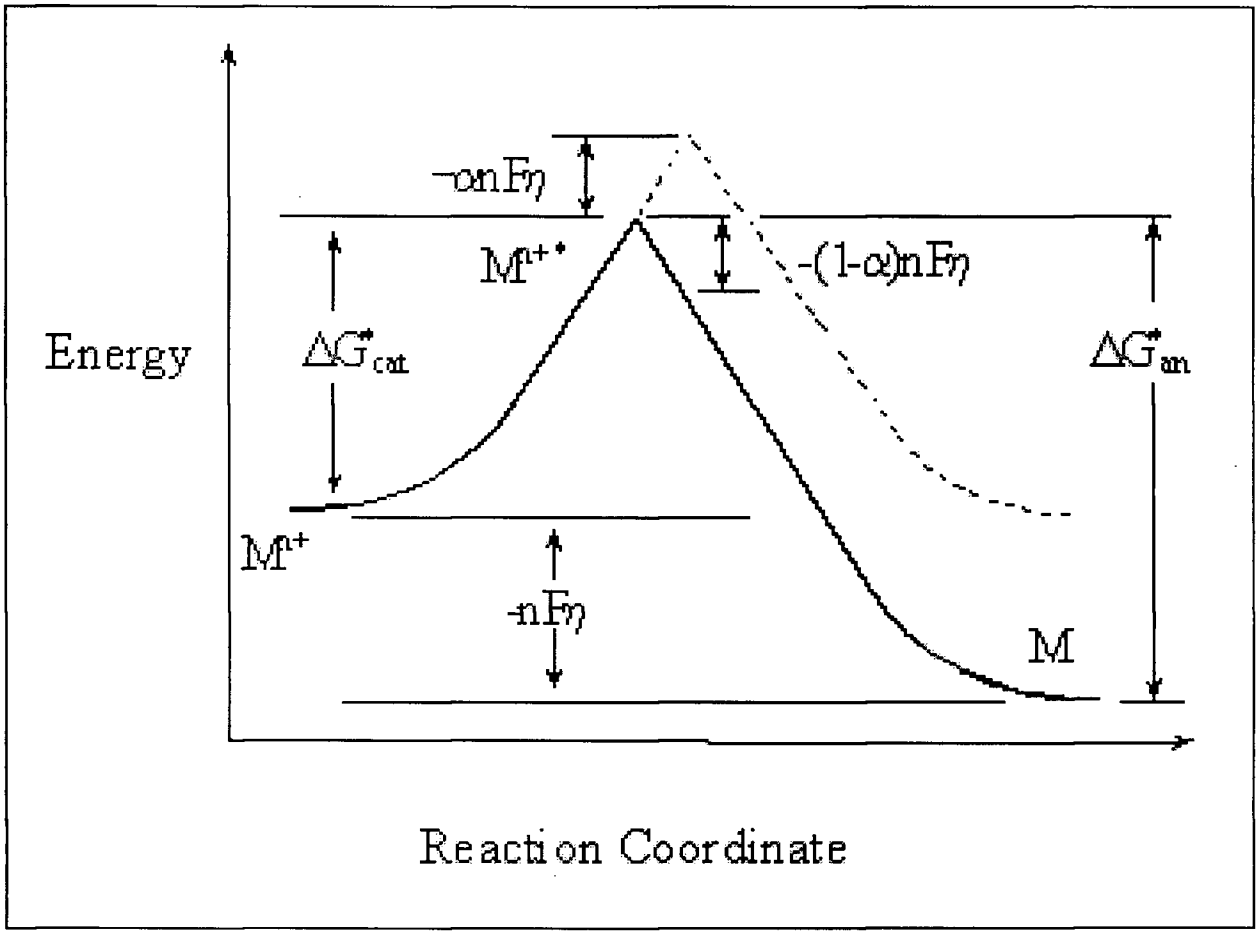

Fig 4: Reaction coordinate diagram of a polarized electrode

The activation energy barrier for the cathodic and anodic processing can be written with respect to the activation energy barrier under equilibrium conditions, ΔG^*_{eqm}:

$$\Delta G_{cat}^* = \Delta G^*_{eqm} - (-\alpha nF\eta) = \Delta G^*_{eqm} + \alpha nF\eta \qquad \text{Eq 39}$$

$$\Delta G_{an}^* = \Delta G^*_{eqm} + [-(1-\alpha)nF\eta] = \Delta G^*_{eqm} - (1-\alpha)nF\eta \qquad \text{Eq 40}$$

By substituting the above expressions into Eq 22, one obtains the following equation containing the rate constants for the forward and reverse reactions:

$$j_{net} = -nFx_f \frac{kT}{h} e^{\frac{-\Delta G^*_{eqm}}{RT}} e^{\frac{-\alpha nF\eta}{RT}} [M^{n+}] + nFx_r \frac{kT}{h} e^{\frac{-\Delta G^*_{eqm}}{RT}} e^{\frac{+(1-\alpha)nF\eta}{RT}} [M] \qquad \text{Eq 41}$$

Multiplying the forward current term of the equation, top and bottom, by the bulk metal ion concentration, $[M^{n+}]^{bulk}$, allows for substitution of the exchange current density, from Eq 29.

$$j_{net} = -nFx_f \frac{kT}{h} e^{\frac{-\Delta G^*_{eqm}}{RT}} [M^{n+}]^{bulk} \frac{[M^{n+}]}{[M^{n+}]^{bulk}} e^{\frac{-\alpha nF\eta}{RT}} + nFx_r \frac{kT}{h} e^{\frac{-\Delta G^*_{eqm}}{RT}} [M] e^{\frac{+(1-\alpha)nF\eta}{RT}} = -j_0 \frac{[M^{n+}]}{[M^{n+}]^{bulk}} e^{\frac{-\alpha nF\eta}{RT}} + j_0 e^{\frac{+(1-\alpha)nF\eta}{RT}} \quad \text{Eq 42}$$

If mass transfer effects are neglected, the concentration of metal ions at the electrode surface is taken to be equal to its bulk concentration and Eq 42 reduces to the common form of the Butler-Volmer Equation:

$$j_{net} = -j_0 \left[e^{\frac{-\alpha nF\eta}{RT}} - e^{\frac{(1-\alpha)nF\eta}{RT}} \right] \quad \text{Eq 43}$$

The mass transport of metal ions to the electrode surface occurs by a combination of migration, under the influence the potential gradient that exists between the anode and cathode, and diffusion, due to the concentration gradient in the diffusion boundary layer, which is assumed to obey Fick's law:

$$\left(\frac{dM^{n+}}{dt} \right)_{mig} = \frac{t_{M^{n+}} I_{total}}{nF} \quad \text{Eq 44}$$

$$\left(\frac{dM^{n+}}{dt} \right)_{dif} = -\frac{D_{M^{n+}}}{\delta} A_e \left([M^{n+}]^{bulk} - [M^{n+}] \right) \quad \text{Eq 45}$$

where; t_M^{n+} is the transport number of the metal ions, which, by definition, corresponds to the fraction of the total current carried by the metal ions through the electrolyte, D_M^{n+} ($m^2\ s^{-1}$) is the diffusion coefficient of the metal ion, and δ (m) is the diffusion boundary layer thickness.

Since mass transport of metal ions to the electrode and the electron transfer reaction at the electrode surface occur in series, at steady state, the fluxes are equal.

$$\left(\frac{dM^{n+}}{dt} \right)_{rxn} = \left(\frac{dM^{n+}}{dt} \right)_{mig} + \left(\frac{dM^{n+}}{dt} \right)_{dif} \quad \text{Eq 46}$$

It is important to recognize that I_{net}, as defined in Eq 17, is the electric current corresponding to the net rate of the electrochemical reaction of interest, whereas I_{total} is the total current that is being passed between the anode and the cathode by the electrolyte, and that the two are not necessarily equal. However, the case where there is only one reaction occurring at the electrode will be the condition considered, i.e. $I_{total} = I_{net}$ Thus, from Eq 17, Eq 44 and Eq 45, we may rewrite Eq 46 as follows:

$$\frac{I_{net}}{nF} = \frac{t_{M^{n+}} I_{net}}{nF} - \frac{D_{M^{n+}}}{\delta} A\left([M^{n+}]^{bulk} - [M^{n+}]\right) \qquad \text{Eq 47}$$

Rearranging the above equation and converting currents to current densities, we obtain the following equation:

$$j_{net} = \frac{-D_{M^{n+}}}{\delta(1 - t_{M^{n+}})} nF\left([M^{n+}]^{bulk} - [M^{n+}]\right) \qquad \text{Eq 48}$$

The current density corresponding to the maximum flux of metal ions, when the surface concentration of the metal ion species approaches zero, is the limiting current density, j_{lim}.

$$j_{\lim} = \frac{-D_{M^{n+}}}{\delta(1 - t_{M^{n+}})} nF\left([M^{n+}]^{bulk}\right) \qquad \text{Eq 49}$$

Dividing Eq 48 by Eq 49 and rearranging, we obtain the following expression for the ratio of the concentration of metal ions at the electrode surface to their bulk concentration as a function of the net current density of the metal deposition reaction:

$$\frac{[M^{n+}]}{[M^{n+}]_{bulk}} = 1 - \frac{j_{net}}{j_{\lim}} \qquad \text{Eq 50}$$

The above expression is inserted into Eq 42 as follows:

$$j_{net} = -j_0 \left[\left(1 - \frac{j_{net}}{j_{\lim}}\right) e^{\frac{-\alpha nF\eta}{RT}} - e^{\frac{(1-\alpha)nF\eta}{RT}} \right] \qquad \text{Eq 51}$$

Rearranging the above equation to isolate the net current density, results in the final form of the extended Butler-Volmer Equation for a simple metal deposition reaction:

$$j_{net} = \frac{-j_0\left[e^{\frac{-\alpha nF\eta}{RT}} - e^{\frac{(1-\alpha)nF\eta}{RT}}\right]}{1 - \frac{j_0}{j_{\lim}} e^{\frac{-\alpha nF\eta}{RT}}} \qquad \text{Eq 52}$$

References:

1 G.W. Castellan, Physical Chemistry, 3rd Ed., The Benjamin/Cummings Publishing Company, Inc., Menlo Park, CA, U.S.A., (1983).

2 P. Dehlaney, in P. Dehlaney (Ed.), Advances in Electrochemistry and Electrochemical Engineering, Vol. 1, Interscience Publishers, Inc., New York, NY, U.S.A., pg. 238, (1961).

Appendix B: Procedure for Determination of Pitzer Parameters from Osmotic Data

Though the basic equations and nomenclature of the Pitzer Model are well established [1, 2], in the authors opinion, there is no simple and concise procedure for its implementation in the literature. This section is meant as a basic guide for fitting Pitzer parameters to a set of osmotic data for strong electrolytes containing multiple components.

Fitting of the Pitzer Model appears to be most commonly based on sets of isopiestic data, where a number of observations, N_{obs}, of solvent activity, a_s (which is often water), are directly made for corresponding solute(s) molalities, m, (mol kg^{-1}). The stoichiometric molal osmotic coefficient, ϕ_{st}, is calculated, for each solute molality as follows:

$$\phi_{st} = \frac{-1000\ln(a_s)}{vmM_s} \qquad \text{Eq 53}$$

where; v is the number of mols of ions created by complete dissociation of a mol of solute, and M_s (g mol^{-1}) is the molar mass of the solvent. If some knowledge exists for the actual degree of dissociation of the solute at each salt molality, e.g. from Raman data, then the observed osmotic coefficient, ϕ_{obs}, may be adjusted as follows:

$$\phi_{obs} = \frac{vm\phi_{st}}{\sum m_i} \qquad \text{Eq 54}$$

where; Σm_i is the sum of all the molalities of solvated species. Otherwise, it is conventional to assume complete dissociation, i.e. $\phi_{obs} = \phi_{st}$.

The first step in modelling the observed data is to estimate the set of adjustable parameters for specific interactions of each particular cation, M, and anion, X:

a) $\beta^{(0)}_{MX}, \beta^{(1)}_{MX}, \beta^{(2)}_{MX}$: second viral coefficients for interactions of oppositely charged ions including ion-pair formation.

b) C^{ϕ}_{MX} : third viral coefficient describing ion triplet formation.

c) $\theta_{MM'}$ and $\theta_{XX'}$: terms which account for interactions between like charged ions, where $M \neq M'$ and $X \neq X'$.

d) $\psi_{MM'X}$ and $\psi_{XX'M}$: terms which account for the modifying influence of an oppositely charged ion on θ interactions.

The parameters listed in a) and b) should be derived from binary mixtures of the ions with parameters in c) and d) being added to account for the influence of additional ions in more complex solutions.

The following sequence of calculations is then followed with the ionic strength of the electrolyte being calculated first:

$$I = \frac{1}{2}\sum_i z_i^2 m_i \qquad \text{Eq 55}$$

where; z_i and m_i are the charge and molality of species i.

For all specific cation-anion interactions, the third viral coefficients, C_{MX}, are calculated:

$$C_{MX} = \frac{C^{\phi}_{MX}}{2|z_M z_X|^{1/2}} \qquad \text{Eq 56}$$

where; z_M and z_X are the charges of M and X, respectively.

Next, the second viral coefficients, B^{ϕ}_{MX}, are calculated:

$$B^{\phi}_{MX} = \beta^{(0)}_{MX} + \beta^{(1)}_{MX} e^{-\alpha_1 I^{1/2}} + \beta^{(2)}_{MX} e^{-\alpha_2 I^{1/2}} \qquad \text{Eq 57}$$

where; $\alpha_1 = 2$ and $\alpha_2 = 0$ for 1-1 and 1-2 interactions, or $\alpha_1 = 1.4$ and $\alpha_2 = 12$ for higher charge interactions.

For each specific cation-cation or anion-anion interaction, the higher order electrostatic mixing terms ${}^E\theta_{ij}$ and ${}^E\theta_{ij}'$ are calculated as follows:

$${}^E\theta_{ij} = \frac{z_i z_j}{4I}\left[J(x_{ij}) - 0.5J(x_{ii}) - 0.5J(x_{jj})\right] \qquad \text{Eq 58}$$

$$ {}^{E}\theta_{ij}' = \frac{-{}^{E}\theta_{ij}}{I} + \frac{z_i z_j}{8I^2}\left[x_{ij}J'(x_{ij}) - 0.5x_{ii}J'(x_{ii}) - 0.5x_{jj}J'(x_{jj})\right] \qquad \text{Eq 59} $$

where;

$$ x_{ij} = 6z_i z_j A_\phi I^{1/2} \qquad \text{Eq 60} $$

The Debye-Hückel osmotic coefficient, A_ϕ, may be calculated from the following expression [3]:

$$ A_\phi \approx 0.377 + 0.0004684(T - 273.15) + 0.00000374(T - 273.15)^2 \qquad \text{Eq 61} $$

The terms $J(x_{ij})$ and $J'(x_{ij})$ may be calculated using the following approximations [4]:

$$ J(x_{ij}) \approx \frac{x_{ij}}{4 + 4.581x_{ij}^{-0.7237}e^{-0.012x_{ij}^{0.528}}} \qquad \text{Eq 62} $$

$$ J'(x_{ij}) \approx \frac{J(x_{ij} + dx_{ij}) - J(x_{ij})}{dx_{ij}} \qquad \text{Eq 63} $$

The electrostatic mixing terms, calculated in Eq 58 and Eq 59, are used to calculate the mixed electrolyte second viral coefficients, Φ^{ϕ}_{ij}, as follows:

$$ \Phi^{\phi}_{ij} = \theta_{ij} + {}^{E}\theta_{ij} + I\,{}^{E}\theta_{ij}' \qquad \text{Eq 64} $$

All the above-calculated coefficients are then used to calculate the osmotic coefficient at each solute molality:

$$ \phi_{calc} = 1 + \frac{2}{\sum_i m_i}\left[\begin{array}{l} \dfrac{-A_\phi I^{3/2}}{1 + 1.2I^{1/2}} + \sum_c \sum_a m_c m_a \left(B^{\phi}_{ca} + ZC_{ca}\right) + \\ \sum_{c<} \sum_c m_c m_{c'} \left(\Phi^{\phi}_{cc'} + \sum_a m_a \psi_{cc'a}\right) + \\ \sum_{a<} \sum_a m_a m_{a'} \left(\Phi^{\phi}_{aa'} + \sum_c m_c \psi_{aa'c}\right) \end{array}\right] \qquad \text{Eq 65} $$

where;

$$Z = \sum_i m_i |z_i| \qquad \text{Eq 66}$$

Typically, deviations from observed and calculated osmotic coefficients are represented by the sum of the square of the errors, *SSE*:

$$SSE = \sum_{N_{obs}} (\phi_{calc} - \phi_{obs})^2 \qquad \text{Eq 67}$$

The *SSE* is minimized by modifying the adjustable interaction parameters and repeating the calculation process, Eq 55 through Eq 67, until convergence. Fitting always begins with the minimum number of adjustable parameters and acceptance or rejection of an additional parameters is made from examination of the corresponding value of chi-square, χ^2:

$$\chi^2 = \frac{\sum_{N_{obs}} \left[\frac{\phi_{obs} - \phi_{calc}}{\sigma_{obs}} \right]^2}{N_{obs} - \nu} \qquad \text{Eq 68}$$

where; σ_{obs} is the estimated uncertainty in the observed osmotic coefficient data, and ν, in this case, is the number of adjustable parameters. An additional parameter is, generally, accepted if the value of χ^2 decreases from that calculated for the previous set of parameters.

EMF data may be used to directly calculate the activity coefficient of a particular species to influence fitting or simply be calculated after the fact. The process of calculating a single ion activity coefficient begins by, first, calculating the second viral coefficients, B_{MX}, and B'_{MX} as follows:

$$B_{MX} = \beta_{MX}^{(0)} + \beta_{MX}^{(1)} f(\alpha_1 I^{1/2}) + \beta_{MX}^{(2)} f(\alpha_2 I^{1/2}) \qquad \text{Eq 69}$$

$$B_{MX}' = \frac{\beta_{MX}^{(1)} f'(\alpha_1 I^{1/2})}{I} + \frac{\beta_{MX}^{(2)} f'(\alpha_2 I^{1/2})}{I} \qquad \text{Eq 70}$$

where; the functions $f(x)$ and $f'(x)$ are given as follows:

$$f(x) = \frac{2\left[1 - (1+x)e^{-x}\right]}{x^2} \qquad \text{Eq 71}$$

$$f'(x) = e^{-x} - f(x) \qquad \text{Eq 72}$$

Next, the following mixed electrolyte second viral coefficients, Φ^{ϕ}_{ij} and Φ'_{ij}, are calculated:

$$\Phi_{ij}' = {}^{E}\theta_{ij}' \qquad \text{Eq 73}$$

$$\Phi^{\phi}_{ij} = \theta_{ij} + {}^{E}\theta_{ij} + I\,{}^{E}\theta_{ij}' \qquad \text{Eq 74}$$

These coefficients are used to calculate the term F:

$$F = -A_{\phi}\left[\frac{I^{1/2}}{1+1.2I^{1/2}} + \frac{2}{1.2}\ln\left(1+1.2I^{1/2}\right)\right] + \sum_{c}\sum_{a} m_c m_a B_{ca}' + \sum_{c<}\sum_{c'} m_c m_{c'} \Phi_{cc'}' + \sum_{a<}\sum_{a'} m_a m_{a'} \Phi_{aa'}' \qquad \text{Eq 75}$$

The activity coefficient of a specific cation, M, or anion, X, are then be calculated as follows:

$$\ln(\gamma_M) = z_M^{\,2} F + \sum_{a} m_a (2B_{Ma} + ZC_{Ma}) + \sum_{c} m_c \left(2\Phi_{Mc} + \sum_{a} m_a \psi_{Mca}\right) + \sum_{a<}\sum_{a'} m_a m_{a'} \psi_{Maa'} + z_M \sum_{c}\sum_{a} m_c m_a C_{ca} \qquad \text{Eq 76}$$

$$\ln(\gamma_X) = z_X^{\,2} F + \sum_{c} m_c (2B_{cX} + ZC_{cX}) + \sum_{a} m_a \left(2\Phi_{Xa} + \sum_{c} m_c \psi_{Xac}\right) + \sum_{c<}\sum_{c'} m_c m_{c'} \psi_{Xcc'} + |z_X| \sum_{c}\sum_{a} m_c m_a C_{ca} \qquad \text{Eq 77}$$

References:

1 H. Kim, and W.J. Frederick, *J. Chem. Eng. Data*, **33**, pp. 177-184, (1988).

2 H. Kim, and W.J. Frederick, *J. Chem. Eng. Data*, **33**, pp. 278-283, (1988).

3 K.S. Pitzer, R.N. Roy, and L.F. Silvester, *J. Am. Chem. Soc.*, **99**(15), pp. 4930-4936, (1977).

4 S.L. Clegg, J.A. Rard, and K.S. Pitzer, *J. Chem. Soc. Faraday Trans.*, **90**(13), pp. 1875-1894, (1994).

Appendix C: Wiart's Model of Zinc Electrocrystallisation from Acidic Sulphate Electrolytes

The reaction of Wiarts Model are given below along with their respective rate constants, K_i (m^{-2} s^{-1}) [1] for pure acidic zinc sulphate electrolytes at 25 °C:

$$Zn + H^+ + e^- \xrightarrow{K_1} ZnH_{ad} \qquad K_1 = 3.57\times10^{-4}[H^+]\exp(-5\eta_{Zn}) \qquad \text{Eq 78}$$

$$ZnH_{ad} + H^+ + e^- \xrightarrow{K_2} Zn + H_2 \qquad K_2 = 5.00\times10^{-6}[H^+]\exp(-32\eta_{Zn}) \qquad \text{Eq 79}$$

$$Zn^{2+} + e^- \xrightarrow{K_3} Zn^+{}_{ad} \qquad K_3 = 5.95\times10^{-6}[Zn^{2+}]\exp(-40\eta_{Zn}) \qquad \text{Eq 80}$$

$$Zn^+{}_{ad} + e^- \xrightarrow{K_4} Zn \qquad K_4 = 8.40\times10^{-4}\exp(-10\eta_{Zn}) \qquad \text{Eq 81}$$

$$Zn^+{}_{ad} + e^- \xrightarrow{K_5} Zn^* \qquad K_5 = 5.00\times10^{-7}[Zn^{2+}]\exp(-16\eta_{Zn}) \qquad \text{Eq 82}$$

$$Zn^* \xrightarrow{K_6} Zn \qquad K_6 = 1.70\times10^{-5} \qquad \text{Eq 83}$$

$$Zn^{2+} + Zn^* + 2e^- \xrightarrow{K_7} Zn + Zn^* \qquad K_7 = 6.67\times10^{-3}[Zn^{2+}]\exp(-16\eta_{Zn}) \qquad \text{Eq 84}$$

$$Zn \xrightarrow{K_8} Zn^{2+} + 2e^- \qquad K_8 = 2.50\times10^{-4}\exp(40\eta_{Zn}) \qquad \text{Eq 85}$$

where; zinc and proton concentrations, $[Zn^{2+}]$ and $[H^+]$, are inputted in mol dm^{-3}, and the zinc overpotential, η_{Zn}, is inputted in V. Where applicable, the pre-exponents have been normalized for the calculated H^+ concentration, 1.40 mol dm^{-3}, corresponding to the stoichiometric H_2SO_4 concentration employed in the study of Cachet and Wiart, 1.22 mol dm^{-3}.

The fractional coverages of surface active species are calculated as follows:

$$\theta_{ZnH_{ad}} = \frac{K_1}{K_1 + K_2(1 + K_3/K_4)} \qquad \text{Eq 86}$$

$$\theta_{Zn^+_{ad}} = \frac{K_2 K_3}{K_1 K_4} \qquad \text{Eq 87}$$

$$\theta_{Zn^*} = \frac{K_5}{K_6}\theta_{Zn^+_{ad}} \qquad \text{Eq 88}$$

The partial current densities are calculated as follows:

$$j_{Zn} = -2F\left(K_4\theta_{Zn^+_{ad}} + K_7\theta_{Zn^*}\right) \quad \text{Eq 89}$$

$$j_H = -2FK_2\theta_{ZnH_{ad}} \quad \text{Eq 90}$$

The current efficiency is calculated in the standard manner:

$$\Phi_e = \frac{j_{Zn}}{j_{Zn} + j_H} \quad \text{Eq 91}$$

References:

1 R. Cachet, and R. Wiart, *Electrochim. Acta*, **44**, pp. 4743-4751, (1999).

Appendix D: Calibration of Rotating Ring-Disc Electrode

The ring-disc electrode used in this study was calibrated using a ferro/ferricyanide solution [1], composed of 0.01 mol dm^{-3} $K_3Fe(CN)_6$ and 0.03 mol dm^{-3} $K_4Fe(CN)_6$ in 0.5 mol dm^{-3} K_2CO_3 at approximately 22 °C, from which the collection efficiency was measured to be 0.2505 ± 0.002, from the limiting currents at rotation rates between 500 and 3500 rpm. However, when calibrated to detect hydrogen evolution, in 0.007 M H_2SO_4 at approximately 22 °C, the observed collection efficiency was lower than that observed for ferri/ferrocyanide and decayed with time. Dissolved hydrogen is a neutral molecule, which must first adsorb onto platinum before being oxidized [2]. Popić [3] observed a similar decay in collection efficiency for detection of hydrogen, using an aluminium disc-platinum ring electrode, which was attributed to progressive poisoning of the ring electrode surface by trace levels of contaminants. The following potential step sequence, similar to that proposed by Popić [3], was developed to activate the ring electrode for hydrogen oxidation; 1) 900 mV (SCE) for 60 seconds (oxidizes the ring and drives off contaminants while avoiding oxygen evolution), 2) -250 mV (SCE) for 10 seconds (reduces the electrode), and 3) 250 mV (SCE) to hydrogen detection (large overpotential for hydrogen oxidation while avoiding oxidation of the ring). These procedures are referred to as "Ring Oxidation", "Ring Activation" and Ring Reduction", respectively in Appendix F. The theoretical collection efficiency was consistently achieved immediately following each application of this procedure. However, the collection efficiency was still unstable and continued to decay with time.

Frazer and Hamilton [4] employed a gold rotating ring-disc electrode to measure current efficiency during electrowinning of zinc from an electrolyte containing 0.8 mol dm^{-3} $ZnSO_4$ and 1.07 mol dm^{-3} H_2SO_4. Because gold is an ineffective electrocatalyst for hydrogen oxidation, the ring of their electrode was platinised in order to detect evolved hydrogen. Frazer and Hamilton did not report any problems related to the decay in ring response other than due to hydrogen bubble formation, occurring at hydrogen evolution rates > *ca.* 19.5 A m^{-2} at 1200 rpm, even though deposition times were in the order of 2 hours. Thus, it was surmised that the increase in the real surface area of the ring electrode, resulting from platinisation, must have been sufficient to maintain an excess of active sites for hydrogen adsorption throughout the test period. The ring electrode of the platinum ring-disc electrode used in this study was subsequently platinised using a standard procedure described elsewhere [5]. The stability of collection efficiency of evolved hydrogen for the platinised ring-disc electrode was evaluated in sulphuric acid, in the presence of zinc, after applying the previously outlined procedure for activating the ring (see Fig 5). Overall,

the collection efficiency was calculated to be 0.228 ±0.011, close to the theoretical value 0.240, and observed to be stable up to 30 minutes (the longest period tested).

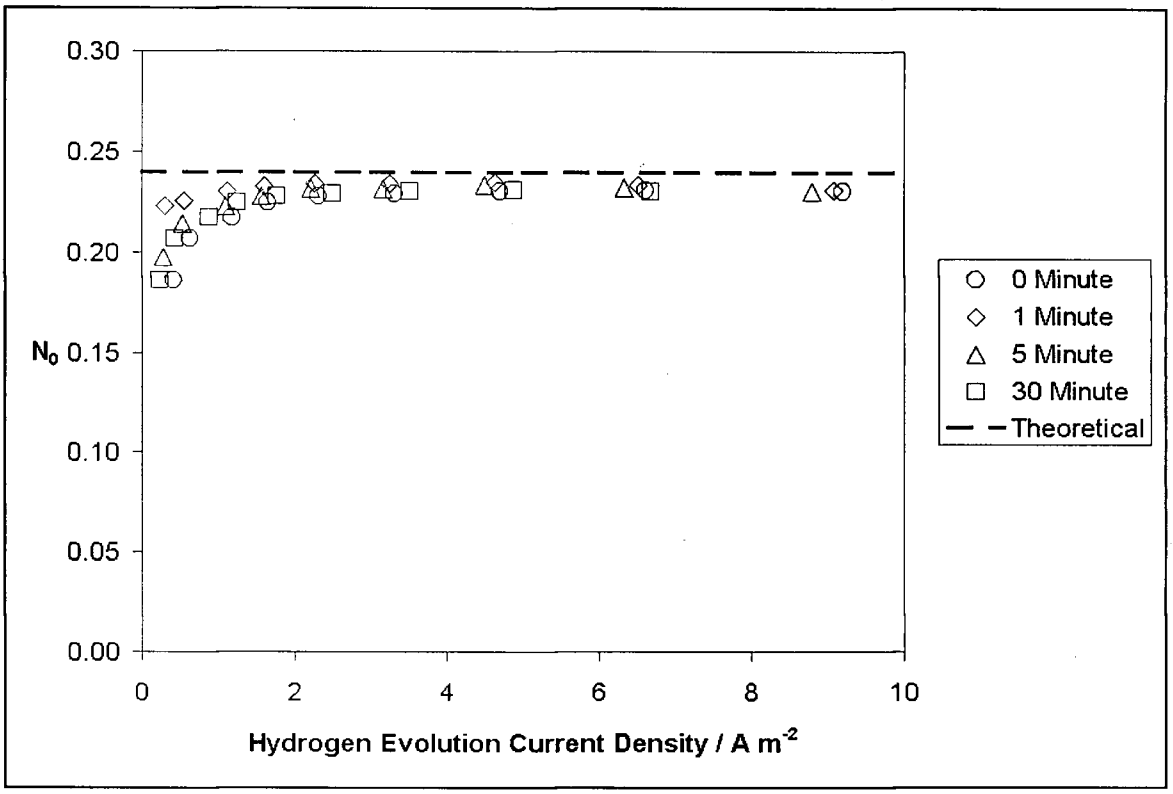

Fig 5: Collection efficiency of a platinised ring electrode, in 0.1 mol dm^{-3} H_2SO_4 with 2×10^{-3} mol dm^{-3} $ZnSO_4$ at 25 °C, 1600 rpm electrode rotation rate, for hydrogen evolved at a platinum disc from a series of 5 second potential steps at; -240 mV, -250 mV, -260 mV, -265 mV, -270 mV, -275 mV, -280 mV, -290 mV, and -300 mV (SCE), as a function of ring conditioning time at 250 mV (SCE).

References:

1 W.M. Taama, R.E. Plimley, and K. Scott, *Electrochimica Acta*, **41**(4), pp. 549-551, (1996).

2 G. Jerkiewicz, *Progress in Surface Science*, **57**(2), 137-186, (1998).

3 J.P. Popić, M. Avromov-Ivić, and D.M. Dražić, *J. Serb. Chem. Soc.*, **61**(12), 1233-1240, (1996).

4 E.J. Frazer, and I.C. Hamilton, *J. Appl. Electrochem.*, **16**, 387-392, (1986).

5 M.J. Joncich, and N. Hackerman, *J. Electrochem. Soc.*, **111**(11), pp. 1286-1289, (1964).

Appendix E: Matlab Script for Calculating Surface Area from an AFM Image

```
function R = surface_area(inputdata,L);
%
% function surface_area(inputdata,L);
%
% This file calculates the actual area of a (rough) surface.
% Approach is to divide surface into 2*(m-1)^2 triangles and calculating
%    the area of these individual surfaces; then summing them up.
%
% INPUT:
%    h - square, nxn surface matrix to calculate area of (heights in Angstroms);
%    L - length of side in microns.
%
% OUTPUT:
%    R - ratio of actual surface area to L^2
%
% EXAMPLE:
%    load('filename');
%    R = surface_area(filename,10)
%
% Anders BALLESTAD, August 08 2002.

m = min(size(inputdata));
ic = inputdata/10000;   % Input data is now in micron heights.
h = ic;
dx = L/(m-1);          %  x increment; dx=dy.
dx2 = dx*dx;

% CALCULATIONS

[h2,a,b,c] = get_abc(h,m);
local_area = 1/2*(sqrt(dx2+(a-h2).^2).*sqrt(dx2+(c-a).^2)+...
   sqrt(dx2+(c-b).^2).*sqrt(dx2+(b-h2).^2));
total_area = sum(sum(local_area));
R = total_area/L/L;

h_rms = mean(std(h))*1000;
disp(['Surf. Area = ',num2str(total_area), 'um^2, and RMS = ', num2str(h_rms), 'nm']);
disp(['Area/L^2 = ',num2str(total_area/L/L)])

%-----------------------------------------------------------------------------
function [h2,a,b,c] = get_abc(h,m)
   h2 = h(1:m-1,1:m-1);          % The lower m-2 points
   a = h(1:m-1,2:m);             % +1 in x
   b = h(2:m,1:m-1);             % +1 in y.
   c = h(2:m,2:m);               % +1 in x and +1 in y
```

Appendix F: Autolab Zinc Deposition Procedure

```
Procedure!Method = CM

Procedure!Open("D:\Procedures\Normal Pulse Procedures\Ring Oxidation")
Procedure!Start
Procedure!Open("D:\Procedures\Normal Pulse Procedures\Ring Reduction")
Procedure!Start
Procedure!Open("D:\Procedures\Normal Pulse Procedures\Ring Activation")
Procedure!Start

Procedure!Open("D:\Procedures\Normal Pulse Procedures\-1100 mV Pulse")
Procedure!Start
Dataset!SaveAs("D:\Data\Current Data\-1100 mV Pulse")

Procedure!Open("D:\Procedures\Normal Pulse Procedures\-1125 mV Pulse")
Procedure!Start
Dataset!SaveAs("D:\Data\Current Data\-1125 mV Pulse")

Procedure!Open("D:\Procedures\Normal Pulse Procedures\-1150 mV Pulse")
Procedure!Start
Dataset!SaveAs("D:\Data\Current Data\-1150 mV Pulse")

Procedure!Open("D:\Procedures\Normal Pulse Procedures\-1200 mV Pulse")
Procedure!Start
Dataset!SaveAs("D:\Data\Current Data\-1200 mV Pulse")

Procedure!Open("D:\Procedures\Normal Pulse Procedures\-1250 mV Pulse")
Procedure!Start
Dataset!SaveAs("D:\Data\Current Data\-1250 mV Pulse")

Procedure!Open("D:\Procedures\Normal Pulse Procedures\-1300 mV Pulse")
Procedure!Start
Dataset!SaveAs("D:\Data\Current Data\-1300 mV Pulse")

Procedure!Open("D:\Procedures\Normal Pulse Procedures\-1400 mV Pulse")
Procedure!Start
Dataset!SaveAs("D:\Data\Current Data\-1400 mV Pulse")

Procedure!Open("D:\Procedures\Normal Pulse Procedures\-1500 mV Pulse")
Procedure!Start
Dataset!SaveAs("D:\Data\Current Data\-1500 mV Pulse")

Procedure!Open("D:\Procedures\Normal Pulse Procedures\-1750 mV Pulse")
Procedure!Start
Dataset!SaveAs("D:\Data\Current Data\-1750 mV Pulse")

Procedure!Open("D:\Procedures\Normal Pulse Procedures\-2000 mV Pulse")
Procedure!Start
```

```
Dataset!SaveAs("D:\Data\Current Data\-2000 mV Pulse")

Procedure!Open("D:\Procedures\Normal Pulse Procedures\-2500 mV Pulse")
Procedure!Start
Dataset!SaveAs("D:\Data\Current Data\-2500 mV Pulse")

Procedure!Open("D:\Procedures\Progessive Pulse Procedures\Progressive Pulse")
Procedure!Start
Dataset!SaveAs("D:\Data\Current Data\Progressive Pulse")

Procedure!Method = CV

Procedure!Open("D:\Procedures\CV Procedures\Reversible Potential")
Procedure!Start
Dataset!SaveAs("D:\Data\Current Data\Reversible Potential")

Fra!Start("D:\Procedures\FRA Low Acid Project")

System!Beep
```

Appendix G: Pitzer Parameters for H_2SO_4.

Parameter	Value[1]
$\beta^{(0)}$ H^+-HSO_4^-	0.222970
$\beta^{(1)}$ H^+-HSO_4^-	0.460016
C^{ϕ} H^+-HSO_4^-	-0.0026601
$\beta^{(0)}$ H^+-SO_4^{2-}	0.0642129
$\beta^{(1)}$ H^+-SO_4^{2-}	0.2259017
C^{ϕ} H^+-SO_4^{2-}	0.0311257
ψ H^+-HSO_4^-- SO_4^{2-}	0.0278059
θ HSO_4^-- SO_4^{2-}	-0.1353418

References:

1 J.K. Hovey, K.S. Pitzer, and J.A. Rard, *J. Chem. Thermodynamics*, 25, pp. 173-192, (1993).

Appendix H: Estimation of Current Inefficiency due to Oxygen Reduction at the Cathode

Conventional zinc electrowinning is carried out in unsegmented cells with oxygen evolution as the anode reaction and thus, the electrolyte is probably saturated with dissolved oxygen. During zinc electrowinning there is an enormous overpotential for oxygen reduction at the cathode, *ca.* 3V, and so oxygen is probably reduced at its limiting current density. The elements necessary for estimating the current inefficiency due to oxygen reduction, j_{O_2}, are the solubility of dissolved oxygen, $[O_2]$ (mol m^{-3}), the boundary layer thickness, δ (m), and the diffusion coefficient of dissolved oxygen, D_{O_2} (m^2 s^{-1}):

$$j_{O_2} = -\frac{4FD_{O_2}[O_2]}{\delta} \qquad \text{Eq 92}$$

The level of dissolved oxygen in zinc electrolyte may be estimated according to the procedure outlined by Tromans[1], which estimates the fraction of water available to interact with oxygen as a function of electrolyte composition and temperature. The effective fraction of water, ϕ, available to interact with oxygen is calculated by calculating ϕ–factors for each individual salt, as a function of salt molality, *mSalt* (mol kg^{-1}), according to the following expression:

$$\phi_{Salt}(mSalt) = \left[\frac{1}{1+\kappa_{Salt}\, mSalt^{y_{Salt}}}\right]^{\eta_{Salt}} \qquad \text{Eq 93}$$

where; κ_{Salt} , y_{Salt} , and η_{Salt} are constants for each salt, some of which are tabulated below:

Table 1: Selected constants for calculating ϕ–factors. Taken from [1].

Salt	κ	y	η
H_2SO_4	2.01628	1.253475	0.168954
$ZnSO_4$	0.232671	1.010428	2.655655
Na_2SO_4	0.629498	0.911841	1.440175
K_2SO_4	0.55	0.911841	1.440175
$MgSO_4$	0.119674	1.107738	5.455537
$Al_2(SO_4)_3$	0.641163	0.954719	3.3033594

Another empirical term that must be determined is q, which is the average of q_{Salt} values, calculated for each salt, according to the following expression:

$$q_{Salt} = \frac{\ln(\phi_{Salt}(1.5))}{2\ln(\phi_{Salt}(0.5))} - 0.5 \qquad \text{Eq 94}$$

Once q has been calculated along with all ϕ_{Salt} values, the ϕ_{Salt} parameters are arranged such that the $\phi_{Salt1} > \phi_{Salt2} > \phi_{Salt3}$ etc., and substituted into the following expression to calculate the equilibrium molality of dissolved oxygen in the electrolyte, mO_2 (mol kg^{-1}):

$$mO_2 = pO_2 \exp\left[\frac{-0.046T^2 - 1.378T + 203.35T\ln(T/298) + 68624}{8.3144T}\right]\phi_{Salt1}\left({}^{z}{}_{2}\Pi\phi_{Salti}\right)^q \qquad \text{Eq 95}$$

where; pO_2 (atm) is the partial pressure of oxygen, and T (K) is the absolute temperature, and (${}^{z}{}_{2}\Pi\phi_{Salti}$.) is the product of $\phi_{Salt2} \times \phi_{Salt3} \times \ldots \phi_{Saltz}$. Converting the units for oxygen concentration to mol m^{-3} is accomplished as described in Section 3.2. The value of the diffusion coefficient of dissolved oxygen, D_{O_2}, may be estimated from the following expression, also developed by Tromans [2]:

$$D_{O_2} = 1.363\times10^{-6} \exp\left\{-\frac{14277 + 4.661\times10^{19}T^{-6.8132}}{RT}\right\} \qquad \text{Eq 96}$$

As indicated in Section 2.4.3, the boundary layer thickness, δ (m), is dominated by micro-convection due to hydrogen evolution and may be estimated using one of the expressions in Table 2. However, due to general lack of agreement between these expressions, there is obviously considerable uncertainty in this calculation. Previously, the only reported estimation of current inefficiency due to the reduction of oxygen was that of Biegler and Swift [3], who claimed that it was in the order of 1% of the total current.

Table 2: Selected expressions for calculating mass transport coefficient of zinc.

Electrolyte	Hydrogen Evolution Current Density Range / A m^{-2}	$k_m = \frac{D_{Zn^{2+}}}{\delta}$ / m s^{-1}	Source
80 g dm^{-3} Zn^{2+}, 135 g dm^{-3} H_2SO_4, 5 mg dm^{-3} Cd^{2+}, 50°C	25-16000	$5.69\times10^{-4}(j_{H_2})^{0.5}$	4
1 mol dm^{-3} Zn^{2+}, 1.8 mol dm^{-3} H_2SO_4, 30-70°C	25-6000	$3.9\times10^{-6}(j_{H_2})^{0.5}$	5
25-65 g dm^{-3} Zn^{2+}, 65-215 g dm^{-3} H_2SO_4, 35-45°C	5-30	$1.66\times10^{-3}\left(\frac{j_{H_2}A_e}{2F}\frac{RT}{P}\right)^{0.3}$	6
0.05 mol dm^{-3} Cu^{2+}, 1.85 mol dm^{-3} H_2SO_4, 25°C	70-800	$4.59\times10^{-5}(j_{H_2})^{0.5}$	7
1 mol dm^{-3} KOH, 0.1 mol dm^{-3} KCN, 0.02 mol dm^{-3} AgCN, 25-65°C	0-4000	$1.3\times10^{\left[-5+0.24\left(\frac{j_{H_2}}{1000}\right)^{0.38}\right]}$	8

References:

1 D. Tromans, *Hydrometallurgy*, **50**, pp. 279-296, (1998).

2 D. Tromans, *Corrosion*, **55**(10), pp. 942-947, (1999).

3 Bielger, T., and Swift, D.A., *Hydrometallugy*, **6**, 299-309, (1981).

4 H.M. Wang, S.F. Chen, T.J. O'Keefe, M. Degrez, and R. Winand, *J. Appl. Electrochem.*, **19**, pp. 174-182, (1989).

5 K.J. Cathro, *J. Electrochem. Soc.*, **139**(8), pp. 2186-2192, (1992).

6 G.W. Barton, and A.C. Scott, *J. Appl. Electrochem.*, **22**, pp. 104-115, (1992).

7 Y. Fukunaka, K. Suzuki, A. Ueda, and Y. Kondo, *J. Electrochem. Soc.*, **136**(4), pp. 1002-1009, (1989).

8 H.F.M. Gijsbers, and L.J.J. Janssen, *J. Appl. Electrochem.*, **19**, pp. 637-648, (1989).

Appendix I: Estimation of Oxygen Evolution Overpotential

The conventional anode reaction in zinc electrowinning is oxygen evolution from the electrolysis of water, which is conventionally carried out using Pb based anodes. Since the electrolyte is aqueous, mass transfer limitations due to depletion of water at the anode may be ignored and the relationship between anode overpotential, η_{H_2O} (V), and oxygen evolution current density, j_{H_2O} (A m^{-2}), may be adequately described by the Tafel equation:

$$\eta_{H_2O} = \frac{2.303RT}{\alpha nF}\log\left(j_{0,H_2O}\right) + \frac{2.303RT}{\alpha nF}\log\left(j_{H_2O}\right) = a + b\log\left(j_{H_2O}\right) \qquad \text{Eq 97}$$

where; a (V) is the is the Tafel constant and b (V decade^{-1}) is the Tafel slope.

Barton and Scott [1], in their model of zinc electrowinning, quote Tafel parameters (0.306 V for a and 0.146 V dec^{-1} for b) for their Pb anode (0.75 % Ag) which was covered in a manganese dioxide scale, as is typical for the relatively impure conditions employed in industry. The use of solvent extraction to purify electrolytes would avoid ingress of manganese into the electrolyte and thus, it may be useful to consider Tafel parameters for Pb based anodes which are free of manganese dioxide. Hein and Schierle[2] have published Tafel parameters, see Table 1, for a wide range of Pb based anodes which may be applicable for electrowinning from purified zinc electrolytes.

Table 1: Tafel constants for various Pb based Pb-Ag-Ca anodes in 200 g dm^{-3} H_2SO_4 at 25°C. Taken from [2].

Ag / %	Ca / %	a / V	b / V dec^{-1}	Ag / %	Ca / %	a / V	b / V dec^{-1}
0	0	1.732	0.077	0	1	1.661	0.096
0.1	0	1.718	0.079	0	1.5	1.634	0.093
0.25	0	1.692	0.087	0.05	0.2	1.718	0.093
0.5	0	1.668	0.102	0.05	0.8	1.664	0.097
1	0	1.599	0.131	0.1	0.4	1.706	0.088
2.5	0	1.598	0.120	0.1	0.7	1.655	0.106
0	0.1	1.757	0.072	0.25	0.2	1.647	0.120
0	0.3	1.725	0.079	0.25	0.8	1.613	0.117
0	0.7	1.701	0.082				

Dimensionally stable anodes, DSAs, are known to catalyzing oxygen evolution and their application in zinc electrowinning could result in significant cost savings [3 ,4 ,5 ,6 ,7]. However, their use has not been adopted since they tend to fail prematurely due to impurities in

industrial electrolytes. Solvent extraction has shown considerable promise as a means of producing a high purify zinc electrolyte to extend DSA service life [8, 9]. Lui et al. [7] have published Tafel parameters for various DSAs, which are tabulated below.

Table 2: Tafel constants for oxygen evolution for four DSAs and one Pb-Ag anode in 50 g dm^{-3} Zn^{2+}, 150 g dm^{-3} H_2SO_4, at 35°C. Taken from [7].

Anode	*a* / V	*b* / V dec^{-1}	Current Density Range / A m^{-2}
Ti/SbO_x-SnO_2/RuO_2-TiO_2	0.45	0.095	63-630
Ti/SbO_x-SnO_2/MnO_2	0.63	0.138	30-100
Graphite/ RuO_2-TiO_2	0.39	0.132	30-100
Ceramic/ RuO_2-TiO_2	0.20	0.120	30-100
Pb-Ag (1% Ag)	1.18	0.134	30-180

References

1 G.W. Barton, and A.C. Scott, *J. Appl. Electrochem.*, **22**, pp. 104-115, (1992).

2 K. Hein, T. Schierle, *Erzmetall*, **44**(9), pp. 447-451, (1991).

3 E.R. Cole, T.J. O'Keefe, *United States Bureau of Mines Investigation*, **8531**, (1981).

4 K.R. Koziol, and E.F. Wenk, *Schiftenreiche der Gesellschaft Deutscher Metallhutten und Bergleute*, **37**, pp. 409-428, (1982).

5 K. Mushiake, N. Masuko, and M. Takahashi, *Metallurgical Review of MMIJ*, **2**(2), pp. 37-51, (1985).

6 D.P. Ziegler, M. Dubrovsky, and J.W. Evans, *J. Appl. Electrochem.*, **11**, pp. 625-637, (1981).

7 Y. Liu, L. Wu, and B. Yuan, *Nonferrous Met (China)*, **37**(3), pp. 53-58, (1985).

8 U. Ducati, M. Bestetti, D. Colombo, L. Nodari, L. Belitrandi, and A. Cagol, A., in S.R. Rao (Ed.), Waste Processing and Recycling in Mineral and Metallurgical Industries, CIM, Montreal, Canada, pp. 65-77, (1998).

9 G. Diaz, D. Martin, and C. Lombera, in P.B. Queneau and R.D. Peterson (Eds.), Third International Symposium, Recycling of Metals and Engineered Materials, TMS/AIME, Warrendale, PA, U.S.A., pp. 623-635, (1995).